



HAL
open science

Hydro-mechanical modelling of damage-plasticity couplings in unsaturated geomaterials

Solenn Le Pense

► **To cite this version:**

Solenn Le Pense. Hydro-mechanical modelling of damage-plasticity couplings in unsaturated geomaterials. Other. Université Paris-Est, 2013. English. NNT : 2013PEST1122 . pastel-00975225

HAL Id: pastel-00975225

<https://pastel.hal.science/pastel-00975225>

Submitted on 8 Apr 2014

HAL is a multi-disciplinary open access archive for the deposit and dissemination of scientific research documents, whether they are published or not. The documents may come from teaching and research institutions in France or abroad, or from public or private research centers.

L'archive ouverte pluridisciplinaire **HAL**, est destinée au dépôt et à la diffusion de documents scientifiques de niveau recherche, publiés ou non, émanant des établissements d'enseignement et de recherche français ou étrangers, des laboratoires publics ou privés.



Thèse présentée pour obtenir le grade de
Docteur de l'Université Paris-Est

Spécialité : Géotechnique

par

Solenn Le Pense

Ecole Doctorale : SCIENCES, INGÉNIERIE ET ENVIRONNEMENT

***Modélisation hydro-mécanique du couplage
endommagement-plasticité dans les géomatériaux
non saturés***

Thèse soutenue le 3 octobre 2013 devant le jury composé de :

Djimédo Kondo	<i>Rapporteur</i>
Farid Benboudjema	<i>Rapporteur</i>
Antonio Gens	<i>Examineur</i>
Chloé Arson	<i>Examineur</i>
Ahmad Pouya	<i>Directeur de thèse</i>
Behrouz Gatmiri	<i>CoDirecteur de thèse</i>

REMERCIEMENTS

Le travail de thèse présenté dans ce mémoire a été effectué au sein de l'équipe géotechnique (CERMES) du laboratoire Navier, et financé par une allocation de recherche de l'École Normale Supérieure de Cachan.

Je tiens à remercier chaleureusement mes deux directeurs de thèse, Behrouz Gatmiri et Ahmad Pouya. Behrouz a été à l'origine de cette thèse et je le remercie de m'avoir fait confiance et de m'avoir laissé une grande liberté dans mes choix scientifiques. Je remercie Ahmad pour ses conseils avisés et sa présence lors de mes derniers mois de rédaction.

Je tiens également à remercier les membres de mon jury de thèse, Djimédo Kondo et Farid Benboudjema pour avoir accepté de rapporter ma thèse, et Antonio Gens pour être venu de Barcelone participer à ma soutenance.

Je remercie bien sûr vivement Chloé Arson pour son soutien et son aide scientifique tout au long de ma thèse et plus particulièrement lors de mon séjour à GeorgiaTech. J'espère que ce ne sont que les débuts d'une longue collaboration.

J'ai également beaucoup apprécié l'environnement de travail au CERMES. Merci à tous les chercheurs, doctorants et post-doctorants pour l'ambiance chaleureuse et les interactions scientifiques constructives. Je tiens à remercier plus particulièrement Jean-Michel Pereira pour ses conseils scientifiques et son aide lors de ma recherche d'emploi.

La thèse, ce n'est pas tous les jours facile. Je tiens donc à remercier mes collègues doctorants Valérie, Jean-François, Simona et Vinh, avec qui j'ai partagé des bureaux, des inquiétudes et des moments de détente. C'était un plaisir de faire ce bout de chemin ensemble.

Merci enfin à mes amis et à ma famille pour les bons moments passés en dehors du travail, et bien sûr à Antoine, de m'avoir soutenu et d'avoir toujours cru en moi.

This thesis work objective is the development of a hydro-mechanical constitutive model which accounts for damage-plasticity couplings in unsaturated geomaterials. The coupling of this model with hydraulic transfers is made possible by its implementation into the Finite Element code Θ -Stock. In order to achieve this implementation, a specific stress-point algorithm has been developed. Fully coupled hydro-mechanical problems have been simulated, such as the creation of the Excavation Damaged Zone around a tunnel and the initiation of damage due to desiccation and humidification.

A double effective stress incorporating both the effect of suction and damage (assumed isotropic) is defined based on thermodynamical considerations. The advantage of this approach is that it results in a unique stress variable being thermodynamically conjugated to elastic strains. A pressure-dependent hyperelastic formulation is used to describe the behaviour inside the elastic domain. The evolution of elastic rigidities with damage is then studied. Two hypotheses are compared, the principle of strain equivalence and the principle of equivalent energy.

Coupling between damage and plasticity phenomena is achieved by following the principle of strain equivalence and incorporating the effective stress into plasticity equations. The plasticity framework is based on the Barcelona Basic Model (Alonso *et al.*, 1990), itself based on the Cam-Clay model. Two distinct criteria are defined for damage and plasticity, which can be activated either independently or simultaneously. Their formulation in terms of effective stress and suction allows them to evolve in the total stress space with suction and damage changes. This leads to a direct coupling between damage and plasticity and allows the model to capture the ductile/brittle behaviour transition occurring when clays are drying.

A specific explicit algorithm has been developed to handle the association of the two dissipative phenomena. The implementation of the constitutive model into the Finite Element code Θ -Stock allowed for the simulation of fully coupled hydro-mechanical problems. The hydraulic transfer laws also consider the saturation state.

This fully coupled model is first applied to simulate the development of micro-cracks during dessication of a soil sample. Damage initiation is explained mainly by the important

pressure gradient appearing at the boundary when applying a high suction change.

Finally, a full-scale problem is simulated. The excavation of a tunnel, the desaturation of the surrounding soil and the creation of the excavation damaged zone are studied.

Cette thèse a pour but le développement d'un modèle constitutif hydromécanique prenant en compte le couplage de l'endommagement et de la plasticité dans les géomatériaux non-saturés. Le couplage de ce modèle avec les transferts hydrauliques est rendu possible par son implémentation dans le code aux éléments finis Θ -Stock. Un algorithme local a été développé spécifiquement dans ce but. Des problèmes hydromécaniques complètement couplés, tels que la création de la zone endommagée par excavation autour d'un tunnel ou la création d'un endommagement de dessiccation et d'humidification ont été simulés.

Une contrainte doublement effective incorporant les effets de la succion et de l'endommagement (considéré isotrope) a été définie en s'appuyant sur des bases thermodynamiques. Cette approche a l'avantage de considérer une unique variable de contrainte étant thermodynamiquement conjuguée aux déformations élastiques. Une formulation hyperélastique dépendante de la pression de confinement est utilisée pour décrire le comportement dans le domaine élastique. L'évolution des rigidités élastiques avec l'endommagement est comparée en considérant deux hypothèses : le principe des déformations équivalentes et le principe de l'énergie élastique équivalente.

L'hypothèse d'équivalence des déformations permet d'introduire la contrainte doublement effective dans les équations de plasticité et ainsi de coupler plasticité et endommagement. Les équations de plasticité sont dérivées du modèle de Barcelone (Alonso *et al.*, 1990), lui même basé sur le modèle de Cam-Clay. Deux critères distincts d'endommagement et de plasticité sont définis qui peuvent être activés aussi bien indépendamment que simultanément. Les surfaces de charges étant exprimées en fonction de la contrainte effective et de la succion, elles évoluent automatiquement en fonction de la succion et de l'endommagement dans l'espace des contraintes totales. Cela permet de représenter la transition d'un comportement ductile vers un comportement fragile lorsque le matériau est asséché.

Un algorithme local explicite a été développé pour gérer le couplage des deux phénomènes dissipatifs. L'implémentation du modèle constitutif dans le code aux éléments finis Θ -Stock permet l'étude de problèmes hydromécaniques complètement couplés, les lois de transfert dépendant elles aussi de l'état de saturation du matériau.

Ce modèle a d'abord été appliqué à la simulation du développement de micro-fissures lors du séchage d'une éprouvette. L'apparition de l'endommagement est expliqué principalement par le gradient de pression très important créé à la surface de l'échantillon lorsqu'on applique une forte variation de succion.

Enfin, un problème à échelle réelle est simulé. L'excavation d'un tunnel, la désaturation du sol environnant dû à la ventilation, ainsi que la création de la zone endommagée par excavation sont étudiés. L'étendue des zones d'endommagement et de déformations plastiques autour du tunnel est étudiée.

TABLE OF CONTENTS

Remerciements	i
Abstract	iii
Table of contents	vii
List of Symbols	xi
Introduction	1
1 Definition of the double effective stress	5
1.1 Unsaturated soils	6
1.1.1 Modelling approaches in the literature	8
1.1.2 Constitutive stress based on energy considerations	11
1.1.3 Water retention properties and their impact on constitutive stress .	13
1.2 Principle of effective stress in Continuum Damage Mechanics	18
1.3 Introduction of a double effective stress	19
2 Elastic behaviour	21
2.1 Preliminaries	22
2.2 Pressure dependence of moduli in Cam-Clay	24
2.3 Pressure dependent hyperelastic models	25
2.4 Effect of damage on elastic behaviour	27
2.4.1 Principle of strain equivalence	30
2.4.2 Principle of equivalent elastic energy	30
2.4.3 Comparison of both assumptions	31
2.5 Unsaturated elastic behaviour	33

2.5.1	Effect of suction on the mechanical elastic rigidity	34
2.5.2	Elastic strains due to suction changes	34
2.6	General elasticity law	36
3	Dissipative phenomena (damage and plasticity)	37
3.1	Thermodynamics	38
3.1.1	Second law	38
3.1.2	Helmholtz free energy	39
3.1.3	Clausius-Duhem Inequality – dissipation	39
3.1.4	Hypotheses on the form of Helmholtz free energy	40
3.2	Damage criterion and evolution	41
3.2.1	General framework	41
3.2.2	Specific functions	42
3.3	Plasticity	46
3.3.1	Definition of the preconsolidation pressure and hardening law	48
3.3.2	Dependence of the preconsolidation pressure on suction	50
3.3.3	Yield surface	52
3.3.4	Plastic flow rule	54
3.4	Derivation of the incremental law	55
4	Hydraulic transfers	59
4.1	Water phase	60
4.1.1	Liquid water flow	60
4.1.2	Water vapour flow	63
4.1.3	Water mass conservation equation	64
4.2	Air phase	65
5	Numerical implementation	69
5.1	Strong form of the coupled problem	70
5.1.1	Synthesis of the equations	70
5.1.2	Boundary conditions	71
5.1.3	Initial conditions	72
5.2	Weak form	72
5.3	Application of the Finite Element Method	75
5.3.1	Spatial discretisation	75
5.3.2	Numerical integration	79
5.3.3	System to solve	80
5.4	Discretisation in time	81

5.5	Iterative resolution of equilibrium equations system	83
5.6	Stress point algorithm	85
5.6.1	Input	85
5.6.2	Trial elastic state	86
5.6.3	Plasticity	87
5.6.4	Damage	89
5.6.5	Final state	90
6	Simulation of laboratory experiments	91
6.1	Callovo-Oxfordian Argillite	92
6.1.1	Specific model for argillite	92
6.1.2	Simulation of mechanical laboratory tests	94
6.1.3	Effect of damage hardening parameter	100
6.2	Boom Clay	101
6.2.1	Model parameters	102
6.2.2	Simulation of mechanical laboratory tests	103
6.2.3	Suction effects on mechanical behaviour	108
6.3	Conclusion	110
7	Application to hydro-mechanical problems	111
7.1	Damage induced by hydric loading	112
7.1.1	Material parameters	113
7.1.2	Geometry and boundary conditions	114
7.1.3	Desiccation	115
7.1.4	Humidification	117
7.2	Excavation modelling	120
7.2.1	Impact of suction on the extent and properties of the excavation damaged zone	120
7.2.2	Simulation of excavation under undrained conditions	125
	Conclusions and perspectives	129
	A Derivatives for Cam-Clay plasticity	133
	References	135

This list of symbols aims at listing the main symbols which are used throughout the thesis.

Operators

- $\dot{(\cdot)}, d(\cdot)$ Variable increment
- $\nabla \cdot (\cdot)$ Divergence
- $\nabla (\cdot)$ Gradient
- \cdot Inner product with single contraction
- $:$ Inner product with double contraction
- \otimes Tensorial product
- $tr(\cdot)$ Trace of a tensor
- $det(\cdot)$ Determinant

Superscripts

- e Elastic component
- p Plastic component
- $*$ Effective quantities in relation to suction
- \sim Effective quantities in relation to damage

Subscripts

- g Refers to gas
- l Refers to liquid

Roman letters

- K_a Air permeability
- \mathbf{C}_e Elastic compliance tensor
- \mathbf{D}_e Elastic rigidity tensor
- d Damage parameter

e	Void ratio
G	Shear modulus
g	Shear stiffness factor in HAR hyperelastic model
G_{app}	Apparent shear modulus
\mathbf{I}	Identity matrix
J	Coupling modulus
K	Bulk modulus
k	Bulk stiffness factor in HAR hyperelastic model
K_{app}	Apparent bulk modulus
K_w	Water permeability
M	Slope of the critical state line
m_{vg}	Parameter of the Van Genuchten equation
n	Pressure exponent in HAR hyperelastic model
n_{vg}	Parameter of the Van Genuchten equation
p	Mean stress
p_g	Air pressure
p_l	Water pressure
p_r	Reference pressure in HAR hyperelastic model
p_0	Preconsolidation pressure for saturated condition (hardening parameter in BBM)
p_e	Equivalent stress in HAR hyperelastic model
q	Deviatoric stress
s	Suction
S_e	Effective degree of saturation
S_l	Degree of saturation
S_r	Residual degree of saturation
v	Specific volume ($v = 1 + e$)

Greek Symbols

α_{vg}	Parameter of the Van Genuchten equation
β_p	Water compressibility
$\boldsymbol{\varepsilon}$	Strain tensor
$\boldsymbol{\varepsilon}_d$	Deviatoric strain tensor
ε_s	Deviatoric strain
ε_v	Volumetric strain
ϕ	Porosity

γ_w	Water volumetric weight
\mathcal{G}	Gibbs free energy
κ	Elastic compressibility
λ	Plastic compressibility
ν	Poisson's ratio
ψ	Helmholtz free energy
$\boldsymbol{\sigma}$	Stress tensor
$\boldsymbol{\sigma}'$	Saturated effective stress ($\boldsymbol{\sigma}' = \boldsymbol{\sigma} - p_l \mathbf{I}$)
$\boldsymbol{\sigma}^*$	Constitutive stress (effect of suction)
$\boldsymbol{\sigma}^{net}$	Net stress tensor ($\boldsymbol{\sigma}^{net} = \boldsymbol{\sigma} - p_g \mathbf{I}$)
$\boldsymbol{\sigma}_d$	Deviatoric stress tensor
$\tilde{\boldsymbol{\sigma}}$	Damaged stress (effect of damage)
$\tilde{\boldsymbol{\sigma}}^*$	Double effective stress (effect of damage and suction)

Acronyms

BBM	Barcelona Basic Model
CC	Cam-Clay
HAR	Houlsby, Amorosi and Rojas hyperelastic model
RH	Relative Humidity
WRC	Water Retention Curve

The role of a mathematical model for the description of soil behaviour is twofold: firstly, as a simple qualitative framework against which soil behaviour may be assessed and, secondly, as a complete quantitative model for analysis and design. In its first role the model is of use both in judging the quality and consistency of data, and in predicting the character and trends of behaviour of a soil under a variety of circumstances. For this purpose the model must represent the essential features of soil behaviour in as simple a manner as possible.

A simple model is also desirable for the second role; this is because, in a detailed numerical calculation, an excessively complex model may be difficult to implement and expensive to use. Very often the quality of the available data about the actual soil from the field will not warrant the additional precision of calculation achieved using a complex model. If, however, the model is to be used for mathematical calculations, it is important that it should be properly founded in the theory of continuum mechanics and should be internally consistent.

A simple model will require few parameters for the description of a soil, and each of these should have a definite physical significance so that an assessment can easily be made of its importance and the likely results of any changes in its value. The parameters should be measurable directly in a small number of simple tests.

Both the purpose and the limitations of the model should be well understood.

Wroth and Houlsby (1980)

Geotechnical engineering's primary purpose has been to provide methods to engineers so as to predict how the ground would react to man-made constructions, with a focus on settlements (small-strain behaviour) and rupture.

With the rise of ecological and energy concerns, research in geotechnical engineering now goes beyond soil-structure problems, and has been extended to a wide range of soil-environment interactions issues (Gens, 2010). Among the various environmental components which have an impact on soil, water plays a major role. Water invades or leaves the ground during rainfall and evaporation, sometimes provoking damage such as landslides or desiccation cracks. Underground flows also have their importance when digging deep galleries. Nearing the contact with atmosphere, soil often is in an unsaturated state, which affects the material mechanical properties as well as the fluid transfer laws. Great progress has been made in the last decades in a view to provide modelling frameworks capable of reproducing soil behaviour in all their states, saturated or not. This research field is still very active, with many more issues to cope with (Sheng et al., 2013).

In parallel, degradation of geomaterials has also received much interest. Soils and rocks properties, such as rigidity, strength, or permeability, are known to be subject to changes after being submitted to hydric or mechanical solicitations. Several approaches have been used to model this degradation. Some works assume the elastic properties to evolve with plastic strains (Sulem et al., 1999; Kavvadas and Amorosi, 2000; Rouainia and Muir wood, 2000; Stallebrass and Baudet, 2004). This type of model is sometimes called structured model. Another approach, the one that is used in this thesis, is to use the framework of Continuum Damage Mechanics, first developed for metals and later extended to concrete and rocks. This approach assumes that the degradation of material properties is due to the initiation and propagation of microcracks. Contrary to the previous approach, it allows damage and plastic strains to be developed independently. The main modelling difference is the postulate of an effective stress, applied on the intact solid matrix, which controls the global material behaviour. Concerning granular materials, a new family of models consider the crushing, or breakage, of grains submitted to compressive loads (Einav, 2007).

Up to now, few attempts have been made to model damage in unsaturated geomaterials.

Some models have been developed which consider damage in unsaturated geomaterials (Arson and Gatmiri, 2009), damage-plasticity couplings in saturated geomaterials (Chiarelli et al., 2003; Conil et al., 2004) and even damage-plasticity couplings in unsaturated geomaterials (Hoxha et al., 2007; Jia et al., 2007). However, these models, initially formulated for rock, ignore some specific important features of clay soil behaviour, such as the dependence of elastic moduli to pressure. Moreover, damage-plasticity models proposed for rock so far fail at predicting the transition between ductile and brittle behaviour associated with suction increase.

The proposed work aims to develop a framework to couple damage and plasticity in unsaturated porous media, for which clay minerals in the solid matrix are expected to play an important role.

Two approaches have to be considered when constructing a modelling framework. One can either make assumptions about the nature of phenomena taking place at the microscale, develop micromechanical behaviour laws and upscale them to obtain the macroscopic behaviour. This is the micromechanical approach. The other strategy is to define macroscopic laws, which aim at reproducing some of the observed phenomena. These laws depend on some state variables, chosen for their sound physical meaning, and are developed in order to respect thermodynamic principles. This is the phenomenological approach, which is mainly based on energy considerations, and which is used in the present work.

An accurate prediction of all aspects of a material behaviour leads to very complex models requiring a great number of parameters, which makes calibration difficult. Since this work mainly aims to develop a flexible constitutive framework and to highlight its main characteristics concerning damage-plasticity couplings and non saturation, we chose not to account for certain features, such as intrinsic and damage-induced anisotropy of the material.

Chapters 1 to 3 present the mechanical constitutive model assumptions and equations. They develop how damage and suction enter in the definition of the double effective stress, which is the stress considered to be applied on the solid skeleton and to drive the overall behaviour (chapter 1). It is then shown how this double effective stress, coupled with a hyperelastic pressure dependent formulation, results in a dependence of apparent rigidities on suction and damage (chapter 2). Finally, damage and plasticity criteria are presented. Their expression in terms of the double effective stress results in an automatic dependence on suction and damage when compared to total stresses (chapter 3).

Chapter 4 develops the air and water transfer laws needed to simulate fully coupled hydro-mechanical problems. These transfer laws depend on the saturation state, which makes the problem non-linear, not only for the mechanical part, but also for the hydraulic part.

In chapter 5 the strong and weak forms of the partial differential equation system are developed. Spatial and time discretisations are presented, as well as the resulting matricial form of the problem. The global algorithm, used to solve the boundary value problem, consists in dividing the load in small load increments, and to perform iterations, using the Newton-Raphson algorithm, in order to find the displacement and pore pressure fields respecting equilibrium. A specific local algorithm has been developed for the present

damage-plasticity model.

Chapters 6 and 7 present applications of the constitutive and numerical model. Chapter 6 is limited to purely mechanical simulations. Laboratory experiments on two materials, Callovo-Oxfordian argillite and Boom clay, are simulated at different confining pressures and water contents. A good adequation between experimental results and numerical simulations is observed. The transition between ductile and brittle behaviour associated with suction increase is well captured. Chapter 7 presents illustrative applications to fully coupled hydro-mechanical problems. It is first shown how our model allows to simulate damage due to desiccation and humidification. Then, the model is applied to study the creation of the Excavation Damaged Zone due to excavation of deep galleries.

The literature review related to the different aspects of the problem is introduced along the different chapters, where it was judged to be the most appropriate to help with the understanding of the following developments.

CHAPTER 1

DEFINITION OF THE DOUBLE EFFECTIVE STRESS

This chapter aims at introducing a double effective stress incorporating both suction and damage effects. The formulation of this stress is based on thermodynamical considerations. Elastic strains will be directly related to this double effective stress through elastic potentials. A strong emphasis is put on the soil water retention properties which have a great impact on this double effective stress.

Ce chapitre a pour but d'introduire une contrainte doublement effective incorporant les effets aussi bien de la succion que de l'endommagement. Sa formulation est basée sur des considérations thermodynamiques. Cette contrainte doublement effective sera directement liée aux déformations élastiques à travers des potentiels élastiques. Une attention particulière est apportée aux propriétés de rétention du sol, celles-ci ayant une influence importante sur la contrainte doublement effective.

Contents

1.1	Unsaturated soils	6
1.1.1	Modelling approaches in the literature	8
1.1.2	Constitutive stress based on energy considerations	11
1.1.3	Water retention properties and their impact on constitutive stress	13
1.2	Principle of effective stress in Continuum Damage Mechanics	18
1.3	Introduction of a double effective stress	19

1.1 Unsaturated soils

This work deals with unsaturated geomaterials. Unsaturated soils have first been treated as specific materials different from the saturated ones. However, it is clear nowadays that, although suction has a great impact on unsaturated porous media behaviour, non saturation should only be considered as a specific state of the material.

Unsaturated soils are multiphasic. They are constituted of a solid phase and two fluid phases, the water liquid phase and the air gaseous phase (see figure 1.1). More complex models can consider dissolved air into the liquid phase and water vapour into the gaseous phase.

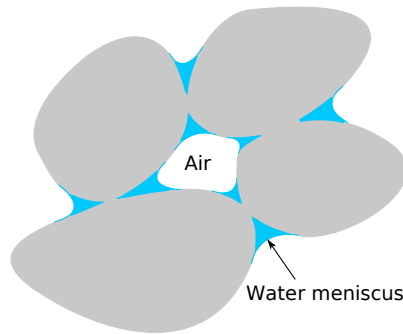


Fig. 1.1: Schematic view of an unsaturated medium

The total volume, V_{tot} , is the sum of the volume occupied by the solid phase, V_s , and the volume of the pores, V_v , itself divided between a volume filled by water, V_w , and a volume filled by gas, V_g (see figure 1.2).

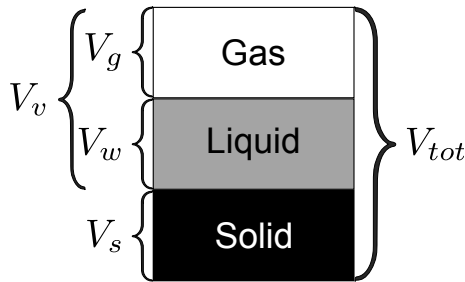


Fig. 1.2: Repartition of the different phases

The relative proportions of these phases can be described by the *porosity*, ϕ , and the *saturation degree*, S_l :

$$\phi = \frac{V_v}{V_{tot}} \quad (1.1)$$

$$S_l = \frac{V_w}{V_v} \quad (1.2)$$

When water evaporates from the saturated soil, a difference between the air and water pressures arises. This pressure difference, $s = p_g - p_l$, is called *suction*. In the case in which air remains equal to the atmospheric pressure, water pressure is negative and suction takes a positive value. The air-water interface (called meniscus) starts to curve

when suction increases. The radius of the meniscus decreases when suction increases, and once it becomes as small as the pore throats, air can invade the porous structure, which becomes unsaturated. Fine soils can be submitted to a high suction level before starting to desaturate. The suction for which air breaks through the soil mass is called the *air entry value*.

The combination of the water surface tension, F_t , and the negative pore water pressure, p_l , results in a force that tends to pull the soil grains towards one another. The resulting force, F_c , on the solid skeleton is similar to a compressive stress (see figure 1.3).

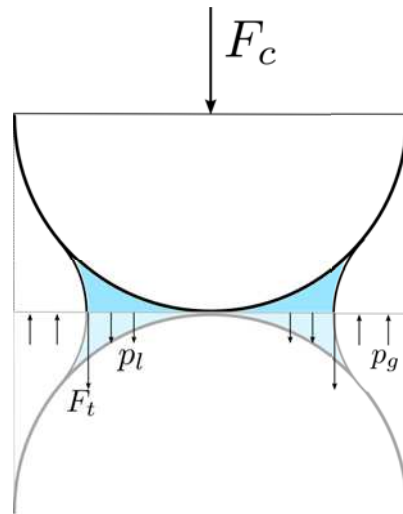


Fig. 1.3: Air-water-solid interaction for two spherical particles

An increase in suction will therefore lead to a decrease of the total volume (shrinkage), and wetting soils (i.e. decreasing suction) will usually make them swell. Suction also contributes to stiffen the soil against external loading thanks to the bounding between grains created by water menisci in tension. The additional component of normal force at the contact will also prevent slippage between grains and thus increase the external force needed to cause plastic strains. However, when wetting a soil under constant mechanical loading, the resaturation destroys the bounds due to water menisci and may induce an irrecoverable volumetric compression (called *collapse*). These main characteristics of unsaturated soils mechanical behaviour are represented on figure 1.4. Changes in suction may also induce irreversible processes (plasticity or damage) during a drying process.

Suction is closely related to the degree of saturation through the water retention curve (see section 1.1.3).

Unsaturated soil models are usually extensions of saturated soil ones. The most widely used of them is the Cam-clay model, first developed by Roscoe et al. (1958) and later modified by Roscoe and Burland (1968). However, the debate still goes on about which stress framework to use to extend saturated soil models to account for unsaturated states.

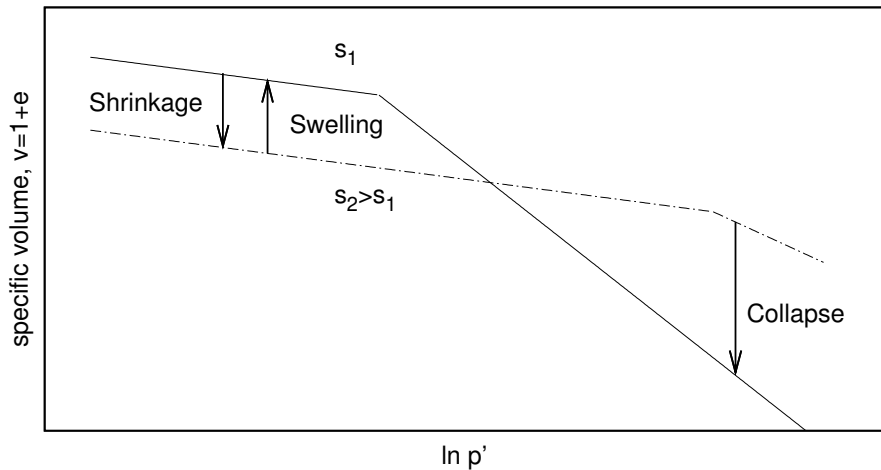


Fig. 1.4: Influence of suction on volumetric compression and volume changes due to wetting and drying

1.1.1 Modelling approaches in the literature

A comprehensive review of the existing stress frameworks can be found in the paper of Nuth and Laloui (2008).

In the following we use the convention of soil mechanics which means that compressive stresses are positive.

Bishop's effective stress

Bishop (1959) attempted to extend Terzaghi's effective stress principle for saturated soils to unsaturated soils. He proposed the following form for the effective stress:

$$\boldsymbol{\sigma}^* = \boldsymbol{\sigma} - [(1 - \chi)p_g + \chi p_l]\mathbf{I} \quad (1.3)$$

in which χ is a parameter weighting the contributions of liquid and gas pressures on the effective stress. The relative effect of each phase on the overall behaviour depends on the saturation state of the material. Indeed, at very low saturation states, even if suction is high, the contact surface between water and grains is so small that the resulting effect will be negligible. χ is therefore often considered as being a function of the degree of saturation, ranging from 0 for dry states to 1 for saturated states.

The stress defined in equation (1.3), sometimes called Bishop's stress, generalised effective stress, or constitutive stress, can also be expressed in terms of net stress and suction:

$$\boldsymbol{\sigma}^* = \boldsymbol{\sigma} - [p_g - \chi(p_g - p_l)]\mathbf{I} = \boldsymbol{\sigma}^{net} + \chi s\mathbf{I} \quad (1.4)$$

Early experimental and theoretical works have attempted to find a unique relationship between the χ parameter and the degree of saturation. Some experimental data are shown in figure 1.5.

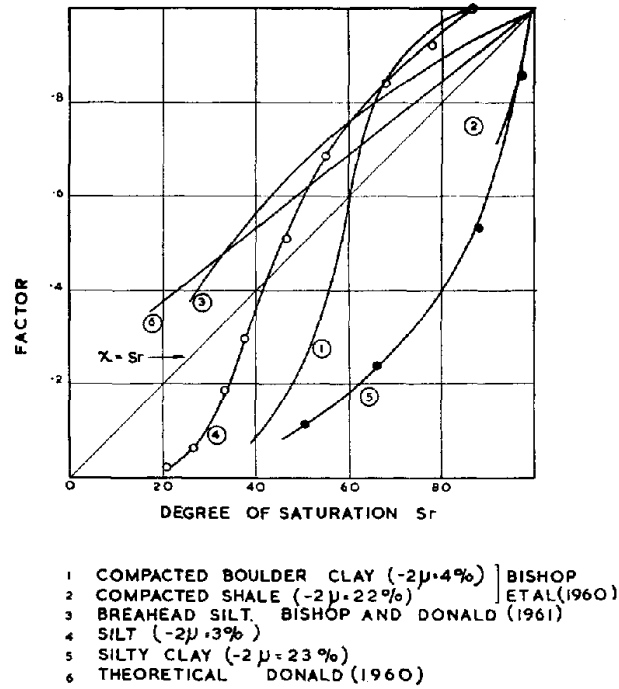


Fig. 1.5: Evolution of χ parameter with the degree of saturation (Jennings and Burland, 1962)

Some theoretical propositions are summarised in table 1.1. These formulations are either based on micromechanical or thermodynamical considerations. Their aim is usually to represent correctly the evolution of stiffness and shear strength with suction.

Reference	χ	
Lewis and Schrefler (1987) Schrefler (1995) Houlsby (1997) Hutter et al. (1999) Gray and Schrefler (2001) Chateau and Dormieux (2002)	S_l	
Khalili and Khabbaz (1998)	$1 \quad \text{if } S_l = 1$ $\left(\frac{s}{s_e}\right)^{-0.55} \quad \text{if } S_l < 1$	s_e : air entry value (for $s = s_e$, $S_l = 1$ and $\chi = 1$)
Alonso et al. (2010)	$\frac{S_l - S_l^m}{1 - S_r^m}$	S_l^m : microscopic degree of saturation
Alonso et al. (2010)	S_l^α	$\alpha \geq 1$

Table 1.1: Formulas used in the literature for $\chi = \chi(S_l)$

The difficulty of finding a unique relationship led to some doubts in the scientific community about the validity of Bishop's effective stress approach. Moreover, using Bishop's stress alone within an elastic framework doesn't allow the collapse phenomenon described previously to be captured (figure 1.4). Indeed, decreasing suction induces a decrease in the effective stress, which can not be associated to opposite volume changes depending on the external applied load (swelling for low stress and collapse for high stress). This appeared to be the main limitation to the use of an effective stress for partially saturated soils at that time (until it was incorporated into an elasto-plastic framework).

Independent stress variables

As a response to the limitations of the single effective stress approach, Coleman (1962) was the first to introduce the idea of using two independent variables to describe unsaturated soils behaviour.

Fredlund and Morgenstern (1977) proposed to use one of the following combinations of the total stress $\boldsymbol{\sigma}$, the water pressure p_l and the air pressure p_g :

$$(\boldsymbol{\sigma} - p_g \mathbf{I}) \text{ and } (p_g - p_l) \quad (1.5)$$

$$(\boldsymbol{\sigma} - p_l \mathbf{I}) \text{ and } (p_g - p_l) \quad (1.6)$$

$$(\boldsymbol{\sigma} - p_g \mathbf{I}) \text{ and } (\boldsymbol{\sigma} - p_l \mathbf{I}) \quad (1.7)$$

The first of these combinations is the most frequently used. However, the use of net stress, $\boldsymbol{\sigma}^{net} = \boldsymbol{\sigma} - p_g \mathbf{I}$, and suction to model unsaturated soils behaviour fails to provide a smooth transition between unsaturated and saturated states when suction becomes zero. Indeed, if the constitutive model is expressed in terms of net stress and suction, as soon as suction becomes equal to zero, the net stress remains the only variable controlling the soil behaviour, which means that elastic strains and shear strength will depend on net stress only, and that the effect of a positive water pressure is not accounted for. It would be of course possible to switch to a saturated soil model when suction reaches zero, but it would not be efficient in terms of numerical implementation, when one wants to be able to consider positive water pressures as well as suction.

Bishop's effective stress combined with an extra variable

Due to the limitations expressed above, recent works have been focusing on combining an effective stress following the definition of Bishop with an extra variable, usually linked to suction. Collapse can then be accounted for by using an elasto-plastic framework.

As it is shown in the next section, the effective stress and suction related variables can be derived from thermodynamic principles.

1.1.2 Constitutive stress based on energy considerations

References about the thermodynamics of open porous media can be found in Coussy (2004), Collins and Houlsby (1997), Hansen and Schreyer (1994) and Coussy and Dangla (2002).

The energy balance can be written as (chemical or electrical energies are neglected):

$$\dot{K} + \dot{U} = \mathcal{P}_{ext} + \dot{Q} \quad (1.8)$$

with:

- K , the kinetic energy
- U , the specific internal energy
- \mathcal{P}_{ext} , the power of external force
- \dot{Q} , the heat flow into the system

The kinetic energy theorem gives (Coussy, 1991):

$$\dot{K} + \mathcal{P}_{def} + \mathcal{P}_f = \mathcal{P}_{ext} \quad (1.9)$$

with

- $\mathcal{P}_{def} = \dot{W}$, the strain work rate
- \mathcal{P}_f , the power of inertia forces (relative movement of fluids to solid skeleton)

So we have the variation of internal energy

$$\dot{U} = \dot{W} + \dot{Q} + \mathcal{P}_f \quad (1.10)$$

which, expressed locally becomes:

$$\dot{u} = \dot{w} - \nabla \cdot \vec{q} + p_f \quad (1.11)$$

The local strain work rate is given by (deformation of the solid skeleton):

$$\dot{w} = \boldsymbol{\sigma} : \dot{\boldsymbol{\varepsilon}} + p_l \dot{\phi}_l + p_g \dot{\phi}_g \quad (1.12)$$

in which ϕ_l is the relative liquid porosity:

$$\phi_l = \phi S_l \quad (1.13)$$

$$\dot{\phi}_l = \dot{\phi} S_l + \phi \dot{S}_l \quad (1.14)$$

and ϕ_g is the relative gas porosity.

$$\phi_g = \phi - \phi S_l \quad (1.15)$$

$$\dot{\phi}_g = \dot{\phi} - \dot{\phi}S_l + \phi\dot{S}_l \quad (1.16)$$

Equation 1.12 can be rewritten as

$$\begin{aligned} \dot{w} &= \boldsymbol{\sigma} : \dot{\boldsymbol{\varepsilon}} + p_l S_l \dot{\phi} + p_l \phi \dot{S}_l + p_g \dot{\phi} - p_g S_l \dot{\phi} - p_g \phi \dot{S}_l \\ &= \boldsymbol{\sigma} : \dot{\boldsymbol{\varepsilon}} + (S_l p_l + (1 - S_l) p_g) \dot{\phi} + (p_l - p_g) \phi \dot{S}_l \end{aligned} \quad (1.17)$$

If we assume the incompressibility of the solid skeleton, the porosity change is directly related to the volumetric strain, $\dot{\phi} = -\mathbf{I} : \dot{\boldsymbol{\varepsilon}}$, which gives:

$$\begin{aligned} \dot{w} &= [\boldsymbol{\sigma} - (S_l p_l + (1 - S_l) p_g) \mathbf{I}] : \dot{\boldsymbol{\varepsilon}} - (p_g - p_l) \phi \dot{S}_l \\ &= \boldsymbol{\sigma}^* : \dot{\boldsymbol{\varepsilon}} - s^* \dot{S}_l \end{aligned} \quad (1.18)$$

with

$$\begin{cases} \boldsymbol{\sigma}^* &= \boldsymbol{\sigma} - (S_l p_l + (1 - S_l) p_g) \mathbf{I} = \boldsymbol{\sigma} - p_g \mathbf{I} + (p_g - p_l) S_l \mathbf{I} = \boldsymbol{\sigma}^{net} + s S_l \mathbf{I} \\ s^* &= (p_g - p_l) \phi = s \phi \end{cases} \quad (1.19)$$

$\boldsymbol{\sigma}^*$ can be called the average skeleton stress tensor (Jommi, 2000), the constitutive stress (Sheng et al., 2003) or the generalised effective stress (Laloui and Nuth, 2009).

s^* is called the modified suction.

Constitutive equations can be derived from Clausius-Duhem Inequality (see part 3, equations 3.13 and 3.15):

$$\boldsymbol{\sigma}^* = \frac{\partial \psi}{\partial \boldsymbol{\varepsilon}^e} \quad (1.20)$$

$$s^* = -\frac{\partial \psi}{\partial S_l} \quad (1.21)$$

in which ψ is the Helmholtz free energy.

A possible extension of the model could be to consider a compressible solid skeleton and to take the biot coefficient $b \neq 1$.

We would then have:

$$\boldsymbol{\sigma}^* = [\boldsymbol{\sigma} - b(S_l p_l + (1 - S_l) p_g) \mathbf{I}] \quad (1.22)$$

Equation 1.19 is identical to one of the combinations given by Houlsby (1997). We will therefore use from now the following set of state variables:

$$\boldsymbol{\sigma}^* = \boldsymbol{\sigma}^{net} + s S_l \mathbf{I} \quad (1.23)$$

$$s^* = \phi s \quad (1.24)$$

When the material becomes saturated, i.e. when $S_l = 1$, equation 1.23 becomes

$$\boldsymbol{\sigma}^* = \boldsymbol{\sigma} - p_l \mathbf{I} = \boldsymbol{\sigma}' \quad (1.25)$$

which is the saturated effective stress of Terzaghi.

With this stress choice, it is easy to model the behaviour of a soil submitted to negative as well as positive water pressures, without any discontinuity between these two cases. This is a real advantage for numerical implementation.

1.1.3 Water retention properties and their impact on constitutive stress

The wetting-drying process in a single pore is illustrated in figure 1.6. During drying, suction increases and the meniscus radius decreases until it becomes as small as the pore throat and air is able to invade the pore. This process is not reversible since a small reduction of suction will not induce an immediate filling of the pore by water. During resaturation, water will entirely refill the pore when the meniscus radius will coincide with the largest pore dimension.

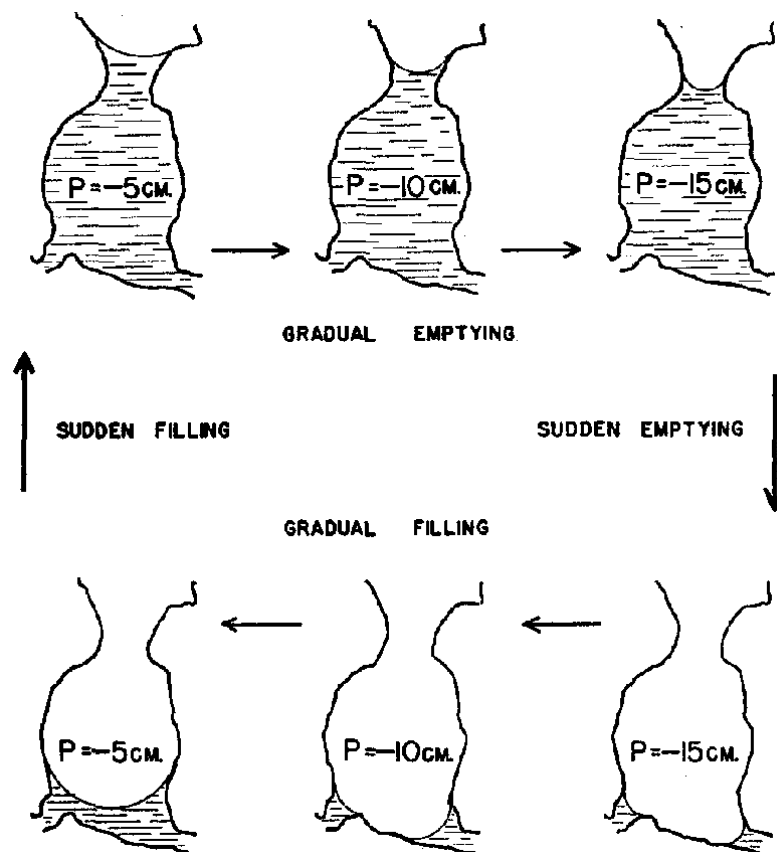


Fig. 1.6: Hysteresis in the movement of water meniscus during drying-wetting cycles (from Miller and Miller (1956))

A typical drying and wetting curve resulting from this hysteretic process is shown in figure 1.7.

The air-entry value of the soil is the suction for which air starts to enter the largest pores in the soil. The residual saturation degree is the saturation degree for which a large suction change is required to remove additional water from the soil. The adsorption curve differs from the desorption curve as a result of the hysteretic process explained before.

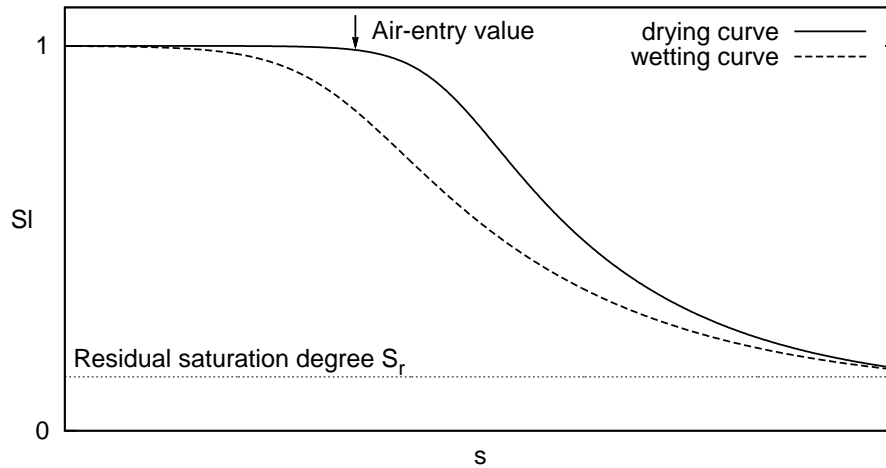


Fig. 1.7: Typical Desorption and absorption curves

Water retention curve basic formulas

The effective degree of saturation is defined as

$$S_e = \frac{S_l - S_r}{1 - S_r} \quad (1.26)$$

with S_r the residual degree of saturation.

For the sake of simplicity, hysteresis effects will be neglected in the following study.

In this case the degree of saturation can be expressed as a bijective function of suction.

$$S_e = f(s) \quad (1.27)$$

The two most commonly used models are the one of Brooks and Corey (1964),

$$S_e = \left(\frac{s_e}{s}\right)^\lambda \quad (1.28)$$

in which s_e is the air entry suction value, and the one of Van Genuchten (1980).

$$S_e = \left(\frac{1}{1 + (\alpha_{vg}s)^{n_{vg}}}\right)^{m_{vg}} \quad (1.29)$$

for which the number of parameters is sometimes reduced by stating

$$n_{vg} = \frac{1}{1 - m_{vg}} \quad (1.30)$$

The formulation of Brooks and Corey as the advantage of needing less parameters and being mathematically simpler. However, the Van Genuchten formulation usually fits better to experimental data and we will therefore use it in the next developments.

When the porosity changes or when damage occurs, this relationship changes due to the change of pores size and connectivity. Moreover, to respect the thermodynamic framework exposed in the previous section, the degree of saturation should be a function of the modified suction. The following section will therefore deal with the incorporation of porosity into equation 1.29.

Effect of porosity on the water retention curve

Water retention curves (WRC) are usually obtained under constant stress. Strains due to drying or wetting are therefore already taken into account. However, larger changes in porosity due changes in the stress state can notably modify the water retention properties since it depends on the pore size distribution. Several recent works have studied the dependency of water retention curves on porosity and proposed ways to incorporate porosity into WRC formulas (Gallipoli et al., 2003a; Sun et al., 2007; Tarantino, 2009; Masin, 2010; Sheng and Zhou, 2011; Buscarnera and Einav, 2012; Le et al., 2012).

Our primary goal is to respect thermodynamical consistency. We will therefore simply replace s by $s^* = \phi s$ in Van Genuchten equation and see how it affects water retention properties.

This is equivalent as considering that the α_{vg} coefficient of equation 1.29 depends on porosity:

$$\alpha(\phi) = \alpha_{vgref} \frac{\phi}{\phi_{ref}} \quad (1.31)$$

$$S_e = \left(\frac{1}{1 + (\alpha_{vgref} \frac{\phi}{\phi_{ref}} s)^{n_{vg}}} \right)^{m_{vg}} \quad (1.32)$$

Suction as a function of the effective degree of saturation is expressed as:

$$s = \frac{\phi_{ref}}{\phi \alpha_{vgref}} \left[S_e^{-\frac{1}{m_{vg}}} - 1 \right]^{\frac{1}{n_{vg}}} \quad (1.33)$$

This is the simplest way to incorporate modified suction into the WRC formula. Moreover this approach has the advantage of not requiring new parameters. We will now compare WRCs obtained by this formula with porosity dependent WRCs found in the literature.

Boom clay: Water retention curves used by Delahaye and Alonso (2002) are given for different porosities in figure 1.8.

The reference curve gives $\phi_{ref} = 0.39$, $\alpha_{vgref} = \frac{1}{3.44 \cdot 10^6} = 2.91 \cdot 10^{-7}$, $n_{vg} = 1.49$ and $m_{vg} = 0.33$.

Porosity dependent water retention curves computed using equation 1.32 are represented in figure 1.9.

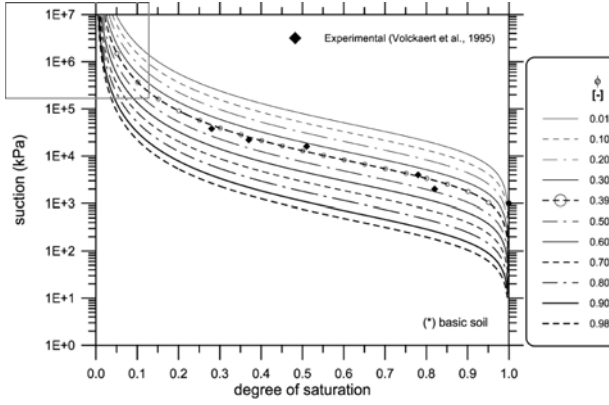


Fig. 1.8: (Delahaye and Alonso, 2002)

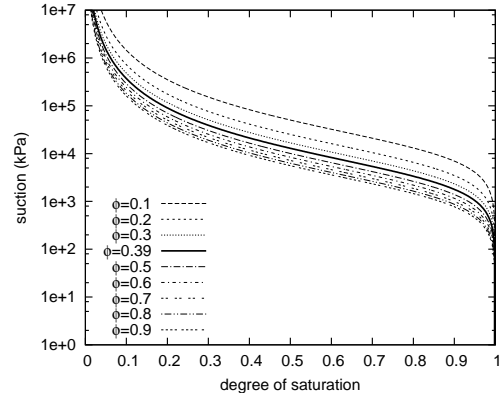


Fig. 1.9: (eq. 1.32)

We can see that our proposition underestimates the influence of porosity on water retention properties, especially for porosities larger than the reference porosity. However, since the calculated WRCs are situated between the reference porosity WRC and the ones calculated by Delahaye and Alonso, we can consider that it is pertinent to incorporate suction effects into WRCs by replacing s by s^* , especially since this solution doesn't require the determination of additional parameters.

Compacted Speswhite kaolin: Gallipoli et al. (2003b) proposed the following relationship:

$$S_e = \left(\frac{1}{1 + (\alpha_{vg}(v-1)^\beta s)^{n_{vg}}} \right)^{m_{vg}} \quad (1.34)$$

in which $v - 1 = e = \frac{\phi}{1 - \phi}$

with the following values for compacted speswhite kaolin :

$$m_{vg} = 0.03586, n_{vg} = 3.746, \alpha_{vg} = 0.02691 \text{ kPa}^{-1}, \beta = 8.433$$

We will take as a reference the values for a porosity $\phi_{ref} = 0.5$, which gives $\alpha_{vg_{ref}} = \alpha_{vg} \left(\frac{\phi_{ref}}{\phi_{ref} - 1} \right)^\beta = 0.093$.

Figure 1.10 shows the WRCs obtained by equation 1.34 (Gallipoli et al., 2003b), which can be compared with the ones given by our proposition (equation 1.32) shown in figure 1.11.

With our proposal, we can see that the changes in water retention curves due to small variations of porosity is seriously underestimated. However, since the induced curve shift follows the logical direction and that it helps ensuring thermodynamical consistency, we will keep this formulation in the following work.

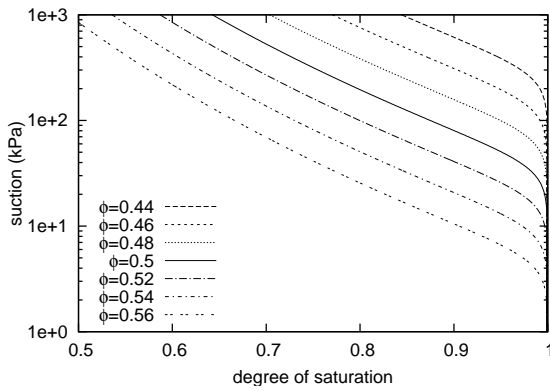


Fig. 1.10: (Gallipoli et al., 2003b)

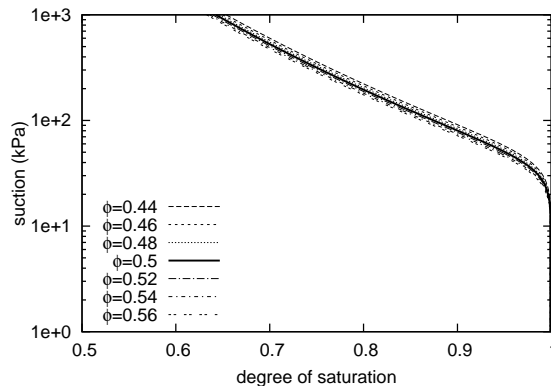


Fig. 1.11: (eq. 1.32)

Variation of the constitutive stress with suction and degree of saturation

The constitutive stress, σ^* , varies with the product $S_l s$. It can therefore be interesting to study how this component evolves with suction.

Van Genuchten parameters for different materials are given in table 1.2 (Leong and Rahardjo, 1997).

Material	S_r	α_{vg} (kPa^{-1})	n_{vg}	m_{vg}
Lakeland Sand	0.12	0.35	3.8	0.41
Mine tailings	0.10	0.018	3.4	18.6
Yolo light clay	0.39	0.35	2.41	0.24
Beit Netofa clay	0	$3.6 \cdot 10^{-3}$	0.75	0.39

Table 1.2: Van Genuchten parameters for different materials (Leong and Rahardjo, 1997) ($\phi = \phi_{ref}$)

The suction component of the constitutive stress as well as the WRC are represented in figures figures 1.12 to 1.15 for the different materials.

For coarse materials, such as mine tailings for instance, this component reaches a maximum for an intermediate saturation state during desaturation, and then decreases when the dry state is approached. It will therefore never reach high values and suction will thus have a low influence on the material mechanical behaviour.

Concerning fine-grained soils, such as clays, however, this component tends to infinity for low saturation states. Alonso et al. (2010) saw this as a major drawback from this simple expression for the constitutive stress since, as suction increases, it predicts an unrealistic compression. However, this issue only concerns very high suctions and we will consider that the previously chosen approach remains valid as long as the degree of saturation does not take low values.

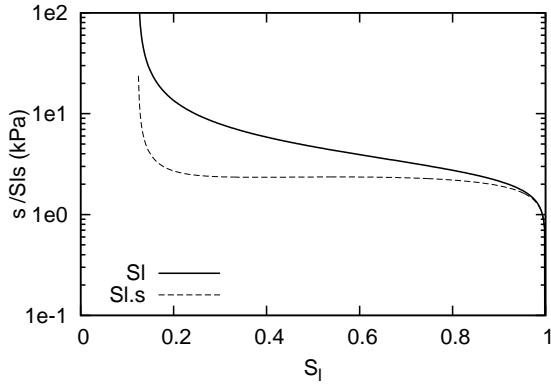


Fig. 1.12: Lakeland Sand

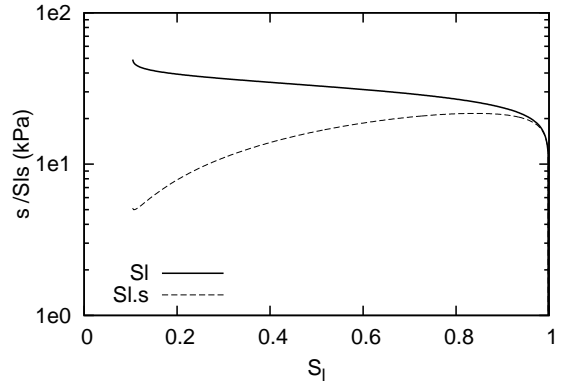


Fig. 1.13: Mine tailings

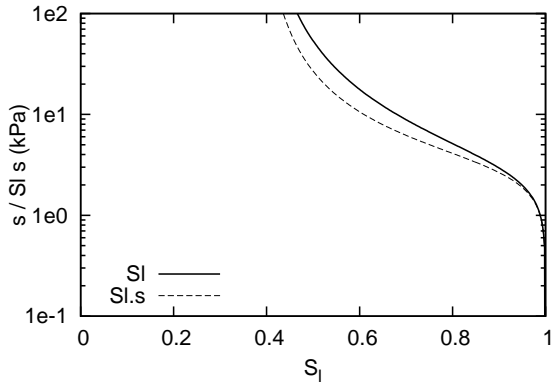


Fig. 1.14: Yolo light clay

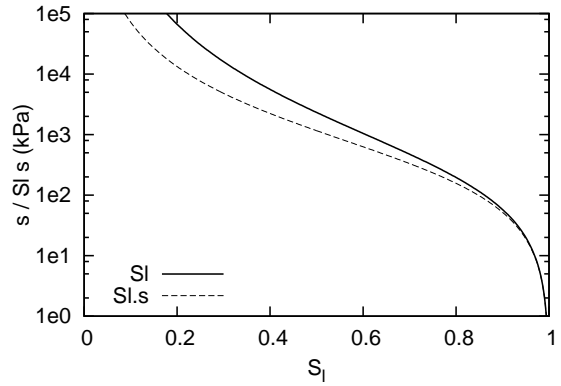


Fig. 1.15: Beit Netofa Clay

1.2 Principle of effective stress in Continuum Damage Mechanics

Introduced by Kachanov (1958), the effective stress in the sense of damage mechanics is based on the fact that the resisting section decreases when micro-cracks develop.

Since the applied force, F , at the sample scale is not affected by damage, the effective stress, $\tilde{\sigma}$, applied on the remaining section, S_{eff} , increases (see figure 1.16)

$$F = \sigma S = \tilde{\sigma} S_{eff} \quad (1.35)$$

which leads to the introduction of a new quantity $\tilde{\sigma} > \sigma$ such as

$$\tilde{\sigma} = \sigma \frac{S}{S - S_D} \quad (1.36)$$

If the damage variable is taken as an average of the proportion of damaged surfaces in the material, $d = \frac{S_D}{S}$, then the effective stress takes the following form:

$$\tilde{\sigma} = \frac{\sigma}{1 - d} \quad (1.37)$$

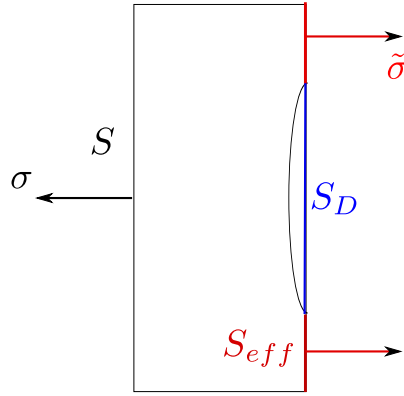


Fig. 1.16: Principle of effective stress

We consider that damage affects similarly all components of the stress tensor. The effective stress tensor then becomes

$$\tilde{\sigma} = \frac{\sigma}{1-d} \quad (1.38)$$

1.3 Introduction of a double effective stress

The two previous sections allowed us to introduce two quantities describing the stress applied on the solid matrix. On one hand, the constitutive stress, in unsaturated soils, takes into account the effect of water menisci in tension, acting like a compressive stress on the solid matrix. On the other hand, the effective stress, in the sense of damage mechanics, allows us to account for the decreasing material surface sustaining mechanical loads, resulting from the creation of micro-cracks. There is a need to define a new quantity, representing the stress applied on the solid matrix when the material is affected by both suction and damage simultaneously. This quantity will be called the *double effective stress* and is assumed to control the porous material mechanical behaviour.

Two simple combinations of the previous effective stresses can be imagined to incorporate both damage and suction into this double effective stress, $\tilde{\sigma}^*$:

$$\tilde{\sigma}_1^* = \frac{\sigma - p_g \mathbf{I} + S_l s \mathbf{I}}{1-d} = \frac{\sigma^*}{1-d} \quad (1.39)$$

$$\tilde{\sigma}_2^* = \frac{\sigma}{1-d} - p_g \mathbf{I} + S_l s \mathbf{I} = \tilde{\sigma} - p_g \mathbf{I} + S_l s \mathbf{I} \quad (1.40)$$

To choose between these two expressions, we consider that a damaged sample submitted to a change in suction should behave differently compared to the intact sample. This hypothesis has been considered by other authors, such as Carmeliet and Van Den Abeele (2000), who consider that damaged materials experience more swelling when wetted than intact ones.

Considering that the total applied stress, the gas pressure, as well as damage are kept

constant, the change in the double effective stress due to a suction increment would be:

$$\dot{\boldsymbol{\sigma}}_1^* = \frac{(\dot{S}_l s + S_l \dot{s})\mathbf{I}}{1-d} \quad (1.41)$$

$$\dot{\boldsymbol{\sigma}}_2^* = (\dot{S}_l s + S_l \dot{s})\mathbf{I} \quad (1.42)$$

Since elastic strains are directly related to the double effective stress, for the second expression, the strain change due to suction change would be the same for an intact and a damaged sample.

We will thus choose the first expression for the double effective stress:

$$\tilde{\boldsymbol{\sigma}}^* = \frac{\boldsymbol{\sigma} - p_g \mathbf{I} + S_l s \mathbf{I}}{1-d} \quad (1.43)$$

We define the following quantities:

- Mean stress: $p = \frac{1}{3} \text{tr}(\boldsymbol{\sigma})$
- Deviatoric stress tensor: $\boldsymbol{\sigma}_d = \boldsymbol{\sigma} - p \mathbf{I}$
- Deviatoric stress: $q = \sqrt{\frac{3}{2} \boldsymbol{\sigma}_d : \boldsymbol{\sigma}_d}$

Then the double effective triaxial variables are:

$$\tilde{p}^* = \frac{p - p_g + S_l s}{1-d} \quad (1.44)$$

$$\tilde{q}^* = \tilde{q} = \frac{q}{1-d} \quad (1.45)$$

It can be noted that with this definition of the double effective stress, suction effects are isotropic, and thus don't have any impact on the deviatoric stress.

The existence of a double effective stress, in which suction and damage effects on mechanical behaviour are included, is a key assumption in the following modelling developments. It will be shown in the next chapters how this double effective stress allows for damage and suction effects on elastic and dissipative behaviours to be reproduced. Of course its expression could be refined based on micromechanical studies. It will be shown, however, that this expression already allows us to capture well enough the main behaviour features observed during coupled hydromechanical loadings.

This chapter details the elastic part of the constitutive model. An hyperelastic pressure dependent formulation is used, in order to ensure energy conservation. The impact of damage modelling assumptions on the evolution of elastic mechanical rigidities is presented. The evolution of elastic stiffness with suction is presented, as well as elastic strains due to suction changes.

Ce chapitre traite de la partie élastique du modèle constitutif. Une formulation hyperélastique dépendante de l'état de contrainte est utilisée afin d'assurer un modèle conservatif. L'impact des choix de modélisation sur l'évolution des rigidités mécaniques élastiques avec l'endommagement est présenté. L'évolution de la rigidité élastique avec la succion ainsi que les déformations élastiques dues aux variations de succion sont étudiées.

Contents

2.1	Preliminaries	22
2.2	Pressure dependence of moduli in Cam-Clay	24
2.3	Pressure dependent hyperelastic models	25
2.4	Effect of damage on elastic behaviour	27
2.4.1	Principle of strain equivalence	30
2.4.2	Principle of equivalent elastic energy	30
2.4.3	Comparison of both assumptions	31
2.5	Unsaturated elastic behaviour	33
2.5.1	Effect of suction on the mechanical elastic rigidity	34
2.5.2	Elastic strains due to suction changes	34
2.6	General elasticity law	36

Usual elasto-plastic constitutive models for soils assume that soil behaves elastically for small strains. Although this assumption is idealistic, it is still reasonable, especially for overconsolidated clays, to consider an elastic domain in which the mechanical behaviour is reversible. Even for soils undergoing large plastic strains, the influence of the elastic part of the constitutive model should not be underestimated. Indeed, when modelling boundary value problems, the elastic component of the elastoplastic constitutive model determines the stress state of the soil at the onset of plasticity, which has a non negligible influence on the final plastic strains.

The small-strain stiffness of soils is known to be highly non-linear and has been experimentally studied extensively (Viggiani and Atkinson, 1995; Jovicic and Coop, 1997; Rampello et al., 1997; Atkinson, 2000; Callisto and Rampello, 2002). Dynamics methods are usually used to deduce the elastic shear stiffness from shear waves velocities. The resonant column test consists in measuring the response of a cylindrical sample subjected to forced harmonic torsional vibrations. Another technique consists in transmitting and receiving shear waves using bender elements (electro-mechanical transducers). The small-strain shear modulus is usually assumed dependent on the stress state, the porosity (through the specific volume or the void ratio) and the loading history (through the overconsolidation ratio, the preconsolidation pressure or plastic strains).

In this chapter, we consider the initial elastic stiffness to depend on the double effective stress state. It will be shown how relating the double effective stress to elastic strains through constitutive equations results in a dependence of the apparent stiffness on damage and suction.

2.1 Preliminaries

Triaxial variables: In the following, potentials are written in terms of triaxial variables, so that

$$\boldsymbol{\sigma} : d\boldsymbol{\varepsilon} = pd\varepsilon_v + qd\varepsilon_s = pd\varepsilon_v + \boldsymbol{\sigma}_d : d\boldsymbol{\varepsilon}_d \quad (2.1)$$

$$p = \frac{1}{3}tr(\boldsymbol{\sigma}) \quad (2.2)$$

$$q = \sqrt{\frac{3}{2}\boldsymbol{\sigma}_d : \boldsymbol{\sigma}_d} \quad (2.3)$$

$$\varepsilon_v = tr(\boldsymbol{\varepsilon}) \quad (2.4)$$

$$\varepsilon_s = \sqrt{\frac{2}{3}\boldsymbol{\varepsilon}_d : \boldsymbol{\varepsilon}_d} \quad (2.5)$$

$$\boldsymbol{\sigma}_d = \boldsymbol{\sigma} - p\mathbf{I} \quad (2.6)$$

$$\boldsymbol{\varepsilon}_d = \boldsymbol{\varepsilon} - \frac{1}{3}\varepsilon_v\mathbf{I} \quad (2.7)$$

These relationships are also true for elastic strains ($\boldsymbol{\varepsilon}^e$) and effective stresses ($\boldsymbol{\sigma}^*$, $\tilde{\boldsymbol{\sigma}}$ and $\tilde{\boldsymbol{\sigma}}^*$).

Elasticity definitions: Different forms can be used to define elasticity which can be summarised as follows (Houlsby and Puzrin, 2006):

A material is said to be *elastic* if the stress can be expressed as a single-valued function of the strain:

$$\boldsymbol{\sigma} = f(\boldsymbol{\varepsilon}^e) \quad (2.8)$$

The incremental stress-strain relationship is then written :

$$\dot{\boldsymbol{\sigma}} = \frac{\partial f(\boldsymbol{\varepsilon}^e)}{\partial \boldsymbol{\varepsilon}^e} \dot{\boldsymbol{\varepsilon}}^e \quad (2.9)$$

If the stress-strain relationship is originally expressed in its incremental form, the material is described as *hypoelastic*:

$$\dot{\boldsymbol{\sigma}} = f(\boldsymbol{\varepsilon}^e) \dot{\boldsymbol{\varepsilon}}^e \quad (2.10)$$

If the stresses can be derived from a strain energy potential, the material is said to be *hyperelastic*:

$$\boldsymbol{\sigma} = \frac{\partial f(\boldsymbol{\varepsilon}^e)}{\partial \boldsymbol{\varepsilon}^e} \quad (2.11)$$

which gives the following stress-strain relationship :

$$\dot{\boldsymbol{\sigma}} = \frac{\partial^2 f(\boldsymbol{\varepsilon}^e)}{\partial \boldsymbol{\varepsilon}^{e2}} \dot{\boldsymbol{\varepsilon}}^e \quad (2.12)$$

It should be noted that hyperelastic materials automatically respect also the elasticity and hypoelasticity definitions. Elastic materials are also hypoelastic but not necessarily hyperelastic. When starting from the definition of the incremental law for hypoelastic materials, it is not always possible to find a potential from which the hypoelastic formulation could be derived.

Elastic potentials: Different energy functions can be defined depending on which variables are used as independent state parameters.

The elastic strain energy (Helmholtz free energy) used in equation 2.11 is written as a function of strains and will be noted from now $\psi_\theta^e(\boldsymbol{\varepsilon}^e)$. Deriving the incremental constitutive equations from this potential results in a fourth-order rigidity tensor, $\mathbf{D}_e(\boldsymbol{\varepsilon}^e)$, being a function of strains.

$$\dot{\boldsymbol{\sigma}} = \frac{\partial^2 \psi_\theta^e(\boldsymbol{\varepsilon}^e)}{\partial \boldsymbol{\varepsilon}^{e2}} \dot{\boldsymbol{\varepsilon}}^e = \mathbf{D}_e(\boldsymbol{\varepsilon}^e) \dot{\boldsymbol{\varepsilon}}^e \quad (2.13)$$

Yet, moduli expressed as functions of stresses are often preferred. The complementary energy function (Gibbs free energy, noted \mathcal{G}_θ^e), which is expressed in terms of stresses, is related to Helmholtz free energy through a Legendre transform:

$$\mathcal{G}_\theta^e(\boldsymbol{\sigma}) = -\psi_\theta^e(\boldsymbol{\varepsilon}^e) + \boldsymbol{\sigma} : \boldsymbol{\varepsilon}^e \quad (2.14)$$

and strains may be derived as

$$\boldsymbol{\varepsilon}^e = \frac{\partial \mathcal{G}_\theta^e(\boldsymbol{\sigma})}{\partial \boldsymbol{\sigma}} \quad (2.15)$$

Deriving equation 2.15 results in a compliance tensor, $\mathbf{C}_e(\boldsymbol{\sigma})$, expressed as a function of stresses,

$$\dot{\boldsymbol{\varepsilon}}^e = \frac{\partial^2 \mathcal{G}_0^e(\boldsymbol{\sigma})}{\partial \boldsymbol{\sigma}^2} \dot{\boldsymbol{\sigma}}^e = \mathbf{C}_e(\boldsymbol{\sigma}) \dot{\boldsymbol{\sigma}}^e \quad (2.16)$$

from which the rigidity tensor expressed in stresses can be deduced.

$$\mathbf{D}_e(\boldsymbol{\sigma}) = [\mathbf{C}_e(\boldsymbol{\sigma})]^{-1} \quad (2.17)$$

Linear elasticity: For linear elasticity, the elastic potential takes the form:

$$\psi_0^e(\boldsymbol{\varepsilon}^e) = \frac{K}{2} (\varepsilon_v^e)^2 + \frac{3G}{2} (\varepsilon_s^e)^2 = \frac{p\varepsilon_v^e}{2} + \frac{q\varepsilon_s^e}{2} = \frac{p^2}{2K} + \frac{q^2}{6G} = \mathcal{G}_0^e(\boldsymbol{\sigma}) \quad (2.18)$$

which after derivation gives,

$$\begin{Bmatrix} p \\ q \end{Bmatrix} = \begin{bmatrix} K & 0 \\ 0 & 3G \end{bmatrix} \begin{Bmatrix} \varepsilon_v^e \\ \varepsilon_s^e \end{Bmatrix} \quad (2.19)$$

and its incremental form:

$$\begin{Bmatrix} dp \\ dq \end{Bmatrix} = \begin{bmatrix} K & 0 \\ 0 & 3G \end{bmatrix} \begin{Bmatrix} d\varepsilon_v^e \\ d\varepsilon_s^e \end{Bmatrix} \quad (2.20)$$

2.2 Pressure dependence of moduli in Cam-Clay

Experimental evidence shows that, for geomaterials, bulk and shear moduli vary with confining pressure. This non-linearity is sometimes attributed to the closure of micro-cracks or to imperfect bonding between grains (Zimmerman, 1990).

It is usually taken into account in Cam-Clay based models (Roscoe and Burland, 1968) by choosing the following expression for the bulk modulus:

$$K = \left(\frac{1+e}{\kappa_{CC}} \right) p \quad (2.21)$$

To complete the stress-strain relationship, either the shear modulus or Poisson's ratio are assumed to take a constant value.

Assuming a constant Poisson's ratio gives a pressure dependant shear modulus which is in accordance with experimental data (Baldi et al., 1991).

$$G = \frac{3(1-2\nu)}{2(1+\nu)} K = \frac{3(1-2\nu)}{2(1+\nu)} \left(\frac{1+e}{\kappa_{CC}} \right) p \quad (2.22)$$

However, this hypoelastic formulation does not derive from a thermodynamic potential. It has been demonstrated by Zytynski et al. (1978) that this model is non-conservative since it can produce permanent shear strains during a closed stress cycle (see figure 2.1). One could argue that this would have an impact only under cyclic loading. However, Einav and Puzrin (2004) compared tunnelling induced settlement predicted with either an hypoelastic

model or a hyperelastic model and highlighted significant differences between both results.

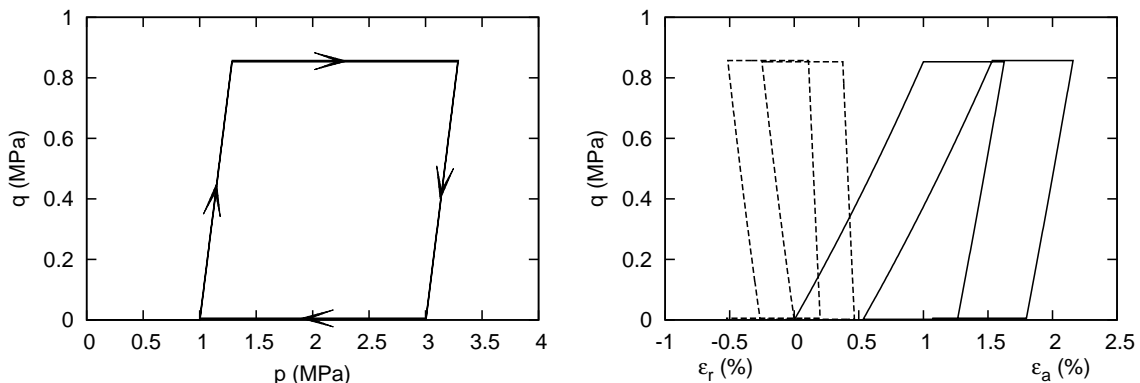


Fig. 2.1: Permanent strains resulting from a closed stress cycle in the elastic domain assuming a constant Poisson's ratio within a hypoelastic formulation

On the contrary, choosing a constant shear modulus gives a conservative model. However, this does not agree with experimental observations and Poisson's ratio may take negative values for low confining stresses which makes this choice not pertinent.

2.3 Pressure dependent hyperelastic models

In order to ensure thermodynamical consistency and energy conservation, several researchers have been working on developing hyperelastic potentials with shear moduli dependent on pressure (Houlsby, 1985; Borja et al., 1997; Sulem et al., 1999; Einav and Puzrin, 2004; Houlsby et al., 2005).

Deriving constitutive equations from potentials, considering pressure dependent bulk and shear moduli, necessarily leads to a rigidity matrix comporting an additional coupling modulus, J :

$$\begin{Bmatrix} dp \\ dq \end{Bmatrix} = \begin{bmatrix} K & J \\ J & 3G \end{bmatrix} \begin{Bmatrix} d\varepsilon_v^e \\ d\varepsilon_s^e \end{Bmatrix} \quad (2.23)$$

The presence of the coupling modulus, J , results in stress induced anisotropy. This means that, even if the material properties are initially isotropic, a change in mean stress can create deviatoric strains, and that a change in deviatoric stress only can lead to volumetric strains. Houlsby (1985), Borja et al. (1997) and Houlsby et al. (2005) drew constant volume (undrained) stress paths in the $p - q$ plane. It gives curved lines instead of the straight lines usually obtained when taking $J^* = 1$. This form of the undrained stress path is in accordance with experimental results (Shaw and Brown, 1988; Borja et al., 1997), which advocates for the use of this form for the rigidity matrix.

Models are usually derived in a way to recover the following expression for the bulk modulus along the isotropic axis:

$$\frac{K}{p_r} = \frac{1}{\kappa} \left(\frac{p}{p_r} \right)^n = k \left(\frac{p}{p_r} \right)^n \quad (2.24)$$

This expression 2.24 is slightly different from equation 2.21, since, for $n = 1$, it gives straight swelling lines in the plane $\ln v - \ln \tilde{p}^*$, instead of in the plane $v - \ln \tilde{p}^*$ as commonly assumed. Butterfield (1979) showed that this gives a better adequation with experimental results, and Hashiguchi (1995) advanced several advantages of this choice. This expression also makes the use of the natural (logarithmic) strains which allows for an easier extension to finite strains.

The two main hyperelastic formulations found in the literature are presented in table 2.1.

	Houlsby (1985)	Houlsby et al. (2005)
ψ_0^e	$p_r \kappa \exp\left(\frac{\varepsilon_v^e}{\kappa}\right) + \frac{3}{2} \alpha p_r \exp\left(\frac{\varepsilon_v^e}{\kappa}\right) \varepsilon_d^e : \varepsilon_d^e$	$p_r \frac{[k(1-n)]^{\frac{2-n}{1-n}}}{k(2-n)} \left[(\varepsilon_v^*)^2 + \frac{3g\varepsilon_s^e}{k(1-n)} \right]^{\frac{2-n}{2-2n}}$ $\varepsilon_v^* = \varepsilon_v^e + \frac{1}{k(1-n)}$
\mathcal{G}_0^e		$\frac{p_e^{(2-n)}}{p_r^{(1-n)} k(1-n)(2-n)} - \frac{p}{k(1-n)}$ $p_e^2 = p^2 + \frac{k(1-n)q^2}{3g}$
K	$\frac{p}{\kappa}$	$\left[1 - \frac{n(1-n)kq^2}{3gp_e^2} \right] k p_r^{(1-n)} p_e^n$
G	$\frac{q}{\sqrt{\varepsilon_d^e : \varepsilon_d^e}}$	$\frac{1}{1 - \frac{n(1-n)kq^2}{3g(p_e^2 - np^2)}} g p_r^{(1-n)} p_e^n$
J	$\frac{q}{\kappa}$	$n k p q p_r^{(1-n)} p_e^{(n-2)}$

Table 2.1: Hyperelastic pressure dependent models from the literature

The first formulation of Houlsby (1985) (also used by Borja et al. (1997)) exhibits a maximum attainable stress ratio $(q/p)_{max} = \sqrt{3\alpha\kappa/2}$ (the rigidity matrix becomes singular).

Moreover, no simple form of the corresponding Gibbs energy exists, and the rigidity matrix can therefore not be expressed in terms of stresses only.

Houlsby et al. (2005) derived a new expression for which both Gibbs and Helmholtz energies are given. This formulation also has the advantage of letting the freedom to choose any value between 0 and 1 for the mean pressure exponent.

The resulting deviatoric and volumetric strains occurring during a closed stress cycle are represented in figure 2.2.

Since the second potential (Houlsby et al., 2005) is expressed in terms of stresses and allows the pressure exponent, n , to be chosen in the whole range from 0 to 1, we will use this one in the following.

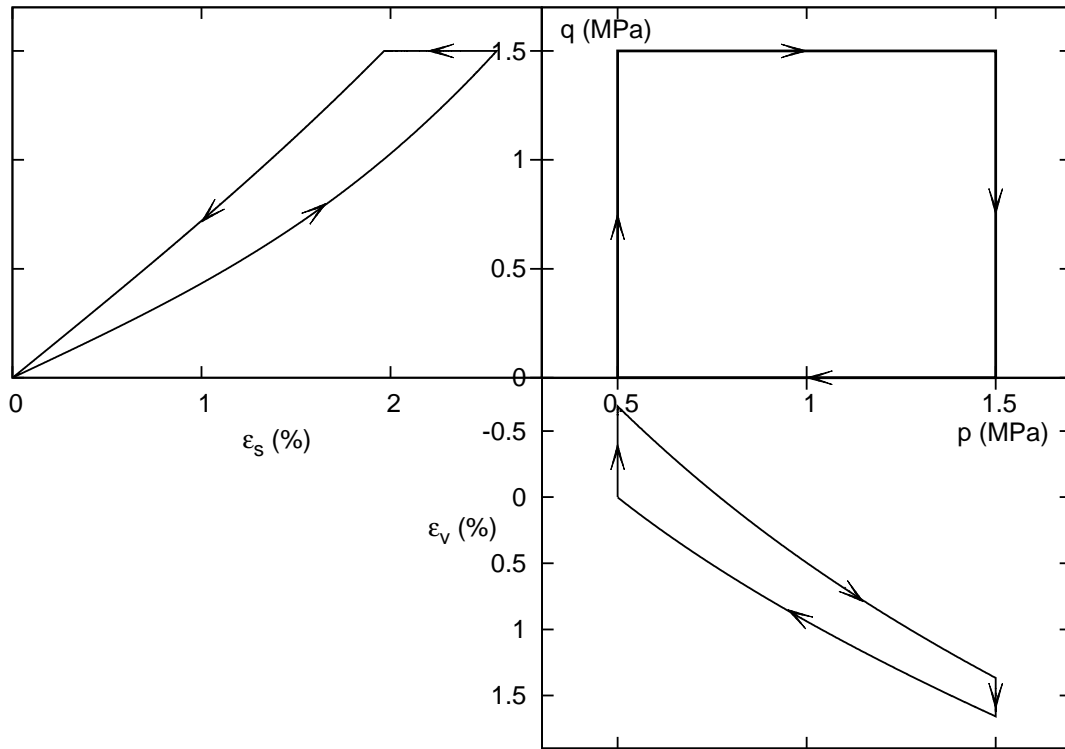


Fig. 2.2: Deviatoric and volumetric strains obtained during an elastic cycle with pressure dependent hyperelasticity

For general stress states, the rigidity tensor is expressed as:

$$D_{e_{ijkl}} = p_r \left(\frac{p_e}{p_r} \right)^n \left[nk \frac{\sigma_{ij}\sigma_{kl}}{p_e^2} + k(1-n)\delta_{ij}\delta_{kl} + 2g \left(\delta_{ik}\delta_{jl} - \frac{1}{3}\delta_{kl}\delta_{ij} \right) \right] \quad (2.25)$$

2.4 Effect of damage on elastic behaviour

Damage modelling is based on the existence of an effective stress, as defined by Kachanov (1958), such as

$$\tilde{\sigma} = \frac{\sigma}{1-d} \quad (2.26)$$

To derive the elastic behaviour of the damaged materials, two main assumptions have been used in previous works:

- The principle of *strain equivalence*, which states that the strain associated with a damaged state under the applied stress is equivalent to the strain associated with its undamaged state under the effective stress (Lemaitre and Chaboche, 1978). This principle is represented on figure 2.3.
- The principle of *equivalent elastic energy* which stipulates that the elastic energy of the damaged material is the same in form as that of an undamaged material except that the stress is replaced by the effective stress (Cordebois and Sidoroff, 1982).

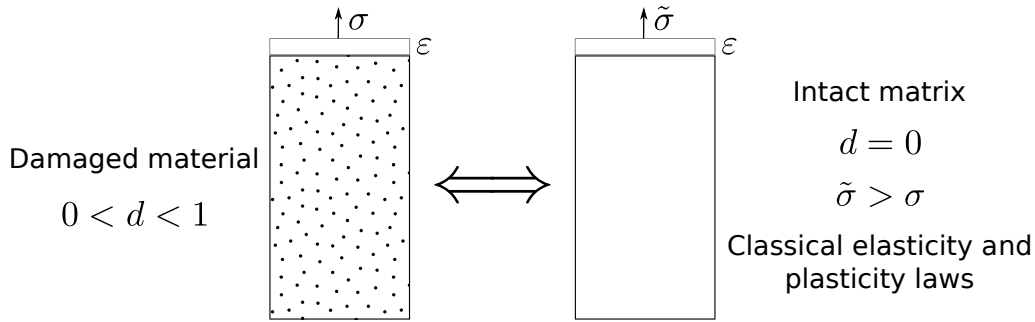


Fig. 2.3: Principle of strain equivalence

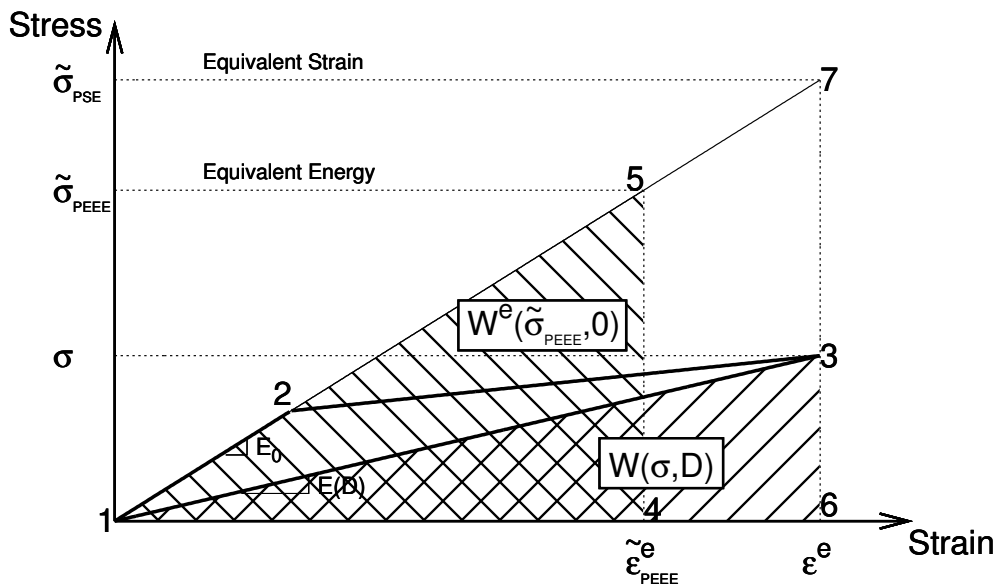


Fig. 2.4: Difference between equivalent energy and strain equivalence principles (from Hansen and Schreyer (1994))

Hansen and Schreyer (1994) compared these two assumptions. In figure 2.4, damage is initiated at point 2 of the stress path 1-2-3. Point 7 denotes the effective state using the principle of strain equivalence. The stored energy associated with the final state, given by the area 1-3-6, is equated to the area in the effective space using the undamaged modulus, which is given by the area 1-5-4. This results in an effective state defined by an effective stress and an effective strain (point 5). The effective stress obtained by the principle of strain equivalence is much higher than the one for the principle of equivalent elastic energy. The choice between these two assumptions will therefore strongly influence the model behaviour.

In the numerical algorithm (see chapter 5.6), the stress-strain behaviour is solved within the double effective stress space and conversion back to total stresses is the last step of the algorithmic process. Apparent rigidities are therefore not explicitly needed.

However, to show the effect of damage and pressure dependency on apparent moduli, we will study them along the isotropic compression line (i.e. for $q = 0$) for both principles.

Along the isotropic axis, apparent moduli reduce to:

$$K_{app}(\boldsymbol{\sigma}, d = 0) = kp_r \left(\frac{p}{p_r} \right)^n \quad (2.27)$$

$$G_{app}(\boldsymbol{\sigma}, d = 0) = gp_r \left(\frac{p}{p_r} \right)^n \quad (2.28)$$

$$J_{app}(\boldsymbol{\sigma}, d = 0) = 0 \quad (2.29)$$

A graphical definition of these moduli is given in figures 2.5 and 2.6.

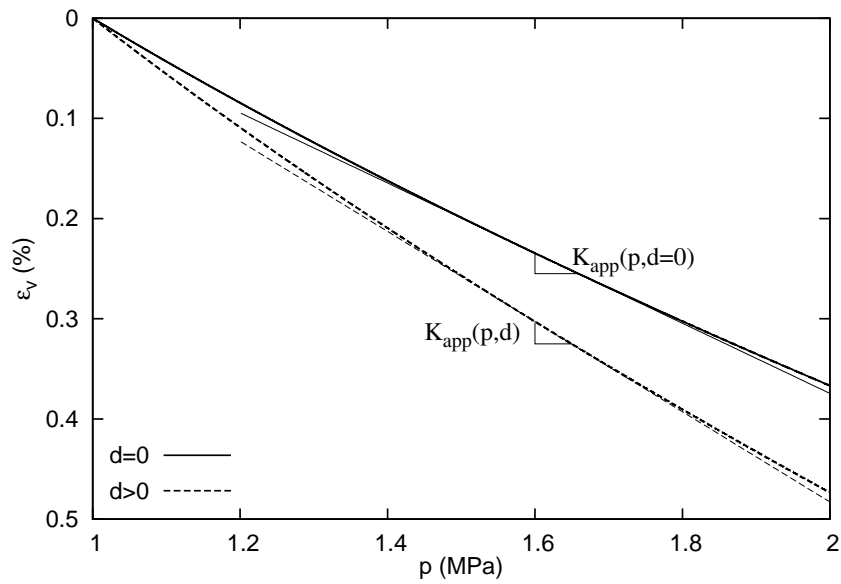


Fig. 2.5: Definition of the apparent bulk modulus - isotropic compression

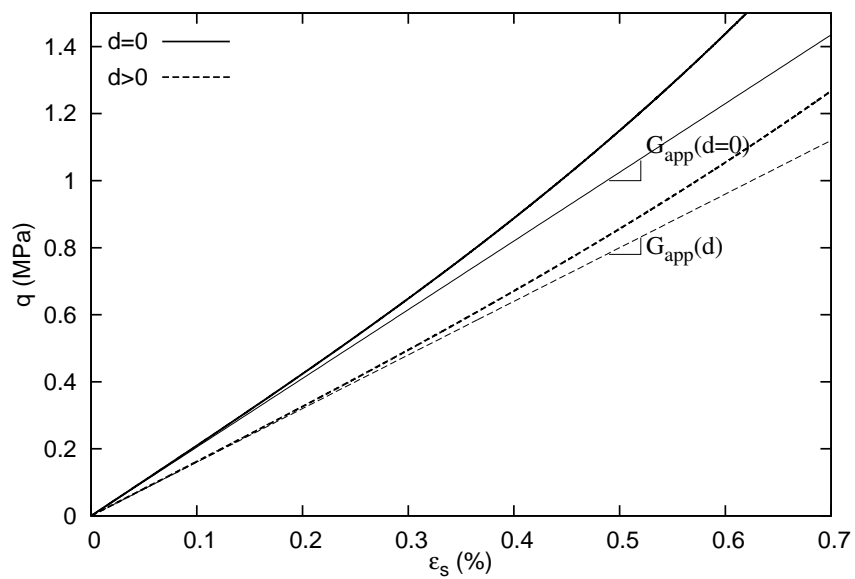


Fig. 2.6: Definition of the apparent shear modulus for a given initial confining pressure

The ratios, R_K and R_G , between the apparent damaged and intact moduli are defined as:

$$R_K = \frac{K_{app}(p, d)}{K_{app}(p, d = 0)} \quad (2.30)$$

$$R_G = \frac{G_{app}(p, d)}{G_{app}(p, d = 0)} \quad (2.31)$$

2.4.1 Principle of strain equivalence

The principle of strain equivalence can be expressed as

$$\boldsymbol{\varepsilon}^e(\boldsymbol{\sigma}, d) = \boldsymbol{\varepsilon}^e(\tilde{\boldsymbol{\sigma}}) = \frac{\partial \mathcal{G}_0^e(\tilde{\boldsymbol{\sigma}})}{\partial \tilde{\boldsymbol{\sigma}}} \quad (2.32)$$

and the incremental form,

$$\frac{\partial \boldsymbol{\varepsilon}^e}{\partial \boldsymbol{\sigma}} = \frac{\partial \boldsymbol{\varepsilon}^e}{\partial \tilde{\boldsymbol{\sigma}}} \frac{\partial \tilde{\boldsymbol{\sigma}}}{\partial \boldsymbol{\sigma}} = \frac{1}{1-d} \frac{\partial^2 \mathcal{G}_0^e(\tilde{\boldsymbol{\sigma}})}{\partial \tilde{\boldsymbol{\sigma}}^2} \quad (2.33)$$

which gives the relationship between the damaged and the intact compliance matrices,

$$\mathbf{C}_e(\boldsymbol{\sigma}, d) = \frac{1}{1-d} \mathbf{C}_{e_0}(\tilde{\boldsymbol{\sigma}}) \quad (2.34)$$

and the rigidity matrix,

$$\mathbf{D}_e(\boldsymbol{\sigma}, d) = [\mathbf{C}_e(\boldsymbol{\sigma}, d)]^{-1} = (1-d) [\mathbf{C}_{e_0}(\tilde{\boldsymbol{\sigma}})]^{-1} = (1-d) \mathbf{D}_{e_0}(\tilde{\boldsymbol{\sigma}}) \quad (2.35)$$

hence the apparent moduli:

$$K_{app} = (1-d)K \left(\frac{\boldsymbol{\sigma}}{1-d} \right) = (1-d)kp_r \left(\frac{p}{(1-d)p_r} \right)^n = (1-d)^{1-n}kp_r \left(\frac{p}{p_r} \right)^n \quad (2.36)$$

$$G_{app} = (1-d)G \left(\frac{\boldsymbol{\sigma}}{1-d} \right) = (1-d)gp_r \left(\frac{p}{(1-d)p_r} \right)^n = (1-d)^{1-n}gp_r \left(\frac{p}{p_r} \right)^n \quad (2.37)$$

Bulk and shear moduli are affected similarly by damage and by the pressure exponent, n . A single ratio can therefore be defined to represent rigidity degradation.

$$R = R_K = R_G = (1-d)^{(1-n)} \quad (2.38)$$

The evolution of R with damage for different values of n is given in figure 2.7.

2.4.2 Principle of equivalent elastic energy

The principle of equivalent elastic energy can be expressed as

$$\mathcal{G}^e(\boldsymbol{\sigma}, d) = \mathcal{G}_0^e(\tilde{\boldsymbol{\sigma}}) \quad (2.39)$$

which gives after derivation,

$$\varepsilon^e = \frac{\partial \mathcal{G}_0^e(\tilde{\sigma})}{\partial \sigma} = \frac{\partial \mathcal{G}_0^e(\tilde{\sigma})}{\partial \tilde{\sigma}} \frac{\partial \tilde{\sigma}}{\partial \sigma} = \frac{1}{1-d} \frac{\partial \mathcal{G}_0^e(\tilde{\sigma})}{\partial \tilde{\sigma}} \quad (2.40)$$

and the incremental form,

$$\frac{\partial \varepsilon^e}{\partial \sigma} = \frac{\partial \varepsilon^e}{\partial \tilde{\sigma}} \frac{\partial \tilde{\sigma}}{\partial \sigma} = \frac{1}{(1-d)^2} \frac{\partial^2 \mathcal{G}_0^e(\tilde{\sigma})}{\partial \tilde{\sigma}^2} \quad (2.41)$$

which gives the relationship between the damaged and the intact compliance matrix,

$$\mathbf{C}_e(\sigma, d) = \frac{1}{(1-d)^2} \mathbf{C}_{e_0}(\tilde{\sigma}) \quad (2.42)$$

and the rigidity matrix:

$$\mathbf{D}_e(\sigma, d) = [\mathbf{C}_e(\sigma, d)]^{-1} = (1-d)^2 [\mathbf{C}_{e_0}(\tilde{\sigma})]^{-1} = (1-d)^2 \mathbf{D}_{e_0}(\tilde{\sigma}) \quad (2.43)$$

hence the apparent moduli

$$K_{app} = (1-d)^2 K \left(\frac{\sigma}{1-d} \right) = (1-d)^2 k p_r \left(\frac{p}{(1-d)p_r} \right)^n = (1-d)^{2-n} k p_r \left(\frac{p}{p_r} \right)^n \quad (2.44)$$

$$G_{app} = (1-d)^2 G \left(\frac{\sigma}{1-d} \right) = (1-d)^2 g p_r \left(\frac{p}{(1-d)p_r} \right)^n = (1-d)^{2-n} g p_r \left(\frac{p}{p_r} \right)^n \quad (2.45)$$

Bulk and shear moduli are again affected similarly by damage and by the pressure exponent, n . The ratio between damaged and intact rigidities is therefore:

$$R = R_K = R_G = (1-d)^{(2-n)} \quad (2.46)$$

The evolution of R with damage for different values of n is given in figure 2.8.

2.4.3 Comparison of both assumptions

Figures 2.7 and 2.8 both show that the influence of damage on apparent moduli decreases when n is higher. It is due to the fact that when effective stresses increase, the rigidity of the intact matrix increases too since it is pressure dependent. This phenomenon partly compensates the rigidity degradation due to the diminution of effective surface on which loads are applied.

We can also notice that this effect is much more important for the hypothesis of strain equivalence.

Figure 2.9 shows the evolution of radial stiffness during triaxial compression tests as a function of radial strain obtained by Chiarelli et al. (2003). The radial stiffness was obtained by calculating the slope of unloading-reloading loops.

Since axial strains include both elastic and plastic strains, it is difficult at this point to determine which of the two hypotheses would better fit experimental results. Indeed,

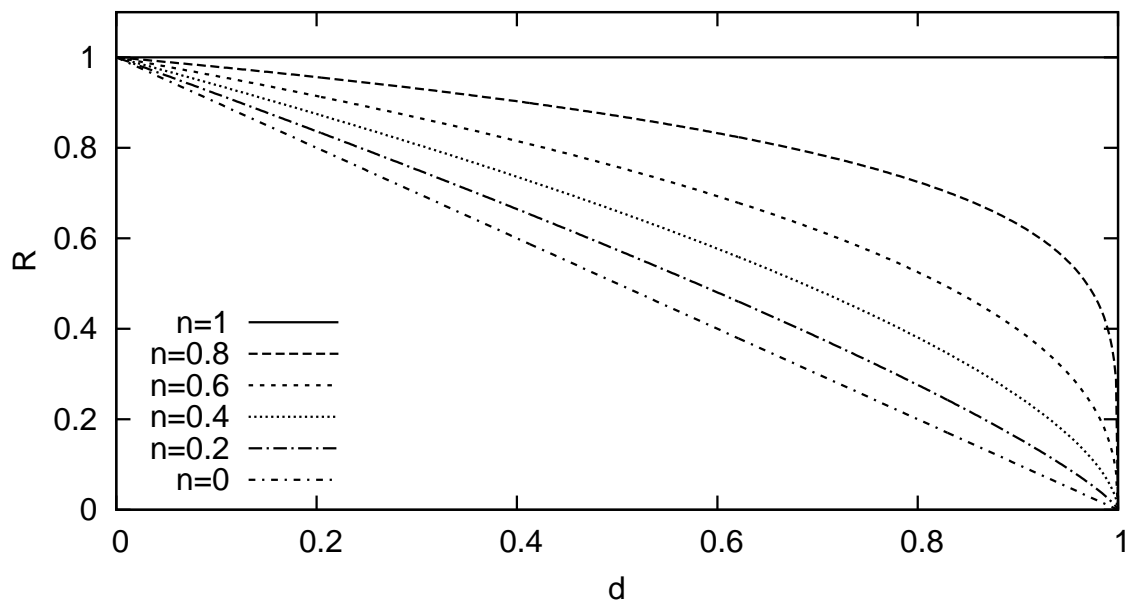


Fig. 2.7: Effect of damage on apparent moduli for several pressure exponents - Principle of Strain equivalence

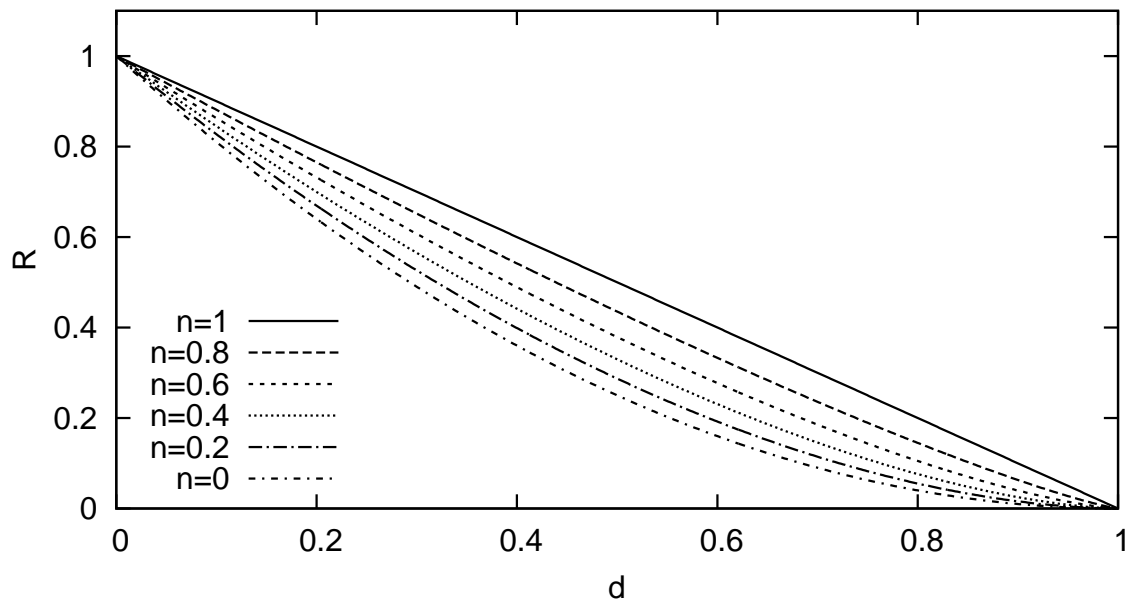


Fig. 2.8: Effect of damage on apparent moduli for several pressure exponents - Principle of equivalent elastic energy

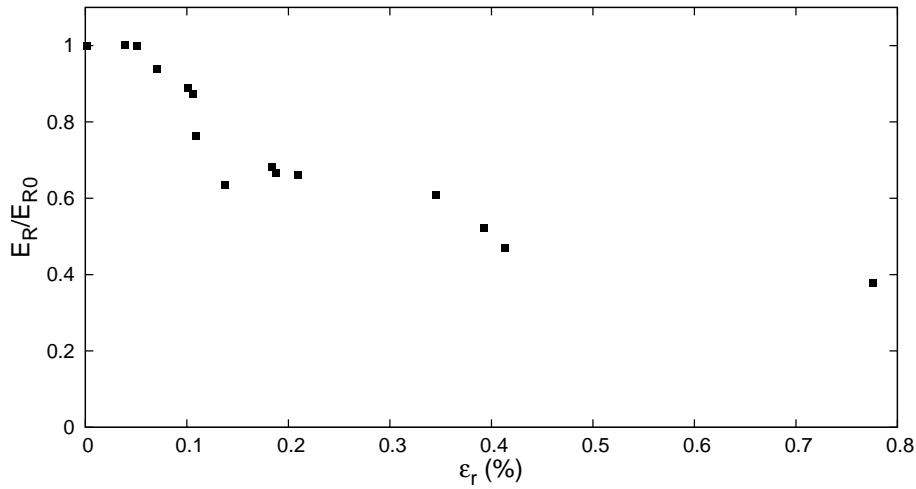


Fig. 2.9: Evolution of radial stiffness during triaxial compression tests as a function of radial strain (Chiarelli et al., 2003)

since stiffness degradation can be chosen as a way to calibrate the damage evolution law, both assumptions should be able to represent the same stiffness degradation with different damage evolution parameters.

However, when damage reaches 50 %, the stress-strain behaviour becomes unstable under increasing stress loading and reaches the softening part of the stress-strain curve. One should therefore check that the loss of stiffness obtained experimentally can be attained by the model for damage values under 0.5.

In the following developments we will use the hypothesis of strain equivalence since it provides a straightforward way to couple damage and plasticity phenomena.

2.5 Unsaturated elastic behaviour

This section aims to study how suction affects the elastic response to mechanical loads, and also how hydric loading, represented by a suction change, induces elastic strains.

The incremental stress-strain relationship expressed in terms of the constitutive stress is:

$$\dot{\boldsymbol{\sigma}}^* = \mathbf{D}_e(\boldsymbol{\sigma}^*)\dot{\boldsymbol{\epsilon}}^e \quad (2.47)$$

with

$$D_{eijkl}(\boldsymbol{\sigma}^*) = p_r \left(\frac{p_e^*}{p_r} \right)^n \left[nk \frac{\sigma_{ij}^* \sigma_{kl}^*}{p_e^{*2}} + k(1-n)\delta_{ij}\delta_{kl} + 2g \left(\delta_{ik}\delta_{jl} - \frac{1}{3}\delta_{kl}\delta_{ij} \right) \right] \quad (2.48)$$

To simplify the following expressions, we assume a constant null gas pressure ($p_g = 0$).

2.5.1 Effect of suction on the mechanical elastic rigidity

The increment of total stress due to a mechanical load at constant suction is:

$$\dot{\boldsymbol{\sigma}} = \dot{\boldsymbol{\sigma}}^* = \mathbf{D}_e(\boldsymbol{\sigma}^*)\dot{\boldsymbol{\varepsilon}}^e \quad (2.49)$$

Let us now compare the unsaturated rigidity matrix with the saturated one. The apparent rigidity matrix will be studied for isotropic stress states (i.e. when $q = 0$). Replacing stresses by constitutive stresses, the formula of table 2.1 become:

$$p_e^* = p^* = p + S_l s \quad (2.50)$$

$$K_{app_{unsat}} = k p_r^{(1-n)} p^{*n} \quad (2.51)$$

$$G_{app_{unsat}} = g p_r^{(1-n)} p^{*n} \quad (2.52)$$

Then the ratio between unsaturated and saturated moduli is:

$$R_{unsat} = \left(\frac{p^*}{p}\right)^n = \left(\frac{p + S_l s}{p}\right)^n \quad (2.53)$$

Figures 2.10 to 2.12 show the evolution of this ratio with mean pressure and with $S_l s$. It can first be noticed that soil stiffen against mechanical loading when suction increases, except in the case where linear elasticity is assumed. The rigidity change due to suction is higher for high values of the pressure exponent, n . Moreover, the influence of suction on rigidity decreases when the mean pressure increases. Indeed, mean pressure effects then become predominant compared to suction effects.

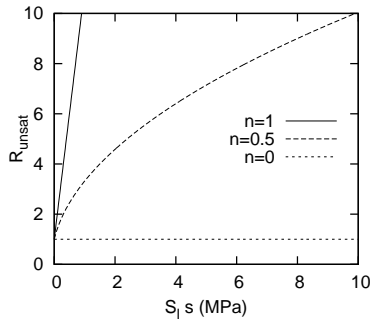


Fig. 2.10: $p = 1e5$ Pa

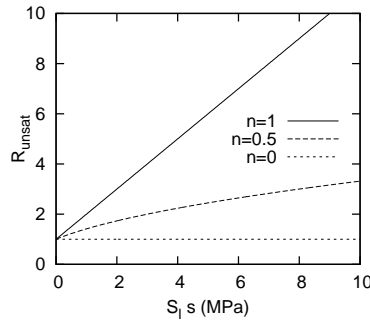


Fig. 2.11: $p = 1e6$ Pa

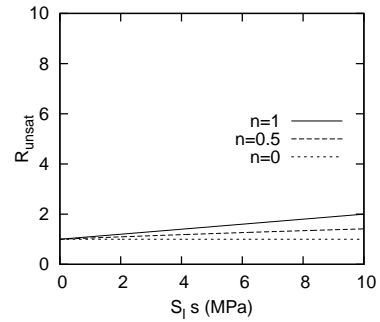


Fig. 2.12: $p = 1e7$ Pa

2.5.2 Elastic strains due to suction changes

The increment of elastic strain due to a suction increment under constant total stress is:

$$\dot{\boldsymbol{\varepsilon}}^e = \mathbf{D}_e(\boldsymbol{\sigma}^*)^{-1} \dot{\boldsymbol{\sigma}}^* = \mathbf{D}_e(\boldsymbol{\sigma}^*)^{-1} (\dot{S}_l s + S_l \dot{s}) \mathbf{I} \quad (2.54)$$

A significant advantage of the effective stress approach is the ability to capture suction

induced strains without the need of extra parameters in addition to mechanical parameters. This approach is validated against an oedometer swelling test performed by Volckaert et al. (1996) on Boom clay. The vertical stress is kept constant ($\sigma_v = 0.1$ MPa) while suction is decreased from 230 to 0 MPa.

Mechanical and retention properties are given in table 2.2.

Elasticity				Retention			
n	p_r kPa	κ	ν	S_r	α_{vg} kPa ⁻¹	n_{vg}	m_{vg}
0.6	10	0.007	0.35	0	$0.17 \cdot 10^{-3}$	2	0.4

Table 2.2: Elasticity and retention parameters

Retention properties are chosen to fit the experimental retention curve represented in figure 2.13.

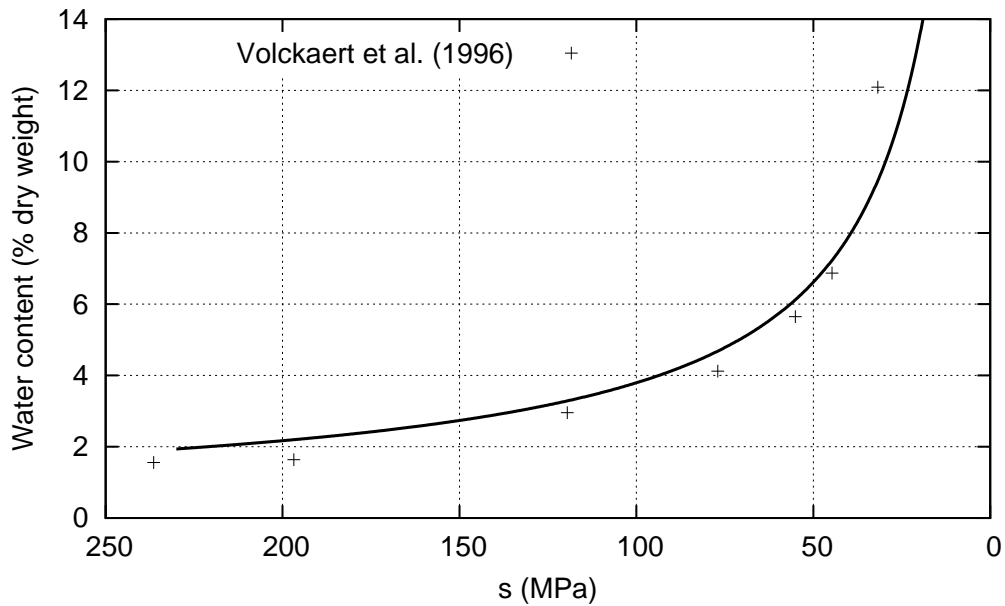
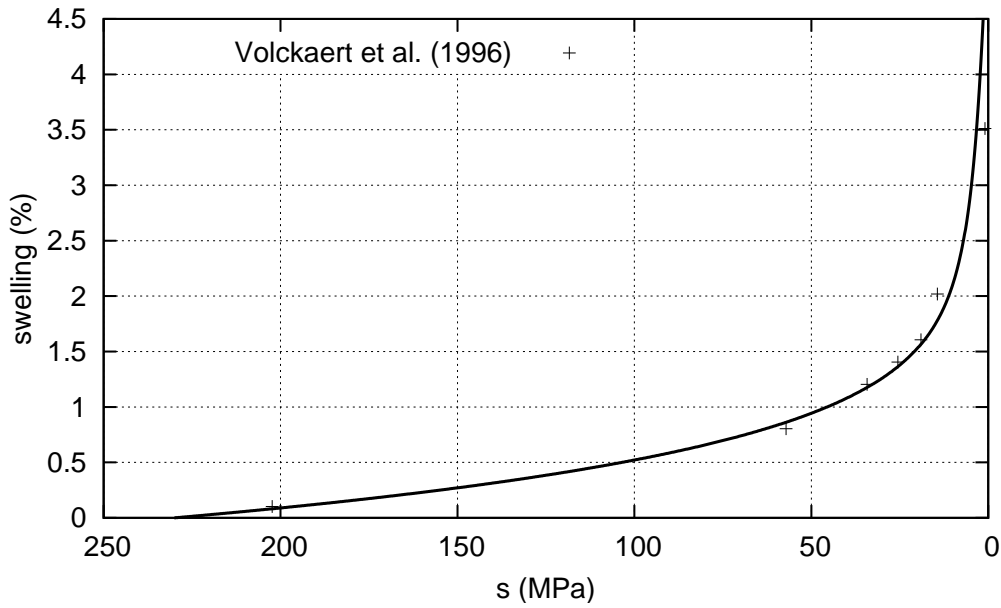


Fig. 2.13: Water Retention Curve

Experimental values of the resulting swelling strains are represented in figure 2.14. Swelling strains are also computed thanks to equation 2.47, giving the relationship between the constitutive stress increment and the elastic strain increment. The numerical simulation is in good agreement with experimental data. Knowledge of the water retention properties in addition to mechanical rigidity parameters therefore allows us to reproduce adequately the elastic swelling behaviour observed during wetting.

Fig. 2.14: swelling $\sigma_v = 0.1$ MPa

2.6 General elasticity law

The two previous sections have highlighted how suction and damage, independently, affect the elastic stiffness.

Combining the definition of the double effective stress with the principle of strain equivalence gives the following elasticity law, accounting for both damage and suction effects:

$$\dot{\tilde{\sigma}}^* = \mathbf{D}_e(\tilde{\sigma}^*) \dot{\tilde{\epsilon}}^e \quad (2.55)$$

with

$$D_{e_{ijkl}}(\tilde{\sigma}^*) = p_r \left(\frac{\tilde{p}_e^*}{p_r} \right)^n \left[nk \frac{\tilde{\sigma}_{ij}^* \tilde{\sigma}_{kl}^*}{\tilde{p}_e^{*2}} + k(1-n) \delta_{ij} \delta_{kl} + 2g \left(\delta_{ik} \delta_{jl} - \frac{1}{3} \delta_{kl} \delta_{ij} \right) \right] \quad (2.56)$$

It has been shown that this formulation, combining the mechanical properties of the intact, dry, material, with the definition of a double effective stress representing the stress applied on the solid skeleton, allows us to adequately represent the principal effects of damage and suction on the apparent mechanical behaviour in the reversible domain.

The following chapter will deal with dissipative phenomena, i.e. the evolution of damage and plastic strains under mechanical loading. The principle of strain equivalence, despite its limitations in reproducing rigidity degradation, will be used in the following developments due to its ability to be easily coupled with plasticity.

CHAPTER 3

DISSIPATIVE PHENOMENA (DAMAGE AND PLASTICITY)

The purpose of this chapter is to describe the dissipative part of the constitutive model. Damage criterion and evolution law are introduced as well as the plasticity framework. Damage and plasticity equations are expressed in terms of the double effective stress. It is shown how damage and plasticity criteria evolve with suction and damage in the double effective stress space as well as in the total stress space.

Le but de ce chapitre est de décrire la partie dissipative du modèle constitutif. Le critère d'endommagement et sa loi d'évolution ainsi que le cadre élasto-plastique sont introduits. Les équations d'endommagement et de plasticité sont exprimées en fonction de la contrainte doublement effective. Nous montrons comment les critères d'endommagement et de plasticité évoluent avec la succion et l'endommagement dans l'espace des contraintes doublement effectives ainsi que dans l'espace des contraintes totales.

Contents

3.1	Thermodynamics	38
3.1.1	Second law	38
3.1.2	Helmholtz free energy	39
3.1.3	Clausius-Duhem Inequality – dissipation	39
3.1.4	Hypotheses on the form of Helmholtz free energy	40
3.2	Damage criterion and evolution	41
3.2.1	General framework	41
3.2.2	Specific functions	42
3.3	Plasticity	46
3.3.1	Definition of the preconsolidation pressure and hardening law	48
3.3.2	Dependence of the preconsolidation pressure on suction	50
3.3.3	Yield surface	52
3.3.4	Plastic flow rule	54
3.4	Derivation of the incremental law	55

The dissipative behaviour of geomaterials can be due to two different phenomena. The first one is plasticity, which causes irreversible strains, the second one is damage, which can be seen as the creation of microcracks and expresses itself by the degradation of elastic properties. These behaviours can appear independently or simultaneously depending on the material. (See figures 3.1 to 3.3)

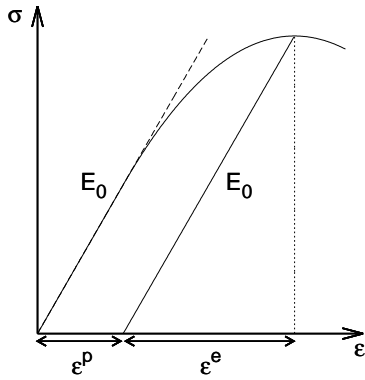


Fig. 3.1: Plastic

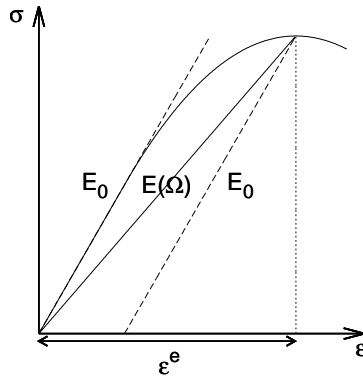


Fig. 3.2: Brittle

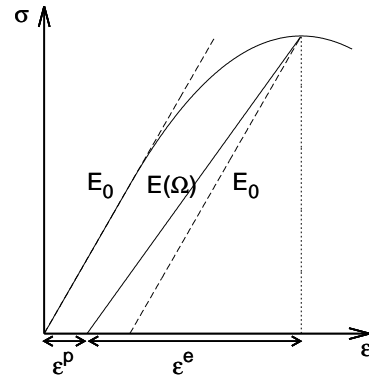


Fig. 3.3: Coupling of damage and plasticity

Early damage models were developed for purely brittle materials (Krajcinovic and Fonseka, 1981; Mazars, 1984; Ortiz, 1985). Some of them considered permanent strains due to residual opening of micro-cracks (Halm and Dragon, 1998; Swoboda and Yang, 1999; Arson and Gatmiri, 2009). However, they didn't account for the large plastic strains observed in geomaterials. This led to the development of models combining damage and elastoplasticity, first for concrete which were later extended to rock behaviour. These models are based either on phenomenological (Simo and Ju, 1987; Ju, 1989; Yazdani and Schreyer, 1990; Hansen and Schreyer, 1994; Abu Al-Rub and Voyiadjis, 2003; Grassl and Jirásek, 2006; Einav et al., 2007) or on micromechanical approaches (Zhu et al., 2008; Abou-Chakra Guéry et al., 2008; Zhu et al., 2011).

The following developments are based on thermodynamics, whose basic principles are recalled in the next section.

3.1 Thermodynamics

3.1.1 Second law

The second law of thermodynamics states that the change of entropy, S , is such that

$$\dot{S} \geq \frac{\dot{Q}}{T} \quad (3.1)$$

which gives, with local quantities:

$$\dot{\eta} + \nabla \cdot \left(\frac{\vec{q}}{T} \right) \geq 0 \quad (3.2)$$

$$\nabla \cdot \left(\frac{\vec{q}}{T} \right) = \frac{\nabla \cdot \vec{q}}{T} - \frac{\vec{q} \cdot \nabla T}{T^2} \quad (3.3)$$

Incorporation of the expression of internal energy (equation 1.11) and strain work rate (equation 1.18) leads to:

$$T\dot{\eta} - \frac{\vec{q} \cdot \nabla T}{T} \geq -\nabla \cdot \vec{q} = \dot{u} - \boldsymbol{\sigma}^* : \dot{\boldsymbol{\varepsilon}} + s^* \dot{S}_l - p_f \quad (3.4)$$

$$T\dot{\eta} - \dot{u} + \boldsymbol{\sigma}^* : \dot{\boldsymbol{\varepsilon}} - s^* \dot{S}_l - \frac{\vec{q} \cdot \nabla T}{T} + p_f \geq 0 \quad (3.5)$$

3.1.2 Helmholtz free energy

It is more convenient to use temperature as a state variable instead of entropy. We will thus use the specific Helmholtz free energy defined through a Legendre transform as:

$$\psi = u - T\eta \quad (3.6)$$

$$\dot{\psi} = \dot{u} - T\dot{\eta} - \eta\dot{T} \quad (3.7)$$

We assume that the material state is described by the values of the following state variables: The elastic strain, $\boldsymbol{\varepsilon}^e$, the degree of saturation, S_l , temperature, T , damage, d , and a hardening variable, $\boldsymbol{\chi}$. Helmholtz free energy can therefore be written as:

$$\psi = \psi(\boldsymbol{\varepsilon}^e, S_l, T, d, \boldsymbol{\chi}) \quad (3.8)$$

$$\dot{\psi} = \frac{\partial \psi}{\partial \boldsymbol{\varepsilon}^e} \dot{\boldsymbol{\varepsilon}}^e + \frac{\partial \psi}{\partial S_l} \dot{S}_l + \frac{\partial \psi}{\partial T} \dot{T} + \frac{\partial \psi}{\partial d} \dot{d} + \frac{\partial \psi}{\partial \boldsymbol{\chi}} \dot{\boldsymbol{\chi}} \quad (3.9)$$

3.1.3 Clausius-Duhem Inequality – dissipation

We assume the following strain partition:

$$\boldsymbol{\varepsilon} = \boldsymbol{\varepsilon}^e + \boldsymbol{\varepsilon}^p \quad (3.10)$$

Combining equations 3.5 and 3.7 leads to the Clausius-Duhem inequality:

$$\boldsymbol{\sigma}^* : \dot{\boldsymbol{\varepsilon}} - s^* \dot{S}_l - (\dot{\psi} + \eta\dot{T}) - \frac{\vec{q} \cdot \nabla T}{T} + p_f \geq 0 \quad (3.11)$$

which gives, introducing equation 3.9:

$$\left(\boldsymbol{\sigma}^* - \frac{\partial \psi}{\partial \boldsymbol{\varepsilon}^e} \right) : \dot{\boldsymbol{\varepsilon}}^e - \left(\eta + \frac{\partial \psi}{\partial T} \right) \dot{T} - \left(s^* + \frac{\partial \psi}{\partial S_l} \right) \dot{S}_l + \boldsymbol{\sigma}^* : \dot{\boldsymbol{\varepsilon}}^p - \frac{\partial \psi}{\partial d} \dot{d} - \frac{\partial \psi}{\partial \boldsymbol{\chi}} \dot{\boldsymbol{\chi}} - \frac{\vec{q}}{T} \cdot \nabla T + p_f \geq 0 \quad (3.12)$$

We can obtain the following constitutive equations by constructing specific loading paths, with $\dot{\boldsymbol{\varepsilon}}^p = 0$, $\dot{d} = 0$, $\dot{\boldsymbol{\chi}} = 0$, $\nabla T = 0$ and $p_f = 0$:

$$\dot{\boldsymbol{\varepsilon}}^e \neq 0, \dot{T} = 0 \text{ and } \dot{S}_l = 0 \implies \boldsymbol{\sigma}^* = \frac{\partial \psi}{\partial \boldsymbol{\varepsilon}^e} \quad (3.13)$$

$$\dot{T} \neq 0, \dot{\boldsymbol{\varepsilon}}^e = 0 \text{ and } \dot{S}_l = 0 \implies \eta = -\frac{\partial \psi}{\partial T} \quad (3.14)$$

$$\dot{S}_l \neq 0, \dot{\boldsymbol{\varepsilon}}^e = 0 \text{ and } \dot{T} = 0 \implies s^* = -\frac{\partial \psi}{\partial S_l} \quad (3.15)$$

By analogy with the previous relationships, the following thermodynamic conjugate forces are defined:

$$Y_d = -\frac{\partial \psi}{\partial d} \quad \boldsymbol{\xi} = -\frac{\partial \psi}{\partial \boldsymbol{\chi}} \quad (3.16)$$

The pairs of conjugated variables are summarised in table 3.1.

Strain-like variables		Work conjugate variables	
$\boldsymbol{\varepsilon}^e$	Elastic strain tensor	$\boldsymbol{\sigma}^*$	Average skeleton stress tensor
S_l	Degree of saturation	s^*	Modified suction
T	Temperature	η	Entropy
d	Damage	Y_d	
$\boldsymbol{\chi}$	Hardening variables	$\boldsymbol{\xi}$	

Table 3.1: List of variables

The dissipation is then given by

$$\mathcal{D} = \boldsymbol{\sigma}^* : \dot{\boldsymbol{\varepsilon}}^p + Y_d \dot{d} + \boldsymbol{\xi} : \dot{\boldsymbol{\chi}} - \frac{\vec{q}}{T} \cdot \nabla T + p_f \geq 0 \quad (3.17)$$

We can assume that there exist several dissipation potentials, which are decoupled so that each of them is positive:

$$\mathcal{D} = \mathcal{D}_M + \mathcal{D}_T + \mathcal{D}_f \quad (3.18)$$

with:

- The mechanical (intrinsic) dissipation: $\mathcal{D}_M = \boldsymbol{\sigma}^* : \dot{\boldsymbol{\varepsilon}}^p + Y_d \dot{d} + \boldsymbol{\xi} : \dot{\boldsymbol{\chi}} \geq 0$
- The thermal dissipation: $\mathcal{D}_T = -\frac{\vec{q}}{T} \cdot \nabla T \geq 0$
- The dissipation due to fluid flow: $\mathcal{D}_f = p_f \geq 0$

The following work will be focused on the mechanical dissipation \mathcal{D}_M .

3.1.4 Hypotheses on the form of Helmholtz free energy

In this work, isothermal processes are considered.

The following form is assumed for the Helmholtz free energy:

$$\psi = \psi(\boldsymbol{\varepsilon}^e, S_l, \boldsymbol{\chi}, d) = \psi^e(\boldsymbol{\varepsilon}^e, d) + \psi_l(S_l) + \psi^p(\boldsymbol{\varepsilon}^p, \boldsymbol{\chi}) \quad (3.19)$$

This choice leads to certain couplings between the different phenomena involved.

Concerning the damage-elastic part of Helmholtz free energy, we chose to use the form proposed by Ju (1989):

$$\psi^e(\boldsymbol{\varepsilon}^e, d) = \psi_0^e(\boldsymbol{\varepsilon}^e)(1 - d) \quad (3.20)$$

This form is in accordance with the principle of strain equivalence combined with the existence of an effective stress:

$$\boldsymbol{\sigma}^* = \frac{\partial \psi}{\partial \boldsymbol{\varepsilon}^e} = \frac{\partial \psi_0^e}{\partial \boldsymbol{\varepsilon}^e} (1 - d) \quad (3.21)$$

$$\tilde{\boldsymbol{\sigma}}^* = \frac{\boldsymbol{\sigma}^*}{1 - d} = \frac{\partial \psi_0^e}{\partial \boldsymbol{\varepsilon}^e} \quad (3.22)$$

3.2 Damage criterion and evolution

The thermodynamic force conjugated to damage is:

$$Y_d = -\frac{\partial \psi}{\partial d} = -\frac{\partial \psi^e}{\partial d} = \psi_0^e(\boldsymbol{\varepsilon}^e) \quad (3.23)$$

This expression of Helmholtz free energy implies that the force conjugated to damage only depends on elastic strains. This is equivalent as saying that it depends on the double effective stress state since they are related through the constitutive equation 3.13.

This is a strong assumption since it implies that the initiation and evolution of damage is driven by elastic strains. Some researches proposed that damage should be created by plastic strains. However, our approach decoupling both dissipative phenomena allows both of them to appear independently, and thus to simulate brittle material as well as plastic materials. Moreover, we will see later that plastic processes can still indirectly influence damage by modifying the stress state (see part 7.2.1).

3.2.1 General framework

To describe damage initiation and evolution, a damage criterion, $f_d = 0$, is defined. The equation $f_d = 0$ defines a surface, which separates the double effective stress space into a domain in which no dissipative phenomena occur (inside) and a domain of non-attainable stress states (outside). This surface is assumed to be convex.

Ideally, this function should depend on the thermodynamic force conjugated to damage:

$$f_d(Y_d(\boldsymbol{\varepsilon}_e), d) = 0 \quad (3.24)$$

Checking the sign of this function allows to determine in which state the material is in relation to damage.

If the stress state lies inside the damage surface, or in the case in which the stress state

lies on the damage yield surface but the point goes towards the inside of the yield surface (unloading), then there is no evolution of damage.

If the stress state lies on the damage criterion and the loading is increasing, damage increases and hardening causes the damage surface to extend so that the stress state always remains on the surface.

These conditions can be summarised as follow:

$$\begin{cases} \text{if } f_d < 0 \text{ or } \dot{f}_d < 0 & \text{then } \dot{d} = 0 \\ \text{if } f_d = 0 \text{ and } \dot{f}_d = 0 & \text{then } \dot{d} \geq 0 \end{cases} \quad (3.25)$$

The stress state has to remain on the damage criterion during loading, which means that, at any time, $f_d = 0$ and $\dot{f}_d = 0$. Deriving equation 3.24 gives the consistency condition:

$$0 = \dot{f}_d = \frac{\partial f_d}{\partial Y_d} \dot{Y}_d + \frac{\partial f_d}{\partial d} \dot{d} \quad (3.26)$$

from which the damage evolution law can be deduced:

$$\dot{d} = - \frac{\dot{Y}_d \frac{\partial f_d}{\partial Y_d}}{\frac{\partial f_d}{\partial d}} \quad (3.27)$$

3.2.2 Specific functions

Damage criterion based on the thermodynamic force conjugated to damage

The expression of the thermodynamic force conjugated to damage given by the hyperelastic potential of Houlsby et al. (2005) can be derived from equation 3.23 and table 2.1:

$$Y_d = \psi_\theta^e(\boldsymbol{\varepsilon}^e) = p_r \frac{[k(1-n)]^{\frac{2-n}{1-n}}}{k(2-n)} \left[(\varepsilon_v^*)^2 + \frac{3g\varepsilon_s^{e2}}{k(1-n)} \right]^{\frac{2-n}{2-2n}} \quad (3.28)$$

This expression can also be expressed in terms of stresses. Deriving Gibbs free energy gives:

$$\varepsilon_v^e = \frac{\partial \mathcal{G}_\theta^e(\tilde{\boldsymbol{\sigma}}^*)}{\partial \tilde{p}^*} = \frac{1}{k(1-n)} \left[\frac{\tilde{p}^*}{p_r^{(1-n)} \tilde{p}_0^{*n}} - 1 \right] \quad (3.29)$$

$$\varepsilon_v^* = \varepsilon_v^e + \frac{1}{k(1-n)} = \frac{1}{k(1-n)} \frac{\tilde{p}^*}{p_r^{(1-n)} \tilde{p}_0^{*n}} \quad (3.30)$$

$$\varepsilon_s^e = \frac{\partial \mathcal{G}_\theta^e(\tilde{\boldsymbol{\sigma}}^*)}{\partial q} = \frac{q}{3gp_r^{(1-n)} \tilde{p}_0^{*n}} \quad (3.31)$$

Introducing equation 3.30 and 3.31 into equation 3.28 leads to:

$$Y_d(\tilde{\sigma}^*) = \frac{p_r^{(n-1)}}{k(2-n)} \tilde{p}_0^{*(2-n)} = \frac{p_r^{(n-1)}}{k(2-n)} \left[\tilde{p}^{*2} + \frac{k(1-n)\tilde{q}^{*2}}{3g} \right]^{\frac{(2-n)}{2}} \quad (3.32)$$

A simple choice for the damage criterion would be:

$$f_d = Y_d - C_0 = 0 \quad (3.33)$$

The shape of this criterion is given in figure 3.4, in the plane of the normalised variables:

$$\bar{p} = \tilde{p}^* [C_0 k (2-n) p_r^{(1-n)}]^{\frac{1}{2-n}} \quad (3.34)$$

$$\bar{q} = \tilde{q}^* \frac{\sqrt{\frac{k(1-n)}{3g}}}{[C_0 k (2-n) p_r^{(1-n)}]^{\frac{1}{2-n}}} \quad (3.35)$$

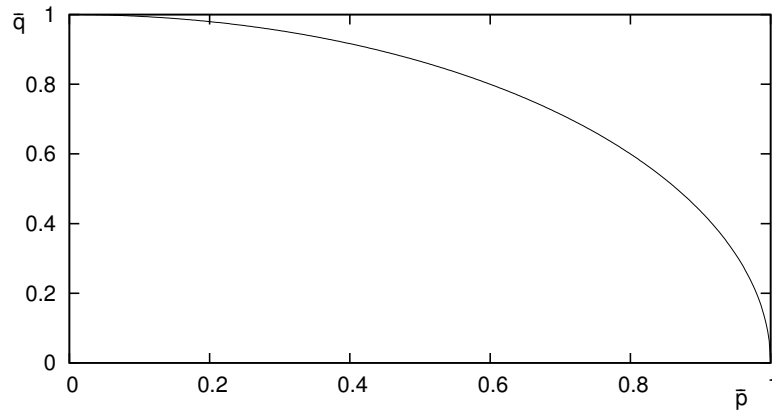


Fig. 3.4: Shape of damage criterion $Y_d - C_0 = 0$

The choice of this criterion has two disadvantages. The first one is that it makes it possible to damage the material by isotropic compression, which is arguable. The second and main issue is that damage will initiate for a lower deviatoric stress when the confining pressure is higher, which is in disagreement with experimental evidence. Indeed, geomaterials are known to be more brittle at low confining pressure and more plastic at high confining pressures.

Damage criterion based on Drucker-Prager

For this reason, we choose to use a more empirical damage criterion which will enable us to represent the fact that geomaterials are less damageable at high confining pressure.

We propose to base this criterion on Drucker-Prager, which gives the following simple form for the damage loading function:

$$f_d(Y_d^*, d) = Y_d^* - C_0 - C_1 d \quad (3.36)$$

with

$$Y_d^* = \sqrt{3J_2} - C_2 I_1 = \tilde{q} - C_2 \tilde{p}^* \quad (3.37)$$

which gives, for the expression of the yield surface,

$$\tilde{q} - C_2 \tilde{p}^* - C_0 - C_1 d = 0 \quad (3.38)$$

in which C_1 is a hardening parameter. The lower C_1 , the faster d will increase with deviatoric stress.

The shape of the damage criterion in the effective stress space is given in figure 3.5 for different values of damage. It can be seen that when damage increases, the material is hardening with respect to effective stresses.

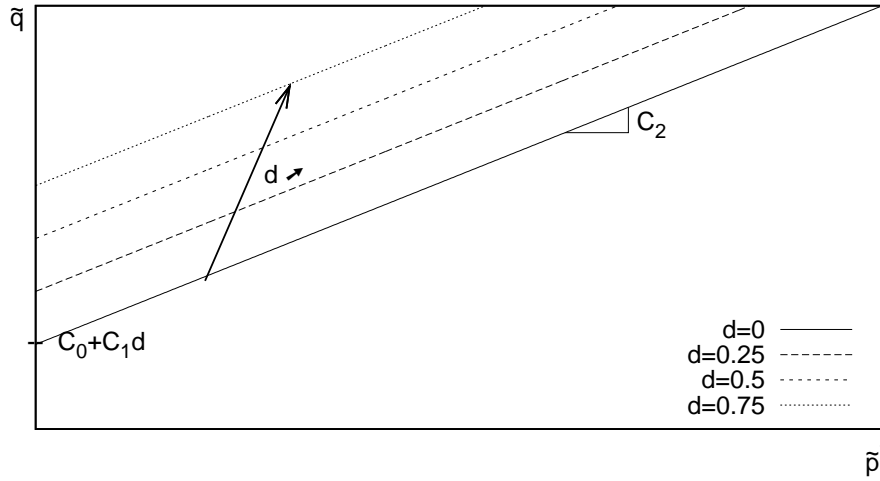


Fig. 3.5: Shape of damage criterion, Drucker-Prager - Effective stress space

Expressed in total stresses, equation 3.38 becomes:

$$\frac{q}{1-d} - C_2 \frac{p + sS_l}{1-d} - C_0 - C_1 d = 0 \quad (3.39)$$

$$q - C_2(p + sS_l) - (1-d)(C_0 + C_1 d) = 0 \quad (3.40)$$

The shape of the corresponding damage criterion in the total stress space is given in figures 3.6 and 3.7.

Figure 3.6 shows the evolution of the damage criterion with damage. It can be seen that, although the intact fraction of the material is hardening, an apparent softening behaviour appears after a certain value of damage is reached, when considering total stresses.

Figure 3.7 shows the evolution of the damage criterion with suction. Although suction doesn't have an effect on the damage criteria in the effective stress space, when considering total stresses, suction increases the size of the undamaged domain.

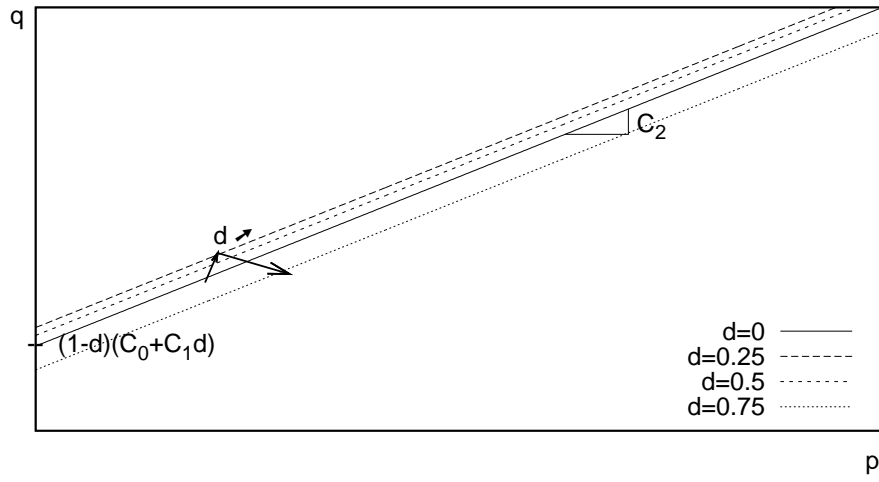


Fig. 3.6: Effect of damage on damage criterion - Total stress space

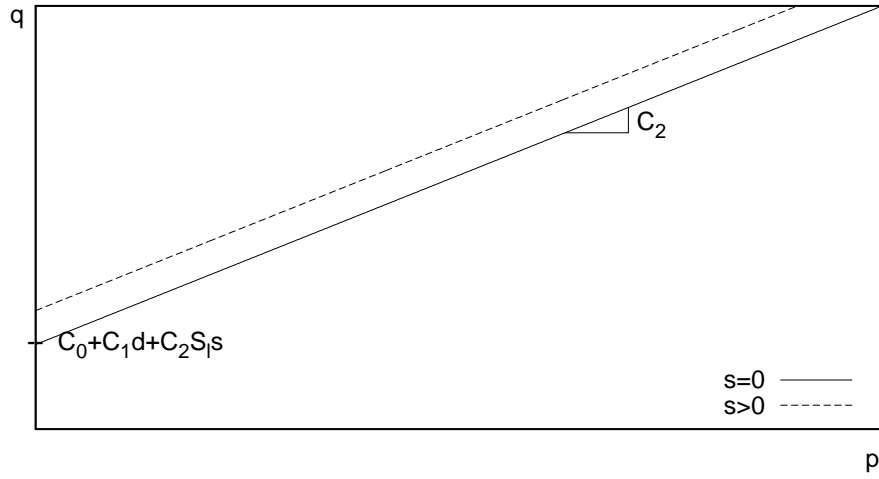


Fig. 3.7: Effect of suction on damage criterion - Total stress space

Damage evolution: Deriving equation 3.36 gives:

$$\frac{\partial f_d}{\partial d} = -C_1 \quad (3.41)$$

$$\frac{\partial f_d}{\partial Y_d^*} = 1 \quad (3.42)$$

$$\dot{Y}_d^* = \frac{\partial Y_d^*}{\partial \tilde{\boldsymbol{\sigma}}^*} \dot{\tilde{\boldsymbol{\sigma}}^*} = \left[\frac{\partial Y_d^*}{\partial \tilde{p}^*} \frac{\mathbf{I}}{3} + \frac{\partial Y_d^*}{\partial \tilde{q}} \frac{3\tilde{\boldsymbol{\sigma}}_d}{2\tilde{q}} \right] : \dot{\tilde{\boldsymbol{\sigma}}^*} = \left[-\frac{C_2}{3} \mathbf{I} + \frac{\tilde{\boldsymbol{\sigma}}_d}{\tilde{q}} \right] : \dot{\tilde{\boldsymbol{\sigma}}^*} \quad (3.43)$$

from which the damage evolution law can be deduced:

$$\dot{d} = -\frac{Y_d^*}{\frac{\partial f_d}{\partial d}} \frac{\partial f_d}{\partial Y_d^*} = \frac{1}{C_1} \left[-\frac{C_2}{3} \mathbf{I} + \frac{\tilde{\boldsymbol{\sigma}}_d}{\tilde{q}} \right] : \dot{\tilde{\boldsymbol{\sigma}}^*} \quad (3.44)$$

If we define $\mathbf{A}_d = \frac{1}{C_1} \left[-\frac{C_2}{3} \mathbf{I} + \frac{\tilde{\boldsymbol{\sigma}}_d}{\bar{q}} \right]$, the damage evolution law becomes:

$$\dot{d} = \mathbf{A}_d(\tilde{\boldsymbol{\sigma}}) : \dot{\tilde{\boldsymbol{\sigma}}}^* \quad (3.45)$$

A typical evolution of damage with deviatoric stress during a triaxial loading is given in figure 3.8.

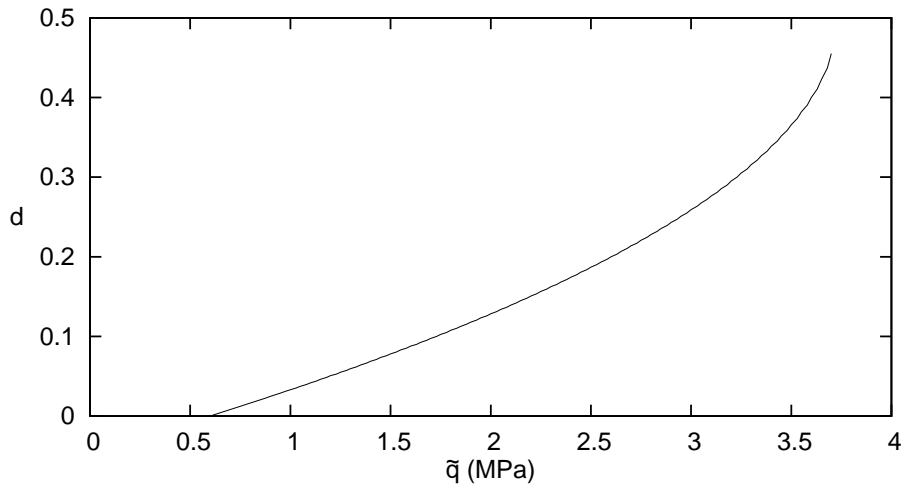


Fig. 3.8: Evolution of damage with deviatoric stress

3.3 Plasticity

According to Jommi (2000), a possible way to construct a model for unsaturated soils, starting from a saturated one, may be summarised in two steps :

- the substitution of the average skeleton stress for effective stress
- introduction in the basic saturated elastoplastic model of the modifications necessary to take into account the effects of the interfaces on the overall mechanical behaviour

According to Ju (1989), it appears reasonable to state that the plastic flows occur only in the undamaged material by means of effective quantities. Therefore, the characterisation of the plastic response should be formulated in the damaged effective stress space and the stress tensor is replaced by the damaged stress tensor, $\tilde{\boldsymbol{\sigma}}$, into the equations of plasticity. This follows the principle of strain equivalence.

We combine these two approaches and choose as a basis a model for saturated soils, in which we will replace the saturated effective stress by our double effective stress. A dependence of the yield criterion on suction will be added.

We will therefore need to define:

- A yield criterion, which determines the boundary of the elastic domain:

$$f_p = f_p(\tilde{\boldsymbol{\sigma}}^*, \chi) \quad (3.46)$$

such as

$$\begin{cases} \text{if } f_p < 0 \text{ or } \dot{f}_p < 0 & \text{then } \dot{\boldsymbol{\epsilon}}^p = 0 \\ \text{if } f_p = 0 \text{ and } \dot{f}_p = 0 & \text{then } \dot{\boldsymbol{\epsilon}}^p \geq 0 \end{cases} \quad (3.47)$$

- A plastic potential:

$$g_p = g_p(\tilde{\boldsymbol{\sigma}}^*, \chi) \quad (3.48)$$

- A plastic flow rule (if the plastic potential is taken equal to the yield criterion, the flow rule is said to be associated):

$$\dot{\boldsymbol{\epsilon}}^p = \dot{\Lambda}_p \frac{\partial g_p}{\partial \tilde{\boldsymbol{\sigma}}^*} \quad (3.49)$$

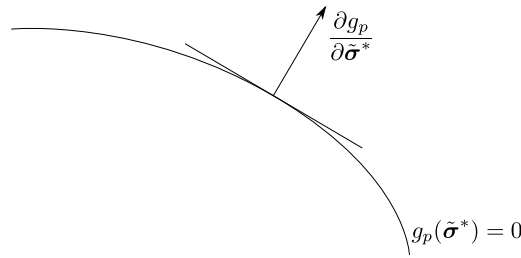


Fig. 3.9: Plastic potential and direction of plastic flow

- A hardening variable, $\chi = \chi(\chi_0, s)$, depending on suction and on χ_0 , the hardening parameter for the saturated state
- A hardening law:

$$\dot{\chi}_0 = f(\dot{\boldsymbol{\epsilon}}^p) \quad (3.50)$$

The saturated soil model that we chose to develop to highlight how our modelling assumptions affect the plastic behaviour is the **Cam-Clay model** (CC). It was at first proposed by Roscoe et al. (1963) for clays and later modified by Roscoe and Burland (1968). The different components of this model are described below. In this way, it is similar to the most widely used model for unsaturated soils, the Barcelona Basic Model (BBM) (Alonso et al., 1990). However some slight modifications are introduced, most of them being already used by other researchers. The main difference is the fact that the BBM model is expressed in terms of net stresses, whereas ours is expressed in term of the unsaturated effective stress.

Any other plasticity model could be implemented following the same approach in order to fit better the behaviour of different materials.

3.3.1 Definition of the preconsolidation pressure and hardening law

The typical volumetric response for an isotropic compression on a saturated sample is given in figure 3.10. The specific volume, $v = 1 + e$, is often used to represent soil volumetric behaviour.

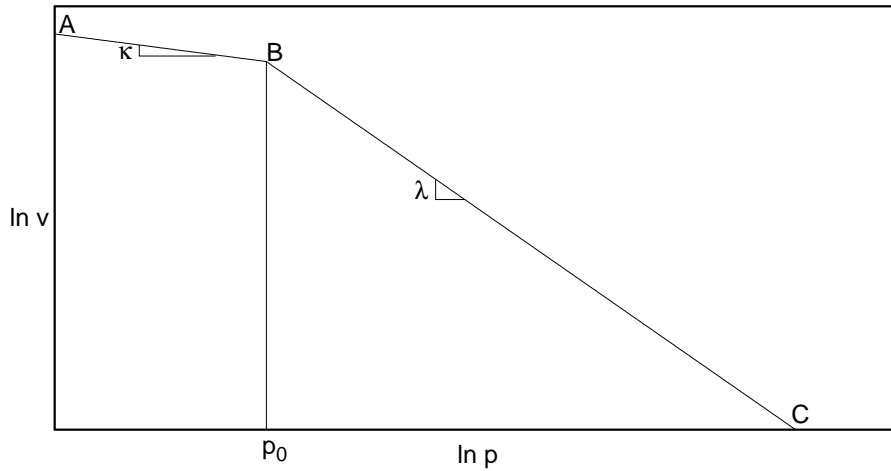


Fig. 3.10: Volumetric behaviour in Cam-Clay

Along path AB, the soil behaves elastically and we recover the stress-strain relationship already seen in chapter 2.3, for the case $n = 1$.

$$\dot{\epsilon}_v = \dot{\epsilon}_v^e = -\frac{\dot{v}}{v} = \kappa \frac{\dot{p}}{p} \quad (3.51)$$

When the mean pressure reaches the **preconsolidation pressure** p_0 , the materials yields and undergoes plastic strains. The preconsolidation pressure is chosen to be the **hardening parameter**. Along path BC, the volumetric stress-strain relationship is:

$$\dot{\epsilon}_v = \dot{\epsilon}_v^e + \dot{\epsilon}_v^p = -\frac{\dot{v}}{v} = \lambda \frac{\dot{p}}{p} \quad (3.52)$$

Integration of these equations leads to straight swelling (equation 3.51) and consolidation (equation 3.52) lines in the plane $\ln v - \ln p$. This represents a slight alteration of the Cam-Clay model for which these lines were taken as straight in the $v - \ln p$ plane. This modification is supported by experimental evidence (Butterfield, 1979), and has been used by many authors (Wroth and Houlsby, 1980; Borja et al., 1997; Sheng et al., 2004). Hashiguchi (1995) presented physical arguments in favour of a bilogarithmic law.

When yielding along path BC, the preconsolidation pressure increases and remains equal to the mean pressure. Equations 3.51 and 3.52 therefore become:

$$\dot{\epsilon}_v^e = \kappa \frac{\dot{p}_0}{p_0} \quad (3.53)$$

$$\dot{\varepsilon}_v = \dot{\varepsilon}_v^e + \dot{\varepsilon}_v^p = \lambda \frac{\dot{p}_0}{p_0} \quad (3.54)$$

from which the hardening law can be deduced:

$$\dot{\varepsilon}_v^p = \dot{\varepsilon}_v - \dot{\varepsilon}_v^e = (\lambda - \kappa) \frac{\dot{p}_0}{p_0} \quad (3.55)$$

$$\dot{p}_0 = \frac{p_0}{\lambda - \kappa} \dot{\varepsilon}_v^p \quad (3.56)$$

Extension to $n \neq 1$: To consistently derive the hardening law in the case in which the pressure exponent is not equal to 1, the previous equation needs to be modified. It is assumed that the dependence of the normal consolidation line on mean pressure follows the same law as for the swelling line.

Swelling line:

$$\dot{\varepsilon}_v = \dot{\varepsilon}_v^e = -\frac{\dot{v}}{v} = \frac{\kappa}{p_r^{(1-n)}} \frac{\dot{p}}{p^n} \quad (3.57)$$

Normal consolidation line:

$$\dot{\varepsilon}_v = \dot{\varepsilon}_v^e + \dot{\varepsilon}_v^p = -\frac{\dot{v}}{v} = \frac{\lambda}{p_r^{(1-n)}} \frac{\dot{p}}{p^n} \quad (3.58)$$

It should be noted that these lines are not straight lines anymore (see figure 3.11).

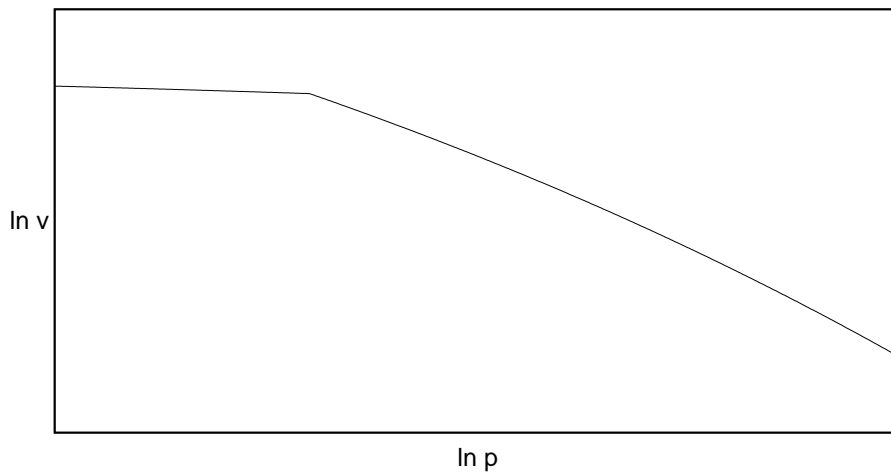


Fig. 3.11: Volumetric behaviour - mean pressure exponent $n \neq 1$

The hardening law becomes:

$$\dot{\varepsilon}_v^p = \dot{\varepsilon}_v - \dot{\varepsilon}_v^e = \frac{(\lambda - \kappa)}{p_r^{(1-n)}} \frac{\dot{p}_0}{p_0^n} \quad (3.59)$$

$$\dot{p}_0 = \frac{p_0^n p_r^{(1-n)}}{\lambda - \kappa} \dot{\varepsilon}_v^p \quad (3.60)$$

3.3.2 Dependence of the preconsolidation pressure on suction

To be able to reproduce the extension of the elastic domain with suction, the preconsolidation pressure has to depend on suction and on the saturated preconsolidation pressure, p_0 :

$$p_c^* = p_c^*(p_0, s) \quad (3.61)$$

When drawn in the plane $p - s$, this curve is called the Loading-Collapse (LC) curve.

Many expressions have been proposed in the literature. Some of them are summarised in table 3.2.

Reference	
Alonso et al. (1990) (BBM)	$\frac{p_c^{net}}{p_r} = \left(\frac{p_0}{p_r}\right)^{\frac{\lambda(0)-\kappa}{\lambda(s)-\kappa}} \quad (3.62)$ $\lambda(s) = \lambda(0)[(1-r)\exp(-\beta s) + r] \quad (3.63)$
Jommi (2000)	$\frac{p_c^*}{p_r} = \left(\frac{p_0}{p_r}\right)^{\frac{\lambda(0)-\kappa}{\lambda(s)-\kappa}} + S_l s \quad (3.64)$ $\lambda(s) = \frac{\lambda_0(p^* - S_l s)}{p^*} \quad (3.65)$
Wheeler et al. (2003)	$p_c^* = p_0 \quad (3.66)$
Sheng et al. (2004)	$p_c^* = p_r \left(\frac{p_0}{p_r}\right)^{\frac{\lambda(0)-\kappa}{\lambda(s)-\kappa}} + S_l s \quad (3.67)$ $\lambda(s) = \lambda(0)[(1-r)\exp(-\beta s) + r] \quad (3.68)$
Sun et al. (2008)	$\frac{p_c^*}{p_r} = \left(\frac{p_0}{p_r}\right)^{\frac{\lambda(0)-\kappa}{\lambda(s)-\kappa}} \quad (3.69)$ $\lambda(s) = \lambda(0) + \frac{\lambda_s s}{p_g + s} \quad (3.70)$

Table 3.2: Different expressions used for the LC curve in the literature

In the following we will use the proposition of Sheng et al. (2004), because this is the closest one to that used in BBM. Since most of experimental works are based on the BBM,

the values of the different parameters obtained from experimental studies are usually given for this expression of the LC curve.

The shape of the LC curve in both total and effective stress space is given in figure 3.12.

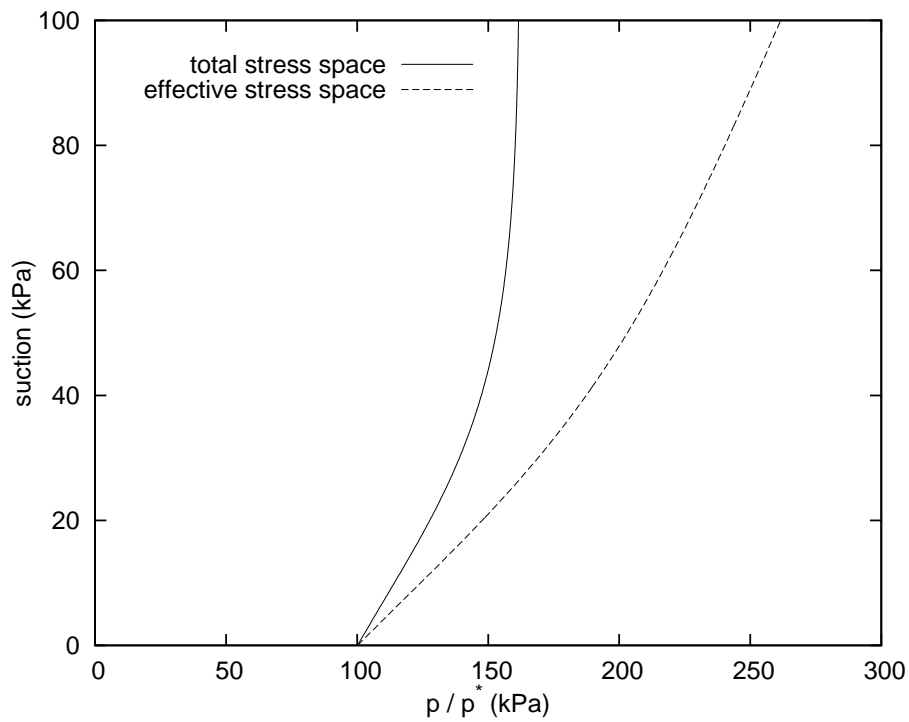


Fig. 3.12: Shape of the yield surface in $p - s$ plane

The volumetric behaviour (in total stresses) for an unsaturated material is shown in figure 3.13.

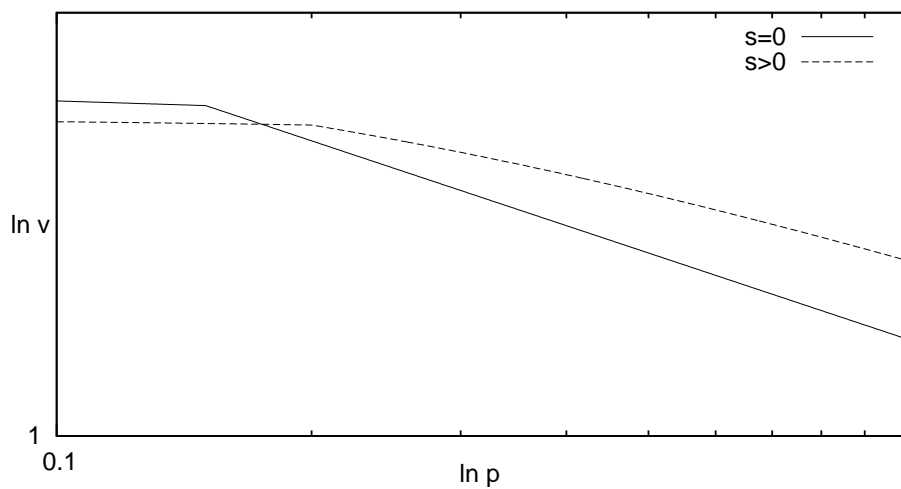


Fig. 3.13: Effect of suction on yield point and consolidation curve for $n = 1$

3.3.3 Yield surface

Cam-clay models have been developed in the framework of Critical State Soil Mechanics (Roscoe et al., 1958; Schofield and Wroth, 1968). The **critical state** concept states that soils and other granular materials, if continuously distorted until they flow as a frictional fluid, will come into a well-defined critical state. At the onset of the critical state, shear distortions occur without any further changes in mean effective stress, deviatoric stress or void ratio. The critical state is described in the (\tilde{p}^*, \tilde{q}) plane by the line of equation:

$$\tilde{q} = M\tilde{p}^* \quad (3.71)$$

Original Cam-Clay model: The original Cam-Clay model (Roscoe et al., 1963) is based on the assumption that the deviatoric strain is entirely plastic, which is why no shear modulus is defined in the original Cam-Clay model.

It also assumes that, for any stress state lying on the yield surface, the dissipated energy is independent of the volumetric strain and is equal to:

$$\dot{W}^p = Mp\dot{\epsilon}_s^p \quad (3.72)$$

The yield surface is derived by applying the normality condition (in the original versions of CC, the flow rule is assumed to be associated), which gives:

$$f_p = \tilde{q} + M\tilde{p}^* \ln\left(\frac{\tilde{p}^*}{p_0}\right) \quad (3.73)$$

in which p_0 is the preconsolidation pressure. The corresponding yield surface is represented in figure 3.14.

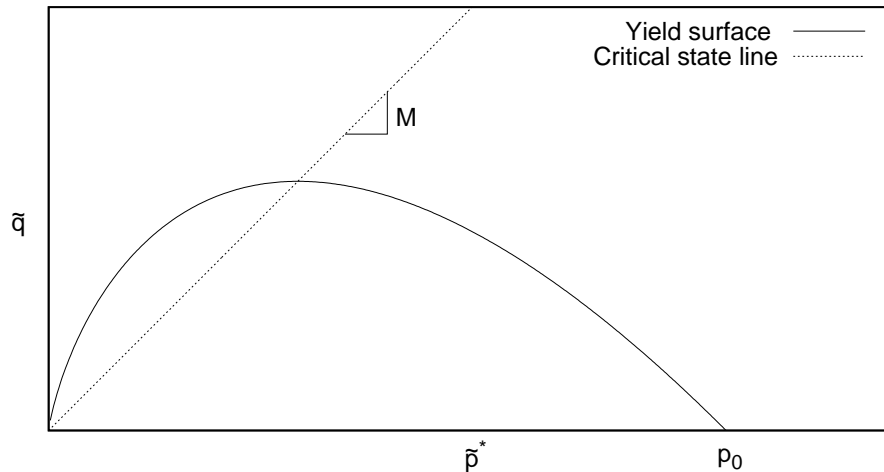


Fig. 3.14: Original Cam-Clay yield surface

The main disadvantage of this expression of the yield surface is the fact that its intersection with the isotropic axis ($q = 0$) is angular. It leads to numerical issues since the derivative of f_p is not unique at this point. Moreover, plastic deviatoric strains are created during

isotropic loading, which is counter-intuitive.

Modified Cam-Clay model: Burland (1965) modified the aforementioned model by stating that the assumption of isotropy requires that under isotropic stress ($q = 0$), there is no distortion ($\dot{\varepsilon}_s^p = 0$), which leads to the following expression for the dissipated work:

$$\dot{W}^p = p \sqrt{(\dot{\varepsilon}_v^p)^2 + (M \dot{\varepsilon}_s^p)^2} \quad (3.74)$$

Applying the normality condition to equation 3.74 gives the equation of the yield surface:

$$f_p = \tilde{q}^2 - M^2 \tilde{p}^* (p_c^*(p_0, s) - \tilde{p}^*) \quad (3.75)$$

in which p_c^* is the preconsolidation pressure.

The shape of the yield criterion in the effective stress space is given in figure 3.15. The yield surface in the effective stress space does depend on suction, but not on damage.

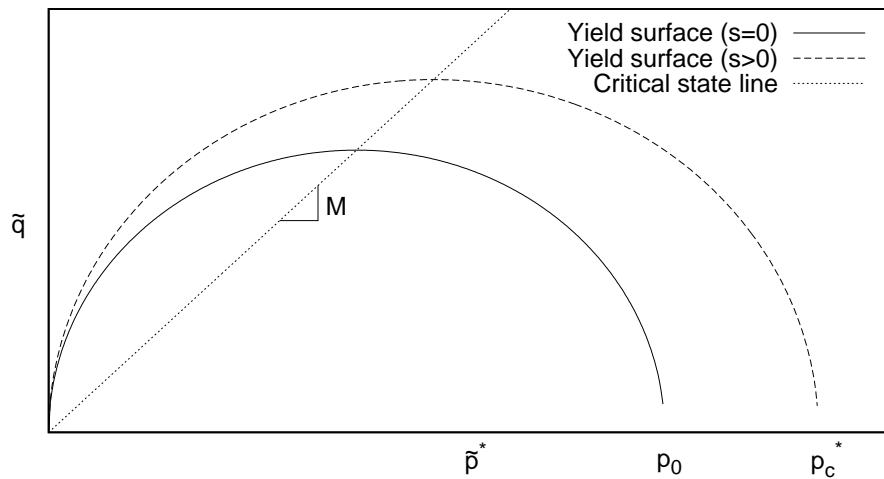


Fig. 3.15: Modified Cam-Clay yield surface

Expressed in total stresses, the equation of the yield surface (equation 3.75) becomes

$$q^2 - M^2(p + S_l s) [(1 - d)p_c^* - (p + S_l s)] = 0 \quad (3.76)$$

and the equation of the critical state line becomes (equation 3.71)

$$q = M(p + S_l s) \quad (3.77)$$

The shape of the yield surface and of the critical state line in the total stress space is given in figures 3.16 and 3.17.

Figure 3.16 shows the evolution of the yield surface with suction. We can see that, with respect to total stresses, the elastic domain increases with suction. Suction also induces an apparent cohesion.

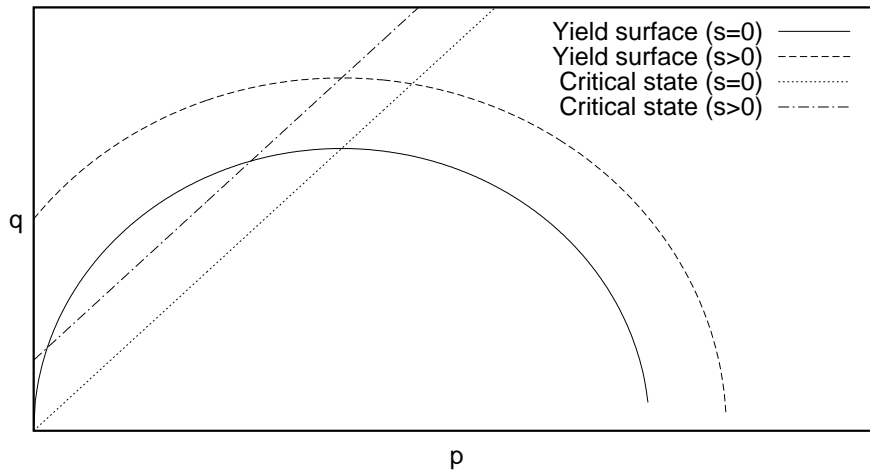


Fig. 3.16: Effect of suction on yield surface - Total stress space

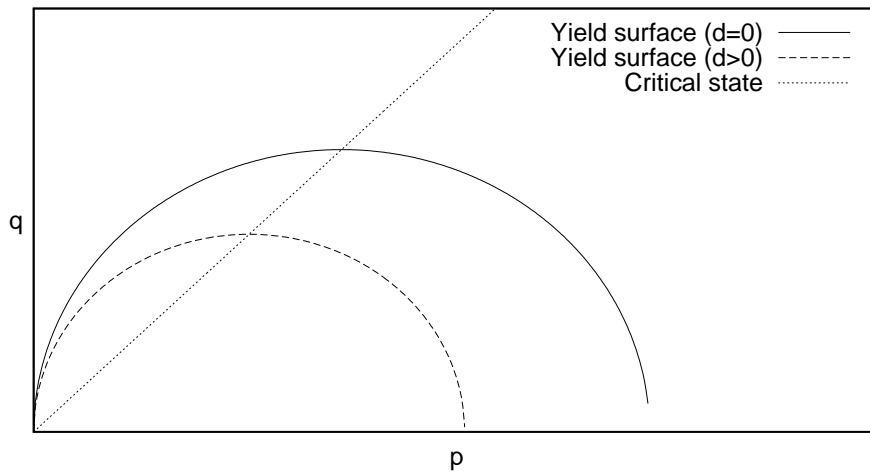


Fig. 3.17: Effect of damage on yield surface - Total stress space

Figure 3.17 shows the evolution of the yield surface with damage. We can see that damage has a softening effect on plastic behaviour. Although plastic and damage dissipative potentials were assumed to be decoupled, we can see that the introduction of the double effective stress into plasticity equations leads to a direct coupling between damage and plasticity.

3.3.4 Plastic flow rule

Cam-clay models have first been designed to consider an associated flow rule. However, it used to overestimate K_0 values and many models (for example BBM) use a non-associated flow rule.

The plastic potential is defined as:

$$g_p = \zeta \tilde{q}^2 - M^2 \tilde{p}^* (p_c^* - \tilde{p}^*) \quad (3.78)$$

in which ζ is calculated to respect the condition of zero lateral strain for K_0 stress states in the usual Cam-Clay model.

$$\zeta = \left(\frac{1}{1 - \frac{\kappa}{\lambda}} \right) \frac{M(M-9)(M-3)}{9(6-M)} \quad (3.79)$$

The shape of the plastic potential is shown in figure 3.18. We can see that the non-associated flow rule will give less deviatoric plastic strains that the associated flow rule.

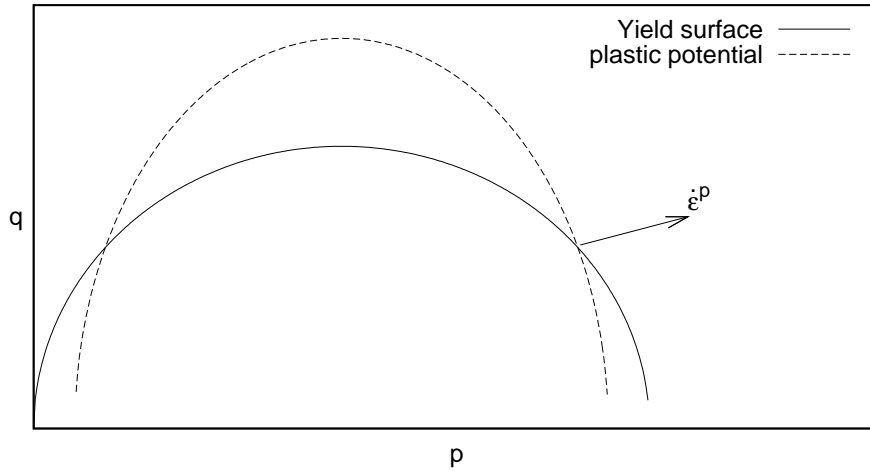


Fig. 3.18: Plastic potential

The non-associative flow rule gives:

$$\dot{\epsilon}^p = \dot{\lambda}_p \frac{\partial g_p}{\partial \tilde{\sigma}^*} = \dot{\lambda}_p \left(\frac{\partial g_p}{\partial \tilde{p}^*} \frac{\mathbf{I}}{3} + \frac{\partial g_p}{\partial q} \frac{3\tilde{\sigma}_d}{2\tilde{q}} \right) \quad (3.80)$$

in which

$$\frac{\partial g_p}{\partial \tilde{\sigma}^*} = \frac{M^2(2\tilde{p}^* - \tilde{p}_c^*)}{3} \mathbf{I} + 3\zeta \tilde{\sigma}_d \quad (3.81)$$

3.4 Derivation of the incremental law

In the following, we derive the incremental stress-strain relationship for the case in which both damage and plastic strains occur at the same time.

Following the method of Sheng et al. (2003), pore fluid pressures are treated like strain components so that we have:

$$\dot{\sigma} = f(\dot{\epsilon}, \dot{p}_g, \dot{p}_l) \quad (3.82)$$

We first express the relationship between the increment of double effective stress and the increment of total strains and suction. Damage is not involved while staying in the effective stress space.

The hypothesis of strain partition, combined with the plastic flow rule (equation 3.80), gives:

$$\dot{\boldsymbol{\varepsilon}} = \dot{\boldsymbol{\varepsilon}}^e + \dot{\boldsymbol{\varepsilon}}^p = \dot{\boldsymbol{\varepsilon}}^e + \dot{\Lambda}_p \frac{\partial g_p}{\partial \tilde{\boldsymbol{\sigma}}^*} \quad (3.83)$$

The elasticity law, defined in chapter 2.6 (equation 2.55) is:

$$\dot{\boldsymbol{\sigma}}^* = \mathbf{D}_e \dot{\boldsymbol{\varepsilon}}^e = \mathbf{D}_e \left(\dot{\boldsymbol{\varepsilon}} - \dot{\Lambda}_p \frac{\partial g_p}{\partial \tilde{\boldsymbol{\sigma}}^*} \right) \quad (3.84)$$

The consistency condition states that the stress state has to remain on the yield surface. Deriving equation 3.75 implies that

$$\dot{f}_p = \frac{\partial f_p}{\partial \tilde{\boldsymbol{\sigma}}^*} : \dot{\boldsymbol{\sigma}}^* + \frac{\partial f_p}{\partial p_c^*} \dot{p}_c^* = 0 \quad (3.85)$$

which, introducing the dependence of the preconsolidation pressure on suction and on the hardening parameter, p_0 , (equation 3.61), becomes

$$\dot{f}_p = \frac{\partial f_p}{\partial \tilde{\boldsymbol{\sigma}}^*} : \dot{\boldsymbol{\sigma}}^* + \frac{\partial f_p}{\partial p_c^*} \frac{\partial p_c^*}{\partial p_0} \dot{p}_0 + \frac{\partial f_p}{\partial p_c^*} \frac{\partial p_c^*}{\partial s} \dot{s} = 0 \quad (3.86)$$

Introducing the elasticity law (equation 3.84) and the plastic hardening law (equation 3.60),

$$\dot{f}_p = \frac{\partial f_p}{\partial \tilde{\boldsymbol{\sigma}}^*} : \mathbf{D}_e \left(\dot{\boldsymbol{\varepsilon}} - \dot{\Lambda}_p \frac{\partial g_p}{\partial \tilde{\boldsymbol{\sigma}}^*} \right) + \frac{\partial f_p}{\partial p_c^*} \frac{\partial p_c^*}{\partial p_0} \frac{\partial p_0}{\partial \varepsilon_v^p} \dot{\Lambda}_p \frac{\partial g_p}{\partial \tilde{p}^*} + \frac{\partial f_p}{\partial p_c^*} \frac{\partial p_c^*}{\partial s} \dot{s} = 0 \quad (3.87)$$

the plastic multiplier can be deduced.

$$\dot{\Lambda}_p = \frac{\frac{\partial f_p}{\partial \tilde{\boldsymbol{\sigma}}^*} : \mathbf{D}_e \dot{\boldsymbol{\varepsilon}} + \frac{\partial f_p}{\partial p_c^*} \frac{\partial p_c^*}{\partial s} \dot{s}}{\frac{\partial f_p}{\partial \tilde{\boldsymbol{\sigma}}^*} : \mathbf{D}_e \frac{\partial g_p}{\partial \tilde{\boldsymbol{\sigma}}^*} - \frac{\partial f_p}{\partial p_c^*} \frac{\partial p_c^*}{\partial p_0} \frac{\partial p_0}{\partial \varepsilon_v^p} \frac{\partial g_p}{\partial \tilde{p}^*}} \quad (3.88)$$

We define the following quantities:

$$\mathbf{A}_f = \frac{\partial f_p}{\partial \tilde{\boldsymbol{\sigma}}^*} \quad (3.89)$$

$$\mathbf{A}_g = \frac{\partial g_p}{\partial \tilde{\boldsymbol{\sigma}}^*} \quad (3.90)$$

$$A = \frac{\partial f_p}{\partial p_c^*} \frac{\partial p_c^*}{\partial p_0} \frac{\partial p_0}{\partial \varepsilon_v^p} \frac{\partial g_p}{\partial \tilde{p}^*} \quad (3.91)$$

$$B = \frac{\partial p_0}{\partial \varepsilon_v^p} \frac{\partial g_p}{\partial \tilde{p}^*} \quad (3.92)$$

$$C = \frac{\partial f_p}{\partial p_c^*} \frac{\partial p_c^*}{\partial s} \quad (3.93)$$

the detailed expressions of the different derivatives are given in appendix A.

We obtain the expressions for the plastic multiplier,

$$\dot{\Lambda}_p = \frac{\mathbf{A}_f : \mathbf{D}_e : \dot{\boldsymbol{\varepsilon}} + C\dot{s}}{\mathbf{A}_f : \mathbf{D}_e : \mathbf{A}_g - A} \quad (3.94)$$

the plastic flow,

$$\dot{\boldsymbol{\varepsilon}}^p = \frac{\mathbf{A}_g \otimes (\mathbf{D}_e : \mathbf{A}_f)}{\mathbf{A}_f : \mathbf{D}_e : \mathbf{A}_g - A} \dot{\boldsymbol{\varepsilon}} + \frac{C\mathbf{A}_g}{\mathbf{A}_f : \mathbf{D}_e : \mathbf{A}_g - A} \dot{s} \quad (3.95)$$

the hardening law,

$$\dot{p}_0 = B \frac{\mathbf{A}_f : \mathbf{D}_e : \dot{\boldsymbol{\varepsilon}} + C\dot{s}}{\mathbf{A}_f : \mathbf{D}_e : \mathbf{A}_g - A} \quad (3.96)$$

and the incremental double effective stress - strain relationship.

$$\dot{\boldsymbol{\sigma}}^* = \mathbf{D}_{\text{ep}}(\tilde{\boldsymbol{\sigma}}^*)\dot{\boldsymbol{\varepsilon}} + \mathbf{W}_{\text{ep}}(\tilde{\boldsymbol{\sigma}}^*)\dot{s} \quad (3.97)$$

with

$$\mathbf{D}_{\text{ep}} = \mathbf{D}_e \left[1 - \frac{\mathbf{A}_g \otimes (\mathbf{D}_e : \mathbf{A}_f)}{\mathbf{A}_f : \mathbf{D}_e : \mathbf{A}_g - A} \right] \quad (3.98)$$

$$\mathbf{W}_{\text{ep}} = -\mathbf{D}_e \frac{C\mathbf{A}_g}{\mathbf{A}_f : \mathbf{D}_e : \mathbf{A}_g - A} \quad (3.99)$$

To be able to use our model with the Newton-Raphson method, we need to express the increment of total stress as a function of the increments of total strains and suction.

Deriving the relationships between effective stresses and total stresses gives

$$\boldsymbol{\sigma} = \boldsymbol{\sigma}^* + p_g \mathbf{I} - S_l(s)s\mathbf{I} \quad (3.100)$$

$$\dot{\boldsymbol{\sigma}} = \dot{\boldsymbol{\sigma}}^* + \dot{p}_g \mathbf{I} - \left(S_l(s)\dot{s} + \frac{\partial S_l}{\partial s} \dot{s}s \right) \mathbf{I} \quad (3.101)$$

$$\boldsymbol{\sigma}^* = (1 - d)\tilde{\boldsymbol{\sigma}}^* \quad (3.102)$$

$$\dot{\boldsymbol{\sigma}}^* = (1 - d)\dot{\tilde{\boldsymbol{\sigma}}^*} - \tilde{\boldsymbol{\sigma}}^* \dot{d} = (1 - d)\dot{\tilde{\boldsymbol{\sigma}}^*} - \tilde{\boldsymbol{\sigma}}^* (\mathbf{A}_d : \dot{\tilde{\boldsymbol{\sigma}}^*}) \quad (3.103)$$

which lead to the expression of total stress rate as a function of total strain rate and pore fluid pressures rate:

$$\dot{\boldsymbol{\sigma}} = [(1 - d)\mathbf{I} - \tilde{\boldsymbol{\sigma}}^* \otimes \mathbf{A}_d](\mathbf{D}_{\text{ep}}\dot{\boldsymbol{\varepsilon}} + \mathbf{W}_{\text{ep}}\dot{s}) + \dot{p}_g \mathbf{I} - \left(S_l(s) + \frac{\partial S_l}{\partial s} s \right) \mathbf{I} \dot{s} \quad (3.104)$$

$$\dot{\boldsymbol{\sigma}} = \mathbf{D}_{\text{dep}}(\tilde{\boldsymbol{\sigma}}^*, d)\dot{\boldsymbol{\varepsilon}} + \dot{p}_g \mathbf{I} - \mathbf{F}_s(\tilde{\boldsymbol{\sigma}}^*, d)\dot{s} \quad (3.105)$$

with

$$\mathbf{D}_{\text{dep}} = [(1 - d)\mathbf{I} - \tilde{\boldsymbol{\sigma}}^* \otimes \mathbf{A}_d]\mathbf{D}_{\text{ep}} \quad (3.106)$$

$$\mathbf{F}_s = \left(S_l(s) + \frac{\partial S_l}{\partial s} s \right) \mathbf{I} - [(1 - d)\mathbf{I} - \tilde{\boldsymbol{\sigma}}^* \otimes \mathbf{A}_d]\mathbf{W}_{\text{ep}} \quad (3.107)$$

The incremental equation is then:

$$\dot{\boldsymbol{\sigma}} = \mathbf{D}_{\text{dep}}(\tilde{\boldsymbol{\sigma}}^*, d)\dot{\boldsymbol{\varepsilon}} + \mathbf{F}_s(\tilde{\boldsymbol{\sigma}}^*, d)\dot{p}_l + (\mathbf{I} - \mathbf{F}_s(\tilde{\boldsymbol{\sigma}}^*, d))\dot{p}_g \quad (3.108)$$

with the different coefficient taking the following values for the four possible loading cases:

- Elastic loading:

$$\mathbf{D}_{\text{dep}} = (1 - d)\mathbf{D}_{\text{e}} \quad (3.109)$$

$$\mathbf{F}_{\text{s}} = \left(S_l(s) + \frac{\partial S_l}{\partial s} s \right) \mathbf{I} \quad (3.110)$$

- Damage loading:

$$\mathbf{D}_{\text{dep}} = [(1 - d)\mathbf{I} - \tilde{\boldsymbol{\sigma}}^* \otimes \mathbf{A}_d]\mathbf{D}_{\text{e}} \quad (3.111)$$

$$\mathbf{F}_{\text{s}} = \left(S_l(s) + \frac{\partial S_l}{\partial s} s \right) \mathbf{I} \quad (3.112)$$

- Plastic loading:

$$\mathbf{D}_{\text{dep}} = (1 - d)\mathbf{D}_{\text{ep}} \quad (3.113)$$

$$\mathbf{F}_{\text{s}} = \left(S_l(s) + \frac{\partial S_l}{\partial s} s \right) \mathbf{I} - (1 - d)\mathbf{W}_{\text{ep}} \quad (3.114)$$

- Damage-Plastic loading:

$$\mathbf{D}_{\text{dep}} = [(1 - d)\mathbf{I} - \tilde{\boldsymbol{\sigma}}^* \otimes \mathbf{A}_d]\mathbf{D}_{\text{ep}} \quad (3.115)$$

$$\mathbf{F}_{\text{s}} = \left(S_l(s) + \frac{\partial S_l}{\partial s} s \right) \mathbf{I} - [(1 - d)\mathbf{I} - \tilde{\boldsymbol{\sigma}}^* \otimes \mathbf{A}_d]\mathbf{W}_{\text{ep}} \quad (3.116)$$

In this chapter, damage and plasticity evolution laws have been presented. The assumption of a double effective stress, associated with the principle of strain equivalence, allows for a direct damage-plasticity coupling. Indeed, although damage and plasticity criteria are expressed in terms of the double effective stress, and consequently do not depend explicitly on damage and suction, they evolve with damage and suction in the total stress space.

This approach, consisting in defining two dissipative criteria in the double effective stress space, appears to be flexible. Each component of the model can be easily modified without any need for heavy changes in the numerical implementation. All that is needed is a definition for the double effective stress, and the derivatives of damage and plasticity functions (developed in appendix A). The numerical implementation will therefore make use of explicit algorithms in order to keep this flexibility.

The following chapter deals with fluid transfer equations, which are required to model fully coupled hydro-mechanical problems.

In order to allow for the representation of fully coupled hydro-mechanical problems, transfer laws have to be defined. The fluid transfer properties of porous media are highly dependent on the microstructure and the saturation state, and the resulting problem is therefore non-linear. This chapter presents a review of some expressions used in the literature, and the different models chosen to be implemented in *θ -Stock*.

Les lois de transfert doivent être définies afin de pouvoir étudier des problèmes hydromécaniques complètement couplés. Les propriétés de transfert de fluides dans les milieux non saturés sont fortement dépendants de la microstructure et de l'état de saturation du milieu poreux. Le problème est donc non linéaire. Ce chapitre présente certaines des expressions utilisées dans la littérature, ainsi que les différents modèles choisis pour être implémentés dans θ -Stock.

Contents

4.1	Water phase	60
4.1.1	Liquid water flow	60
4.1.2	Water vapour flow	63
4.1.3	Water mass conservation equation	64
4.2	Air phase	65

Clays and rocks are known to have very low permeabilities (10^{-12} to 10^{-21} m/s). Fluid transfers will therefore have a great impact on the materials mechanical behaviour since overpressures are likely to develop under mechanical loading, and inhomogeneous stress states will appear during hydric loading.

Fluid mass conservation equations are developed for water and air constituents, which will enable the derivation of equations for FEM implementation. Two phases, liquid and gaseous, are considered. The liquid phase is assumed to contain liquid water and dissolved air. The gaseous phase is assumed to be composed of air as well as water vapour. Transfer laws are assumed to be function of the porosity as well as the saturation state. Significant works about coupled hydro-mechanical flow in unsaturated porous media include the work of Philip and De Vries (1957), Sophocleous (1979), Geraminegad and Saxena (1986), Olivella et al. (1994), Thomas and He (1995), Schrefler et al. (1995), ...

The constitutive laws used in θ -*Stock* have been presented in (Gatmiri and Arson, 2008).

4.1 Water phase

The water mass balance equation is written as

$$\dot{\rho}^m + \nabla \cdot \mathbf{Q}_m = 0 \quad (4.1)$$

in which ρ^m is the average water density of the gas-liquid mixture, and \mathbf{Q}_m is the total moisture flux. These quantities include liquid water (w) and vapour (vap) components.

$$\rho^m = \rho_w \phi S_l + \rho_{vap} \phi (1 - S_l) \quad (4.2)$$

in which ϕ is the porosity, S_l the degree of saturation, ρ_w the water density and ρ_{vap} the vapour density.

$$\mathbf{Q}_m = \mathbf{Q}_w + \mathbf{Q}_{vap} = \rho_w \mathbf{V}_w + \rho_{vap} \mathbf{V}_{vap} = \rho_w (\mathbf{V}_w + \mathbf{V}_{vap}^*) \quad (4.3)$$

in which V_α is the velocity of the α component ($\alpha = w, vap$), and $\mathbf{V}_{vap}^* = \frac{\rho_{vap}}{\rho_w} \mathbf{V}_{vap}$.

4.1.1 Liquid water flow

Water is assumed to flow under suction gradients and gravity, following the generalised Darcy's law:

$$\mathbf{V}_w = -K_w \nabla \left(-\frac{s}{\gamma_w} + z \right) \quad (4.4)$$

in which s is the suction, γ_w the unit weight of water ($\gamma_w = 9.81 \text{ kN.m}^{-3}$), and z the vertical coordinate.

Assuming a constant value for γ_w , equation 4.4 can be rewritten as follows:

$$\mathbf{V}_w = D_{P_l} \nabla s - K_w \nabla z \quad (4.5)$$

with $D_{Pl} = \frac{1}{\gamma_w} K_w$

The water permeability, K_w , is assumed to be isotropic, and to depend on porosity and on the degree of saturation:

$$K_w = k_r(S_l)K_{int}(\phi) \quad (4.6)$$

in which K_{int} is the intrinsic permeability, depending on the material microstructure, and k_r is the water relative permeability, depending on the saturation state.

Intrinsic permeability: Several expressions of the intrinsic permeability as a function of the porosity ϕ , or the void ratio, e , have been proposed in the literature. K_{w0} is the water permeability for a reference porosity.

Lloret and Alonso (1980) proposed to use the following form,

$$K_{int}(e) = K_{w0}10^{\alpha e} \quad (4.7)$$

which is the expression used in most of the models incorporated in θ -Stock (Gatmiri and Delage, 1995; Gatmiri and Arson, 2008).

The Kozeny-Carman's formula,

$$K_{int}(\phi) = K_{w0} \frac{\phi^3}{(1-\phi)^2} \frac{(1-\phi_0)^2}{\phi_0^3} \quad (4.8)$$

in which ϕ_0 is the reference porosity for which $K_{int} = K_{w0}$, has been used by Gens et al. (1998) and Delahaye and Alonso (2002).

Delage et al. (2000) found a linear relationship between the intrinsic permeability and the porosity, for Boom clay (for a porosity between 30 and 40 %).

Although we chose to consider microstructure effects by making K_w dependent on porosity only, it is recognised that this is a simplifying assumption since damage may have a great impact on permeability by creating a new porosity network. The dependence of permeability on damage is a complex problem, which deserves to be handled carefully. Recent research on this subject includes the work of Shao et al. (2005), Arson and Gatmiri (2009), Maleki and Pouya (2010), Arson and Pereira (2013) and Pereira and Arson (2013). These works consider more complex damage models accounting for anisotropy.

Relative permeability: It is well known that water permeability, as well as air permeability, varies strongly with the degree of saturation.

The evolution of relative permeabilities to air and water obtained by Vachaud et al. (1974) on a fine sand are shown in figure 4.1.

A very common expression for water relative permeability, following an empirical approach, is:

$$k_r(S_l) = \left(\frac{S_l - S_r}{1 - S_r} \right)^m \quad (4.9)$$

in which m is determined to fit experiment data, and takes different values in several works

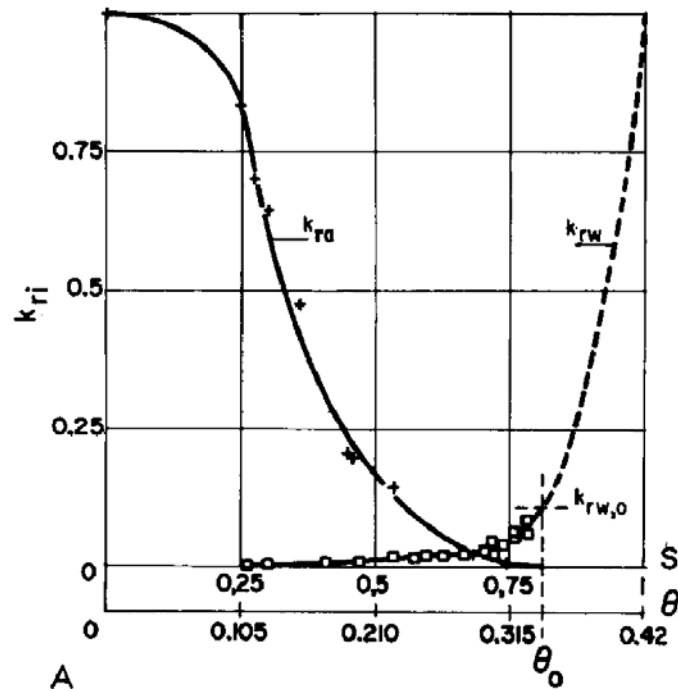


Fig. 4.1: Relative permeabilities to air and water (Vachaud et al., 1974)

($m = 3$ (Irmay, 1954), $m = 3.5$ (Averjanov, 1950), $m = 4$ (Corey, 1956)). Mualem (1976), on the basis of data from 50 soils, found values of m ranging from 2.5 to 24.5.

Another approach, called statistical by Fredlund et al. (1994), consists in deriving the hydraulic conductivity from the water retention curve. This approach is based on the fact that both the permeability function and the water retention curve are primarily determined by the pore-size distribution of the soil.

Mualem (1976) proposed to express the hydraulic conductivity as a function of the normalised water content $\Theta = \frac{\theta - \theta_r}{\theta_{sat} - \theta_r}$:

$$k_r(\Theta) = \sqrt{\Theta} \left[\frac{\int_0^\Theta \frac{1}{s(\Theta)} d\Theta}{\int_0^1 \frac{1}{s(\Theta)} d\Theta} \right]^2 \quad (4.10)$$

Assuming that this relationship is also valid when replacing the normalised water content by the effective degree of saturation (equation 1.26), and applying Mualem's approach to Van Genuchten's water retention curve expression (equation 1.33), the corresponding permeability becomes (Van Genuchten, 1980):

$$k_r(S_l) = \sqrt{S_l} \left[1 - (1 - S_l^{1/m_{vg}})^{m_{vg}} \right]^2 \quad (4.11)$$

which can also be expressed in terms of suction:

$$k_r(s) = \frac{(1 - (\alpha s)^{n_{vg}-1} [1 + (\alpha_{vg} s)^{n_{vg}}]^{-m_{vg}})^2}{(1 + (\alpha_{vg} s)^{n_{vg}})^{m_{vg}/3}} \quad (4.12)$$

Van Genuchten (1980) obtained very good predictions of the hydraulic conductivity of several soils (sandstone, silts, clay and loam) after fitting the parameters on the water retention curves.

4.1.2 Water vapour flow

The water vapour flow is assumed to follow a Fick's diffusion law in a tortuous medium. The vapour diffusion is linked to the gradient of vapour density and the vapour flow follows the formulation proposed by Philip and De Vries (1957):

$$\mathbf{V}_{vap} = \frac{1}{\rho_{vap}} \mathbf{q}_{vap} \quad (4.13)$$

with \mathbf{q}_{vap} the vector of vapour flux density ($\text{kg m}^{-2}\text{s}^{-1}$):

$$\mathbf{q}_{vap} = -D_0 \nu_{vap} \alpha_{vap} \phi (1 - S_l) \nabla \rho_{vap} \quad (4.14)$$

in which,

- D_0 (m^2s^{-1}) is the molecular diffusivity of water vapour in air. The formula used in θ -Stock is the empirical equation given by Geraminegad and Saxena (1986).

$$D_0 = \frac{229.10^{-2}}{p_g} \left(\frac{T + 273.15}{273} \right)^{1.75} \quad (4.15)$$

in which T is the temperature ($^{\circ}\text{C}$), and p_g the gas pressure (Pa).

- ν_{vap} is the “mass-flow factor” introduced to allow for the mass flow of vapour arising from the difference in boundary conditions governing the air and vapour components of the diffusion system.

$$\nu_{vap} = \frac{p_g}{p_g - p_{vap}} \quad (4.16)$$

ν_{vap} is close to 1 at normal soil temperature.

- α_{vap} is a tortuosity factor allowing for the extra path length ($\alpha_{vap} = 1.024$).
- ρ_{vap} (kg m^{-3}) is the density of water vapour. According to Philip and De Vries (1957),

$$\rho_{vap} = \rho_{vap}^0 h \quad (4.17)$$

ρ_{vap}^0 being the density of saturated water vapour, and h the relative humidity, related to suction through Kelvin's law,

$$h(s) = \exp\left(-\frac{sg}{\gamma_w R_{vap} T}\right) \quad (4.18)$$

in which g is the gravitational constant, and R_{vap} is the specific vapour constant ($R_{vap} = 461.5 \text{ m}^2\text{s}^{-2}\text{K}^{-1}$).

In Geraminegad and Saxena (1986), the saturated vapour density depends only on temperature (kg/m^3):

$$\rho_{vap}^0 = 10^{-3} \exp\left(19.819 - \frac{4975.9}{T + 273.15}\right) \quad (4.19)$$

Since temperature is considered homogeneous, the spatial derivation of equation 4.17 becomes:

$$\nabla \rho_{vap} = \rho_{vap}^0 \nabla h = \rho_{vap}^0 \frac{\partial h}{\partial s} \nabla s = -h \rho_{vap}^0 \frac{g}{\gamma_w R_{vap} T} \nabla s \quad (4.20)$$

Combining equations 4.13, 4.14 and 4.20 gives the water velocity,

$$\mathbf{V}_{vap} = \frac{1}{\rho_{vap}} D_0 \nu_{vap} \alpha_{vap} \phi (1 - S_l) h \rho_{vap}^0 \frac{g}{\gamma_w R_{vap} T} \nabla s \quad (4.21)$$

Since experimental data (from Philip and De Vries (1957)) do not appear to show the choking of the vapour at high moisture content, Ewen and Thomas (1989) modified the previous expression, assuming that the vapour flow area is equal to the porosity, and thus replacing $\phi(1 - S_l)$ by ϕ in equation 4.21:

$$\mathbf{V}_{vap} = \frac{1}{\rho_{vap}} D_0 \nu_{vap} \alpha_{vap} \phi h \rho_{vap}^0 \frac{g}{\gamma_w R_{vap} T} \nabla s \quad (4.22)$$

The normalised vapour velocity therefore becomes:

$$\mathbf{V}_{vap}^* = \frac{\rho_{vap}}{\rho_w} \mathbf{V}_{vap} = D_{P_{vap}} \nabla s \quad (4.23)$$

with

$$D_{P_{vap}} = \frac{1.024}{\rho_w} D_0 \nu_{vap} \phi h \rho_{vap}^0 \frac{g}{R_{vap} T} \frac{1}{\gamma_w} \quad (4.24)$$

4.1.3 Water mass conservation equation

Incorporating equations 4.5 and 4.23 into equation 4.3, the total water flux becomes

$$\mathbf{Q}_m = \rho_w (D_P \nabla s - K_w \nabla z) \quad (4.25)$$

in which

$$D_P = D_{P_l} + D_{P_{vap}} \quad (4.26)$$

Deriving equation 4.2, the variation of the average water density can be expressed as

$$\dot{\rho}^m = (\rho_w S_l + \rho_{vap} (1 - S_l)) \dot{\phi} + \phi (\rho_w - \rho_{vap}) \dot{S}_l + \phi S_l \dot{\rho}_w + \phi (1 - S_l) \dot{\rho}_{vap} \quad (4.27)$$

Let now write $\dot{\phi}$, \dot{S}_l , $\dot{\rho}_w$ and $\dot{\rho}_{vap}$ as functions of strain, suction and fluid pressure increments.

Due to the assumption of solid grains incompressibility and with the soil mechanics convention, the porosity increment can be expressed as a function of the strain increment:

$$\dot{\phi} = -\dot{\varepsilon}_v = -\mathbf{I} : \dot{\varepsilon} \quad (4.28)$$

Deriving Van Genuchten's equation (1.29) gives the increment of degree of saturation as a function of the suction increment:

$$\dot{S}_l = \frac{\partial S_l}{\partial s} \dot{s} = -(1 - S_r) \frac{m_{vg} n_{vg} \alpha_{vg}^{n_{vg}} s^{n_{vg}-1}}{(1 + (\alpha_{vg} s)^{n_{vg}})^{m_{vg}+1}} \dot{s} = g_2 \dot{s} \quad (4.29)$$

The water density is assumed to be pressure dependent (temperature dependency is not considered since we only consider isothermal conditions).

$$\dot{\rho}_w = \frac{\partial \rho_w}{\partial p_l} \dot{p}_l = \beta_p \dot{p}_l \quad (4.30)$$

in which β_p is the water compressibility with respect to pressure ($\beta_p = 5.10^{-10} \text{ m}^{-2} \text{ s}^2$).

The vapour density rate can be derived from equation 4.17:

$$\dot{\rho}_{vap} = \rho_{vap}^0 \frac{\partial h}{\partial s} \dot{s} = -h \rho_{vap}^0 \frac{g}{\gamma_w R_{vap} T} \dot{s} = A \dot{s} \quad (4.31)$$

Incorporating equations 4.28, 4.29, 4.30 and 4.31 into equation 4.27, the increment of water density becomes:

$$\dot{\rho}_m = -(\rho_w S_l + \rho_{vap}(1 - S_l)) \mathbf{I} : \dot{\varepsilon} + \phi(\rho_w - \rho_{vap}) g_2 \dot{s} + \phi S_l \beta_p \dot{p}_l + \phi(1 - S_l) A \dot{s} \quad (4.32)$$

Incorporation of equations 4.25 and 4.32 into equation 4.1 gives the mass conservation equation:

$$\begin{aligned} & -[\rho_w S_l + \rho_{vap}(1 - S_l)] \mathbf{I} : \dot{\varepsilon} \\ & + [-\phi(\rho_w - \rho_{vap}) g_2 + \phi S_l \beta_p - \phi(1 - S_l) A] \dot{p}_l \\ & + [\phi(\rho_w - \rho_{vap}) g_2 + \phi(1 - S_l) A] \dot{p}_g \\ & + \nabla \cdot \rho_w (D_P \nabla s - K_w \nabla z) = 0 \end{aligned} \quad (4.33)$$

4.2 Air phase

The air mass balance equation is written as

$$\dot{\rho}^a + \nabla \cdot \mathbf{Q}_a = 0 \quad (4.34)$$

in which ρ^a is the average air density of the gas-liquid mixture, and \mathbf{Q}_a is the total air flux.

$$\rho^a = \rho_a \phi (1 - S_l + H S_l) \quad (4.35)$$

in which ρ_a is the intrinsic air density, and $H = 0.02$ is Henry's constant and is used to account for dissolved air into water.

In the porous space occupied both by air and water vapour, the vapour flux decreases the air flux. The total air flux therefore becomes:

$$\mathbf{Q}_a = \rho_a \mathbf{V}_a + \rho_a H \mathbf{V}_w - \rho_w \mathbf{V}_{vap}^* \quad (4.36)$$

in which \mathbf{V}_a is the gaseous air velocity. \mathbf{V}_w and \mathbf{V}_{vap}^* are respectively the liquid water velocity and the normalised vapour velocity, already defined by equations 4.5 and 4.23.

Gaseous air transfers are supposed to follow Darcy's law

$$\mathbf{V}_a = -K_a \nabla \left(\frac{p_g}{\gamma_a} + z \right) \quad (4.37)$$

Similarly to water permeability, the air permeability depends on the porosity and on the porosity (or void ratio).

Lloret and Alonso (1980) proposed the following formula,

$$K_a = c_a \frac{\gamma_a}{\mu_a} [e(1 - S_l)]^{\alpha_a} \quad (4.38)$$

in which γ_a is the specific weight of air, μ_a its viscosity, and c_a and α_a are constants. This expression has been used by Thomas and He (1995) and Gatmiri et al. (1998) and is implemented in *θ -Stock*.

The air flux can be expressed as a function of fluid pressure gradients:

$$\mathbf{Q}_a = -[\rho_a(K_a + HK_w)\nabla z] - [\rho_a HD_{P_l} - \rho_w D_{P_{vap}}]\nabla p_l + \left[-\frac{\rho_a K_a}{\gamma_a} + \rho_a HD_{P_l} - \rho_w D_{P_{vap}} \right] \nabla p_g \quad (4.39)$$

Deriving equation 4.35, the variation of the average water density can be expressed as

$$\dot{\rho}^a = \dot{\rho}_a \phi(1 - S_l + HS_l) + \rho_a \dot{\phi}(1 - S_l + HS_l) - \rho_a \phi(1 - H)\dot{S}_l \quad (4.40)$$

The increments of porosity and degree of saturation as a function of strain, suction and fluid pressure increments have already been defined by equations 4.28 and 4.29.

Assuming that air is an ideal gas,

$$\dot{\rho}_a = \frac{1}{R_a T} \dot{p}_g = \alpha_p \dot{p}_g \quad (4.41)$$

with $R_a = 287 \text{ J.K}^{-1}.\text{kg}^{-1}$, the specific gas constant of dry air.

Incorporating equations 4.28, 4.29 and 4.41 into equation 4.35, the increment of air density becomes:

$$\dot{\rho}^a = -(1 - S_l + HS_l)\rho_a \mathbf{I} : \dot{\boldsymbol{\varepsilon}} - (H - 1)\phi\rho_a g_2 \dot{p}_l + [(H - 1)\phi\rho_a g_2 + \phi(1 - S_l + HS_l)\alpha_p]\dot{p}_g \quad (4.42)$$

Incorporation of equations 4.39 and 4.42 into equation 4.34 gives the mass conservation equation:

$$\begin{aligned}
& (1 - S_l + HS_l)\rho_a \mathbf{I} : \dot{\boldsymbol{\epsilon}} \\
& + (H - 1)\phi\rho_a g_2 \dot{p}_l \\
& - [(H - 1)\phi\rho_a g_2 + \phi(1 - S_l + HS_l)\alpha_p] \dot{p}_g \\
& + \nabla \cdot [\rho_a(K_a + HK_w)\nabla z] \\
& + \nabla \cdot [(\rho_a HD_{P_l} - \rho_w D_{P_{vap}})\nabla p_l] \\
& - \nabla \cdot \left[\left(-\frac{\rho_a K_a}{\gamma_a} + \rho_a HD_{P_l} - \rho_w D_{P_{vap}} \right) \nabla p_g \right] = 0
\end{aligned} \tag{4.43}$$

The mass conservation equations developed in this chapter together with the mechanical incremental equation derived in chapter 3.4, form a system of partial differential to be solved to determine the solution of boundary value problems. These equations are highly non-linear since permeabilities depend on the saturation state and the porosity of the material. The following chapter will be devoted to the presentation of the numerical methods used to solve this system of equations.

This chapter presents the discretisation in space and time of the weak formulation of the initial boundary value hydromechanical problem. The global iterative resolution algorithm used in θ -Stock as well as the specific local algorithm developed for the damage-plasticity model are also described.

Ce chapitre présente la discrétisation spatiale et temporelle de la formulation faible du problème hydromécanique aux conditions limites. Le schéma de résolution global itératif utilisé dans θ -Stock, ainsi que l'algorithme local développé pour le modèle d'endommagement-plasticité sont également décrits.

Contents

5.1	Strong form of the coupled problem	70
5.1.1	Synthesis of the equations	70
5.1.2	Boundary conditions	71
5.1.3	Initial conditions	72
5.2	Weak form	72
5.3	Application of the Finite Element Method	75
5.3.1	Spatial discretisation	75
5.3.2	Numerical integration	79
5.3.3	System to solve	80
5.4	Discretisation in time	81
5.5	Iterative resolution of equilibrium equations system	83
5.6	Stress point algorithm	85
5.6.1	Input	85
5.6.2	Trial elastic state	86
5.6.3	Plasticity	87
5.6.4	Damage	89
5.6.5	Final state	90

The resolution of bi-dimensional coupled hydro-mechanical problems requires several discretisations. The first spatial discretisation is made possible by means of the use of the Finite Element method. A second discretisation in time is necessary due to the transient fluid flow. Moreover, due to the high non linearity of mechanical and transfer phenomena, loads have to be split into a certain number of increments, and iterative algorithms have to be used to reach a convergent solution.

The solution of the initial boundary value problem will give the fields of displacements, \mathbf{u} , water pressure, p_l , and air pressure, p_g .

5.1 Strong form of the coupled problem

5.1.1 Synthesis of the equations

The problem is represented by a system of three equations, corresponding to the solid skeleton equilibrium and to the mass conservation of water and air.

Solid skeleton:

The equilibrium equation can be written as:

$$\nabla \cdot \dot{\boldsymbol{\sigma}} + \dot{\mathbf{b}} = 0 \quad (5.1)$$

in which \mathbf{b} is the body force vector.

Incorporating the incremental mechanical law (equation 3.108) into the previous equation gives:

$$\nabla \cdot [\mathbf{D}_{\text{dep}}(\tilde{\boldsymbol{\sigma}}^*, d) : \dot{\boldsymbol{\varepsilon}}] + \nabla \cdot [\mathbf{F}_s(\tilde{\boldsymbol{\sigma}}^*, d)\dot{p}_l] + \nabla \cdot [(\mathbf{I} - \mathbf{F}_s(\tilde{\boldsymbol{\sigma}}^*, d))\dot{p}_g] + \dot{\mathbf{b}} = 0 \quad (5.2)$$

Water:

The mass conservation equation of pore water is,

$$\dot{\rho}^m + \nabla \cdot \mathbf{Q}_m = 0 \quad (5.3)$$

which becomes, expressing the average water density rate in terms of strain and pore pressures rates, and the total moisture flux in terms of vertical coordinates and pore

pressure gradients,

$$\begin{aligned}
& - [\rho_w S_l + \rho_{vap}(1 - S_l)] \mathbf{Id} : \dot{\boldsymbol{\varepsilon}} \\
& + [-\phi(\rho_w - \rho_{vap})g_2 + \phi S_l \beta_p - \phi(1 - S_l)A] \dot{p}_l \\
& + [\phi(\rho_w - \rho_{vap})g_2 + \phi(1 - S_l)A] \dot{p}_g \\
& - \nabla \cdot (\rho_w K_w \nabla z) \\
& - \nabla \cdot (\rho_w D_P \nabla p_l) \\
& + \nabla \cdot (\rho_w D_P \nabla p_g) = 0
\end{aligned} \tag{5.4}$$

Air:

The mass conservation equation of air is,

$$\dot{\rho}^a + \nabla \cdot \mathbf{Q}_a = 0 \tag{5.5}$$

which becomes, expressing the average air density rate in terms of strain and pore pressures rates, and the total air flux in terms of vertical coordinates and pore pressure gradients,

$$\begin{aligned}
& - (1 - S_l + H S_l) \rho_a \mathbf{Id} : \dot{\boldsymbol{\varepsilon}} \\
& - (H - 1) \phi \rho_a g_2 \dot{p}_l \\
& + [(H - 1) \phi \rho_a g_2 + \phi(1 - S_l + H S_l) \alpha_p] \dot{p}_g \\
& - \nabla \cdot [\rho_a (K_a + H K_w) \nabla z] \\
& - \nabla \cdot [(\rho_a H D_{P_l} - \rho_w D_{P_{vap}}) \nabla p_l] \\
& + \nabla \cdot \left[\left(-\frac{\rho_a K_a}{\gamma_a} + \rho_a H D_{P_l} - \rho_w D_{P_{vap}} \right) \nabla p_g \right] = 0
\end{aligned} \tag{5.6}$$

5.1.2 Boundary conditions

We note Ω the domain and Γ its boundary. Boundary conditions can be either of Dirichlet's type if values of variables are imposed, or of Neumann's type if it is their flux which is given.

Solid skeleton:

On the solid skeleton it is possible to impose either the value of displacements, \mathbf{u} ,

$$\forall t, \forall \mathbf{x} \in \Gamma_u, \mathbf{u}(\mathbf{x}, t) = \tilde{\mathbf{u}}(\mathbf{x}, t) \tag{5.7}$$

or the value of the normal stress, \mathbf{t} .

$$\forall t, \forall \mathbf{x} \in \Gamma_\sigma, \boldsymbol{\sigma}(\mathbf{x}, t) \cdot \mathbf{n} = \mathbf{t}(\mathbf{x}, t) \tag{5.8}$$

with $\Gamma_u \cup \Gamma_\sigma = \Gamma$ and $\Gamma_u \cap \Gamma_\sigma = \emptyset$

In θ -Stock, imposed displacement can only take a null value.

Water and air:

Equations relative to air and water are similar and will be treated together. The α subscript can represent water, w , or air, a .

Given boundary conditions can be either the fluid pore pressure,

$$\forall t > 0, \forall \mathbf{x} \in \Gamma_{p_\alpha}, p_\alpha(\mathbf{x}, t) = \tilde{p}_\alpha(\mathbf{x}, t) \quad (5.9)$$

or the fluid flux normal to the surface,

$$\forall t > 0, \forall \mathbf{x} \in \Gamma_{Q_\alpha}, \mathbf{Q}_\alpha(\mathbf{x}, t) \cdot \mathbf{n} = \tilde{q}_\alpha(\mathbf{x}, t) \quad (5.10)$$

with $\Gamma_{p_\alpha} \cup \Gamma_{Q_\alpha} = \Gamma$ and $\Gamma_{p_\alpha} \cap \Gamma_{Q_\alpha} = \emptyset$

5.1.3 Initial conditions

The initial state is described by the full field of displacements and pore pressures at $t = 0$.

$$\forall \mathbf{x} \in \Omega, \mathbf{u}(\mathbf{x}, t = 0) = \mathbf{u}_0(\mathbf{x}) \quad (5.11)$$

$$\forall \mathbf{x} \in \Omega, p_\alpha(\mathbf{x}, t = 0) = p_{\alpha 0}(\mathbf{x}) \quad (5.12)$$

5.2 Weak form

The following developments will require some mathematical tools. We consider that second order tensors are represented by capitalised bold letters, \mathbf{A} , vectors by italic bold letters, \mathbf{a} , and scalars by italic letters, a .

Divergence operator properties:

$$\nabla \cdot (\mathbf{A} \cdot \mathbf{f}) = \mathbf{A} : \nabla \mathbf{f} + \mathbf{f} \cdot (\nabla \cdot \mathbf{A}) \quad (5.13)$$

$$\nabla \cdot (a\mathbf{f}) = \mathbf{f} \cdot \nabla a + a(\nabla \cdot \mathbf{f}) \quad (5.14)$$

Divergence theorem:

$$\int_{\Omega} (\nabla \cdot \mathbf{f}) d\Omega = \int_{\Gamma} (\mathbf{f} \cdot \mathbf{n}) d\Gamma \quad (5.15)$$

in which \mathbf{n} is the outward unit normal to the boundary surface Γ .

Displacements

The variational formulation is obtained by multiplying the equilibrium equation by \mathbf{u}^* , a kinematically admissible displacement field with zero boundary condition ($\mathbf{u}^*_{|\Gamma_u} = 0$), and

integrating over the domain Ω .

$$\forall \mathbf{u}^*, \int_{\Omega} (\nabla \cdot \dot{\boldsymbol{\sigma}}) \cdot \mathbf{u}^* d\Omega + \int_{\Omega} \dot{\mathbf{b}} \cdot \mathbf{u}^* d\Omega = 0 \quad (5.16)$$

Using the symmetry of the stress tensor, the properties of the divergence operator, and the divergence theorem, the variational formulation becomes:

$$\forall \mathbf{u}^*, \int_{\Gamma} (\dot{\boldsymbol{\sigma}} \cdot \mathbf{n}) \cdot \mathbf{u}^* d\Gamma - \int_{\Omega} \dot{\boldsymbol{\sigma}} : \nabla \mathbf{u}^* d\Omega + \int_{\Omega} \dot{\mathbf{b}} \cdot \mathbf{u}^* d\Omega = 0 \quad (5.17)$$

Under the assumption of small strains, strains are defined by

$$\boldsymbol{\varepsilon}(\mathbf{u}^*) = \frac{1}{2}(\nabla \mathbf{u}^* + (\nabla \mathbf{u}^*)^T) \quad (5.18)$$

The symmetry of the stress tensor gives,

$$\dot{\boldsymbol{\sigma}} : \boldsymbol{\varepsilon}(\mathbf{u}^*) = \dot{\boldsymbol{\sigma}} : \frac{1}{2}(\nabla \mathbf{u}^* + (\nabla \mathbf{u}^*)^T) = \dot{\boldsymbol{\sigma}} : \nabla \mathbf{u}^* \quad (5.19)$$

Boundary conditions are:

$$\mathbf{u}^* = 0 \text{ on } \Gamma_u \quad (5.20)$$

$$\dot{\boldsymbol{\sigma}} \cdot \mathbf{n} = \dot{\mathbf{t}} \text{ on } \Gamma_{\sigma} \quad (5.21)$$

Introducing boundary conditions and strains into the variational formulation gives:

$$\forall \mathbf{u}^*, \int_{\Omega} \dot{\boldsymbol{\sigma}} : \boldsymbol{\varepsilon}(\mathbf{u}^*) d\Omega = \int_{\Gamma_{\sigma}} \dot{\mathbf{t}} \cdot \mathbf{u}^* d\Gamma + \int_{\Omega} \dot{\mathbf{b}} \cdot \mathbf{u}^* d\Omega \quad (5.22)$$

We can now introduce the incremental law (equation 1.22) into equation 5.22. The weak form of the problem can be stated as follows:

Find \mathbf{u} , p_l and p_g , such as,

$$\begin{aligned} \forall \mathbf{u}^*, & \int_{\Omega} (\boldsymbol{\varepsilon}(\mathbf{u}^*))^T : \mathbf{D}_{\text{dep}}(\tilde{\boldsymbol{\sigma}}^*, d) : \dot{\boldsymbol{\varepsilon}}(\mathbf{u}) d\Omega \\ & + \int_{\Omega} (\boldsymbol{\varepsilon}(\mathbf{u}^*))^T : \mathbf{F}_s(\tilde{\boldsymbol{\sigma}}^*, d) \dot{p}_l d\Omega \\ & + \int_{\Omega} (\boldsymbol{\varepsilon}(\mathbf{u}^*))^T : [(\mathbf{I} - \mathbf{F}_s(\tilde{\boldsymbol{\sigma}}^*, d)) \dot{p}_g] d\Omega \\ & = \int_{\Gamma_{\sigma}} (\mathbf{u}^*)^T \cdot \dot{\mathbf{t}} d\Gamma + \int_{\Omega} (\mathbf{u}^*)^T \cdot \dot{\mathbf{b}} d\Omega \end{aligned} \quad (5.23)$$

Fluid pressures

The mass conservation of fluid pressure is:

$$\dot{\rho}^{\alpha} + \nabla \cdot \mathbf{Q}_{\alpha} = 0 \quad (5.24)$$

in which the α subscript is either related to water or air.

The variational formulation is obtained by multiplying the mass conservation equation by p_α^* , a kinematically admissible pressure field with zero boundary condition ($p_\alpha^*|_{\Gamma_{p_\alpha}} = 0$), and integrating over the domain Ω .

$$\forall p_\alpha^*, \int_{\Omega} \dot{\rho}^\alpha p_\alpha^* d\Omega + \int_{\Omega} (\nabla \cdot \mathbf{Q}_\alpha) p_\alpha^* d\Omega = 0 \quad (5.25)$$

Using the properties of the divergence operator and the divergence theorem, the variational formulation becomes:

$$\forall p_\alpha^*, \int_{\Omega} \dot{\rho}^\alpha p_\alpha^* d\Omega + \int_{\Gamma} p_\alpha^* (\mathbf{Q}_\alpha \cdot \mathbf{n}) d\Gamma - \int_{\Omega} \mathbf{Q}_\alpha \cdot \nabla p_\alpha^* d\Omega = 0 \quad (5.26)$$

Boundary conditions are:

$$p_\alpha^* = 0 \text{ on } \Gamma_{p_\alpha} \quad (5.27)$$

$$\mathbf{Q}_\alpha \cdot \mathbf{n} = \tilde{q}_\alpha \text{ on } \Gamma_{Q_\alpha} \quad (5.28)$$

Introducing boundary conditions into the variational formulation gives:

$$\forall p_\alpha^*, \int_{\Omega} \dot{\rho}^\alpha p_\alpha^* d\Omega + \int_{\Gamma_{Q_\alpha}} \tilde{q}_\alpha p_\alpha^* d\Gamma - \int_{\Omega} \mathbf{Q}_\alpha \cdot \nabla p_\alpha^* d\Omega = 0 \quad (5.29)$$

Introducing the specific expression of the average densities and fluxes of air and water, the weak form of the water mass conservation is,

Find \mathbf{u} , p_l and p_g , such as,

$$\begin{aligned} \forall p_l^* \in V_{p_l}(\Omega), & \int_{\Omega} -[\rho_w S_l + \rho_{vap}(1 - S_l)] \mathbf{Id} : \dot{\boldsymbol{\varepsilon}}(\mathbf{u}) p_l^* d\Omega \\ & + \int_{\Omega} [-\phi(\rho_w - \rho_{vap})g_2 + \phi S_l \beta_p - \phi(1 - S_l)A] \dot{p}_l p_l^* d\Omega \\ & + \int_{\Omega} [\phi(\rho_w - \rho_{vap})g_2 + \phi(1 - S_l)A] \dot{p}_g p_l^* d\Omega \\ = & - \int_{\Omega} \rho_w K_w (\nabla p_l^*)^T \cdot \nabla z d\Omega \\ & - \int_{\Omega} \rho_w D_P (\nabla p_l^*)^T \cdot \nabla p_l d\Omega \\ & + \int_{\Omega} \rho_w D_P (\nabla p_l^*)^T \cdot \nabla p_g d\Omega \\ & - \int_{\Gamma_{Q_w}} p_l^* \tilde{q}_w d\Gamma \end{aligned} \quad (5.30)$$

and the weak form of the air mass conservation is,

Find \mathbf{u} , p_l and p_g , such as,

$$\begin{aligned}
\forall p_g^* \in V_{p_g}(\Omega), \quad & - \int_{\Omega} p_g^* (1 - S_l + HS_l) \rho_a \mathbf{Id} : \dot{\boldsymbol{\varepsilon}}(\mathbf{u}) d\Omega \\
& - \int_{\Omega} p_g^* (H - 1) \phi \rho_a g_2 \dot{p}_l d\Omega \\
& + \int_{\Omega} p_g^* [(H - 1) \phi \rho_a g_2 + \phi (1 - S_l + HS_l) \alpha_p] \dot{p}_g d\Omega \\
= & - \int_{\Omega} \rho_a (K_a + HK_w) (\nabla p_g^*)^T \cdot \nabla z d\Omega \\
& - \int_{\Omega} (\rho_a HD_{P_l} - \rho_w DP_{vap}) (\nabla p_g^*)^T \cdot \nabla p_l d\Omega \\
& + \int_{\Omega} \left(-\frac{K_a}{g} + \rho_a HD_{P_l} - \rho_w DP_{vap} \right) (\nabla p_g^*)^T \nabla p_g d\Omega \\
& - \int_{\Gamma_{Q_a}} p_g^* \tilde{q}_a d\Gamma
\end{aligned} \tag{5.31}$$

5.3 Application of the Finite Element Method

5.3.1 Spatial discretisation

The initial boundary value problem will be treated in two dimensions, which allow us to study to types of problems, using a plane strain or an axisymmetric analysis. Theses two cases are represented in figure 5.1.

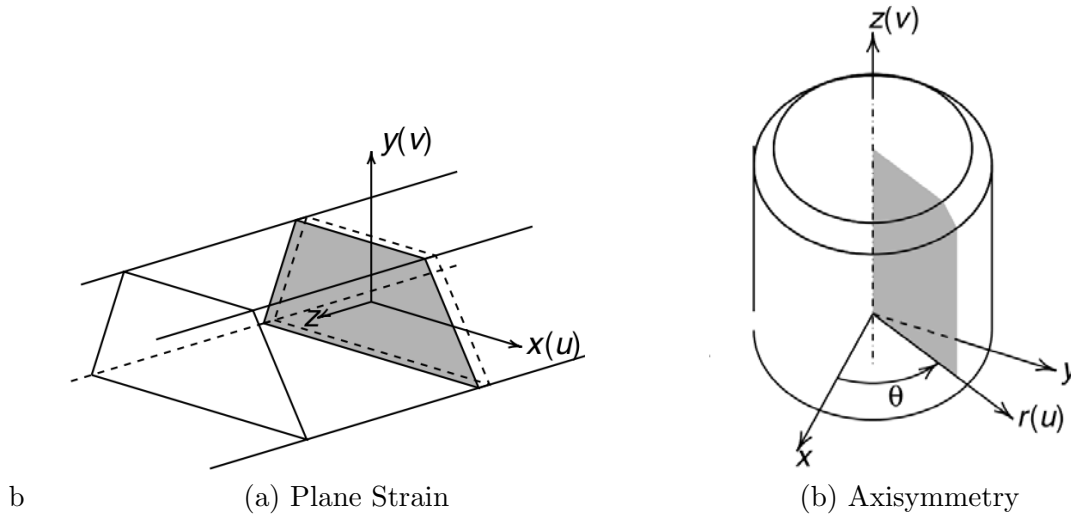


Fig. 5.1: Two-dimensional analysis types (image from Zienkiewicz et al. (2005))

Four degrees of freedom (dofs) are considered.

For plane strain conditions, the dofs are the horizontal displacement, $u_x(\mathbf{x}, t)$, the vertical displacement, $u_y(\mathbf{x}, t)$, the water pore pressure, $p_l(\mathbf{x}, t)$, and the air pore pressure, $p_g(\mathbf{x}, t)$.

$\mathbf{x} = \begin{Bmatrix} x \\ y \end{Bmatrix}$ is the coordinates vector.

For axisymmetric conditions, the dofs are the radial displacement, $u_r(\mathbf{x}, t)$, the axial displacement, $u_z(\mathbf{x}, t)$, the water pore pressure, $p_l(\mathbf{x}, t)$, and the air pore pressure, $p_g(\mathbf{x}, t)$.

$\mathbf{x} = \begin{Bmatrix} r \\ z \end{Bmatrix}$ is the coordinates vector.

The following developments are made for the plane strain configuration, and are valid for axisymmetric analysis (by replacing x by r , y by z and z by θ).

Space is discretised by means of four-nodes quadrilateral isoparametric 2D elements, which means that the dofs are interpolated by the same functions as the geometry.

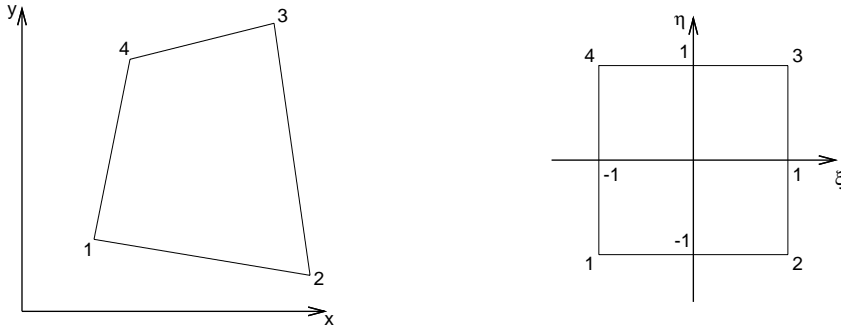


Fig. 5.2: Correspondence between the original and the reference configuration for a 4-node isoparametric element

Coordinates are interpolated by bilinear shape functions:

$$x = \{\mathbf{N}\} \cdot \{x\} = N_1x_1 + N_2x_2 + N_3x_3 + N_4x_4 \quad (5.32)$$

$$y = \{\mathbf{N}\} \cdot \{y\} = N_1y_1 + N_2y_2 + N_3y_3 + N_4y_4 \quad (5.33)$$

with the shape functions:

$$\{\mathbf{N}\} = \begin{Bmatrix} N_1 \\ N_2 \\ N_3 \\ N_4 \end{Bmatrix} = \begin{Bmatrix} (1-\xi)(1-\eta)/4 \\ (1+\xi)(1-\eta)/4 \\ (1+\xi)(1+\eta)/4 \\ (1-\xi)(1+\eta)/4 \end{Bmatrix} \quad (5.34)$$

Displacements and pore pressures are expressed in terms of their values at a finite number of points in space and their values between these points are approximated by using the same bilinear shape functions \mathbf{N} :

$$\begin{cases} u_x(\mathbf{x}, t) = \{\mathbf{N}\} \cdot \{\mathbf{u}_x(t)\} \\ u_y(\mathbf{x}, t) = \{\mathbf{N}\} \cdot \{\mathbf{u}_y(t)\} \\ p_l(\mathbf{x}, t) = \{\mathbf{N}\} \cdot \{\mathbf{p}_l(t)\} \\ p_g(\mathbf{x}, t) = \{\mathbf{N}\} \cdot \{\mathbf{p}_g(t)\} \end{cases} \quad (5.35)$$

For each dof, a vector of its values at nodes is defined:

$$\mathbf{dof}(t) = \begin{Bmatrix} dof_1(t) \\ dof_2(t) \\ dof_3(t) \\ dof_4(t) \end{Bmatrix} \quad (5.36)$$

Due to the specific configurations studied, only 4 components of the stress and strain tensors are needed. Stress and strain tensors can then be represented by vectors. We define the stress and strain vectors, as well as the identity vector \mathbf{i} :

$$\boldsymbol{\sigma} = \begin{Bmatrix} \sigma_{xx} \\ \sigma_{yy} \\ \sigma_{xy} \\ \sigma_{zz} \end{Bmatrix} \quad (5.37)$$

$$\boldsymbol{\varepsilon} = \begin{Bmatrix} \varepsilon_{xx} \\ \varepsilon_{yy} \\ 2\varepsilon_{xy} \\ \varepsilon_{zz} \end{Bmatrix} \quad (5.38)$$

$$\mathbf{i} = \begin{Bmatrix} 1 \\ 1 \\ 0 \\ 1 \end{Bmatrix} \quad (5.39)$$

In plane strain conditions, $\varepsilon_{zz} = 0$

The fourth order elasticity tensor is represented by a second order tensor:

$$[\mathbf{D}_e] = \begin{bmatrix} D_{e_{1111}} & D_{e_{1122}} & D_{e_{1112}}/2 & D_{e_{1133}} \\ D_{e_{2211}} & D_{e_{2222}} & D_{e_{2212}}/2 & D_{e_{2233}} \\ D_{e_{1211}} & D_{e_{1222}} & D_{e_{1212}}/2 & D_{e_{1233}} \\ D_{e_{3311}} & D_{e_{3322}} & D_{e_{3312}}/2 & D_{e_{3333}} \end{bmatrix} \quad (5.40)$$

such as

$$\begin{Bmatrix} \dot{\sigma}_{xx} \\ \dot{\sigma}_{yy} \\ \dot{\sigma}_{xy} \\ \dot{\sigma}_{zz} \end{Bmatrix} = \begin{bmatrix} D_{e_{1111}} & D_{e_{1122}} & D_{e_{1112}}/2 & D_{e_{1133}} \\ D_{e_{2211}} & D_{e_{2222}} & D_{e_{2212}}/2 & D_{e_{2233}} \\ D_{e_{1211}} & D_{e_{1222}} & D_{e_{1212}}/2 & D_{e_{1233}} \\ D_{e_{3311}} & D_{e_{3322}} & D_{e_{3312}}/2 & D_{e_{3333}} \end{bmatrix} \begin{Bmatrix} \dot{\varepsilon}_{xx} \\ \dot{\varepsilon}_{yy} \\ 2\dot{\varepsilon}_{xy} \\ \dot{\varepsilon}_{zz} \end{Bmatrix} \quad (5.41)$$

A generalised displacement vector is defined:

$$\{\mathbf{u}(t)\} = \begin{Bmatrix} u_{x_1} \\ u_{y_1} \\ u_{x_2} \\ u_{y_2} \\ u_{x_3} \\ u_{y_3} \\ u_{x_4} \\ u_{y_4} \end{Bmatrix} \quad (5.42)$$

$$\begin{Bmatrix} u_x(\mathbf{x}, t) \\ u_y(\mathbf{x}, t) \end{Bmatrix} = \{\mathbf{u}(\mathbf{x}, t)\} = [\mathbf{N}_u] \{\mathbf{u}(t)\} \quad (5.43)$$

with

$$[\mathbf{N}_u] = \begin{bmatrix} N_1 & 0 & N_2 & 0 & N_3 & 0 & N_4 & 0 \\ 0 & N_1 & 0 & N_2 & 0 & N_3 & 0 & N_4 \end{bmatrix} \quad (5.44)$$

The strain vector is related to displacements through the strain operator \mathbf{B} .

$$\{\boldsymbol{\varepsilon}(\mathbf{x}, t)\} = [\mathbf{B}] \{\mathbf{u}(t)\} \quad (5.45)$$

Since spatial derivatives depend on the coordinates system, the strain operator takes different values for plane strain and axisymmetric analyses:

Plane strain :

$$[\mathbf{B}] = \begin{bmatrix} \frac{\partial N_1}{\partial x} & 0 & \frac{\partial N_2}{\partial x} & 0 & \frac{\partial N_3}{\partial x} & 0 & \frac{\partial N_4}{\partial x} & 0 \\ 0 & \frac{\partial N_1}{\partial y} & 0 & \frac{\partial N_2}{\partial y} & 0 & \frac{\partial N_3}{\partial y} & 0 & \frac{\partial N_4}{\partial y} \\ \frac{\partial N_1}{\partial y} & \frac{\partial N_1}{\partial x} & \frac{\partial N_2}{\partial y} & \frac{\partial N_2}{\partial x} & \frac{\partial N_3}{\partial y} & \frac{\partial N_3}{\partial x} & \frac{\partial N_4}{\partial y} & \frac{\partial N_4}{\partial x} \\ 0 & 0 & 0 & 0 & 0 & 0 & 0 & 0 \end{bmatrix} \quad (5.46)$$

Axisymmetry :

$$[\mathbf{B}] = \begin{bmatrix} \frac{\partial N_1}{\partial r} & 0 & \frac{\partial N_2}{\partial r} & 0 & \frac{\partial N_3}{\partial r} & 0 & \frac{\partial N_4}{\partial r} & 0 \\ 0 & \frac{\partial N_1}{\partial z} & 0 & \frac{\partial N_2}{\partial z} & 0 & \frac{\partial N_3}{\partial z} & 0 & \frac{\partial N_4}{\partial z} \\ \frac{\partial N_1}{\partial z} & \frac{\partial N_1}{\partial r} & \frac{\partial N_2}{\partial z} & \frac{\partial N_2}{\partial r} & \frac{\partial N_3}{\partial z} & \frac{\partial N_3}{\partial r} & \frac{\partial N_4}{\partial z} & \frac{\partial N_4}{\partial r} \\ \frac{N_1}{r_m} & 0 & \frac{N_2}{r_m} & 0 & \frac{N_3}{r_m} & 0 & \frac{N_4}{r_m} & 0 \end{bmatrix} \quad (5.47)$$

in which r_m is the medium radius of the element.

Spatial derivatives of pore pressure will be given by:

$$\begin{cases} \left\{ \nabla(p_l(\mathbf{x}, t)) \right\} \\ \left\{ \nabla(p_g(\mathbf{x}, t)) \right\} \end{cases} = \begin{bmatrix} \nabla \mathbf{N} \\ \nabla \mathbf{N} \end{bmatrix} \begin{cases} \mathbf{p}_l(t) \\ \mathbf{p}_g(t) \end{cases} \quad (5.48)$$

Plane strain :

$$\begin{bmatrix} \nabla \mathbf{N} \end{bmatrix} = \begin{bmatrix} \frac{\partial N_1}{\partial x} & \frac{\partial N_2}{\partial x} & \frac{\partial N_3}{\partial x} & \frac{\partial N_4}{\partial x} \\ \frac{\partial N_1}{\partial y} & \frac{\partial N_2}{\partial y} & \frac{\partial N_3}{\partial y} & \frac{\partial N_4}{\partial y} \end{bmatrix} \quad (5.49)$$

Axisymmetric analysis :

$$\begin{bmatrix} \nabla \mathbf{N} \end{bmatrix} = \begin{bmatrix} \frac{\partial N_1}{\partial r} & \frac{\partial N_2}{\partial r} & \frac{\partial N_3}{\partial r} & \frac{\partial N_4}{\partial r} \\ \frac{\partial N_1}{\partial z} & \frac{\partial N_2}{\partial z} & \frac{\partial N_3}{\partial z} & \frac{\partial N_4}{\partial z} \end{bmatrix} \quad (5.50)$$

5.3.2 Numerical integration

Numerical integration is performed by a Gauss-Legendre quadrature. The integrands are evaluated at specific points of the element, then weighted, and summed.

$$\int_{-1}^1 \int_{-1}^1 f(\xi, \eta) d\xi d\eta \approx \sum_{i=1}^n \sum_{j=1}^n w_i w_j f(\xi_i, \eta_j) \quad (5.51)$$

In Θ -*Stock*, four integration points are used:

$$n = 2 \quad (5.52)$$

$$\xi_i, \eta_i = \pm \frac{1}{\sqrt{3}} \quad (5.53)$$

$$w_1 = w_2 = 1 \quad (5.54)$$

The determinant of the Jacobian matrix \mathbf{J} is used to transform the volume element from the cartesian coordinates to the natural coordinates:

$$dx dy = \det(\mathbf{J}) d\xi d\eta \quad (5.55)$$

with

$$\mathbf{J} = \begin{bmatrix} \frac{\partial x}{\partial \xi} & \frac{\partial y}{\partial \xi} \\ \frac{\partial x}{\partial \eta} & \frac{\partial y}{\partial \eta} \end{bmatrix} \quad (5.56)$$

The numerical integration becomes:

In Plane strains:

$$\begin{aligned} \int_{\Omega} f d\Omega &= \int \int f(x, y) dx dy = \int_{-1}^1 \int_{-1}^1 f(\xi, \eta) \det(\mathbf{J}) d\xi d\eta \\ &= \left[f\left(-\frac{1}{\sqrt{3}}, -\frac{1}{\sqrt{3}}\right) + f\left(\frac{1}{\sqrt{3}}, -\frac{1}{\sqrt{3}}\right) + f\left(-\frac{1}{\sqrt{3}}, \frac{1}{\sqrt{3}}\right) + f\left(\frac{1}{\sqrt{3}}, \frac{1}{\sqrt{3}}\right) \right] \det(\mathbf{J}) \end{aligned} \quad (5.57)$$

In axisymmetric analysis:

$$\begin{aligned} \int_{\Omega} f d\Omega &= \int \int f(r, z) r dr dz = \int_{-1}^1 \int_{-1}^1 f(\xi, \eta) \det(\mathbf{J}) r d\xi d\eta \\ &= \left[f\left(-\frac{1}{\sqrt{3}}, -\frac{1}{\sqrt{3}}\right) + f\left(\frac{1}{\sqrt{3}}, -\frac{1}{\sqrt{3}}\right) + f\left(-\frac{1}{\sqrt{3}}, \frac{1}{\sqrt{3}}\right) + f\left(\frac{1}{\sqrt{3}}, \frac{1}{\sqrt{3}}\right) \right] r \det(\mathbf{J}) \end{aligned} \quad (5.58)$$

5.3.3 System to solve

After spatial discretisation and numerical integration, the equations to solve can be written in the following matricial form:

$$\begin{bmatrix} \mathbf{R}_{uu} & \mathbf{R}_{uw} & \mathbf{R}_{ua} \\ \mathbf{C}_{wu} & \mathbf{C}_{ww} & \mathbf{C}_{wa} \\ \mathbf{C}_{au} & \mathbf{C}_{aw} & \mathbf{C}_{aa} \end{bmatrix} \begin{Bmatrix} \dot{\mathbf{u}}(t) \\ \dot{\mathbf{p}}_l(t) \\ \dot{\mathbf{p}}_g(t) \end{Bmatrix} + \begin{bmatrix} 0 & 0 & 0 \\ 0 & \mathbf{K}_{ww} & \mathbf{K}_{wa} \\ 0 & \mathbf{K}_{aw} & \mathbf{K}_{aa} \end{bmatrix} \begin{Bmatrix} \mathbf{u}(t) \\ \mathbf{p}_l(t) \\ \mathbf{p}_g(t) \end{Bmatrix} = \begin{Bmatrix} \dot{\mathbf{F}}_{\sigma}(t) \\ \mathbf{F}_w(t) \\ \mathbf{F}_a(t) \end{Bmatrix} \quad (5.59)$$

in which the terms corresponding to the mechanical equilibrium are,

$$[\mathbf{R}_{uu}] = \int_{\Omega} [\mathbf{B}]^T [\mathbf{D}_{\text{dep}}(\tilde{\boldsymbol{\sigma}}^*, d)] [\mathbf{B}] d\Omega \quad (5.60)$$

$$[\mathbf{R}_{uw}] = [\mathbf{B}]^T \left[\{ \mathbf{F}_s(\tilde{\boldsymbol{\sigma}}^*, d) \} \otimes \{ \mathbf{N} \} \right] d\Omega \quad (5.61)$$

$$[\mathbf{R}_{ua}] = [\mathbf{B}]^T \left[\{ \mathbf{I}_d - \mathbf{F}_s(\tilde{\boldsymbol{\sigma}}^*, d) \} \otimes \{ \mathbf{N} \} \right] d\Omega \quad (5.62)$$

$$\{ \dot{\mathbf{F}}_{\sigma}(t) \} = \int_{\Gamma_{\sigma}} [\mathbf{N}_u]^T \{ \dot{\mathbf{t}} \} d\Gamma + \int_{\Omega} [\mathbf{N}_u]^T \{ \dot{\mathbf{b}} \} d\Omega \quad (5.63)$$

the terms corresponding to water flow are,

$$\left[\mathbf{C}_{wu} \right] = - \int_{\Omega} (\rho_w S_l + \rho_{vap}(1 - S_l)) \left[\left\{ \mathbf{N} \right\}^T \otimes \left\{ \mathbf{i} \right\} \right] \left[\mathbf{B} \right] d\Omega \quad (5.64)$$

$$\left[\mathbf{C}_{ww} \right] = \int_{\Omega} [-\phi(\rho_w - \rho_{vap})g_2 + \phi S_l \beta_p - \phi(1 - S_l)A] \left[\left\{ \mathbf{N} \right\}^T \otimes \left\{ \mathbf{N} \right\} \right] d\Omega \quad (5.65)$$

$$\left[\mathbf{C}_{wa} \right] = \int_{\Omega} [\phi(\rho_w - \rho_{vap})g_2 + \phi(1 - S_l)A] \left[\left\{ \mathbf{N} \right\}^T \otimes \left\{ \mathbf{N} \right\} \right] d\Omega \quad (5.66)$$

$$\left[\mathbf{K}_{ww} \right] = \int_{\Omega} \rho_w D_P \left[\nabla \mathbf{N} \right]^T \left[\nabla \mathbf{N} \right] d\Omega \quad (5.67)$$

$$\left[\mathbf{K}_{wa} \right] = - \int_{\Omega} \rho_w D_P \left[\nabla \mathbf{N} \right]^T \left[\nabla \mathbf{N} \right] d\Omega \quad (5.68)$$

$$\left\{ \mathbf{F}_w(t) \right\} = - \int_{\Omega} \rho_w K_w \left[\nabla \mathbf{N} \right]^T \nabla z d\Omega - \int_{\Gamma_{Q_w}} \left\{ \mathbf{N} \right\}^T \tilde{q}_w d\Gamma \quad (5.69)$$

and the terms corresponding to the air flow are:

$$\left[\mathbf{C}_{au} \right] = - \int_{\Omega} (1 - S_l + H S_l) \rho_a \left[\left\{ \mathbf{N} \right\}^T \otimes \left\{ \mathbf{i} \right\} \right] \left[\mathbf{B} \right] d\Omega \quad (5.70)$$

$$\left[\mathbf{C}_{aw} \right] = - \int_{\Omega} (H - 1) \phi \rho_a g_2 \left[\left\{ \mathbf{N} \right\}^T \otimes \left\{ \mathbf{N} \right\} \right] d\Omega \quad (5.71)$$

$$\left[\mathbf{C}_{aa} \right] = \int_{\Omega} [(H - 1) \phi \rho_a g_2 + \phi(1 - S_l + H S_l) \alpha_p] \left[\left\{ \mathbf{N} \right\}^T \otimes \left\{ \mathbf{N} \right\} \right] d\Omega \quad (5.72)$$

$$\left[\mathbf{K}_{aw} \right] = \int_{\Omega} (\rho_a H D_{P_l} - \rho_w D_{P_{vap}}) \left[\nabla \mathbf{N} \right]^T \left[\nabla \mathbf{N} \right] d\Omega \quad (5.73)$$

$$\left[\mathbf{K}_{aa} \right] = - \int_{\Omega} \left(-\frac{K_a}{g} + \rho_a H D_{P_l} - \rho_w D_{P_{vap}} \right) \left[\nabla \mathbf{N} \right]^T \left[\nabla \mathbf{N} \right] d\Omega \quad (5.74)$$

$$\left\{ \mathbf{F}_a(t) \right\} = - \int_{\Omega} \rho_a (K_a + H K_w) \left[\nabla \mathbf{N} \right]^T \nabla z d\Omega - \int_{\Gamma_{Q_a}} \left\{ \mathbf{N} \right\}^T \tilde{q}_a d\Gamma \quad (5.75)$$

5.4 Discretisation in time

The solution of the coupled system (equation 5.59) requires integration to be performed over a discrete number of time increments. Traditionally, most time-stepping schemes are based on the θ -method. In this procedure, all time-dependent quantities are represented by a weighted sum of the values at the start and end of the time step, respectively, with the rate quantities being approximated by average rates over the time step (see figure 5.3).

The value of the quantity, f , at a certain intermediate time, $t_{\theta} = t_n + \theta(t_{n+1} - t_n)$, is determined by considering a linear interpolation between the two extremities of the time step:

$$f(t_{\theta}) = (1 - \theta)f_n + \theta f_{n+1} = f_n + \theta(f_{n+1} - f_n) = f_n + \theta \Delta f \quad (5.76)$$

It is then assumed that $f(t)$ is constant on $[t_n, t_{n+1}]$ and is equal to $f(t_{\theta})$.

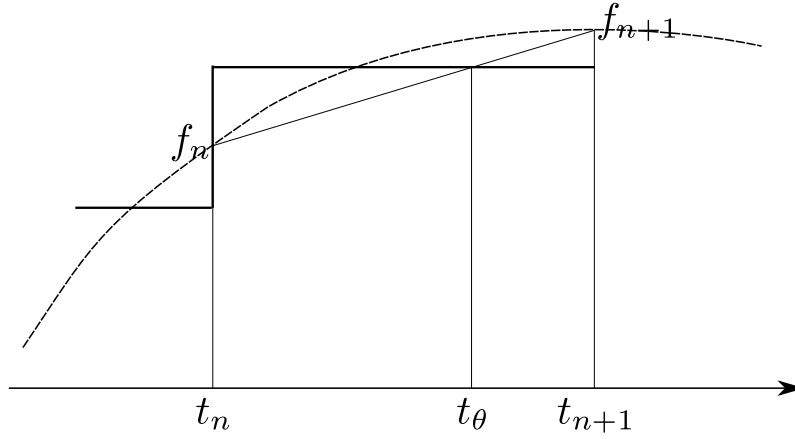


Fig. 5.3: Approximation in the time domain

Hence the integrals:

$$\int_{t_n}^{t_{n+1}} f(t)dt = \int_{t_n}^{t_{n+1}} f(t_\theta)dt = (f_n + \theta\Delta f)\Delta t \quad (5.77)$$

$$\int_{t_n}^{t_{n+1}} \dot{f}(t)dt = \Delta f \quad (5.78)$$

After integration between t and t_{n+1} equation 5.59 becomes :

$$\begin{bmatrix} \mathbf{R}_{uu} & \mathbf{R}_{uw} & \mathbf{R}_{ua} \\ \mathbf{C}_{wu} & \mathbf{C}_{ww} & \mathbf{C}_{wa} \\ \mathbf{C}_{au} & \mathbf{C}_{aw} & \mathbf{C}_{aa} \end{bmatrix} \begin{Bmatrix} \Delta \mathbf{u} \\ \Delta \mathbf{p}_w \\ \Delta \mathbf{p}_g \end{Bmatrix} + \begin{bmatrix} 0 & 0 & 0 \\ 0 & \mathbf{K}_{ww} & \mathbf{K}_{wa} \\ 0 & \mathbf{K}_{aw} & \mathbf{K}_{aa} \end{bmatrix} \begin{Bmatrix} (\mathbf{u}_n + \theta\Delta \mathbf{u})\Delta t \\ (\mathbf{p}_{wn} + \theta\Delta \mathbf{p}_w)\Delta t \\ (\mathbf{p}_{gn} + \theta\Delta \mathbf{p}_g)\Delta t \end{Bmatrix} = \begin{Bmatrix} \Delta \mathbf{F}_\sigma \\ (\mathbf{F}_{wn} + \theta\Delta \mathbf{F}_w)\Delta t \\ (\mathbf{F}_{an} + \theta\Delta \mathbf{F}_a)\Delta t \end{Bmatrix} \quad (5.79)$$

which can be rewritten in the following form:

$$\begin{bmatrix} \mathbf{R}_{uu} & \mathbf{R}_{uw} & \mathbf{R}_{ua} \\ \mathbf{C}_{wu} & \mathbf{C}_{ww} + \theta\Delta t\mathbf{K}_{ww} & \mathbf{C}_{wa} + \theta\Delta t\mathbf{K}_{wa} \\ \mathbf{C}_{au} & \mathbf{C}_{aw} + \theta\Delta t\mathbf{K}_{aw} & \mathbf{C}_{aa} + \theta\Delta t\mathbf{K}_{aa} \end{bmatrix} \begin{Bmatrix} \Delta \mathbf{u} \\ \Delta \mathbf{p}_w \\ \Delta \mathbf{p}_g \end{Bmatrix} = \begin{Bmatrix} \Delta \mathbf{F}_\sigma \\ \theta\Delta t\Delta \mathbf{F}_w \\ \theta\Delta t\Delta \mathbf{F}_a \end{Bmatrix} + \Delta t \begin{Bmatrix} 0 \\ \mathbf{F}_{wn} - \mathbf{K}_{ww}\mathbf{p}_{wn} - \mathbf{K}_{wa}\mathbf{p}_{gn} \\ \mathbf{F}_{an} - \mathbf{K}_{aw}\mathbf{p}_{wn} - \mathbf{K}_{aa}\mathbf{p}_{gn} \end{Bmatrix} \quad (5.80)$$

The stability and accuracy of the θ -method depends on the weighting parameter

$$\theta = \frac{t_\theta - t_n}{t_{n+1} - t_n} \quad (5.81)$$

Particular integration schemes are recovered when θ takes specific values. $\theta = 0$ corresponds to an explicit (Euler) integration, $\theta = 1$ to an implicit (Backward Euler) integration and $\theta = 0.5$ to a trapezoidal (Crank-Nicolson) integration. In θ -Stock, $\theta = 2/3$.

If $\theta \geq 0.5$ the process is unconditionally stable (Booker and Small, 1975).

For mixed pressure-displacements problems, oscillations can appear in the initial pore pressure solution due to the large difference between the order of magnitude of permeability and mechanical rigidities coefficients, resulting in an ill-conditioned matrix.

The best solution to avoid numerical oscillations would be to choose the polynomial

describing the pore pressure rates to be one order lower than the polynomial describing the velocities (Zienkiewicz et al., 2005).

Several stabilisation schemes have been proposed to permit equal-order interpolation for displacements and pore pressures fields. They usually consist in the addition of additional terms to the mass balance equation, modifying the incompressibility constraint. Recent works on this topics include the one of Mira et al. (2003), White and Borja (2008), Aguilar et al. (2008), Preisig and Prévost (2011), ...

We chose to use another option, which does not require strong modifications of the source code. Vermeer and Verruijt (1981), determined a lower limit for the time step, given a specific mesh size,

$$\Delta t \geq \frac{1}{6} \frac{(\Delta h)^2}{\theta C_v} \quad (5.82)$$

in which C_v is the coefficient of consolidation ($C_v = \frac{K_w}{\left[\frac{(1+\nu)}{3(1-\nu)}K + \frac{\phi\beta_p}{\rho_w}\right]\gamma_w}$).

Equation (5.82) can be approximate by:

$$\Delta t \geq \frac{1}{6} \frac{\gamma_w (\Delta h)^2}{\theta K K_w} \quad (5.83)$$

5.5 Iterative resolution of equilibrium equations system

In order to solve equation 5.80, the total applied load is split into several loads increments which are considered to be applied over a period of time Δt .

For each increment, an iterative algorithm based on the Newton-Raphson method is used to obtain a convergent solution. This section develops the iterative algorithm used to determine the response for one load increment. The smaller the increment size, the smaller the number of iterations needed to reach convergence.

The equation to solve is:

$$[\mathbf{K}] \{ \Delta dof \} = \{ \Delta \mathbf{F} \} \quad (5.84)$$

in which

$$[\mathbf{K}] = \begin{bmatrix} \mathbf{R}_{uu} & \mathbf{R}_{uw} & \mathbf{R}_{ua} \\ \mathbf{C}_{wu} & \mathbf{C}_{ww} + \theta \Delta t \mathbf{K}_{ww} & \mathbf{C}_{wa} + \theta \Delta t \mathbf{K}_{wa} \\ \mathbf{C}_{au} & \mathbf{C}_{aw} + \theta \Delta t \mathbf{K}_{aw} & \mathbf{C}_{aa} + \theta \Delta t \mathbf{K}_{aa} \end{bmatrix} \quad (5.85)$$

$$\{ \Delta dof \} = \begin{Bmatrix} \Delta \mathbf{u} \\ \Delta \mathbf{p}_w \\ \Delta \mathbf{p}_g \end{Bmatrix} \quad (5.86)$$

$$\{ \Delta \mathbf{F} \} = \begin{Bmatrix} \Delta \mathbf{F}_\sigma \\ \theta \Delta t \Delta \mathbf{F}_w \\ \theta \Delta t \Delta \mathbf{F}_a \end{Bmatrix} + \Delta t \begin{Bmatrix} 0 \\ \mathbf{F}_{wn} - \mathbf{K}_{ww} \mathbf{p}_{wn} - \mathbf{K}_{wa} \mathbf{p}_{gn} \\ \mathbf{F}_{an} - \mathbf{K}_{aw} \mathbf{p}_{wn} - \mathbf{K}_{aa} \mathbf{p}_{gn} \end{Bmatrix} \quad (5.87)$$

The different steps of the iterative algorithm are described below and represented in figure

5.4.

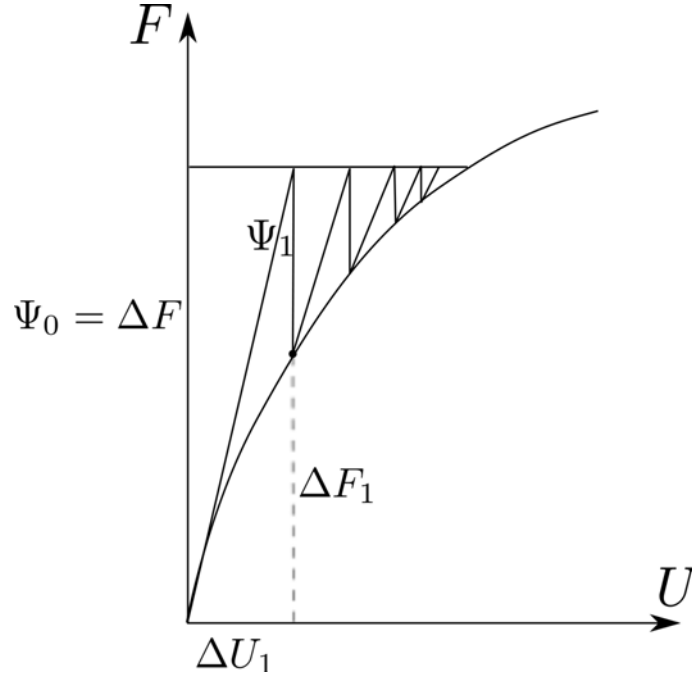


Fig. 5.4: Numerical solving of the non-linear load-displacement equation

1. The residu Ψ is first initialised to be equal to the sum of exterior forces:

$$\Psi_0 = \Delta \mathbf{F} \quad (5.88)$$

2. At iteration n , equation 5.84 is solved, with a rigidity matrix, $\mathbf{K}_{n-1}(\tilde{\boldsymbol{\sigma}}_{n-1}^*, \phi_{n-1}, s_{n-1})$, depending on the stress state at the beginning of the increment, and calculated considering an elastic loading (equations 3.109 and 3.110). The method used is therefore not the original Newton-Raphson method (which would consider elasto-plastic loading), nor exactly the modified Newton-Raphson method (for which we would have $\mathbf{K}_n = \mathbf{K}_0$).

$$\left[\mathbf{K}_{n-1} \right] \left\{ \Delta \mathbf{dof}_n \right\} = \left\{ \Psi_0 \right\} \quad (5.89)$$

Since the problem is non-linear, the dofs values found by solving this system don't respect the mechanical equilibrium and iterations have to be performed to reach mechanical equilibrium.

3. The local stress-point algorithm (see section 5.6) is executed to find the real stress increment $\Delta \boldsymbol{\sigma}_n$ corresponding to the increments in strains $\Delta \boldsymbol{\varepsilon}_n$, (deduced from $\Delta \mathbf{u}_n$), and pore pressures, Δp_{l_n} and Δp_{g_n} .
4. Knowing the updated stress state, the internal force increment is calculated:

$$\Delta \mathbf{F}_{int} = \int_{\Omega} \left[\mathbf{B} \right]^T \left\{ \Delta \boldsymbol{\sigma} \right\} d\Omega \quad (5.90)$$

5. The residual (which represents the unbalanced forces) is updated:

$$\Psi_n = \Psi_{n-1} - \Delta \mathbf{F}_n \quad (5.91)$$

$$\{\Delta \mathbf{F}_n\} = \left\{ \begin{array}{c} \Delta \mathbf{F}_{int} \\ [\mathbf{K}_{WA}] \{\Delta \mathbf{dof}_n\} \end{array} \right\} \quad (5.92)$$

in which

$$[\mathbf{K}_{WA}] = \begin{bmatrix} \mathbf{C}_{wu} & \mathbf{C}_{ww} + \theta \Delta t \mathbf{K}_{ww} & \mathbf{C}_{wa} + \theta \Delta t \mathbf{K}_{wa} \\ \mathbf{C}_{au} & \mathbf{C}_{aw} + \theta \Delta t \mathbf{K}_{aw} & \mathbf{C}_{aa} + \theta \Delta t \mathbf{K}_{aa} \end{bmatrix} \quad (5.93)$$

6. Convergency is reached if the two following criteria are respected:

$$\frac{\|\Psi_n\|}{\|\Psi_0\|} < TOL \quad (5.94)$$

$$\frac{\|\Delta \mathbf{dof}_n\|}{\|\mathbf{dof}_{n-1}\|} < TOL \quad (5.95)$$

7. Steps 2 to 6 are repeated until the two convergence criteria are respected.

5.6 Stress point algorithm

The stress-point algorithm gives the increment in stress and plastic strains associated with the given increment of strains and pore pressures. The algorithmic procedure follows the one proposed by Ju (1989) for damage-plastic couplings.

5.6.1 Input

Mechanical parameters

The following parameters are required as an input for the local algorithm:

- Elasticity parameters: $\kappa, g, n, p_{r_{HAR}}$ (pressure dependent elasticity)
- Plasticity parameters: $M, \lambda, r, \beta, p_{r_{BBM}}$
- Retention properties: $S_r, \alpha_{vg}, m_{vg}, n_{vg}$ (Van Genuchten)
- Damage parameters: C_0, C_1, C_2

Initial state

The state at the start of the loading step is defined by the initial total stress, $\boldsymbol{\sigma}_0$, the total and elastic strains, $\boldsymbol{\varepsilon}_0$ and $\boldsymbol{\varepsilon}_0^e$ (and thus implicitly the plastic strain), the fluid pore pressures, p_{g_0} and p_{l_0} (and therefore the suction $s_0 = p_{g_0} - p_{l_0}$), and the values of the preconsolidation pressure, p_{0_0} , and the damage parameter, d_0 , which act as hardening parameters.

Loading

As in the work of Sheng et al. (2003), pore pressures are treated as additional strain components, even though suction is similar to a stress variable in constitutive modelling.

The load input is then composed of the strain increment, $\Delta\boldsymbol{\varepsilon}$ (deduced from the displacements increment given by the global algorithm), and the pore pressures increments, Δp_g and Δp_l .

The explicit scheme follows the following steps:

1. Calculation of the double effective stress
2. Elastic trial stress state (see section 5.6.2)
3. Plasticity correction (see section 5.6.3)
4. Damage correction (see section 5.6.4)
5. Calculation of the total stress

5.6.2 Trial elastic state

Since plastic and damage criteria are expressed in terms of the double effective stress, the first step is to calculate the initial double effective stress:

$$\tilde{\boldsymbol{\sigma}}_0^* = \frac{\boldsymbol{\sigma} + (-p_{g0} + S_{l_0}(s_0)s_0)\mathbf{i}}{1 - d_0} \quad (5.96)$$

The initial elasticity matrix is calculated with equation (2.56).

$$\mathbf{D}_e(\tilde{\boldsymbol{\sigma}}_0^*) \quad (5.97)$$

Since strain and pore pressures increment are fixed, their final values are:

$$\boldsymbol{\varepsilon}_1 = \boldsymbol{\varepsilon}_0 + \Delta\boldsymbol{\varepsilon} \quad (5.98)$$

$$p_{g1} = p_{g0} + \Delta p_g \quad (5.99)$$

$$p_{l1} = p_{l0} + \Delta p_l \quad (5.100)$$

$$s_1 = s_0 + \Delta s \quad (5.101)$$

The increment of the double effective stress, obtained by assuming that the material behaves elastically, is

$$\Delta\tilde{\boldsymbol{\sigma}}^* = \mathbf{D}_e(\tilde{\boldsymbol{\sigma}}_0^*)\Delta\boldsymbol{\varepsilon} \quad (5.102)$$

from which the trial elastic state is deduced.

$$\tilde{\boldsymbol{\sigma}}_{tr}^* = \tilde{\boldsymbol{\sigma}}_0^* + \Delta\tilde{\boldsymbol{\sigma}}^* \quad (5.103)$$

$$\boldsymbol{\varepsilon}_{tr}^e = \boldsymbol{\varepsilon}_0^e + \Delta \boldsymbol{\varepsilon} \quad (5.104)$$

It will next be checked if this stress state lies inside the plastic and damage surfaces (in this case the trial elastic state is the final one), or if dissipative phenomena are activated.

5.6.3 Plasticity

The plastic criterion is checked first, since plastic laws depend on suction and double effective stress increments, which are not affected by damage.

1. Check yield criterion

The yield criterion is checked for a stress state corresponding to the trial double effective stress, the final suction, and the initial preconsolidation pressure:

$$f_p(\tilde{\boldsymbol{\sigma}}_{tr}^*, p_{0_0}, s_1) = \tilde{q}_{tr}^2 - M^2 \tilde{p}_{tr}^* (p_c^*(p_{0_0}, s_1) - \tilde{p}_{tr}^*) \quad (5.105)$$

- if $f_p \leq FTOL$ then there are no plastic strains. The stress state is updated

$$\tilde{\boldsymbol{\sigma}}_1^* = \tilde{\boldsymbol{\sigma}}_{tr}^* \quad (5.106)$$

$$\boldsymbol{\varepsilon}_1^e = \boldsymbol{\varepsilon}_{tr}^e \quad (5.107)$$

$$\tilde{p}_{0_1}^* = \tilde{p}_{0_0}^* \quad (5.108)$$

and the damage criterion is checked (section 5.6.4)

- if $f_p > FTOL$ then the plastic algorithm is activated. A schematic representation of the plasticity algorithm is given in figure 5.5.

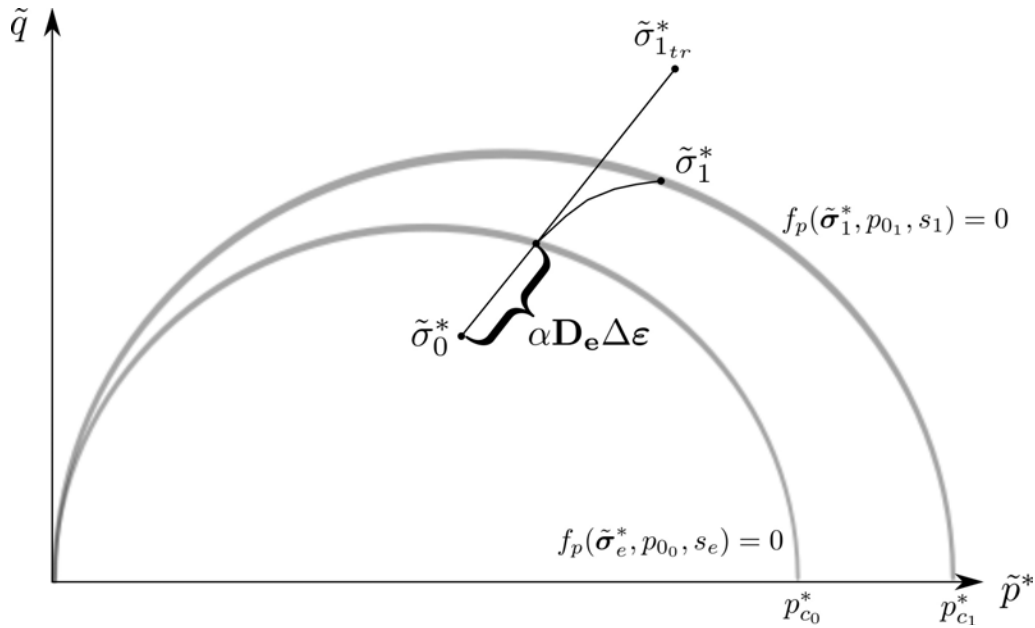


Fig. 5.5: Explicit algorithm for plasticity

2. Intersection with yield surface

If the stress state was previously lying inside the yield surface ($f_p(\tilde{\boldsymbol{\sigma}}_0^*, p_{0_0}, s_0) < 0$), it is necessary to determine for which fraction of the total strain the soil behaves elastically before reaching the yield surface. This is equivalent to finding the scalar quantity, α , for which

$$f_p(\tilde{\boldsymbol{\sigma}}_0^* + \alpha \mathbf{D}_e \Delta \boldsymbol{\varepsilon}, \tilde{p}_{0_0}^*, s_0 + \alpha \Delta s) = 0 \quad (5.109)$$

The starting stress state for stress integration will then be:

$$\tilde{\boldsymbol{\sigma}}_e^* = \tilde{\boldsymbol{\sigma}}_0^* + \alpha \mathbf{D}_e \Delta \boldsymbol{\varepsilon} \quad (5.110)$$

$$s_e = s_0 + \alpha \Delta s \quad (5.111)$$

Various algorithms can be used to solve equation 5.109. In our case, we used the Pegasus algorithm from Dowell and Jarratt (1972).

3. Stress integration

An explicit stress integration scheme is used to determine the increment in double effective stress, plastic strains and preconsolidation pressure.

Equations 3.95 to 3.97 give, (replacing fourth order tensors and second order tensors by the equivalent second order tensors and vectors)

$$\Delta \boldsymbol{\varepsilon}^p = \frac{\mathbf{a}_g \mathbf{a}_f^T \mathbf{D}_e}{\mathbf{a}_f^T \mathbf{D}_e \mathbf{a}_g - A} \Delta \boldsymbol{\varepsilon}_n + \frac{C \mathbf{a}_g}{\mathbf{a}_f^T \mathbf{D}_e \mathbf{a}_g - A} \Delta s_n \quad (5.112)$$

$$\Delta p_0 = \frac{B \mathbf{a}_f^T \mathbf{D}_e}{\mathbf{a}_f^T \mathbf{D}_e \mathbf{a}_g - A} \Delta \boldsymbol{\varepsilon}_n + \frac{BC}{\mathbf{a}_f^T \mathbf{D}_e \mathbf{a}_g - A} \Delta s_n \quad (5.113)$$

$$\Delta \tilde{\boldsymbol{\sigma}}^* = \mathbf{D}_e \left[\mathbf{i} - \frac{\mathbf{a}_g \mathbf{a}_f^T \mathbf{D}_e}{\mathbf{a}_f^T \mathbf{D}_e \mathbf{a}_g - A} \right] \Delta \boldsymbol{\varepsilon}_n + \mathbf{D}_e \frac{C \mathbf{a}_g}{\mathbf{a}_f^T \mathbf{D}_e \mathbf{a}_g - A} \Delta s_n \quad (5.114)$$

Since the problem is highly non-linear, the strain-suction increment is divided in smaller substeps:

$$\Delta \boldsymbol{\varepsilon}_n = \Delta T \Delta \boldsymbol{\varepsilon} \quad (5.115)$$

$$\Delta s_n = \Delta T \Delta s \quad (5.116)$$

and the quantities, \mathbf{D}_e , \mathbf{a}_f , \mathbf{a}_g , A , B and C are updated at the beginning of each subincrement.

The size of the subincrements are adapted to keep the error below a certain tolerance, using the automatic substepping scheme developed by Sloan et al. (2001) for the saturated case, and extended by Sheng et al. (2003) to the unsaturated case.

4. Yield surface drift correction

At the end of stress integration, the stress state may diverge from the yield condition so that $|f_p| > FTOL$. In that case it is necessary to correct the stress state to restore

the stresses to the yield surface.

The method proposed by Potts and Gens (1985), and later used by Sołowski and Gallipoli (2010) for unsaturated soils, is described below.

The algorithm calculates a correction of the double effective stress state $\delta\tilde{\boldsymbol{\sigma}}^*$ while the increment of strains and suction are kept unchanged. This implies an associated change in the elastic and plastic strains partition:

$$\delta\tilde{\boldsymbol{\sigma}}^* = \mathbf{D}_e\delta\varepsilon^e = -\mathbf{D}_e\delta\varepsilon^p = -\delta\lambda\mathbf{D}_e\frac{\partial g_p}{\partial\tilde{\boldsymbol{\sigma}}^*} \quad (5.117)$$

in which the scalar multiplier $\delta\lambda$ is obtained from the consistency condition:

$$\delta\lambda = \frac{f_p}{\mathbf{a}_f^T\mathbf{D}_e\mathbf{a}_g - A} \quad (5.118)$$

The corrected values of the double effective stress, elastic and plastic strains and the hardening parameter are computed. If the stress still lies outside of the yield locus after the first correction, the procedure is repeated until the stress state is mapped back within the set tolerance.

At the end of the plasticity algorithm, the new values of the double effective stress, $\tilde{\boldsymbol{\sigma}}_1^*$, the elastic and plastic strain, ε_1^e and ε_1^p , and the hardening parameter, p_{01} , are known.

5.6.4 Damage

The updated value of the double effective stress, $\tilde{\boldsymbol{\sigma}}_1^*$, serves as an input for the damage algorithm, which is checked in a second time.

1. Check damage criterion

The damage criterion is checked with the final value of the double effective stress and initial damage:

$$f_{d_1} = Y_{d_1}^* - C_0 - C_1d_0 \quad (5.119)$$

with

$$Y_{d_1}^* = Y_d^*(\tilde{\boldsymbol{\sigma}}_1^*) = \tilde{q}_1 - C_2\tilde{p}_1^* \quad (5.120)$$

- if $f_{d_1} \leq FTOL$, there is no damage evolution,

$$d_1 = d_0 \quad (5.121)$$

and the total stress state can be updated (section 5.6.5).

- if $f_{d_1} > FTOL$, the damage algorithm is activated (go to step 2).

2. Intersection with damage criterion

As for the plastic algorithm, the Pegasus algorithm is used to determine which fraction α of the strain is applied before starting to create damage.

$$f_d(\tilde{\boldsymbol{\sigma}}_0^* + \mathbf{D}_e(\tilde{\boldsymbol{\sigma}}_0^*)\alpha\Delta\boldsymbol{\varepsilon}^e, d_0) = 0 \quad (5.122)$$

Damage starts to increase for the stress state:

$$\tilde{\boldsymbol{\sigma}}_c^* = \tilde{\boldsymbol{\sigma}}_0^* + \mathbf{D}_e(\tilde{\boldsymbol{\sigma}}_0^*)\alpha\Delta\boldsymbol{\varepsilon}^e \quad (5.123)$$

3. Damage increment

The damage increment is calculated so that the final stress state lies on the damage surface:

$$\Delta d = \frac{\Delta Y_d}{C_1} = \frac{Y_d(\tilde{\boldsymbol{\sigma}}_1^*) - Y_d(\tilde{\boldsymbol{\sigma}}_c^*)}{C_1} \quad (5.124)$$

The damage algorithms allows to update the value of the damage parameter:

$$d_1 = d_0 + \Delta d \quad (5.125)$$

5.6.5 Final state

Once all variables are updated, it possible to go back to the total stress state:

$$\boldsymbol{\sigma}_1 = (1 - d_1)\tilde{\boldsymbol{\sigma}}_1^* + p_{g1}\mathbf{i} - S_{l_1}(s_1)s_1\mathbf{i} \quad (5.126)$$

The total stress difference $\Delta\boldsymbol{\sigma} = \boldsymbol{\sigma}_1 - \boldsymbol{\sigma}_0$ is used in the global Newton-Raphson algorithm (equation 5.90).

The whole set of equations and numerical procedures needed to study fully coupled hydro-mechanical problems have been presented in this chapter. The following chapters consist in applications of the constitutive and numerical frameworks described previously to simulation of various boundary value problems. Chapter 6 makes use of the local stress-point algorithm to simulate purely mechanical problems at different water contents. Chapter 7 shows the ability of this work to simulate complex problems in which fluid transfers, coupled with mechanics, play a major role.

CHAPTER 6

SIMULATION OF LABORATORY EXPERIMENTS

This chapter presents simulations of mechanical laboratory tests on two materials, Callovo-Oxfordian argillite and Boom Clay. Good agreement is achieved between experimental results and simulations. When no experimental data are available, it is shown that the mechanical behaviour follows expected trends. The argillite exhibits a coupled plastic-damage behaviour with a slight dependence on water content. The high sensibility of Boom clay on suction is well reproduced, with a ductile behaviour at low suctions, and a more brittle behaviour at high suctions.

Ce chapitre présente des résultats de simulation d'essais de laboratoire sur deux matériaux, l'argilite de l'Est et l'argile de Boom. Les résultats de simulations montrent une bonne adéquation avec les résultats expérimentaux. En l'absence de données expérimentales, le comportement mécanique suit les tendances attendues. Le comportement de l'argilite montre un couplage entre endommagement et plasticité, avec une faible dépendance à la teneur en eau. La forte influence de la succion sur le comportement de l'argile de Boom est bien reproduit, le comportement étant très plastique pour les faibles suctions et plus à tendance fragile pour les fortes suctions.

Contents

6.1 Callovo-Oxfordian Argillite	92
6.1.1 Specific model for argillite	92
6.1.2 Simulation of mechanical laboratory tests	94
6.1.3 Effect of damage hardening parameter	100
6.2 Boom Clay	101
6.2.1 Model parameters	102
6.2.2 Simulation of mechanical laboratory tests	103
6.2.3 Suction effects on mechanical behaviour	108
6.3 Conclusion	110

6.1 Callovo-Oxfordian Argillite

Due to their high mechanical strength and their low permeability, argillites are the more serious option to serve as a geological barrier in the context of radioactive waste disposal in France. Numerous research works have been funded in the recent years to study their thermo-hydro-mechanical properties, and many experimental results have been published in the literature. That is why we chose this material to validate our model.

Figure 6.1 shows the typical stress-strain curve obtained from triaxial compression tests. It is clear that argillites exhibit plastic strains. Damage is revealed by elastic properties degradation as well as microstructural microcracks. This material is therefore adapted to be studied by a coupled damage-plastic model.

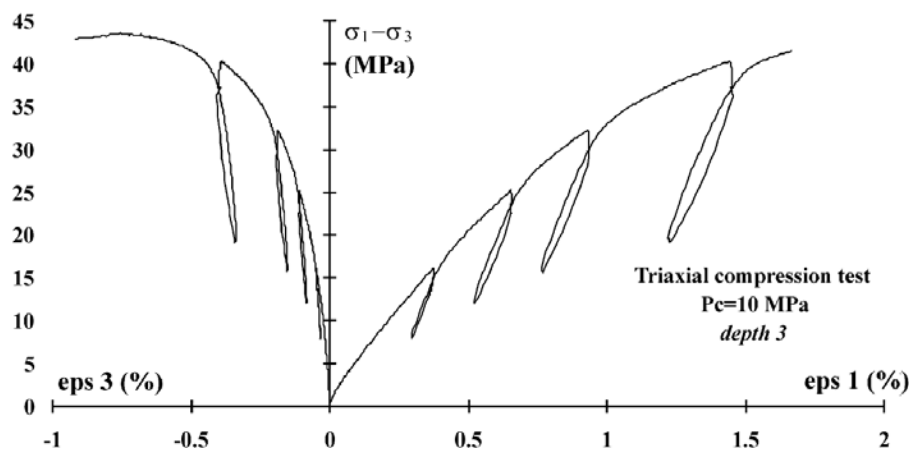


Fig. 6.1: Example of a stress–strain curve from a triaxial compression test with unloading–reloading cycles (from Chiarelli et al. (2003))

The most extensive available experimental study on argillites comes from the PhD thesis of Chiarelli (2000), from which two papers have been derived (Chiarelli et al., 2003; Shao et al., 2006). She performed mechanical tests at different confining pressures and at different water contents.

6.1.1 Specific model for argillite

Mechanical properties

Hydrostatic tests (up to 60 MPa confining pressure) have shown that the bulk modulus can be considered pressure independent, and that the initial anisotropy is small (figure 6.2). We will therefore consider a linear elastic behaviour.

The Cam-clay model described in section 3.3 is not really adapted to model rocks mechanical behaviour. Figure 6.2 shows that during isotropic compression, the stress-strain behaviour remains elastic even for very high pressures. The preconsolidation pressure will therefore be set to a high value (at least superior to 60 MPa). The expression of the plastic potential needs to be modified to obtain a critical state conform to experiments (figure 6.3), i.e. to enable strain hardening for mean pressures well below the preconsolidation pressure.

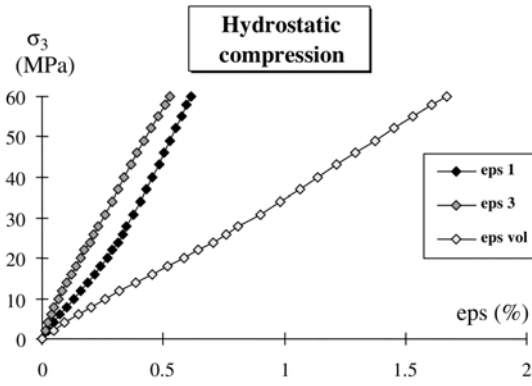


Fig. 6.2: Hydrostatic compression test (Shao et al., 2006)

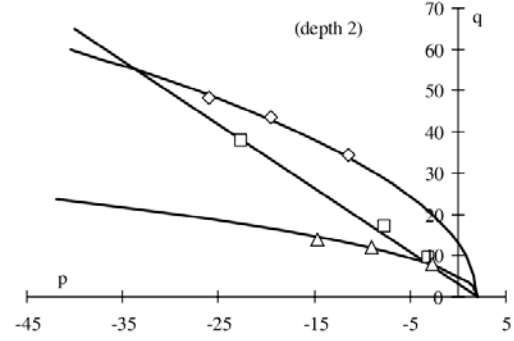


Fig. 6.3: Initial yield surface, compressibility/dilatancy boundary and failure surface (Shao et al., 2006)

The yield surface is

$$f_p = \tilde{q}^2 - M^2 \tilde{p}^* (p_c^* - \tilde{p}^*) \quad (6.1)$$

The new plastic potential is chosen of the form:

$$g_p = \tilde{q}^2 - M^2 \tilde{p}^* (\eta_d p_c^* - \tilde{p}^*) \quad (6.2)$$

Deriving equation 6.2 gives the equation of the critical state line (in the double effective stress space):

$$\tilde{q} = M \tilde{p}^* \sqrt{\frac{2}{\eta_d} - 1} \quad (6.3)$$

For the sake of simplicity, and since no experimental data are available to calibrate the dependence of the yield surface on suction, the preconsolidation pressure is taken independent of suction in the total stress space and we simply have:

$$p_c^* = p_0 + S_l s \quad (6.4)$$

Elastic, plastic and damage parameters chosen in this study are summarised in table 6.1.

Elasticity		Plasticity					Damage		
K	ν	M	λ_0	$\kappa = 1/K$	η_d	p_0	C_0	C_1	C_2
GPa			GPa ⁻¹	GPa ⁻¹		MPa	MPa	MPa	
5	0.19	0.25	0.2005	0.200	0.05	100	0	200	0.2

Table 6.1: Material mechanical parameters

Hydraulic properties

Van Genuchten parameters are chosen to fit the experimental water retention curve given by Hoxha et al. (2007) (see figure 6.4). They are summarised in table 6.2.

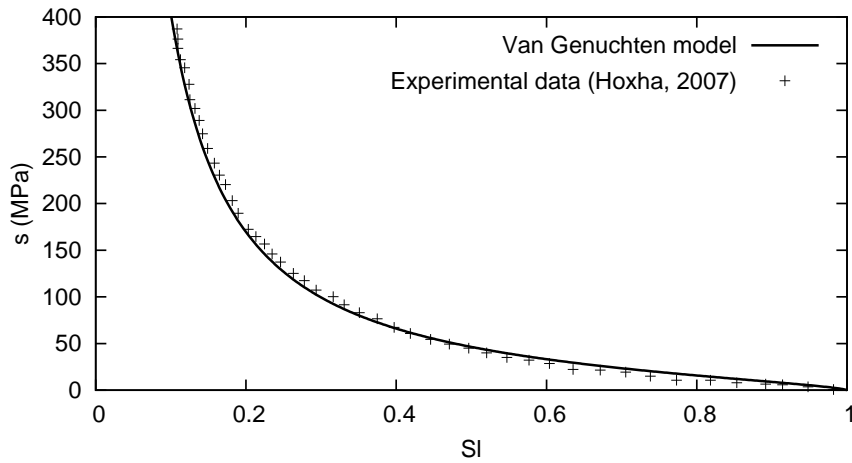


Fig. 6.4: Water retention curve

α_{vg} (MPa^{-1})	n_{vg}	m_{vg}	S_r
0.04	1.5	0.55	0

Table 6.2: Retention parameters

Mechanical tests are carried on for 3 ranges of water content. Table 6.3 gives the saturation degree (given by Chiarelli and Shao (2002)) and the suction value (calculated with Van Genuchten equation) corresponding to each water content range.

w (%)	S_l	s (MPa)
4-5	0.61	32
5-6	0.71	23
7-8	0.93	7

Table 6.3: Hydraulic state for three water content ranges

6.1.2 Simulation of mechanical laboratory tests

Tests at natural water content

Triaxial compression tests, proportional compression tests and lateral extension tests are simulated. All the experimental data comes from the PhD thesis of Chiarelli (2000). The tests are executed on samples at their natural water content, which is in the range $w = 5-6\%$. Suction is therefore taken equal to 23 MPa.

Triaxial compression tests: Triaxial compression tests with unloading-reloading cycles are simulated for four confining pressures (0 MPa, 5 MPa, 10 MPa and 20MPa). The comparison of computed stress-strain curves (a) and volumetric strains (b) with experimental data are represented on figures 6.5 to 6.8.

The agreement between computed and experimental stress-strain curves is quite good.

The plot of the volumetric strains versus axial strains shows that the volumetric strains are systematically underestimated. This could be improved by modifying the plastic potential in order to increase the ratio $\dot{\varepsilon}_v/\dot{\varepsilon}_s$. The transition from volumetric compressibility to dilatancy (shown in figure 6.6.b) can not be represented by the plasticity model since it doesn't allow the stress path to cross the critical state line.

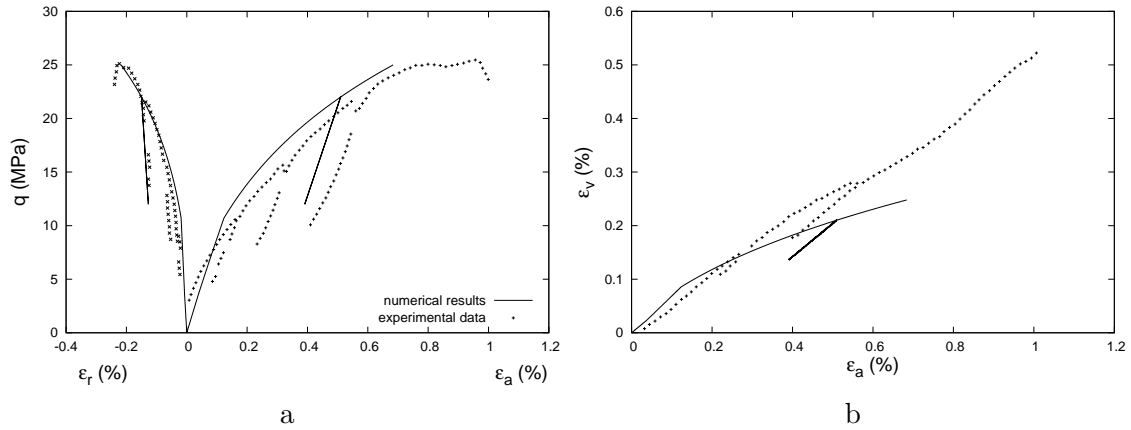


Fig. 6.5: Uniaxial compression test

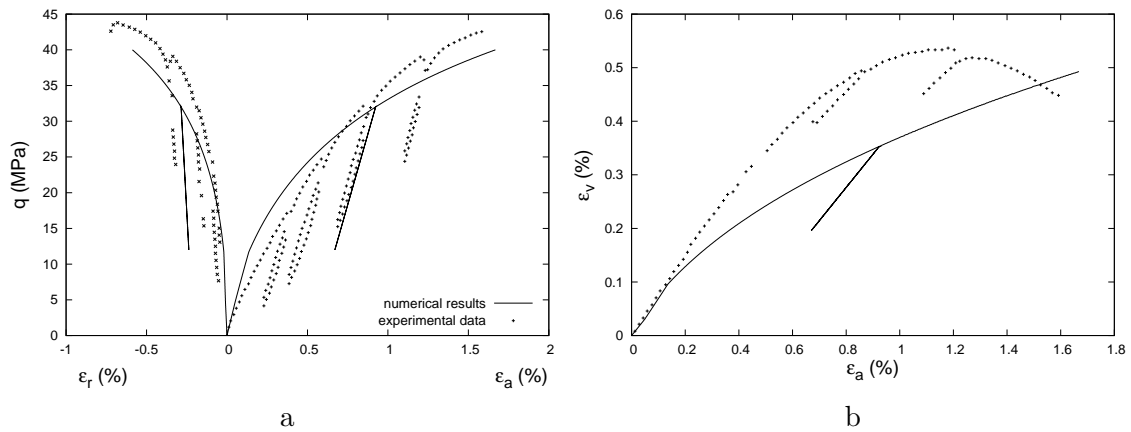


Fig. 6.6: Triaxial compression test - confinement 5 MPa

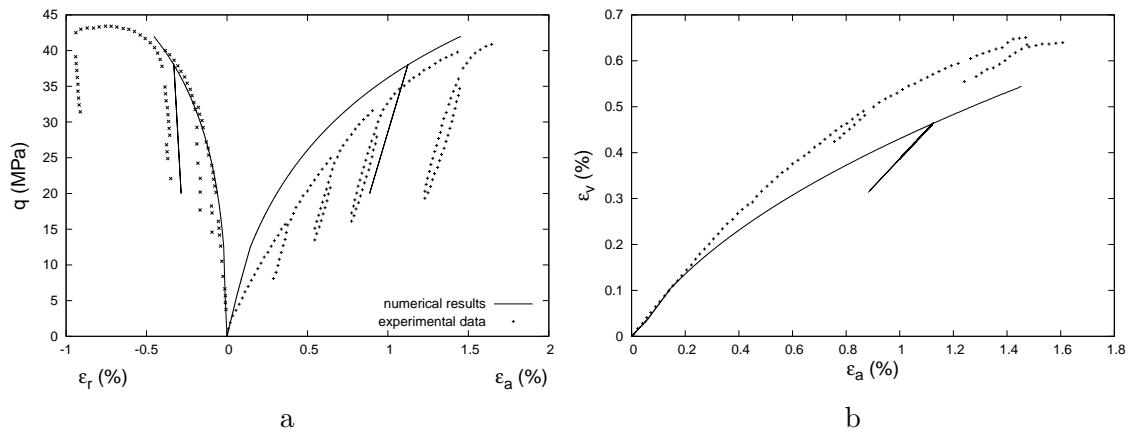


Fig. 6.7: Triaxial compression test - confinement 10 MPa

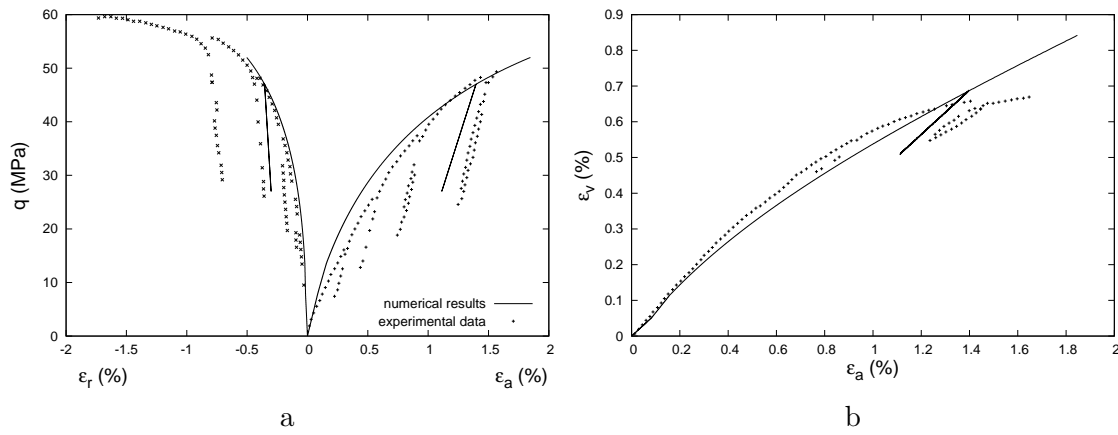


Fig. 6.8: Triaxial compression test - confinement 20 MPa

Figure 6.9 shows the stress-strain curves obtained for the different confining pressures. The corresponding effective stress paths can be seen on figure 6.10. It can be seen that, since the initial elastic domain is small and the onset of plastic yielding is similar for every cases, the main parameter controlling the influence of initial confining pressure on the stress-strain behaviour is the position of the critical state line.

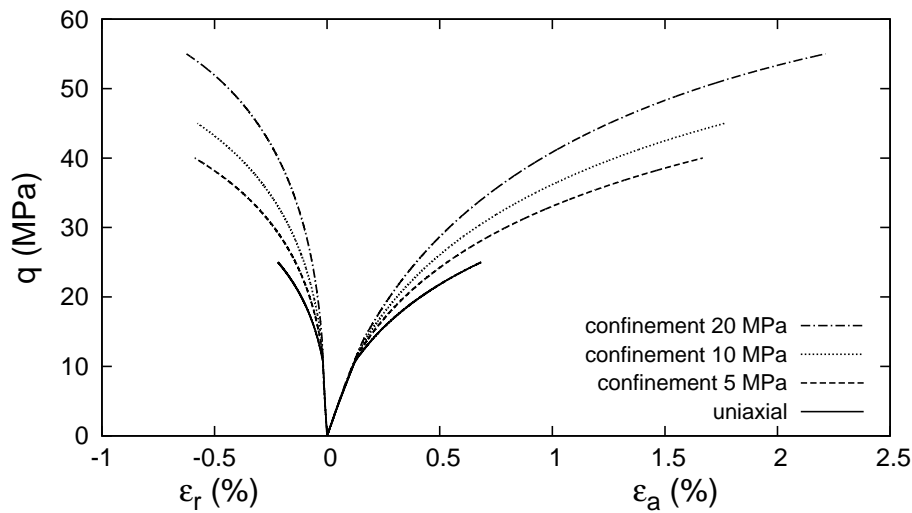


Fig. 6.9: Stress-strain curves for different confining pressures

The evolution of damage with the total deviatoric stress is given in figure 6.11. The confining pressure determines for which value of the deviatoric stress damage initiates. Afterwards, damage evolution is driven by the increase in deviatoric stress, independently of the value of the confining pressure.

The resulting degradation of elastic properties with radial strains is given in figure 6.12. The experimental Young's (E_L) and radial (E_R) moduli have been evaluated from the slopes of unloading-reloading cycles (Chiarelli et al., 2003).

Since we consider a constant Poisson's ratio, the degradation of Young's and radial moduli are the same in our model: $R = \frac{E_L}{E_{L0}} = \frac{E_R}{E_{R0}}$.

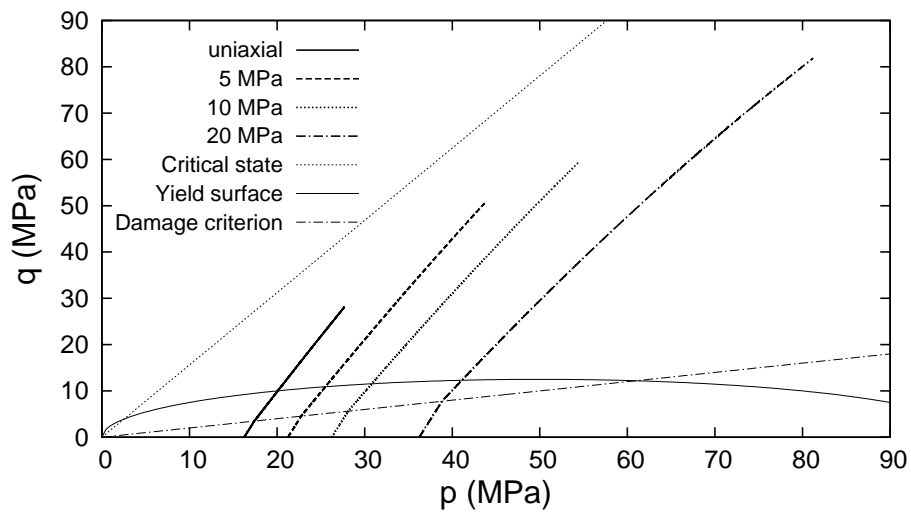


Fig. 6.10: Effective stress paths

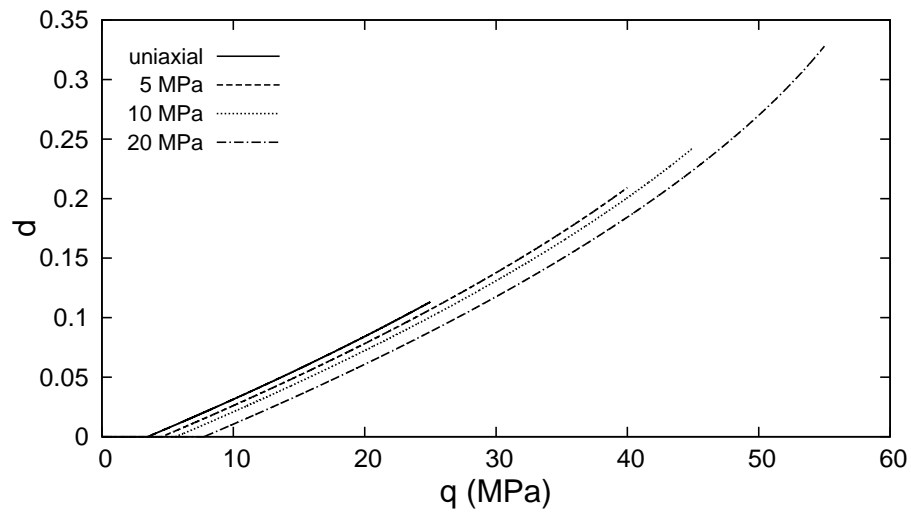


Fig. 6.11: Damage evolution with deviatoric stress

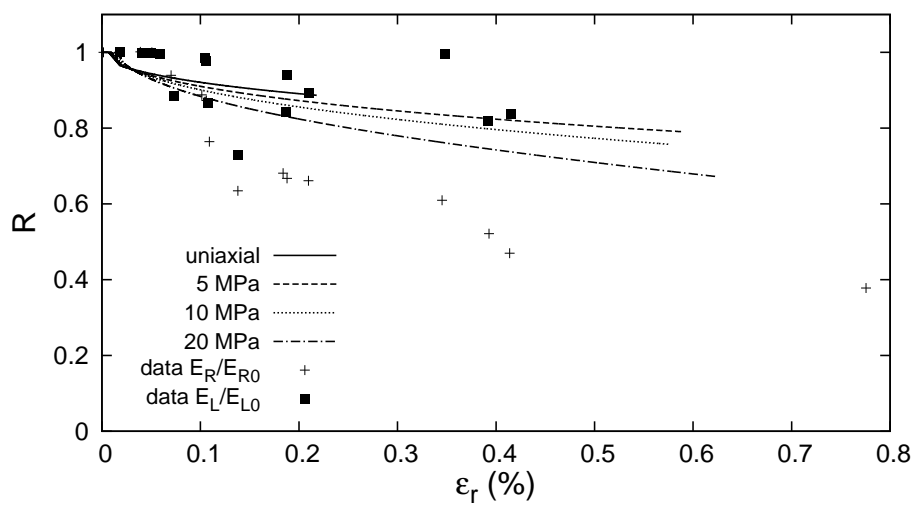


Fig. 6.12: Evolution of apparent bulk modulus with axial strains

The computed Young's modulus degradation is in the same value range as the measured one and follows the same trend. However, due to the important scatter in experimental results, it can not really serve as a quantitative validation. Concerning the radial modulus variation, the computed values are smaller than the experimental data. The shape of the curve remains however similar. It appears that radial and axial stiffnesses evolve differently during the triaxial test. Our damage model should therefore be refined, either by considering an anisotropic damage variable, or, as do Shao et al. (2006), by considering that hydrostatic and deviatoric stresses are affected differently by damage.

Proportional compression tests: The simulation of three proportional loading tests are represented on figure 6.13. In these tests, axial and lateral stresses are simultaneously increased with a constant ratio ($\sigma_3 = k\sigma_1$).

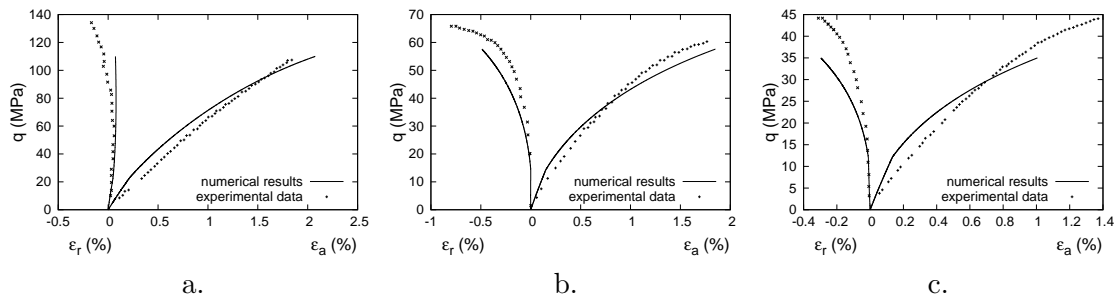


Fig. 6.13: Proportional compression tests (a. $k = 2$, b. $k = 5$, c. $k = 10$)

Lateral extension tests: Figure 6.14 shows the simulation of lateral extension tests for two initial confinements of 30 MPa and 60 MPa. The lateral stress σ_1 is then decreased while keeping the axial stress σ_3 constant. Experimental data and numerical simulation results are in good agreement at the beginning of the test, and start to diverge when the lateral stress reaches one third of its initial value. The effective stress path is given in figure 6.15. At the end of the test, the stress state lies very close to the critical state line, which is most likely the cause of the high plastic strains observed. Figure 6.16 gives the evolution of damage as a function of the lateral stress. Good agreement with this test is as important as with triaxial compression test, since the stress path followed during tunnel excavation is closer to the one followed during a lateral extension test than to the one due to a triaxial compression test.

Effect of water content on mechanical behaviour

Figure 6.17 shows the stress-strain curves simulated for three water contents for a confining pressure of 20 MPa. Although numerical results do not agree perfectly with experimental data, the effect of suction on the mechanical behaviour is similar. Suction acts on the material by adding the component $S_l s$ to the confining pressure.

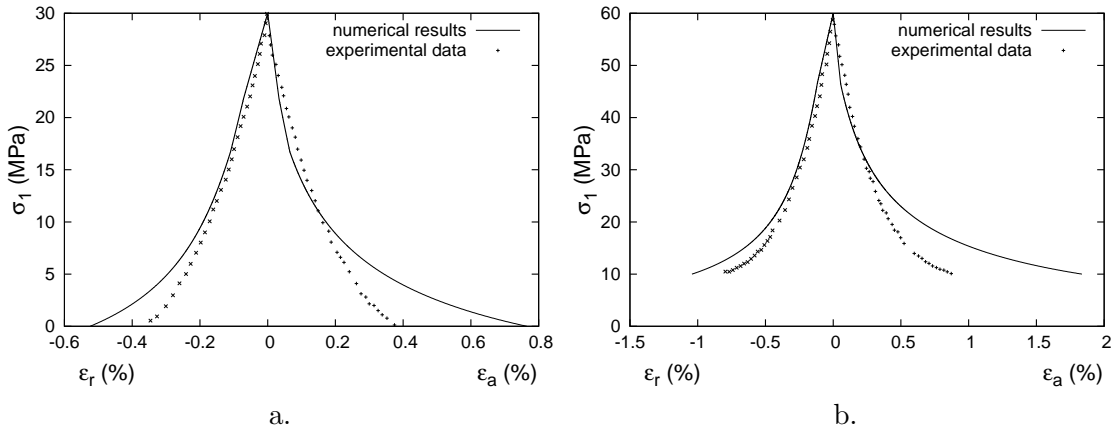


Fig. 6.14: Lateral extension tests (a. $p_c = 30\text{MPa}$, b. $p_c = 60\text{MPa}$)

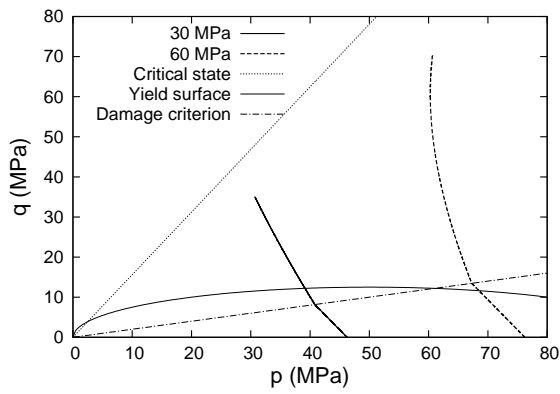


Fig. 6.15: Effective stress paths for the lateral extension tests

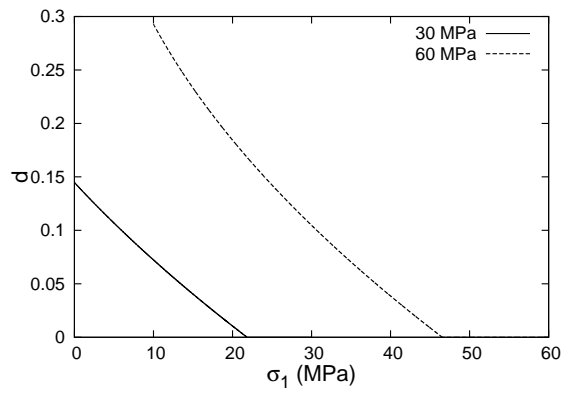


Fig. 6.16: Damage evolution as a function of radial stress

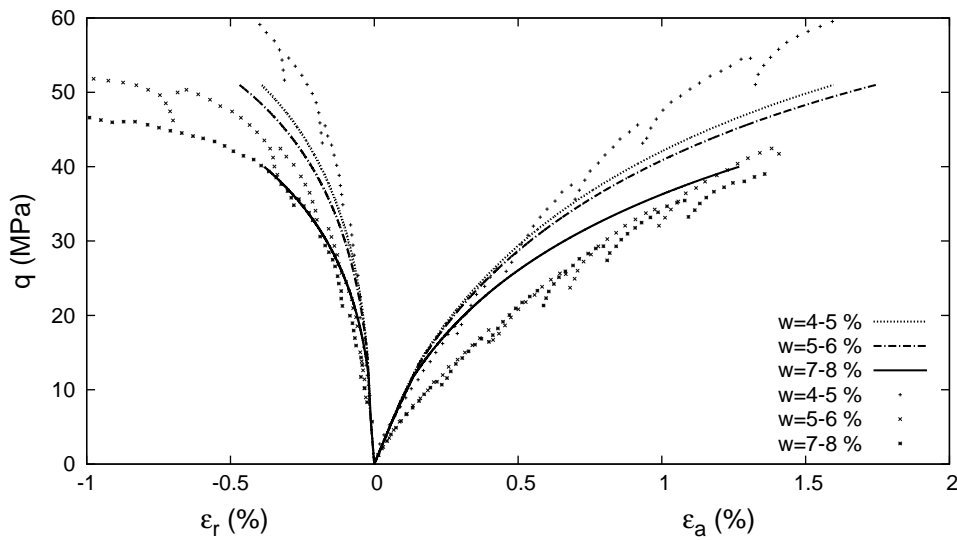


Fig. 6.17: Stress-strain curves for different water contents (confining pressure: 20 MPa)

6.1.3 Effect of damage hardening parameter

During a triaxial test, the rate of damage evolution is given by

$$\Delta d = \left(1 - \frac{C_2}{3}\right) \frac{\Delta q}{C_1} \quad (6.5)$$

C_1 is therefore the parameter controlling damage evolution rate. The lower C_1 , the higher the increment of damage for a given stress increment.

The simulation of the triaxial compression test for a confinement of 20 MPa has been repeated for three values of C_1 (100, 150, 200). The stress-strain curves are represented in figure 6.18, the evolution of damage with deviatoric stress in figure 6.19 and the degradation of the bulk modulus in figure 6.20.

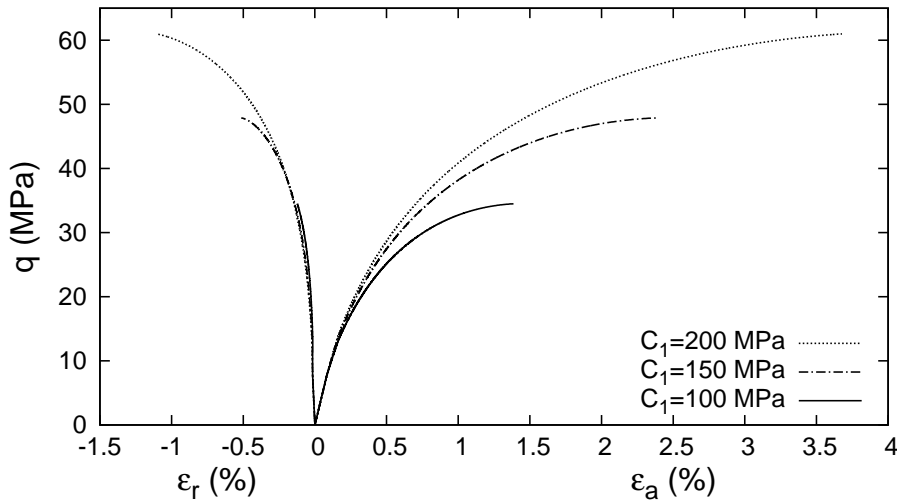


Fig. 6.18: Stress-strain curves for different values of C_1

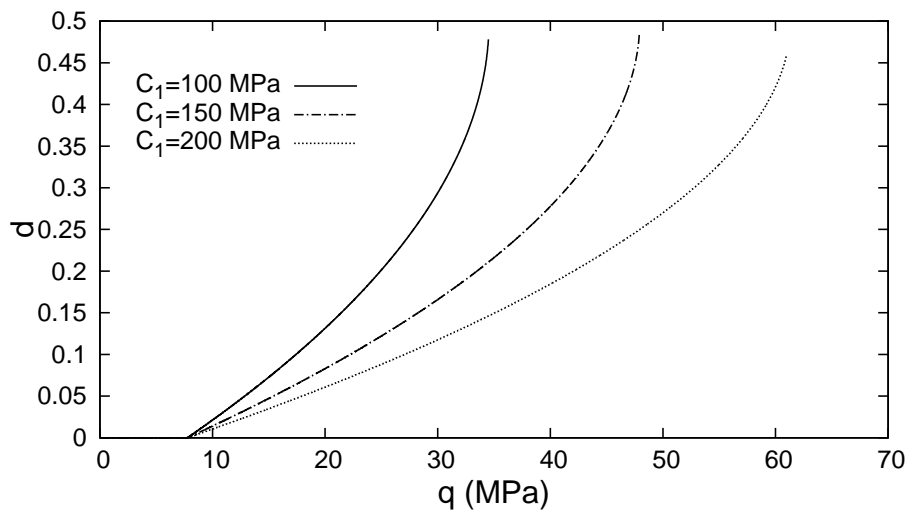


Fig. 6.19: Damage evolution for different values of C_1

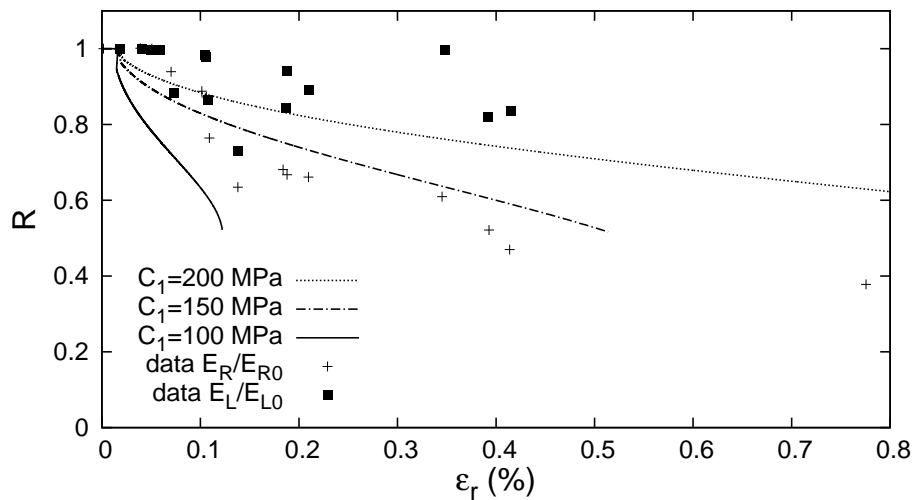


Fig. 6.20: Bulk modulus degradation for different values of C_1

Choosing a low value for C_1 enables the simulation of a quicker rigidity degradation with radial strains. However, when damage reaches 50 %, the behaviour switches from an apparent hardening behaviour to an apparent softening behaviour, which under increasing deviatoric stress leads to failure. In the case of linear elasticity, with the principle of strain equivalence, the final apparent elastic moduli just before failure are equal to 50 % of their initial values. With the hypothesis of equivalent elastic energy, for 50 % of damage, the ratio R would be equal to $R = 0.5^2 = 25\%$. However, the coupling between damage and plasticity would necessitate another strategy.

At this point, the limited amount of experimental data and their scattering do not allow to conclude whether or not the moduli degradation obtained with the principle of strain equivalence is satisfactory. It should also be highlighted that the damage hardening parameter C_1 has an impact on both the rigidities degradation and the stress-strain behaviour. A compromise has to be made when choosing C_1 to correctly reproduce both.

6.2 Boom Clay

Boom Clay has been selected as a possible host rock for deep radioactive waste disposal in Belgium. It has therefore been extensively studied either from experiments on undisturbed natural samples, or on samples prepared by compaction from Boom clay powder. Many experimental data on saturated natural Boom clay are available in the literature (Horseman et al., 1987; Baldi et al., 1991; Coll, 2005; Sultan et al., 2010). However, concerning the unsaturated behaviour, most of the studies have been made on compacted (Bernier et al., 1997; Romero, 1999) or remoulded (Al-Mukhtar et al., 1996) samples, and only a few on undisturbed samples (Cui et al., 2007; Della Vecchia et al., 2011). Moreover, these mechanical tests at different suctions are limited to oedometer and isotropic compression tests. By comparing experiments on natural and compacted samples, Della Vecchia et al. (2011) concluded that the same constitutive framework seems to be applicable to natural Boom clay and to the material compacted from the clay powder. However, the mechanical

parameters have to be adapted to reflect the different microstructure.

Boom clay is considered as an overconsolidated plastic clay. Although no data are available on rigidity degradation, the existence of an Excavation damaged Zone around excavations has been revealed. Excavation induced fractures are observed around galleries (Bastiaens et al., 2007; Bernier et al., 2007; Van Marcke and Bastiaens, 2010). Damage has also been assessed by seismic (Bastiaens et al., 2007) and acoustic (Lavrov et al., 2002) measurements. Boom clay can exhibit both ductile and brittle behaviours (Dehandschutter et al., 2005). The transition between the failure modes depends strongly on the confining pressure and is also influenced by the water content (Al-Shayea, 2001) and by the overconsolidation ratio.

Since all the available data comes from samples of diverse provenance, and that Boom clay parameters vary depending on the coring depth and the mineralogy, we will choose parameters in the range of the ones found in the literature and simulate typical experiments to show that our model is able to reproduce the main trends. However, we do not expect perfect agreement with experimental data coming from different laboratories with a single set of parameters.

6.2.1 Model parameters

Mechanical properties

Elastic, plastic and damage parameters chosen in this study are summarised in table 6.4. The pressure exponent is taken equal to 0.6. Due to the modifications of volumetric compression laws (equations 2.24 and 3.60) to incorporated hyperelasticity with an exponent non equal to 1, the parameters κ and λ take values different from the one usually found in the literature. It also has an impact on the values of the parameters of the Loading-Collapse curve.

Elasticity				Plasticity			LC curve			Damage		
n	p_r	κ	ν	M	λ_0	ζ	p_r	β	r	C_0	C_1	C_2
	MPa						MPa	MPa ⁻¹		MPa	MPa	
0.6	0.1	0.0075	0.15	0.8	0.00755	1.5	0.1	0.5	0.998	0	25	0.3

Table 6.4: Material mechanical parameters

Hydraulic properties:

Water retention properties are chosen to obtain an average of the drying and wetting curves given by Della Vecchia et al. (2011). Van Genuchten parameters are given in table 6.5. The water retention curve as well as the suction stress component (S_{1s}) are represented in figure 6.21.

α_{vg} (MPa ⁻¹)	n_{vg}	m_{vg}	S_r
0.28	2.3	0.21	0

Table 6.5: Retention parameters

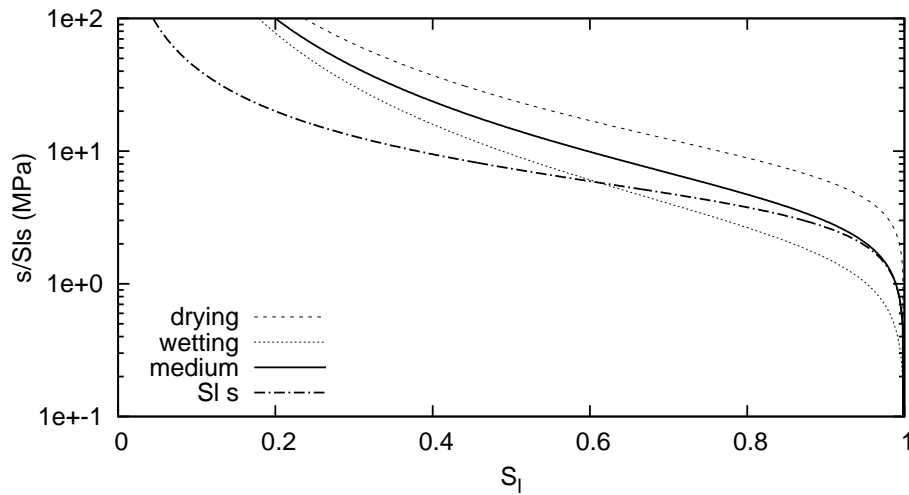


Fig. 6.21: Water retention curve and S_1s component of effective stress for Boom clay

6.2.2 Simulation of mechanical laboratory tests

In the following examples, the preconsolidation pressure is taken equal to 5.5 MPa.

Isotropic compression test: Figure 6.22 shows the simulation of an isotropic compression test with comparison to experimental results from Baldi et al. (1991). The tests consist in drained isotropic cycles starting from 2 MPa of effective isotropic stress up to a maximum of 8 MPa. Back pressure value is 2 MPa. Two different measures of volumetric strains are made, one by calculating three times the vertical strain ($\varepsilon_v = 3\varepsilon_1$), the other one obtained from water displaced from the specimen ($\varepsilon_v = \Delta V_w$).

The different volumetric strains given by the two types of measures makes it difficult to draw conclusions about the quality of our simulations.

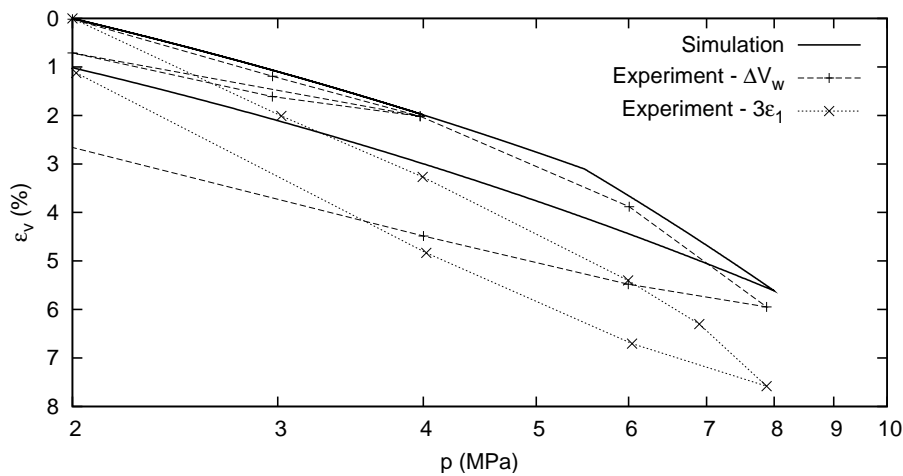


Fig. 6.22: Isotropic compression test (test TBOOM1 from Baldi et al. (1991))

Oedometer tests: Figure 6.23 shows the simulation of an oedometer test in saturated conditions with comparison to the experimental data of Horseman et al. (1987). The agreement is quite good, although the slope of unloading-reloading curves shows that the loss of rigidity is underestimated.

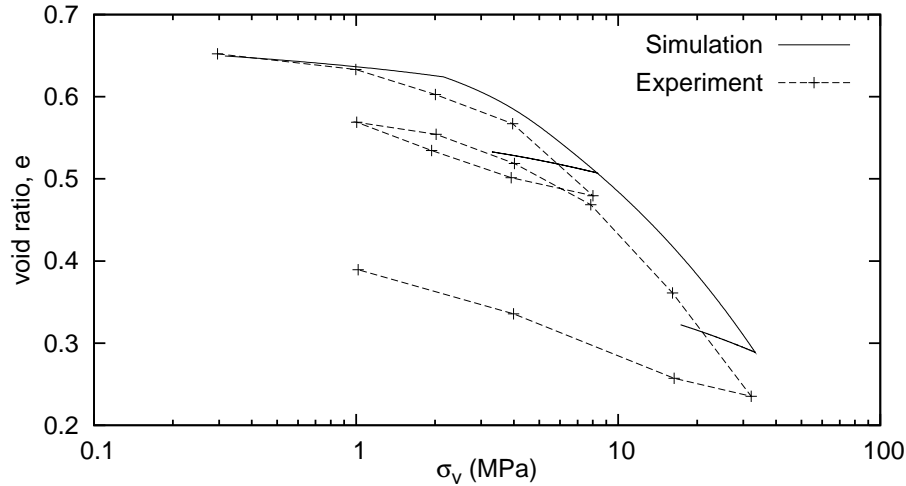


Fig. 6.23: Oedometer test (from Horseman et al. (1987))

Figure 6.24 shows the simulation of a test which experimental results come from Della Vecchia et al. (2011). A soil sample, initially at a suction of 3 MPa, is compressed under undrained conditions up to a vertical stress of 3 MPa, and later put in contact with water. The sample is then compressed up to 8 MPa, under drained conditions, and finally unloaded.

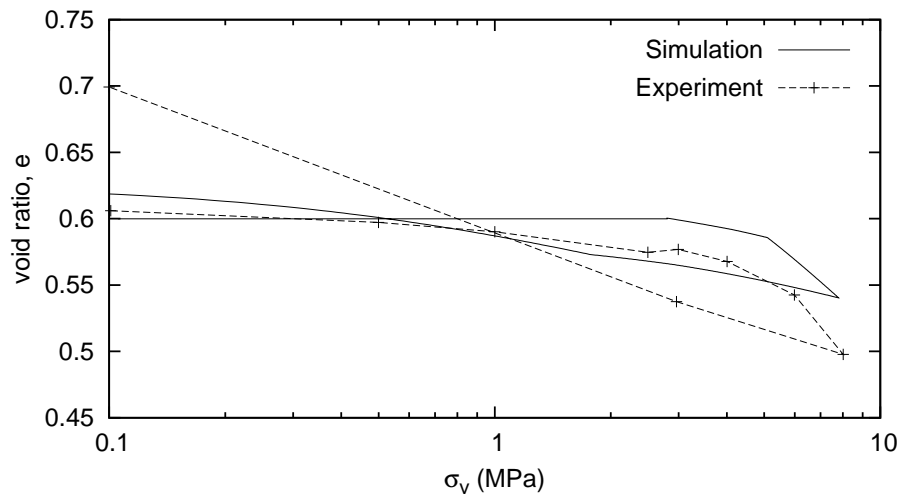


Fig. 6.24: Oedometer test (from Della Vecchia et al. (2011))

We can see that numerical results give no volume change during the undrained loading part, contrary to the experimental results. It may be due to water leakage during the experiment, otherwise it means that we could improve our model by considering soil particles compressibility (or a higher water compressibility). The main behaviour trends

are otherwise well represented, the swelling occurring during unloading being present, although underestimated.

Drained triaxial compression tests: Triaxial drained compression tests with unloading-reloading cycles are simulated for three confining pressures (2 MPa, 3 MPa, 4 MPa). The comparison of computed stress-strain curves (a) and volumetric strains (b) with experimental data are represented on figures 6.25 to 6.27.

The agreement between computed and experimental stress-strain curves is quite good. However, the model does not capture well the smooth transition between elastic and plastic behaviour. This behaviour could be improved by using more advanced versions of the Cam-Clay model, such as bounding surface plasticity (Dafalias, 1986) or continuous hyperplasticity (Puzrin and Housby, 2001).

The plot of the volumetric strains versus axial strains shows a satisfactory agreement between experimental and numerical results. Since damage tends to predict large volumetric strains compared to experimental data, the non-associativity parameter ζ has been chosen equal to 1.5 to increase the deviatoric strains predicted by the plasticity model.

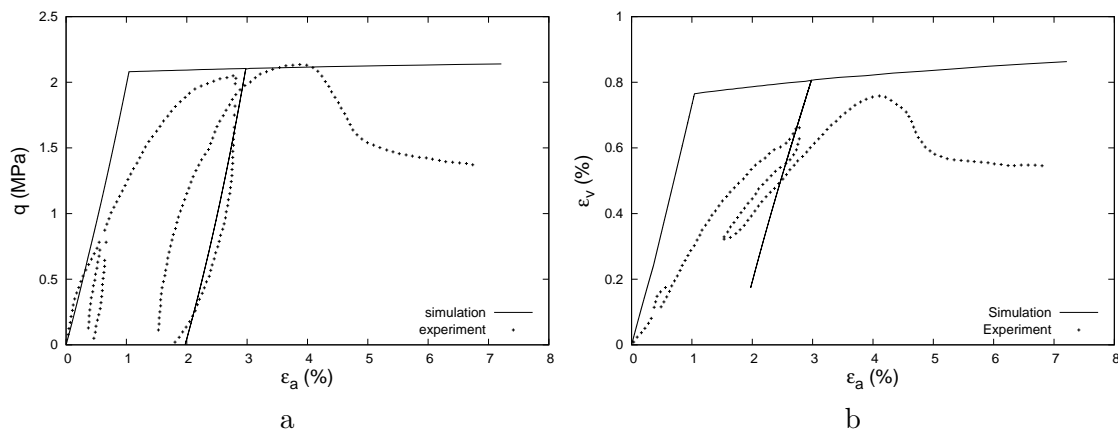


Fig. 6.25: Confinement 2 MPa (Test TBOOM2 from Baldi et al. (1991))

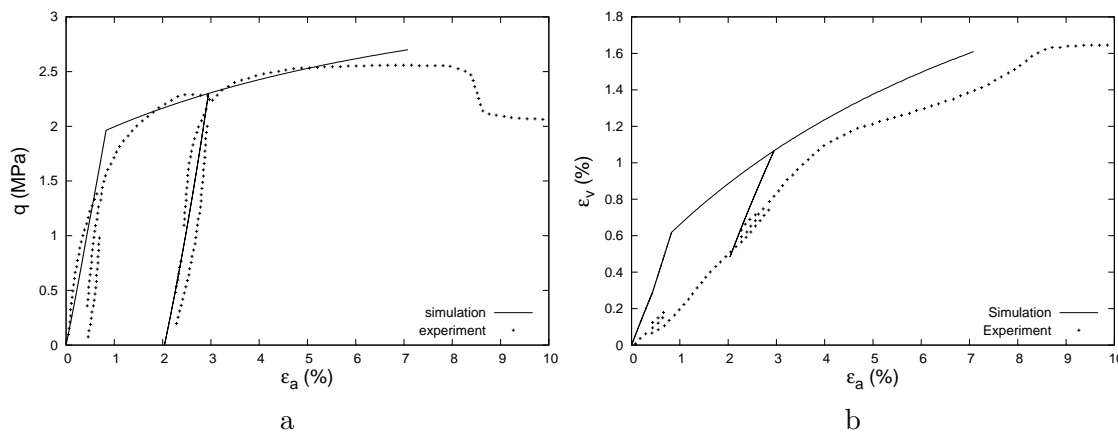


Fig. 6.26: Confinement 3 MPa (Test TBOOM3 from Baldi et al. (1991))

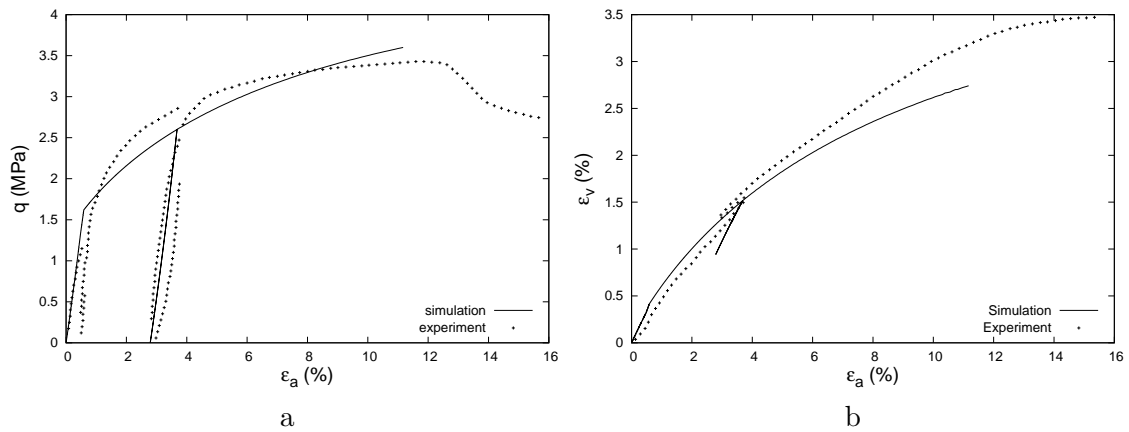


Fig. 6.27: Confinement 4 MPa (Test TBOOM4 from Baldi et al. (1991))

Figure 6.28 shows the stress-strain curves obtained for the different confining pressures. The corresponding effective stress paths can be seen on figure 6.29. The evolution of damage with the total deviatoric stress is given in figure 6.30. It can be seen that failure is mainly due to the plasticity phenomenon, since the effective stress path reaches the critical state before damage attains the critical 50 % value. When the confining pressure increases, it is possible to get more plastic strains before failure, the behaviour is more ductile. For low confining pressures, although the damage value is smaller, the combination of damage with the critical state model leads to less plastic strains before failure, i.e. a more brittle behaviour.

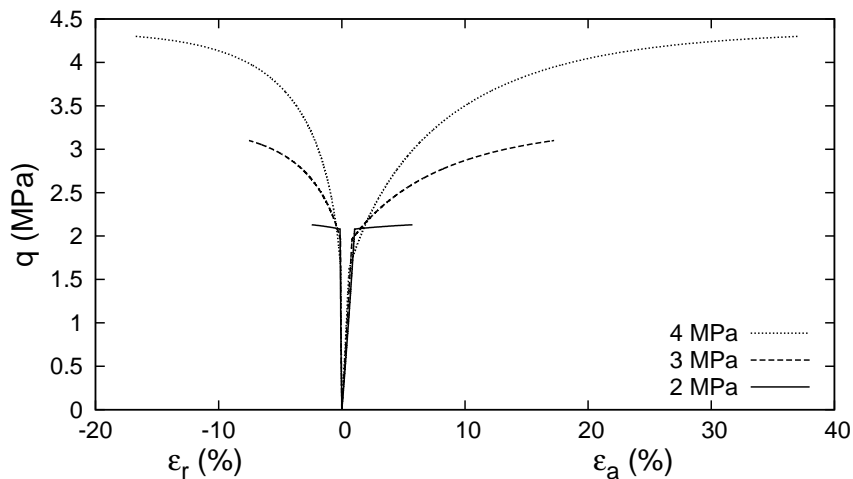


Fig. 6.28: Stress-strain curves for different confining pressures

The resulting degradation of elastic properties with radial strains is given in figure 6.31. The predicted rigidity loss is low, around 10 % at its maximum. Due to the lack of experimental data, it is hard to say whether the principle of strain equivalence is acceptable in this case. However, the slopes of the unloading-reloading curves in figures 6.25 to 6.27 seem to be in good agreement with experiments. It is interesting to note that equation 2.38 gives a maximum possible loss of rigidity, for 50 % of damage, equal to $1 - R = 1 - (1 - d)^{(1-n)} = 1 - 0.5^{0.4} = 24,2\%$.

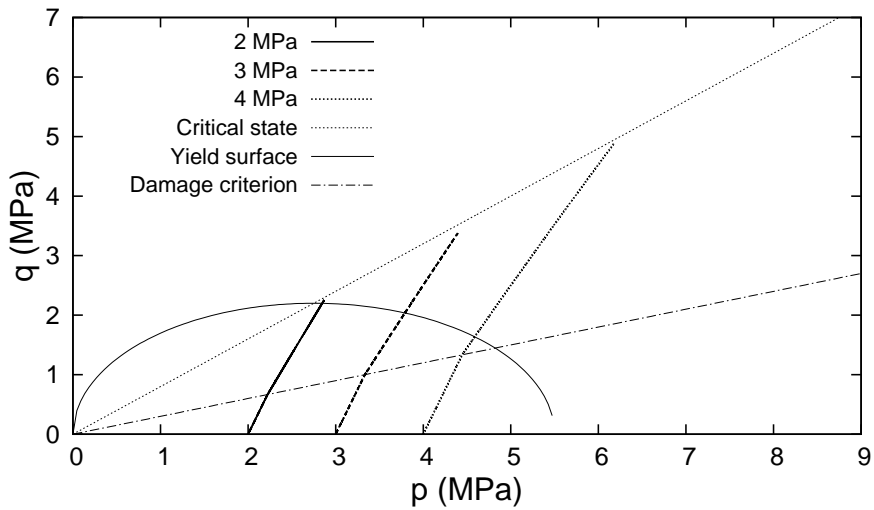


Fig. 6.29: Effective stress paths

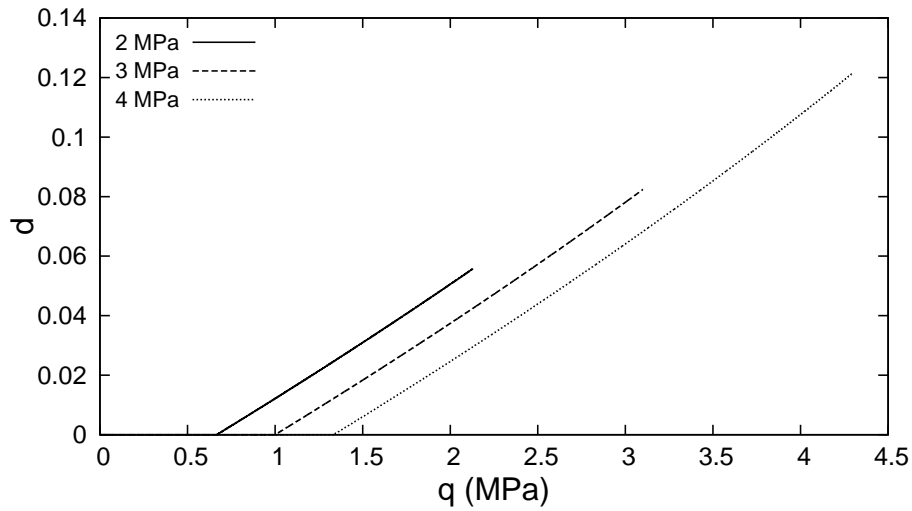


Fig. 6.30: Damage evolution with deviatoric stress

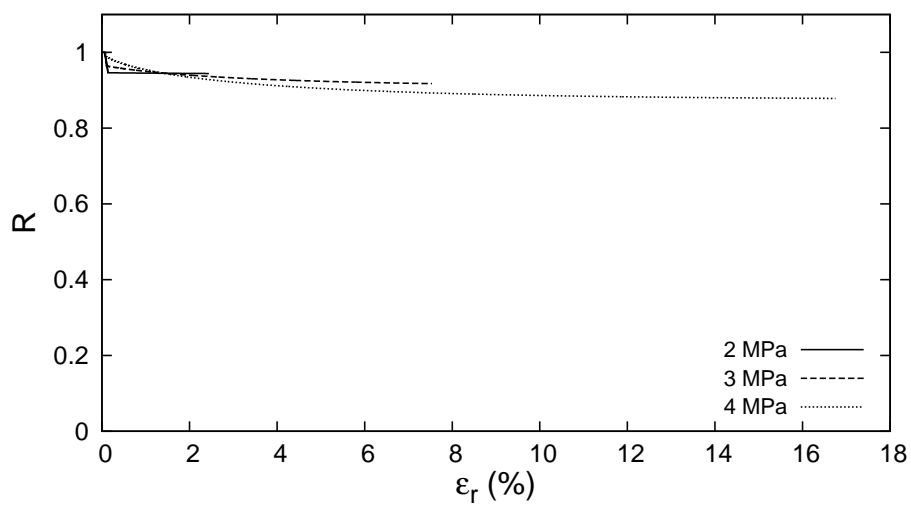


Fig. 6.31: Evolution of apparent bulk modulus with axial strains

6.2.3 Suction effects on mechanical behaviour

Although no experimental data have been found in the literature about Boom clay, Al-Shayea (2001) showed that materials with high clay content exhibit a ductile/brittle behaviour transition when their water content decreases (see figure 6.32).

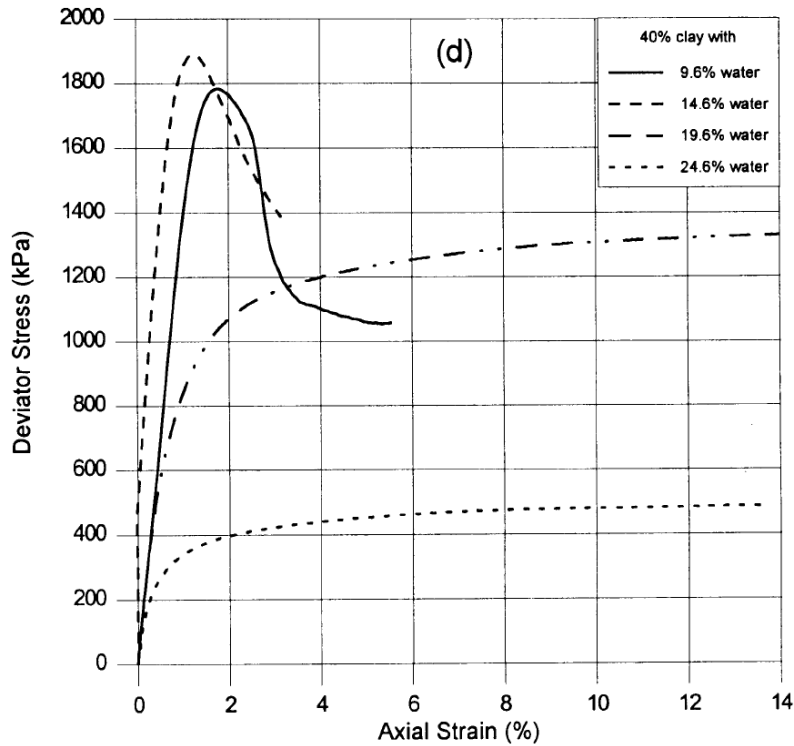


Fig. 6.32: Stress-strain behaviour at different moisture contents (from Al-Shayea (2001))

Ductile behaviour is characterised by the ability to sustain large plastic strains during plastic hardening. Brittle behaviour is characterised by abrupt failure at a well-defined peak strength with strong softening. Figure 6.32 also shows higher shear strength for low water contents.

Simulations of triaxial compression tests are made for different constant suctions (0 MPa, 2 MPa and 6 MPa). The shape of the LC curve corresponding to the chosen parameters is given in figure 6.33.

The stress-strain curves obtained for different suctions are given in figure 6.34. The corresponding effective stress paths can be seen on figure 6.35. The evolution of damage with deviatoric stress is given in figure 6.36.

The ductile/brittle transition linked to the increase of suction is well reproduced. At low suction, large plastic strains occur and damage remains low. At higher suctions, shear strength is higher and the peak stress is attained for lower plastic strains and higher values of the damage parameter. This is due, partly to the shift in the stress path due to the increase in effective stress, and also to the increase of the elastic domain with suction.

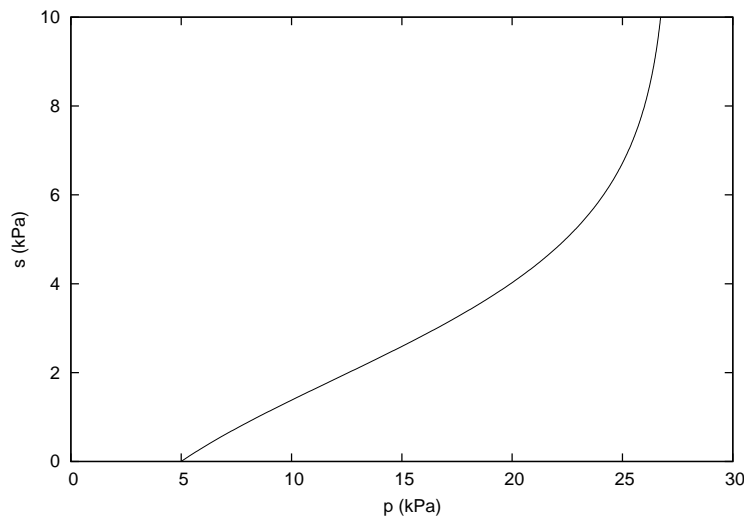


Fig. 6.33: Loading-Collapse curve

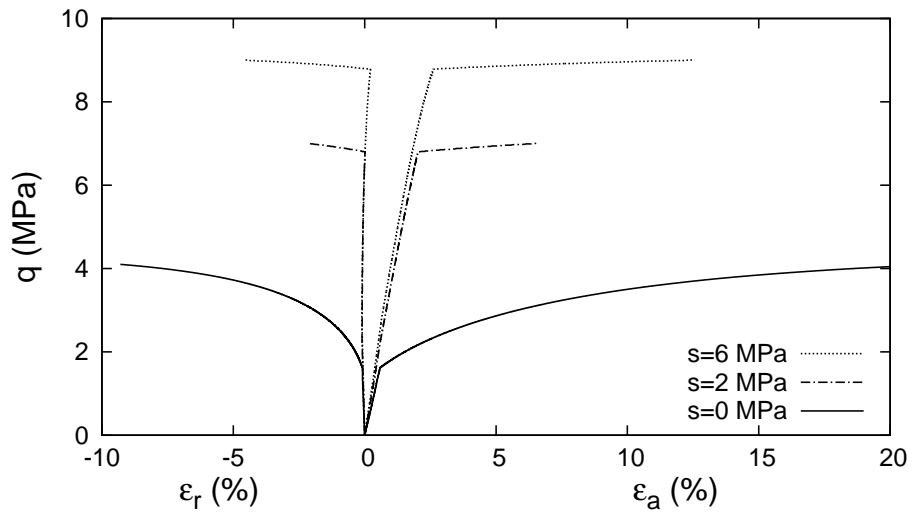


Fig. 6.34: Stress-strain curves for different suctions

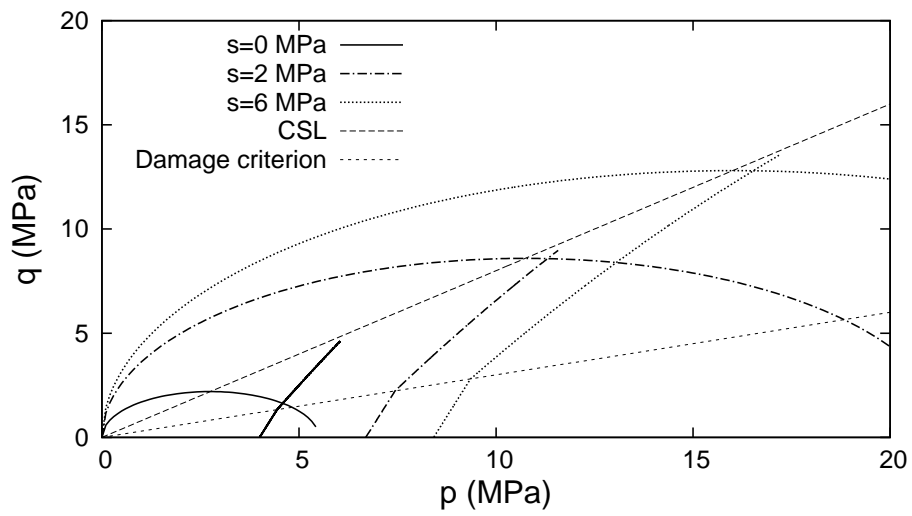


Fig. 6.35: Effective stress paths

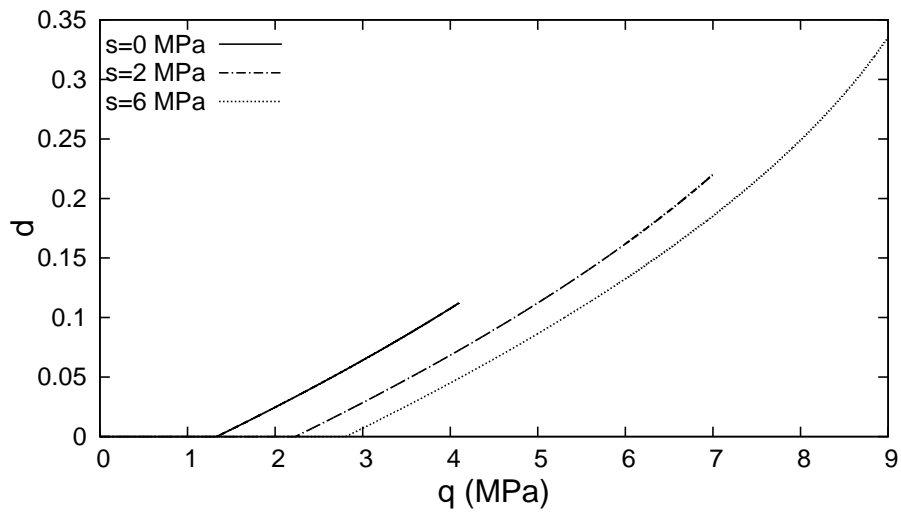


Fig. 6.36: Damage evolution with deviatoric stress

6.3 Conclusion

Simulations of mechanical laboratory tests at different suctions on Callovo-Oxfordian argillite and on Boom clay have shown that the framework developed in sections 1 to 3 enables the reproduction of the main features of the hydro-mechanical behaviour of both indurated and plastic clays. The flexibility of the theoretical and numerical frameworks enables modifications of damage and plasticity laws to fit to experimental behaviour features specific to each material.

CHAPTER 7

APPLICATION TO FULLY-COUPLED HYDRO-MECHANICAL PROBLEMS

This chapter presents illustrative applications of the constitutive modelling framework to fully-coupled hydro-mechanical problems. First, damage induced by hydric loading is simulated, assuming that it is due to differential shrinkage in low permeable media. Then, plastic and damage zones induced by excavation are studied, first at different suctions under drained conditions, then under undrained conditions.

Ce chapitre présente des applications illustrant les capacités du modèle proposé. Premièrement, l'endommagement induit par un chargement hydrique est simulé, en supposant que celui-ci est dû à la contraction hétérogène des milieux peu perméables. Ensuite, les zones plastiques et endommagées dues à l'excavation sont étudiées, premièrement à différentes suctions en considérant des conditions drainées, puis en conditions non drainées.

Contents

7.1	Damage induced by hydric loading	112
7.1.1	Material parameters	113
7.1.2	Geometry and boundary conditions	114
7.1.3	Desiccation	115
7.1.4	Humidification	117
7.2	Excavation modelling	120
7.2.1	Impact of suction on the extent and properties of the excavation damaged zone	120
7.2.2	Simulation of excavation under undrained conditions	125

Accurate excavation modelling is of a great importance in contexts such as tunnelling, mining, or radioactive waste disposal. Coupled hydro-mechanical phenomena have to be taken into account during the different phases of the excavation process. Due to the stress redistribution and the resulting convergence during the initial excavation stage, micro- and macro-fracturing is likely to appear in the surrounding rock. Depending on the type of rock and its permeability, either drained or undrained behaviours can be considered. The following tunnel ventilation dehydrates the rock around the opening. This desaturation tends to strengthen the rock, but, since strains are constrained, can also cause induced fractures and micro-cracks. Although beyond the scope of this thesis, other processes such as heating and long term behaviour (creep, self-sealing, self-healing) have to be taken into account in the context of radioactive waste disposal. A summary of the different processes to consider for different rock types is presented in the paper of Tsang et al. (2005).

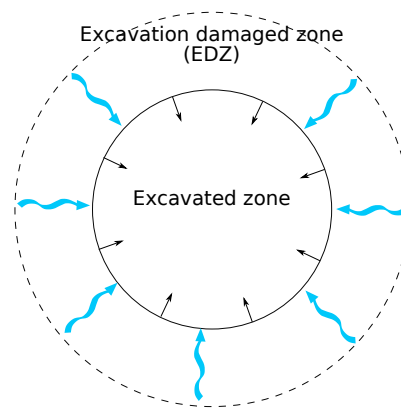


Fig. 7.1: Processes leading to the creation of the Excavation Damaged Zone

Since a validation of our model behaviour under mechanical loading has been made in the previous chapter, the first section of this chapter will deal with purely hydric loading.

7.1 Damage induced by hydric loading

Under natural environmental conditions, evaporation tends to remove water from geomaterials, such as soil or concrete, and thus makes them shrink. If deformation is constrained, cracks may therefore appear.

Understanding how cracks and damage are created in drying geomaterials is of interest in geotechnical engineering applications, in agricultural science and in concrete technology. Although many research works have proposed explanations for the formation of these cracks, no consensus has yet been reached. The work presented here deals with damage, i.e. micro-cracks. However, the mechanisms of damage initiation are similar to the ones leading to macro-cracks.

Desiccating soils with constrained deformations leads to tensile total stresses. The most common approach is therefore to assume a tensile strength determining the onset of cracking. However, the constitutive model presented previously is based on the assumption that the damage criterion is expressed in terms of the double effective stress. This double

effective stress, when suction increases, always remains positive, even under constrained conditions, and desiccation results in an increase of the compressive stress applied on the solid skeleton. A possible alternative could be to consider a tensile strength dependent on suction and becoming positive when suction increases. Péron (2008) proposed the following form for the tensile strength as a function of suction and the tensile strength in saturated conditions: $\sigma_t^* = \sigma_t^{sat} + k_2 \left[1 - \exp\left(-\frac{k_1 s}{k_2}\right) \right]$.

Another process advanced to explain desiccation cracks is the air invasion of the largest pores. The air-water interface membrane then pushes particles away from the invaded pore, which creates a crack (Shin and Santamarina, 2011). Others highlight the role of heterogeneities in cracks initiation (Lagier et al., 2011).

Wang (2012) observed microcracking in argillites due to desiccation, and less intuitively, to humidification (figures 7.2 and 7.3).

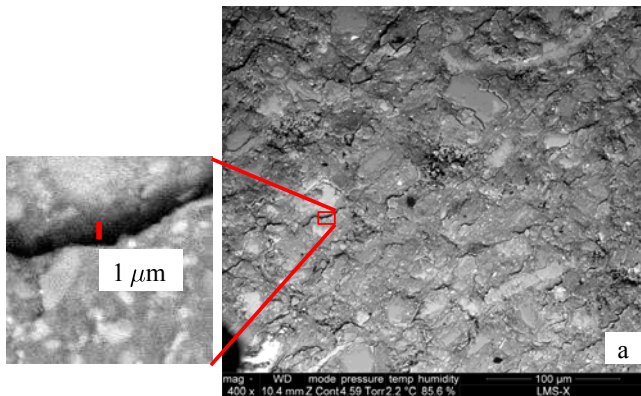


Fig. 7.2: Microcracking due to humidification from 65 to 90 % RH (from Wang (2012))

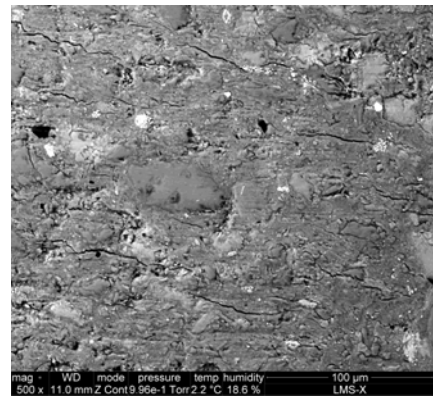


Fig. 7.3: Microcracking due to desiccation from 65 to 20 % RH

He observed that the onset of microcracking occurs during the loading stage and is strongly controlled by humidification or desiccation rate. This microcracking seems therefore to be linked to moisture gradients induced by fast humidification/desiccation when the loading rate doesn't allow pressures to dissipate. Damage due to humidification has also been observed by Valès (2008).

In the following, we will study how moisture gradients affect the stress state in an homogeneous porous media and may lead to damage initiation. Studies considering damage due to differential shrinkage usually find that microcracks are localised at the surface in contact with the atmosphere (de Sa et al., 2008; Jia et al., 2009).

7.1.1 Material parameters

The mechanical parameters are the ones of the Callovo-Oxfordian argillite studied in chapter 6.1. They are summarised in table 7.1. Dissipation is supposed to be due to damage only and plasticity is ignored.

Fluid transfers are taken into account in this study. The permeability functions chosen as well as their parameters values are given in table 7.3.

The initial porosity is taken equal to 15 %.

Elasticity		Damage		
K	ν	C_0	C_1	C_2
GPa		MPa	MPa	
5	0.19	0	200	0.2

Table 7.1: Material mechanical parameters

α_{vg} (MPa ⁻¹)	n_{vg}	m_{vg}	S_r
0.04	1.5	0.55	0

Table 7.2: Retention parameters

Intrinsic permeability	$K_{int}(\phi) = K_{w0} \frac{\phi^3}{(1-\phi)^2} \frac{(1-\phi_0)^2}{\phi_0^3}$	$K_{w0} = 1.10^{-15} \text{ m.s}^{-1}$ $\phi_0 = 15\%$
Relative permeability	$k_r(S_l) = \left(\frac{S_l - S_r}{1 - S_r} \right)^m$	$m = 3$

Table 7.3: Hydraulic functions and parameters

7.1.2 Geometry and boundary conditions

In the following, we simulate the desiccation and the humidification of a cylindric sample of 36 mm diameter and 72 mm height. No external displacement boundary conditions are imposed. The sample is therefore free to shrink and only differential shrinkage due to the heterogeneity of the pressure field is considered. Since the problem is axisymmetric, only one quarter of the sample is meshed (see figure 7.4).

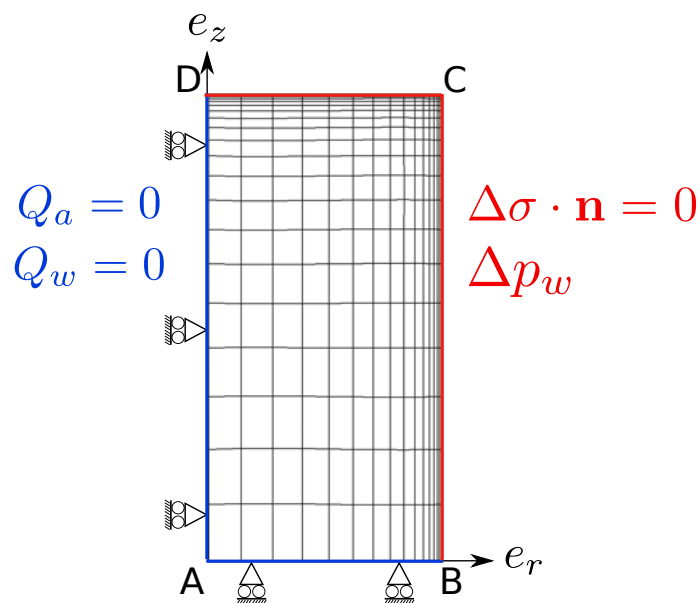


Fig. 7.4: Geometry of the problem

Displacements along e_r direction are set equal to zero on AD axis, and displacements along e_z direction are set equal to zero on surface AB. The fluid fluxes are null on these surfaces.

A water pressure will be applied on surfaces BC and CD, the normal total stress remaining constant. The air pressure takes a constant null value in the whole specimen.

7.1.3 Desiccation

The initial suction is set equal to 2 MPa and increased up to 20 MPa at the sample surface at a rate of 0.2 MPa/min (which corresponds approximatively to 0.1% RH/min).

Figure 7.5 shows the water pressure field at four time steps. Time $t=1h30$ corresponds to the moment at which the total increment of suction has been applied. It can be noticed that, due the high loading rate combined with the low permeability of the material, fluid pressures have not yet had time to equilibrate at that time. The likelihood of induced damage is therefore at its maximum for the given suction increase. We can even notice the appearance of overpressures at the sample core, certainly due to the compression exerted by the external ring which already started to desaturate. The spatial evolution of the total stress components at this time step along line AB are given in figure 7.6. It is verified that this pressure field induces compression at the sample core and traction at its surface. Water evaporates from the soil sample during the following time steps, until pressure equilibrium is reached around $t=10h$.

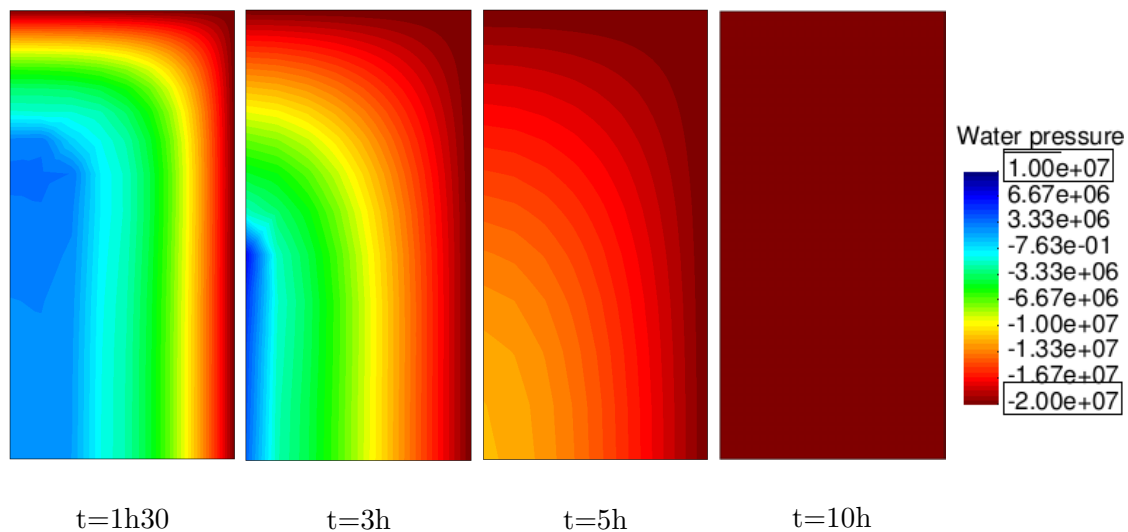


Fig. 7.5: Water pressure field evolution with time

The damage pattern at the end of the test is given in figure 7.7. Most of the damage is concentrated in the few millimetres near the surface of the sample with its highest values far from the sample free extremities. Damage is maximum at the center of the top surface, for which strain constraints are higher. However, the sample core also suffers non negligible damage, which is due to the overpressures appearing at the beginning of the test.

In the following, we will study point B to highlight the principal mechanisms leading to damage in our model.

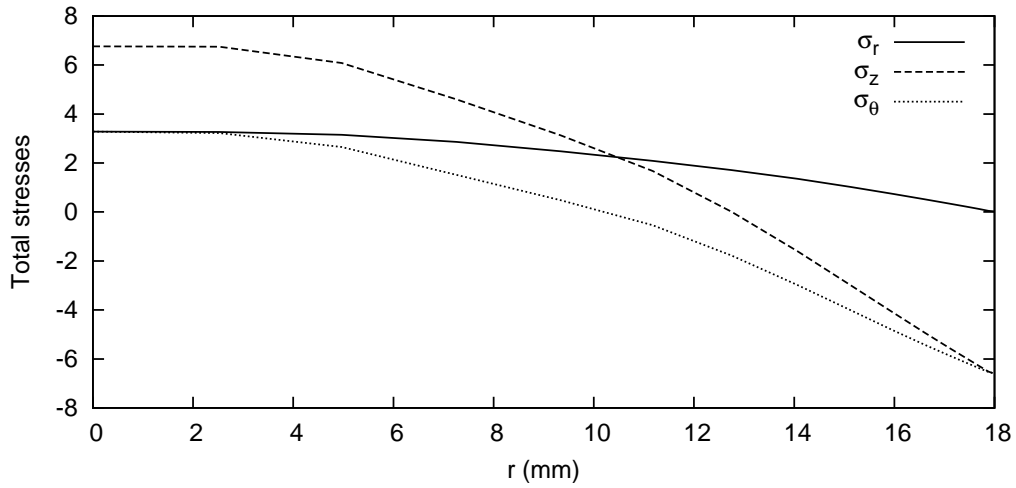


Fig. 7.6: Spatial distribution of total stresses along line AB at $t=1h30$

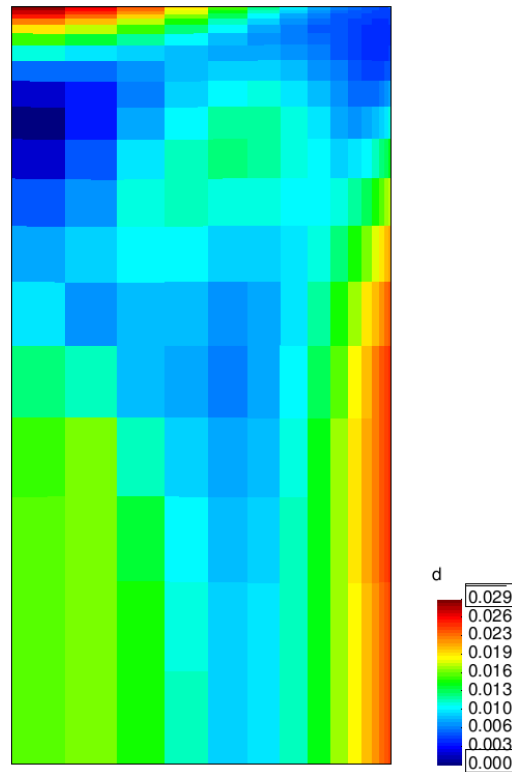


Fig. 7.7: Damage pattern after desiccation

Figure 7.8 shows the time evolution of mean and shear double effective stresses as well as damage. With the increase of suction, the mean pressure continuously increases. The solid skeleton remains in compression despite the apparent tensile total stresses. However, as the applied suction increases, the deviatoric double effective stress increases, reaches a maximum value at the end of suction loading, then decreases when pore pressures homogenise. Damage is initiated from time $t=0$ and gradually develops as long as the deviatoric stress increases before stabilising.

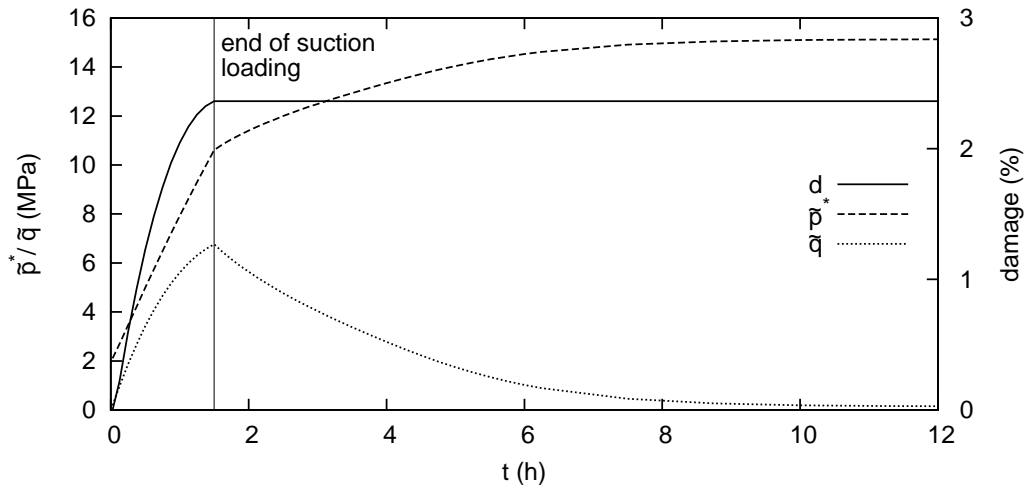


Fig. 7.8: Time evolution of double effective mean and shear stresses and damage at point B

The total and effective stress paths followed at point B are represented in figure 7.9. Although the total mean stress is tensile, the double effective mean stress remains positive due to compressive suction effects. Since we considered all the dissipative processes to be driven by the double effective stress, damage can not be attributed to tensile stresses in the solid matrix within our modelling framework. However, figure 7.9 shows that the increase in deviatoric stress makes the stress path reach the damage criterion, and therefore induces damage.

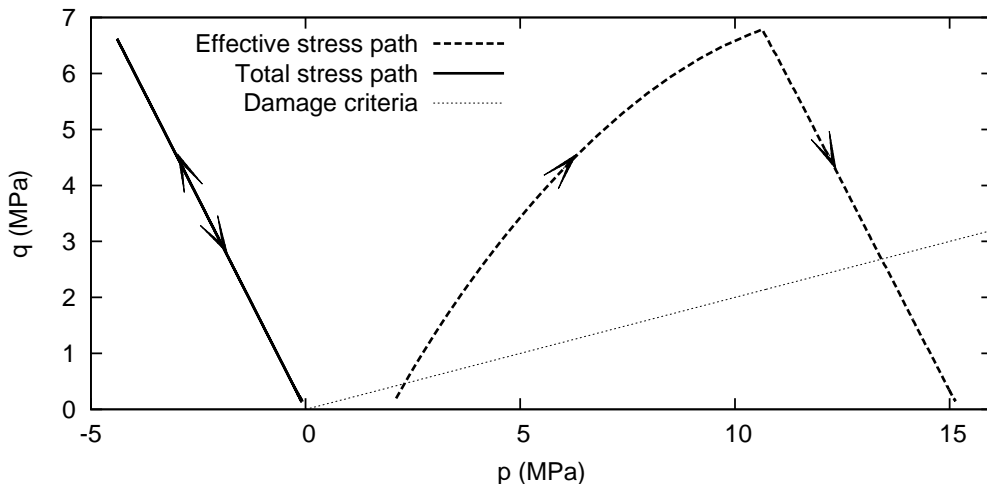


Fig. 7.9: Stress paths at point B during desiccation

7.1.4 Humidification

The initial suction is set equal to 20 MPa and decreased down to 2 MPa at the sample surface at a rate of 0.2 MPa/min.

Figure 7.10 shows the water pressure field at four time steps. As for the desiccation test, the rate at which suction is applied results in a very heterogeneous water pressure distribution

at the end of loading.

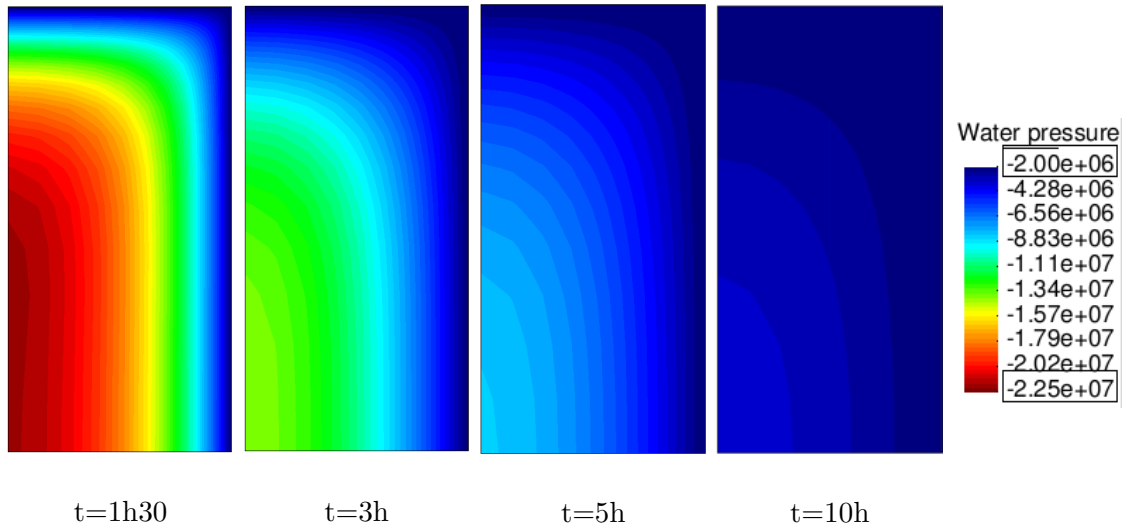


Fig. 7.10: Water pressure field evolution with time

The damage pattern at the end of the test is given in figure 7.11. As for the desiccation test, damage is localised near the surface, far from the sample extremities. However, in this case, the sample core remains intact.

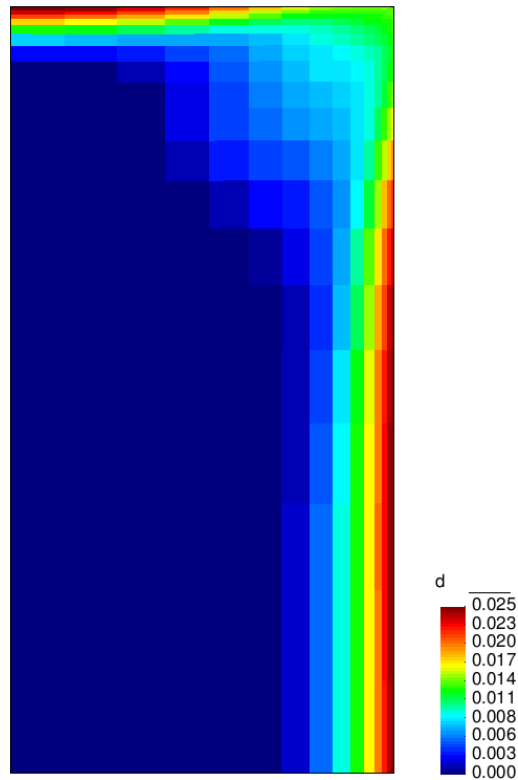


Fig. 7.11: Damage pattern after humidification

Figure 7.12 shows the time evolution of mean and shear double effective stresses as well as damage at point B. With the decrease of suction, the mean pressure continuously

decreases, the solid skeleton remaining in compression. As the applied suction decreases, the deviatoric stress increases due to the heterogeneous pressure field, reaches a maximum value, then decreases when pore pressures homogenise. Damage is not initiated from the beginning of loading, but its evolution afterwards is much more abrupt than for desiccation.

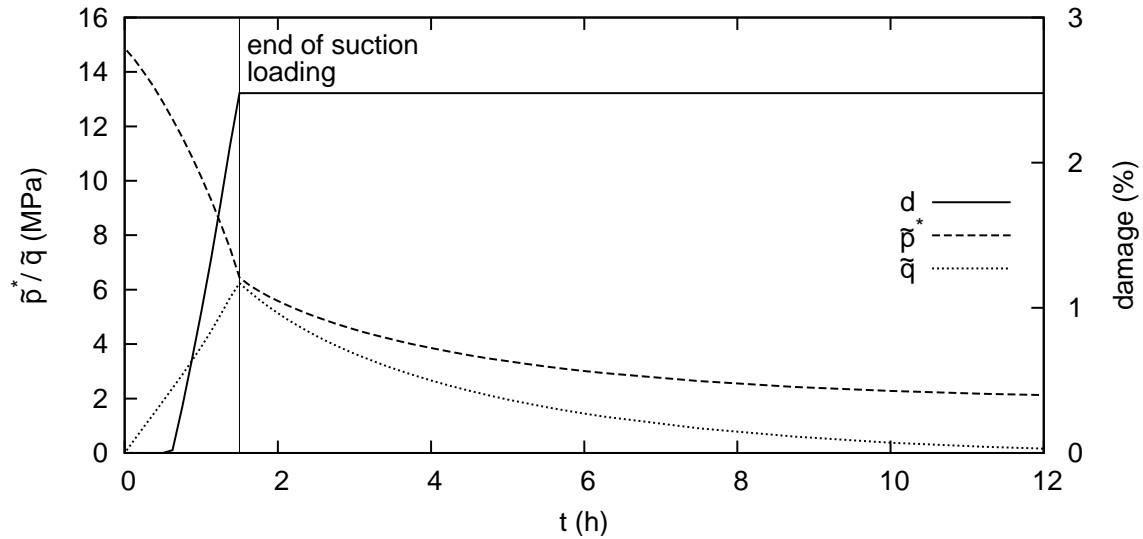


Fig. 7.12: Time evolution of double effective mean and shear stresses and damage at point B

The total and effective stress paths followed at point B are represented in figure 7.13. In this case, even total stresses are compressive. The simulated damage is again linked with the deviatoric stress increase due to differential shrinkage.

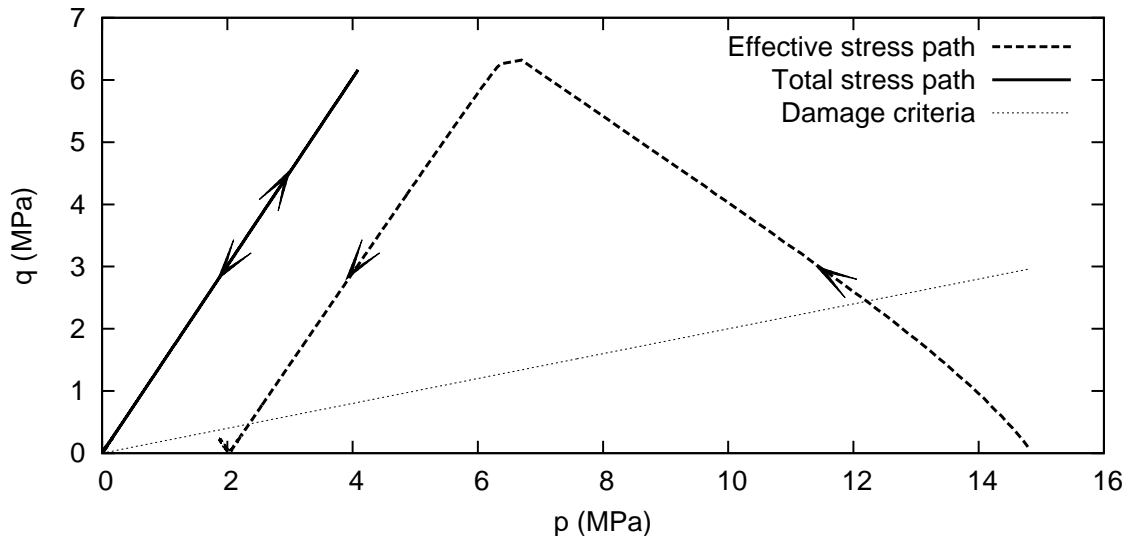


Fig. 7.13: Stress paths at point B during humidification

These examples show that, within a constitutive framework based on the concept of an effective stress with a component related to suction, this double effective stress always remains positive, even when shrinkage is constrained and tensile total stresses develop. Indeed, the compressive effect of suction is more important than the effect of total tensile

stresses due to constrained shrinkage. It is therefore, under this assumption, impossible to model damage initiation by considering it caused by traction of the solid skeleton. However, although this interpretation may need further discussion and experimental evidence, considering that damage is due to deviatoric stresses in the solid skeleton enables the reproduction of damage due to inhomogeneous deformation during desiccation and humidification. This outcome is of interest since none of the existing approaches is capable of modelling damage due to humidification. This approach, although not demonstrated here, is also sensitive to the rate at which suction increments are applied. Indeed, if loading is slow enough, pressures homogenise during suction application and no deviatoric stress is created.

7.2 Excavation modelling

Works about excavation, ventilation and heating of deep galleries can be found in Barnichon (2002); Barnichon and Volckaert (2003); Hoxha et al. (2004); Gatmiri and Hoor (2007); Arson and Gatmiri (2012) and Garitte et al. (2013)

7.2.1 Impact of suction on the extent and properties of the excavation damaged zone

The first study consists in simulation of excavation in Boom clay at different suctions. Although the problem is simplified, assuming drained conditions and a simple model for Boom clay (linear elasticity), this example illustrates well how the saturation state around the tunnel affects the development of damage and plastic zones. This work has been published in the proceedings of the fifth Biot conference on Poromechanics (Le Pense et al., 2013).

The specific equations chosen to represent clay behaviour are summarised in Table 7.4. Elasticity is assumed to be linear. Plasticity is modelled using the Barcelona Basic Model expressed in terms of the double effective stress.

Excavation Modelling

We simulate the excavation of a tunnel of radius R in Boom clay (note that in this conceptual study, the numerical value of R does not need to be specified). Excavation is simulated at different constant suctions, under the assumption that fluid transfers are fast enough to consider drained conditions.

Initial conditions and material parameters are taken of the same order of magnitude as the ones found in the literature for Boom clay at the HADES underground laboratory at Mol, Belgium (Romero, 1999; Della Vecchia et al., 2011).

The goal of the numerical work presented below is not to simulate a real experiment but to illustrate qualitatively the capabilities of the model.

Elasticity	Linear elasticity	$\psi_0^e = \frac{K}{2}(\varepsilon_v^e)^2 + G\varepsilon_d^e : \varepsilon_d^e$
Retention properties	Van Genuchten (1980)	$S_l(s) = \left(\frac{1}{1 + (\alpha s)^n} \right)^m$
Plasticity	Barcelona Basic Model (Alonso <i>et al.</i> , 1990)	$f_p(\tilde{\sigma}^*, \tilde{p}_0^*, s) = \tilde{q}^{*2} - M^2 \tilde{p}^* (\tilde{p}_c^*(\tilde{p}_0^*, s) - \tilde{p}^*)$ $g_p(\tilde{\sigma}^*, \tilde{p}_0^*, s) = \zeta \tilde{q}^{*2} - M^2 \tilde{p}^* (\tilde{p}_c^*(\tilde{p}_0^*, s) - \tilde{p}^*)$ $\tilde{p}_c^* = p_r \left(\frac{\tilde{p}_0^*}{p_r} \right)^{\frac{\lambda_0 - \kappa}{\lambda(s) - \kappa}} + S_l s$ $\lambda(s) = \lambda_0 [(1 - r) \exp(-\beta s) + r]$ $\dot{\tilde{p}}_0^* = \frac{\tilde{p}_0^*}{\lambda_0 - \kappa} \dot{\varepsilon}_v^p$
Damage		$f_d(\tilde{\sigma}^*, d) = \tilde{q}^* - C_2 \tilde{p}^* - C_0 - C_1 d$ $\dot{d} = \frac{1}{C_1} \left[-\frac{C_2}{3} I_d + \frac{3\tilde{\sigma}_d^*}{2\tilde{q}^*} \right] : \dot{\tilde{\sigma}}^*$

Table 7.4: Specific functions for clays

Boom clay parameters Retention and mechanical parameters are given in Table 7.5 and 7.6.

α_{vg}	n_{vg}	m_{vg}
0.28	2.3	0.21

Table 7.5: Retention curve parameters

Elasticity		Plasticity							Damage		
K	G	M	λ_0	κ	p_r	r	β	ζ	C_0	C_1	C_2
MPa	MPa				MPa		MPa ⁻¹		MPa	MPa	
250	115	1	0.16	0.017	5	0.74	1	0.4	0	10	0.8

Table 7.6: Material mechanical parameters

Initial and boundary conditions The initial stress state is supposed to be isotropic : $\sigma_r = \sigma_\theta = \sigma_z = 4.5$ MPa. The preconsolidation pressure is taken equal to $p_0^* = 6$ MPa.

Under the assumption that the initial stress state is isotropic, the problem can be modelled by an axisymmetric analysis (see Figure 7.14).

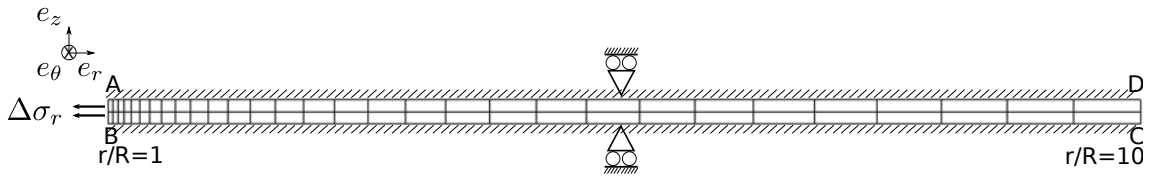


Fig. 7.14: Geometry of the problem.

Displacements along e_z direction are set equal to zero on surfaces AD and BC.

On surface CD, the stress state is supposed not to be disturbed by the excavation, $\Delta\sigma_r = 0$.

On surface AB, radial stress is supposed to be equal to zero after excavation, i.e. during the simulation, a stress difference $\Delta\sigma_r = -4.5$ MPa is applied.

Suction is kept constant at each node of the mesh during simulation.

Results and discussion

Stress path at the tunnel wall To understand better how our model handles the transition between plastic and brittle behaviour, let see the stress paths followed during excavation at tunnel wall. For two different values of suction ($s=0$ and $s=1$ MPa), figures 7.15 and 7.16 show the double effective stress path (thick solid line), the total stress path (thick dashed line) and plasticity (thin solid line) and damage (thin dashed line) criteria.

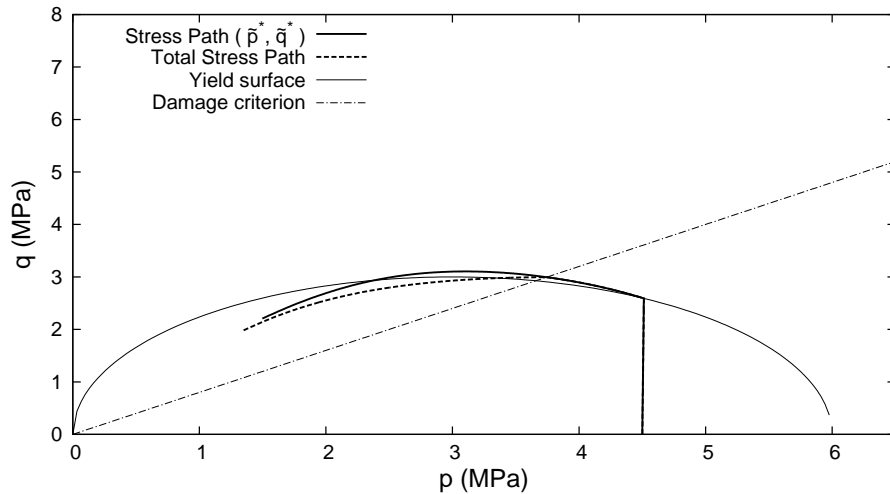


Fig. 7.15: Total and double effective stress path for saturated state

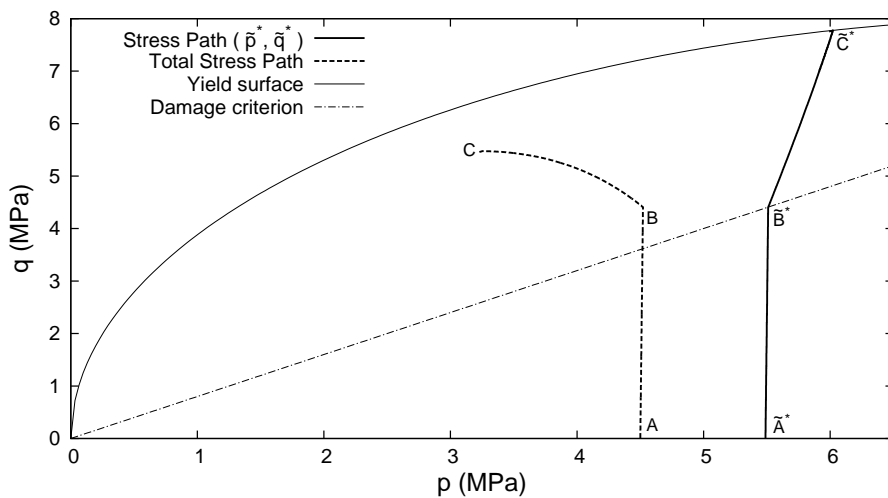


Fig. 7.16: Total and double effective stress path for suction = 1 MPa

These stress paths illustrate the main mechanism allowing for transition from ductile to

brittle behaviour, which is the competition between the two dissipative phenomena. Indeed, for a saturated soil, the stress path reaches the plastic yield surface before reaching the damage criterion. The occurrence of plasticity modifies the stress path and prevents the development of high damage. For high suctions, the elastic domain is much larger, due to the dependence of the yield surface on suction, and the stress path will reach the damage criterion first, which leads to a more brittle behaviour.

Both the double effective stress path ($\tilde{A}^*\tilde{B}^*\tilde{C}^*$) and the total stress path (ABC) are represented in Figure 7.16. Before damage is initiated (AB) the difference between the two stresses is only due to suction, which increases the confining pressure on the soil skeleton. After damage initiation (BC), the stress acting on soil skeleton increases due to the appearance of microcracks, while total stress tends to decrease.

Stress spatial evolution Figures 7.17 and 7.18 below show the evolution of these stresses around the tunnel, for two states of suction: $s=0$ and $s=1\text{MPa}$ (R denotes the radius of the tunnel).

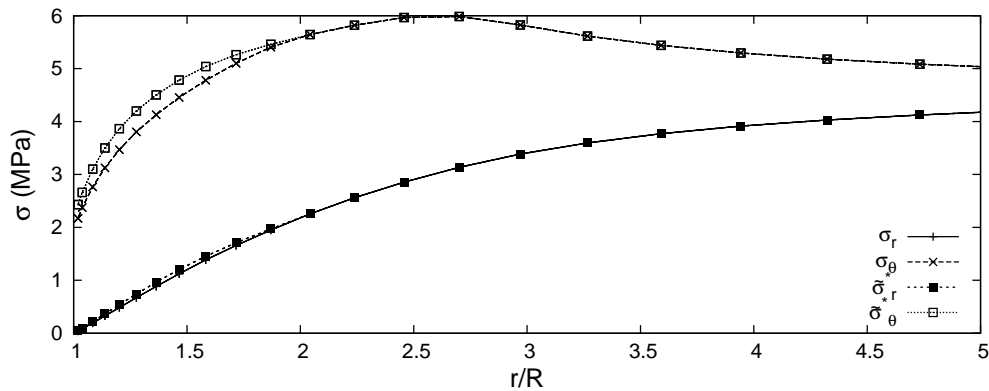


Fig. 7.17: Total and double effective stress for saturated state

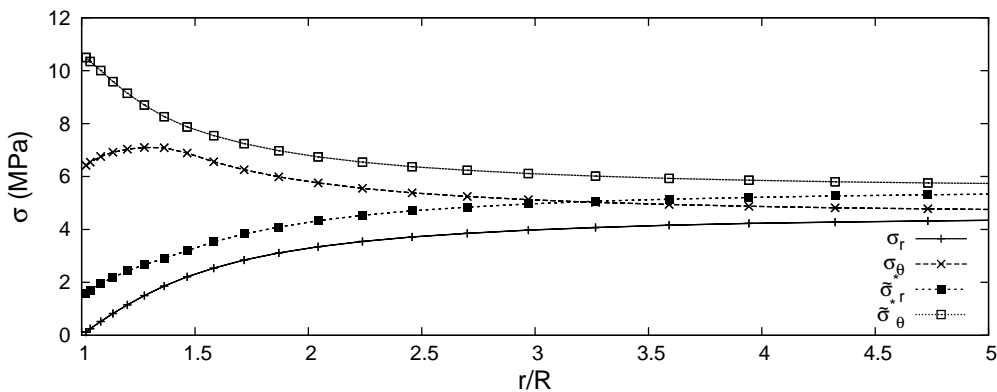


Fig. 7.18: Total and double effective stress for suction = 1 MPa

For the saturated case, plasticity is the main dissipative phenomenon and leads to a decompression of tangential stress around the opening.

In the unsaturated case, there is also a decompression of total stress but the value of double

effective stress is much higher.

Development of plastic and damage zones The spatial evolution of damage and plasticity (represented by the norm of the plastic strain matrix $|\epsilon^p| = \sqrt{\epsilon^p : \epsilon^p}$) are given in figures 7.19 and 7.20.

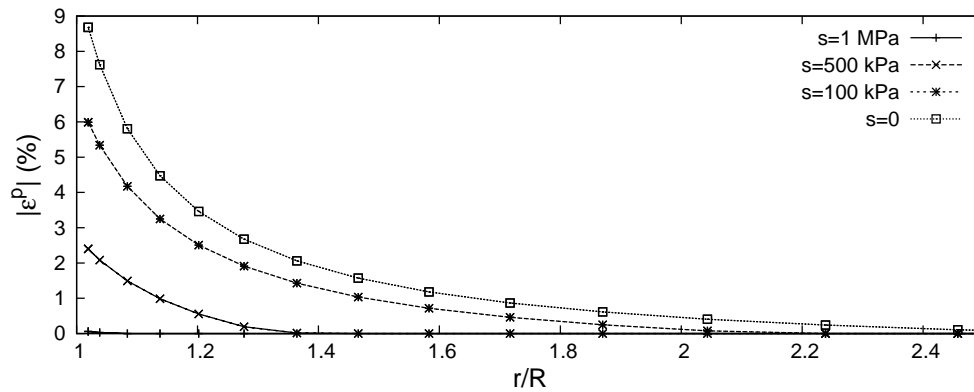


Fig. 7.19: Plastic strain distribution at various constant suctions.

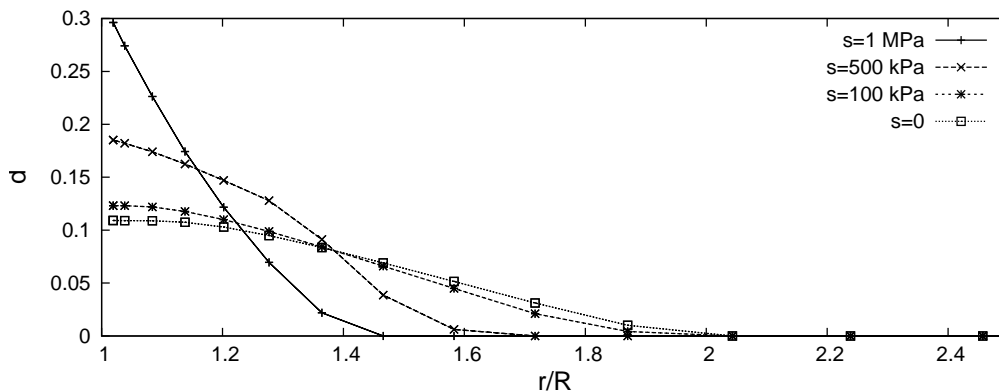


Fig. 7.20: Damage distribution at various constant suctions.

The amplitude of plastic strains and the extent of the plastic zone both decrease with suction.

Damage at the tunnel wall increases when suction is higher, which is consistent with the model formulation, which was aimed to capture the shift from ductile to brittle behaviour associated with suction changes.

Damage develops further away from the excavation as suction is lower and as the plastic zone is wider. This observation is assumed to be due to the choice of constitutive models used for plastic and damage criteria, as explained from the stress paths illustrated in Figures 7.15 and 7.16. Indeed, Figure 7.15 shows that the occurrence of plasticity substantially modifies the stress path which contributes to the development of damage in the plastic zone.

This study allowed to show the effect of suction on the extent of damage and plastic zones created by excavation. When considering a drained behaviour, numerical results predict a

wide plastic zone and high values of plastic strains when the ambient suction applied is low. For low suctions, damage remains low, but develops in the whole plastic zone, as opposed to states of high suction, in which damage is higher but localised in a narrower zone.

7.2.2 Simulation of excavation under undrained conditions

A more realistic excavation simulation is presented in this section. The excavation is assumed to be realised fast enough to take place under undrained conditions.

Geometry and boundary conditions

The initial stress state is supposed to be isotropic : $\sigma_r = \sigma_\theta = \sigma_z = 4.5$ MPa. The preconsolidation pressure is taken equal to $p_0^* = 5.5$ MPa. The initial pore water pressure is taken equal to $p_l = 2$ MPa.

Under the assumption that the initial stress state is isotropic, the problem can be considered unidimensional and be modelled by an axisymmetric analysis (see figure 7.21). The excavation radius is taken equal to $R = 1$ m, and the spatial variable considered is the dimensionless radius, r/R . The problem is meshed from the tunnel wall, $r/R = 1$, to a distance $r/R = 20$, distance at which the stress state is not affected by the excavation (see figure 7.22).

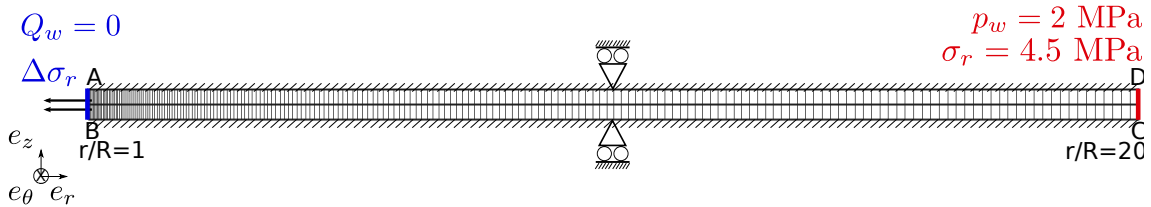


Fig. 7.21: Geometry of the problem.

Displacements along e_z direction are set equal to zero on surfaces AD and BC.

On surface CD, the stress state is supposed not to be disturbed by the excavation, $\Delta\sigma_r = 0$ and $p_w = 2$ MPa.

On surface AB, the radial stress is supposed to be equal to zero after excavation, i.e. during the simulation, a stress difference $\Delta\sigma_r = -4.5$ MPa is applied. The stress release is supposed to be linear with time during excavation, which is supposed to last 15 days. Water flux is prevented across this section, $Q_w = 0$.

The air pressure takes a constant null value in the whole specimen.

Material parameters

The mechanical parameters are the ones of Boom clay studied in chapter 6.2. They are summarised in table 7.7.

Fluid transfers are taken into account in this study. The permeability functions chosen as well as their parameters values are given in table 7.9.

The initial porosity is taken equal to 39 %.

Elasticity				Plasticity			LC curve			Damage		
n	p_r MPa	κ	ν	M	λ_0	ζ	p_r MPa	β MPa ⁻¹	r	C_0 MPa	C_1 MPa	C_2
0.6	0.1	0.0075	0.15	0.8	0.00755	1.5	0.1	0.5	0.998	0	25	0.3

Table 7.7: Material mechanical parameters

α_{vg} (MPa ⁻¹)	n_{vg}	m_{vg}	S_r
0.28	2.3	0.21	0

Table 7.8: Retention parameters

Intrinsic permeability	$K_{int}(\phi) = K_{w0} \frac{\phi^3}{(1-\phi)^2} \frac{(1-\phi_0)^2}{\phi_0^3}$	$K_{w0} = 1.10^{-13} \text{ m.s}^{-1}$ $\phi_0 = 39\%$
Relative permeability	$k_r(S_l) = \left(\frac{S_l - S_r}{1 - S_r} \right)^m$	$m = 3$

Table 7.9: Hydraulic functions and parameters

Results

Figure 7.22 shows the spatial distribution of the different components of the total stress tensor as well as the water pore pressure at the end of excavation.

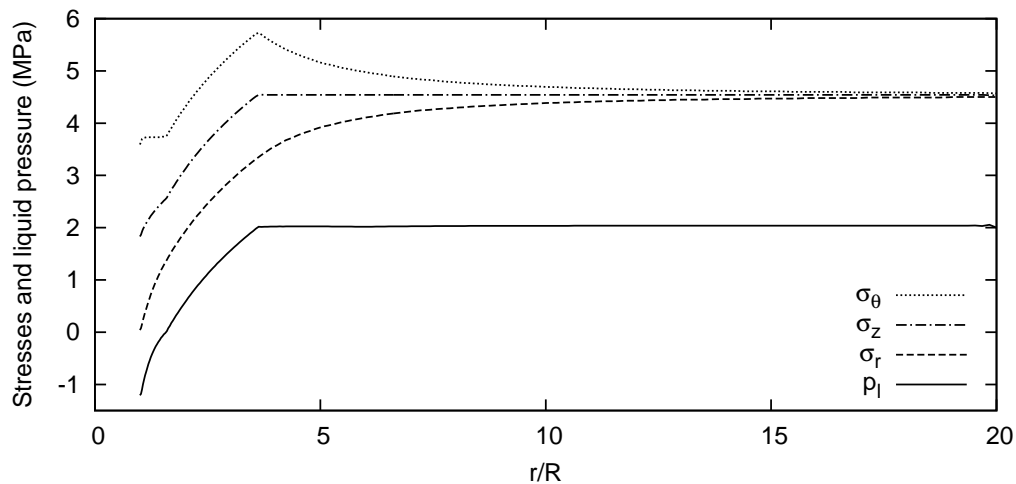


Fig. 7.22: Spatial distribution of total stresses and pore liquid pressure at the end of excavation

It can first be noticed that the stress state is not significantly affected by the excavation from a distance to the tunnel $r/R = 15$ and thus that the choice of the outer boundary, at $r/R = 20$, is acceptable to consider that the response is similar to the one of an infinite

medium. The stress release induces a zone in which water pressure is strongly reduced, which corresponds to the plastic zone. Negative pore pressures are generated close to the tunnel wall, what has been also observed at HADES research laboratory (Bernier et al., 2007).

The spatial evolution of radial displacements is given in figure 7.23. A radial convergence of 9.3 cm is obtained. Although the excavation radius is different, it is worth noting that this value lies in the same range as the radial settlements measured in Boom clay (9 cm for a 4 m diameter gallery with lining (Bernier et al., 2007), 14.5 cm for a 4 m radius gallery with lining (Barnichon and Volckaert, 2003)).

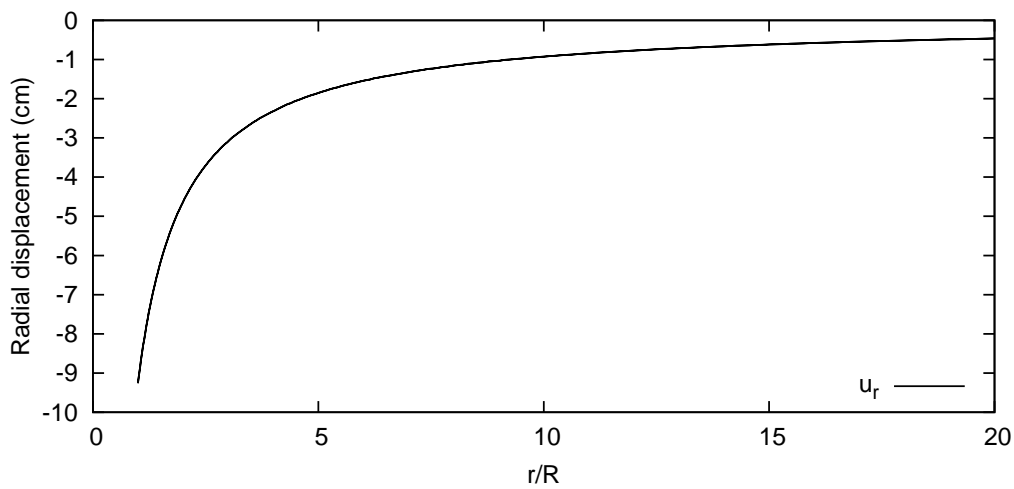


Fig. 7.23: Spatial distribution of radial displacements

The spatial distribution of damage and plasticity (represented by the norm of the plastic strain matrix) is given in figure 7.24.

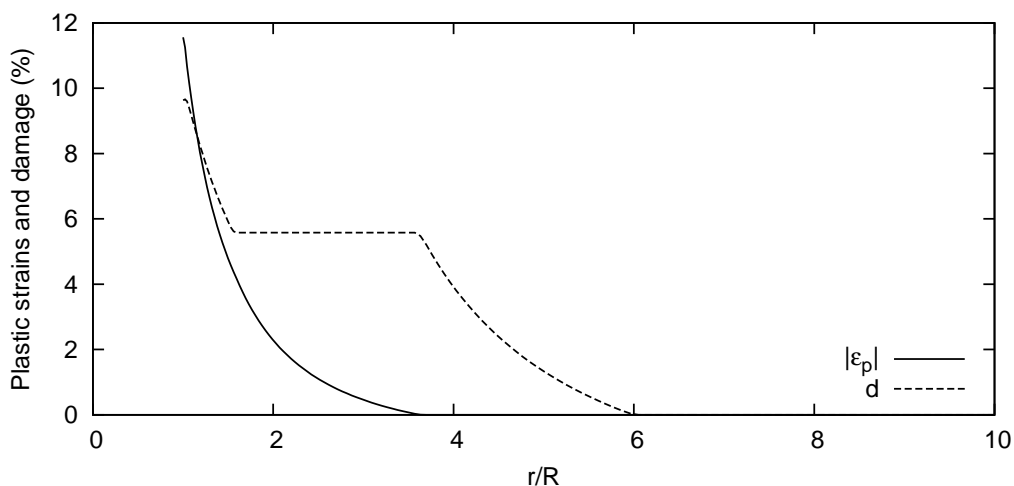


Fig. 7.24: Plastic strain and damage distribution at the end of excavation

The simulated damage zone extends further than the plastic zone. The plastic strain evolution curve has a regular shape. Damage, however, takes a constant value from $r/R = 2$ to $r/R = 4$. To explain this surprising result, the time evolution of damage,

plastic strains, and water pressure at the tunnel wall is represented in figure 7.25. There are three different periods during which different mechanisms take place. Damage is initiated first and water pressure remains unchanged as long as the behaviour remains elastic. When plasticity is activated, water pore pressure starts decreasing and damage stops evolving. Once water pressure reaches negative values, damage starts increasing again. The stress path, represented on figure 7.26, shows that this behaviour is due to the overconsolidated state of the clay, which implies that, once the stress path reaches the yield surface, only the extension of the plastic yield surface with suction can allow further increase of damage.

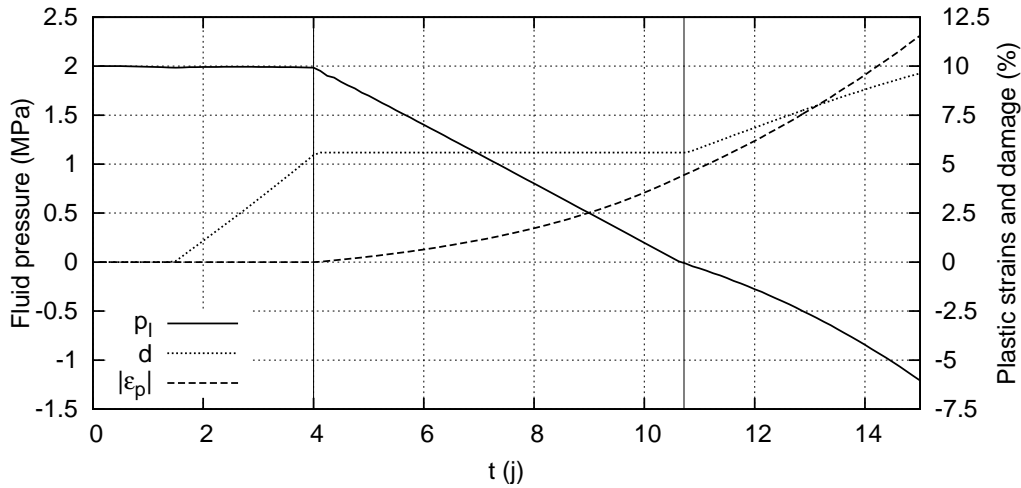


Fig. 7.25: Plastic strain, damage and liquid pressure time evolution at the tunnel wall

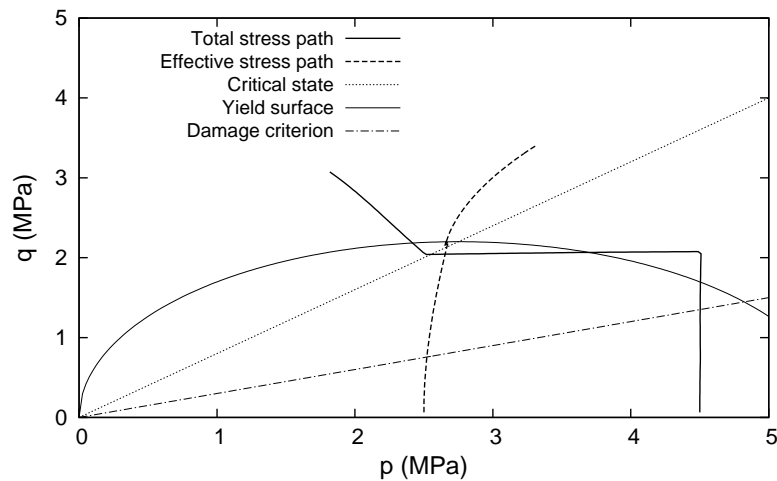


Fig. 7.26: Total and effective stress paths at the tunnel wall

Although these results should be validated against experimental data for other values of the tunnel radius, the values obtained for pore pressures and displacements are realistic. This example illustrates well how our modelling framework allows to simulate both damage and plastic strains. A major improvement would be to incorporate permeability dependence on damage, and study how it affects the overall behaviour.

CONCLUSIONS AND PERSPECTIVES

Conclusions

A constitutive modelling framework allowing for damage-plasticity couplings in unsaturated porous media has been proposed. This framework is based on the assumption of a double effective stress, accounting for damage and suction effects, which controls the material mechanical behaviour. The relationship between suction and the degree of saturation has proved to have a great influence on the value of the double effective stress. Water retention properties have therefore been studied in details and a proposition has been made to incorporate porosity into the water retention curve expression, in order to meet thermodynamical consistency requirements. Although a simple expression has been chosen for the double effective stress, it has been proved to be able to reproduce the main features of damaged unsaturated soils.

An hyperelastic formulation has been chosen to represent pressure dependent elasticity. Energy conservation in the elastic domain is therefore ensured. The two main hypotheses available to incorporate damage into elasticity and plasticity equations have been compared. It has been shown that the principle of equivalent elastic energy predicts a higher rigidity degradation than the principle of strain equivalence for the same value of the damage parameter. The pressure exponent in the hyperelastic formulation also proved to have a strong influence on rigidity degradation with damage. However, too few experimental damage and rigidity measurements are available to choose one hypothesis against the other.

The principle of strain equivalence has therefore been chosen for its ability to provide a straightforward way of coupling damage and plasticity. Damage and suction effects are taken into account by replacing the total stress by the double effective stress into elasticity and plasticity equations, which means that damage and plasticity criteria and evolution laws are expressed in terms of the double effective stress. This allows for a direct dependence of damage and plasticity criteria on suction and damage in the total stress space. Any plasticity model could be accommodated into this framework. The Cam-clay model has been used as an example, with an extra-dependence of the plastic yield criterion on suction, in order to account for the high sensitivity of clay on water content.

A specific local algorithm has been developed, to determine the stress increment associated

to an increment in strain and pore pressures. The model formulation enabled the use of a fully explicit model, in which automatic substepping procedures have been incorporated. The double effective stress increment, as well as the elastic and plastic strains partition, are deduced from the plasticity algorithm. It then serves as an input to the damage algorithm, to determine the damage increment. This algorithm has the advantage of been flexible enough to accommodate modifications of the different model components.

This constitutive and numerical framework has been validated against laboratory mechanical tests for two materials, the Callovo-Oxfordian argillite and Boom clay. Provided that the plasticity model is adapted to fit the specific material behaviour, a good agreement is reached between experimental data and simulations. The effect of confining pressure on the mechanical behaviour is well reproduced, and the ductile/brittle transition associated to suction increase is captured.

In order to be able to simulate fully coupled hydro-mechanical problems, transfer laws depending on the saturation state have been introduced. The balance and mass conservation equations, their weak formulation and the spatial and time discretisations, achieved by means of the Finite Element Method, have been presented. The global resolution method is based on the iterative Newton-Raphson algorithm.

This complete numerical framework allowed us to demonstrate the capabilities of the constitutive framework, by simulating fully-coupled hydro-mechanical problems. The first illustration concerns damage induced by desiccation and humidification. Since the solid skeleton always remains in compression when submitted to hydric loading, effective stress based formulations do not allow for tensile damage to be captured. However, important deviatoric stresses result from high moisture gradients experienced in low permeable materials, which may induce damage. What is interesting in this approach is its ability to capture, not only desiccation-induced damage, but also damage due to humidification, which has been observed but not yet explained. The second application deals with the creation of the excavation damaged zone around deep galleries. A first illustrative example allowed us to study the influence of suction on damage and plasticity zones extent, considering drained conditions. The second example presents the pore pressure field perturbation, and the damage and plasticity zones due to an undrained excavation.

Perspectives

Many improvements could be incorporated into the constitutive model. First, the definition of the double effective stress could benefit from a micromechanical analysis, to determine more accurately the stress resulting from damage and suction on the clay matrix. Since micro-cracks usually appear along preferential directions, depending on loading, an extension to an anisotropic damage tensor would certainly improve the model response. Evolution of the fluid related laws, such as water retention properties or permeabilities, with damage should also be accounted for to give accurate predictions of hydraulic phenomena. In the case of wetting-drying cycles, hysteresis of the water retention curve should not be neglected either. Concerning the plasticity framework, lots of advanced forms of the Cam-clay model are available in the literature, which could be used, provided that the resulting improvements are worth the increased number of required parameters.

Concerning the Finite Element implementation, Θ -Stock is already appropriate to simulate many hydro-mechanical non-linear problems. However, its efficiency could be greatly improved by using Newton-Raphson with the tangent rigidity matrix, instead of the elastic rigidity matrix, which would increase the convergence rate. A valuable improvement would also be to incorporate methods to prevent the appearance of spatial oscillations in the pore pressure field in coupled hydro-mechanical problems. This would allow the choice of small time steps without the need of mesh refinement.

Finally, only a few applications of the proposed model have been presented here. Further validation can be made by simulating full-scale real problems. The excavation and ventilation of deep galleries can already be simulated. However, for more realistic results, we think that the dependence of permeabilities on damage should be accounted for. What would be very interesting is to extend our modelling approach to long term effects, such as viscoplasticity, self-sealing and self-healing. Indeed, although the rock is damaged by excavation, clay-based geomaterials tend to recover part of their original properties after a certain time, due to chemical reactions with water.

APPENDIX A

DERIVATIVES FOR CAM-CLAY PLASTICITY

This appendix presents the derivatives of the plasticity functions used for Boom Clay modelling (based on CC and BBM). They are necessary to calculate the stiffness matrix in the Newton-Raphson method (chapter 3.4), and to calculate strains and stresses increments in the local stress-point algorithm (see chapter 5.6.3).

- $\frac{\partial f_p}{\partial \tilde{\sigma}^*} = \frac{\partial f_p}{\partial \tilde{p}^*} \frac{\mathbf{I}}{3} + \frac{\partial f_p}{\partial q} \frac{3\tilde{\sigma}_d}{2\tilde{q}} = \frac{M^2(2\tilde{p}^* - p_c^*)}{3} \mathbf{I} + 3\tilde{\sigma}_d$
- $\frac{\partial g_p}{\partial \tilde{\sigma}^*} = \frac{\partial g_p}{\partial \tilde{p}^*} \frac{\mathbf{I}}{3} + \frac{\partial g_p}{\partial q} \frac{3\tilde{\sigma}_d}{2\tilde{q}} = \frac{M^2(2\tilde{p}^* - p_c^*)}{3} \mathbf{I} + 3\zeta\tilde{\sigma}_d$
- $\frac{\partial f_p}{\partial p_c^*} = -M^2\tilde{p}^*$
- $\frac{\partial p_c^*}{\partial p_0} = \frac{\lambda(0) - \kappa}{\lambda(s) - \kappa} \left(\frac{p_0}{p_r} \right)^{\frac{\lambda(0) - \kappa}{\lambda(s) - \kappa} - 1}$
- $\frac{\partial p_c^*}{\partial s} = -p_r \log \left(\frac{p_0}{p_r} \right) \left(\frac{p_0}{p_r} \right)^{\frac{\lambda(0) - \kappa}{\lambda(s) - \kappa}} \frac{\lambda(0) - \kappa}{(\lambda(s) - \kappa)^2} \lambda'(s) + S_l(s) + \frac{\partial S_l}{\partial s} s$
with $\lambda'(s) = -\lambda_0[(1-r)\beta \exp(-\beta s)]$
- $\frac{\partial p_0}{\partial \varepsilon_v^p} = \frac{p_0^n p_r^{(1-n)}}{\lambda_0 - \kappa}$
- $\frac{\partial g_p}{\partial \tilde{p}^*} = M^2(2\tilde{p}^* - p_c^*)$
- $\frac{\partial S_l}{\partial s} = -(1 - S_r) \frac{m_{vg} n_{vg} \alpha_{vg}^{n_{vg}} s^{n_{vg}-1}}{(1 + (\alpha_{vg} s)^{n_{vg}})^{m_{vg}+1}} = g_2$

REFERENCES

- Abou-Chakra Guéry, A., Cormery, F., Shao, J., and Kondo, D. A micromechanical model of elastoplastic and damage behavior of a cohesive geomaterial. *International Journal of Solids and Structures*, 45 (5), 1406–1429, 2008.
- Abu Al-Rub, R. K. and Voyiadjis, G. Z. On the coupling of anisotropic damage and plasticity models for ductile materials. *International Journal of Solids and Structures*, 40 (11), 2611–2643, 2003.
- Aguilar, G., Gaspar, F. J., Lisbona, F. J., and Rodrigo, C. Numerical stabilization of Biot’s consolidation model by a perturbation on the flow equation. *International Journal for Numerical Methods in Engineering*, 75 (11), 1282–1300, 2008.
- Al-Mukhtar, M., Belanteur, N., Tessier, D., and Vanapalli, S. K. The fabric of a clay soil under controlled mechanical and hydraulic stress states. *Applied Clay Science*, 11 (2-4), 99–115, 1996.
- Al-Shayea, N. A. The combined effect of clay and moisture content on the behavior of remolded unsaturated soils. *Engineering Geology*, 62 (4), 319–342, 2001.
- Alonso, E. E., Gens, A., and Josa, A. A constitutive model for partially saturated soils. *Géotechnique*, 40 (3), 405–430, 1990.
- Alonso, E. E., Vaunat, J., Pereira, J.-M., and Olivella, S. A microstructurally based effective stress for unsaturated soils. *Géotechnique*, 60 (12), 913–925, 2010.
- Arson, C. and Gatmiri, B. A mixed damage model for unsaturated porous media. *Comptes Rendus Mécanique*, 337 (2), 68–74, 2009.
- Arson, C. and Gatmiri, B. Thermo-hydro-mechanical modeling of damage in unsaturated porous media: Theoretical framework and numerical study of the EDZ. *International Journal for Numerical and Analytical Methods in Geomechanics*, 36 (3), 272–306, 2012.
- Arson, C. and Pereira, J.-M. Influence of damage on pore size distribution and permeability of rocks. *International Journal for Numerical and Analytical Methods in Geomechanics*, 37 (8), 810–831, 2013.

- Atkinson, J. H. Non-linear soil stiffness in routine design. *Géotechnique*, 50 (5), 487–508, 2000.
- Averjanov, S. F. No Title. *English Collection*, 7, 19–21, 1950.
- Baldi, G., Hueckel, T., Peano, A., and Pellegrini, R. Developments in modelling of thermo-hydro-geomechanical behaviour of Boom clay and clay-based buffer materials (vol 1). Technical report, Commission of the European Communities, 1991.
- Barnichon, J.-D. Contribution of the bounding surface plasticity to the simulation of gallery excavation in plastic clays. *Engineering geology*, 64 (2-3), 217–231, 2002.
- Barnichon, J.-D. and Volckaert, G. Observations and predictions of hydromechanical coupling effects in the Boom clay, Mol Underground Research Laboratory, Belgium. *Hydrogeology Journal*, 11 (1), 193–202, 2003.
- Bastiaens, W., Bernier, F., and Li, X.-L. SELFRAC: Experiments and conclusions on fracturing, self-healing and self-sealing processes in clays. *Physics and Chemistry of the Earth, Parts A/B/C*, 32 (8-14), 600–615, 2007.
- Baudet, B. and Stallebrass, S. A constitutive model for structured clays. *Géotechnique*, 54 (4), 269–278, 2004.
- Bernier, F., Volckaert, G., Alonso, E. E., and Villar, M. Suction-controlled experiments on Boom clay. *Engineering Geology*, 47 (4), 325–338, 1997.
- Bernier, F., Li, X.-L., and Bastiaens, W. Twenty-five years' geotechnical observation and testing in the Tertiary Boom Clay formation. *Géotechnique*, 57 (2), 229–237, 2007.
- Bishop, A. W. The effective stress principle. *Teknisk Ukeblad*, 39, 859–863, 1959.
- Booker, J. and Small, J. An investigation of the stability of numerical solutions of Biot's equations of consolidation. *International Journal of Solids and Structures*, 11 (7-8), 907–917, 1975.
- Borja, R. I., Tamagnini, C., and Amorosi, A. Coupling plasticity and energy-conserving elasticity models for clays. *Journal of Geotechnical and Geoenvironmental Engineering*, 123 (10), 948–957, 1997.
- Brooks, R. and Corey, A. T. Hydraulic Properties of Porous Media. *Hydrology Papers, Colorado State University*, 1964.
- Burland, J. B. Correspondence on The yielding and dilation of clay. *Géotechnique*, 15 (2), 211–214, 1965.
- Buscarnera, G. and Einav, I. The yielding of brittle unsaturated granular soils. *Géotechnique*, 62 (2), 147–160, 2012.
- Butterfield, R. A natural compression law for soils (an advance on $e - \log p'$). *Géotechnique*, 29 (4), 469–480, 1979.

- Callisto, L. and Rampello, S. Shear strength and small-strain stiffness of a natural clay under general stress conditions. *Géotechnique*, 52 (8), 547–560, 2002.
- Carmeliet, J. and Van Den Abeele, K. Poromechanical modelling of shrinkage and damage processes in unsaturated porous media. In Baroghel Bouny, V. and Aïtcin, P.-C., editors, *International RILEM Workshop on Shrinkage of Concrete*, pages 287–298. 2000.
- Chateau, X. and Dormieux, L. Micromechanics of saturated and unsaturated porous media. *International Journal for Numerical and Analytical Methods in Geomechanics*, 26 (8), 831–844, 2002.
- Chiarelli, A.-S. *Étude expérimentale et modélisation du comportement mécanique de l'argilite de l'est*. PhD thesis, Université Lille I, 2000.
- Chiarelli, A.-S. and Shao, J. Modélisation élastoplastique couplée à l'endommagement anisotrope induit pour des argilites. *Revue Française de Génie Civil*, 6 (1), 115–130, 2002.
- Chiarelli, A.-S., Shao, J., and Hoteit, N. Modeling of elastoplastic damage behavior of a claystone. *International Journal of Plasticity*, 19 (1), 23–45, 2003.
- Coleman, J. D. Stress/strain relations for partly saturated soil. *Géotechnique*, 12 (4), 348–350, 1962.
- Coll, C. *Endommagement des roches argileuses et perméabilité induite au voisinage d'ouvrages souterrains*. PhD thesis, Université Joseph Fourier, 2005.
- Collins, I. F. and Houlsby, G. T. Application of Thermomechanical Principles to the Modelling of Geotechnical Materials. *Proceedings : Mathematical, Physical and Engineering Sciences*, 453 (1964), 1975–2001, 1997.
- Conil, N., Djéran-Maigre, I., Cabrillac, R., and Su, K. Poroplastic damage model for claystones. *Applied Clay Science*, 26 (1-4), 473–487, 2004.
- Cordebois, J. P. and Sidoroff, F. Endommagement anisotrope en élasticité et plasticité. *Journal de Mécanique Théorique et Appliquée, Numéro Spécial*, 1, 45–60, 1982.
- Corey, A. T. Measurement of Water and Air Permeability in Unsaturated Soil. *Soil Science Society of America Journal*, 21 (1), 7–10, 1956.
- Coussy, O. *Mécanique des milieux poreux*. Editions TECHNIP, 1991.
- Coussy, O. *Poromechanics*. John Wiley & Sons Inc, 2004.
- Coussy, O. and Dangla, P. Approche énergétique du comportement des sols non saturés. In *Mécanique des sols non saturés*, pages 137–174. Hermès Science Publications, Paris, 2002.
- Cui, Y.-J., Le, T., Tang, A. M., Li, X.-L., and Delage, P. Suction effects in deep Boom Clay block samples. *Géotechnique*, 57 (2), 239–244, 2007.

- Dafalias, Y. F. Bounding Surface Plasticity. I: Mathematical Foundation and Hypoplasticity. *Journal of Engineering Mechanics*, 112 (9), 966–987, 1986.
- de Sa, C., Benboudjema, F., Thiery, M., and Sicard, J. Analysis of microcracking induced by differential drying shrinkage. *Cement and Concrete Composites*, 30 (10), 947–956, 2008.
- Dehandschutter, B., Vandycke, S., Sintubin, M., Vandenberghe, N., and Wouters, L. Brittle fractures and ductile shear bands in argillaceous sediments: inferences from Oligocene Boom Clay (Belgium). *Journal of Structural Geology*, 27 (6), 1095–1112, 2005.
- Delage, P., Sultan, N., and Cui, Y.-J. On the thermal consolidation of Boom clay. *Canadian Geotechnical Journal*, 37 (2), 343–354, 2000.
- Delahaye, C. and Alonso, E. E. Soil heterogeneity and preferential paths for gas migration. *Engineering Geology*, 64 (2-3), 251–271, 2002.
- Della Vecchia, G., Jommi, C., Lima, A., and Romero, E. Some remarks on the hydro-mechanical constitutive modelling of natural and compacted Boom clay. In *Unsaturated soils*, pages 803–809, 2011.
- Dowell, M. and Jarratt, P. The “Pegasus” method for computing the root of an equation. *BIT*, 12 (4), 503–508, 1972.
- Einav, I. Breakage mechanics—Part I: Theory. *Journal of the Mechanics and Physics of Solids*, 55 (6), 1274–1297, 2007.
- Einav, I. and Puzrin, A. M. Pressure-Dependent Elasticity and Energy Conservation in Elastoplastic Models for Soils. *Journal of Geotechnical and Geoenvironmental Engineering*, 130 (1), 81–92, 2004.
- Einav, I., Houlsby, G. T., and Nguyen, G. D. Coupled damage and plasticity models derived from energy and dissipation potentials. *International Journal of Solids and Structures*, 44 (7-8), 2487–2508, 2007.
- Ewen, J. and Thomas, H. R. Heating unsaturated medium sand. *Géotechnique*, 39 (3), 455–470, 1989.
- Fredlund, D. G. and Morgenstern, N. R. Stress state variables for unsaturated soils. *Journal of the Geotechnical Engineering Division*, 1977.
- Fredlund, D. G., Xing, A., and Huang, S. Predicting the permeability function for unsaturated soils using the soil-water characteristic curve. *Canadian Geotechnical Journal*, 31 (4), 533–546, 1994.
- Gallipoli, D., Gens, A., Sharma, R. S., and Vaunat, J. An elasto-plastic model for unsaturated soil incorporating the effects of suction and degree of saturation on mechanical behaviour. *Géotechnique*, 53 (1), 123–135, 2003a.
- Gallipoli, D., Wheeler, S. J., and Karstunen, M. Modelling the variation of degree of saturation in a deformable unsaturated soil. *Géotechnique*, 53 (1), 105–112, 2003b.

- Garitte, B., Bond, A., Millard, A., Zhang, C., Mcdermott, C., Nakama, S., and Gens, A. Analysis of hydro-mechanical processes in a ventilated tunnel in an argillaceous rock on the basis of different modelling approaches. *Journal of Rock Mechanics and Geotechnical engineering*, 5 (1), 1–17, 2013.
- Gatmiri, B. and Arson, C. θ -STOCK, a powerful tool of thermohydronechanical behaviour and damage modelling of unsaturated porous media. *Computers and Geotechnics*, 35 (6), 890–915, 2008.
- Gatmiri, B. and Delage, P. Nouvelle formulation de la surface d'état en indice des vides pour un modèle non linéaire élastique des sols non saturés. In *Proceedings of the 1st International Conference on Unsaturated Soils*, volume 2, pages 1049–1056, 1995.
- Gatmiri, B. and Hoor, A. Effect of excavation on the thermo-hydro-mechanical behaviour of a geological barrier. *Physics and Chemistry of the Earth, Parts A/B/C*, 32 (8-14), 947–956, 2007.
- Gatmiri, B., Delage, P., and Cerrolaza, M. Udam: A powerful finite element software for the analysis of unsaturated porous media. *Advances in Engineering Software*, 29 (1), 29–43, 1998.
- Gens, A. Soil–environment interactions in geotechnical engineering. *Géotechnique*, 60 (1), 3–74, 2010.
- Gens, A., Garcia-Molina, A. J., Olivella, S., Alonso, E. E., and Huertas, F. Analysis of a full scale in situ test simulating repository conditions. *International Journal for Numerical and Analytical Methods in Geomechanics*, 22 (7), 515–548, 1998.
- Geraminegad, M. and Saxena, S. K. A coupled thermoelastic model for saturated-unsaturated porous media. *Géotechnique*, 36 (4), 539–550, 1986.
- Grassl, P. and Jirásek, M. Damage-plastic model for concrete failure. *International Journal of Solids and Structures*, 43 (22-23), 7166–7196, 2006.
- Gray, W. G. and Schrefler, B. A. Thermodynamic approach to effective stress in partially saturated porous media. *European Journal of Mechanics - A/Solids*, 20 (4), 521–538, 2001.
- Halm, D. and Dragon, A. An anisotropic model of damage and frictional sliding for brittle materials. *European Journal of Mechanics - A/Solids*, 17 (3), 439–460, 1998.
- Hansen, N. R. and Schreyer, H. L. A thermodynamically consistent framework for theories of elastoplasticity coupled with damage. *International Journal of Solids and Structures*, 31 (3), 359–389, 1994.
- Hashiguchi, K. On the linear relations of v - $\ln p$ and $\ln v$ - $\ln p$ for isotropic consolidation of soils. *International journal for numerical and analytical methods in geomechanics*, 19 (5), 367–376, 1995.

- Horseman, S. T., Winter, M. G., and Entwistle, D. C. Geotechnical characterization of boom clay in relation to the disposal of radioactive waste. Technical report, Commission of the European Communities, 1987.
- Houlsby, G. T. The use of a variable shear modulus in elastic-plastic models for clays. *Computers and Geotechnics*, 1 (1), 3–13, 1985.
- Houlsby, G. T. The work input to an unsaturated granular material. *Géotechnique*, 47 (1), 193–196, 1997.
- Houlsby, G. T. and Puzrin, A. M. *Principles of hyperplasticity: an approach to plasticity theory based on thermodynamic principles*. Springer Verlag, 2006.
- Houlsby, G. T., Amorosi, A., and Rojas, E. Elastic moduli of soils dependent on pressure: a hyperelastic formulation. *Géotechnique*, 55 (5), 383–392, 2005.
- Hoxha, D., Giraud, A., Blaisonneau, A., Homand, F., and Chavant, C. Poroplastic modelling of the excavation and ventilation of a deep cavity. *International Journal for Numerical and Analytical Methods in Geomechanics*, 28 (4), 339–364, 2004.
- Hoxha, D., Giraud, A., Homand, F., and Auvray, C. Saturated and unsaturated behaviour modelling of Meuse-Haute-Marne argillite. *International Journal of Plasticity*, 23 (5), 733–766, 2007.
- Hutter, K., Laloui, L., and Vulliet, L. Thermodynamically based mixture models of saturated and unsaturated soils. *Mechanics of Cohesive-frictional Materials*, 4 (4), 295–338, 1999.
- Irmay, S. On the hydraulic conductivity of unsaturated soils. *Transactions, American Geophysical Union*, 35 (3), 463–467, 1954.
- Jennings, J. E. B. and Burland, J. B. Limitations to the use of effective stresses in partly saturated soils. *Géotechnique*, 12 (2), 125–144, 1962.
- Jia, Y., Song, X., Duveau, G., Su, K., and Shao, J. Elastoplastic damage modelling of argillite in partially saturated condition and application. *Physics and Chemistry of the Earth, Parts A/B/C*, 32 (8-14), 656–666, 2007.
- Jia, Y., Bian, H. B., Su, K., Kondo, D., and Shao, J. Elastoplastic damage modeling of desaturation and resaturation in argillites. *International Journal for Numerical and Analytical Methods in Geomechanics*, 34, n/a–n/a, 2009.
- Jommi, C. Remarks on the constitutive modelling of unsaturated soils. *Experimental evidence and theoretical approaches in unsaturated soils*, pages 139–153, 2000.
- Jovicic, V. and Coop, M. Stiffness of coarse-grained soils at small strains. *Géotechnique*, 47 (3), 545–561, 1997.
- Ju, J. W. On energy-based coupled elastoplastic damage theories: constitutive modeling and computational aspects. *International Journal of Solids and Structures*, 25 (7), 803–833, 1989.

- Kachanov, L. M. Time of the rupture process under creep conditions. *Isv. Akad. Nauk. SSR. Otd Tekh. Nauk*, 8, 26–31, 1958.
- Kavvas, M. J. and Amorosi, A. A constitutive model for structured soils. *Géotechnique*, 50 (3), 263–273, 2000.
- Khalili, N. and Khabbaz, M. H. A unique relationship for X for the determination of the shear strength of unsaturated soils. *Géotechnique*, 48 (5), 681–687, 1998.
- Krajcinovic, D. and Fonseka, G. U. The continuous damage theory of brittle materials - Part 1: General Theory. *Journal of Applied Mechanics*, 48 (December), 809–815, 1981.
- Lagier, F., Jourdain, X., de Sa, C., Benboudjema, F., and Colliat, J. Numerical strategies for prediction of drying cracks in heterogeneous materials: Comparison upon experimental results. *Engineering Structures*, 33 (3), 920–931, 2011.
- Laloui, L. and Nuth, M. On the use of the generalised effective stress in the constitutive modelling of unsaturated soils. *Computers and Geotechnics*, 36 (1-2), 20–23, 2009.
- Lavrov, A., Vervoort, A., Filimonov, Y., Wevers, M., and Mertens, J. Acoustic emission in host-rock material for radioactive waste disposal: comparison between clay and rock salt. *Bulletin of Engineering Geology and the Environment*, 61 (4), 379–387, 2002.
- Le, T. M. H., Gallipoli, D., Sanchez, M., and Wheeler, S. J. Stochastic analysis of unsaturated seepage through randomly heterogeneous earth embankments. *International Journal for Numerical and Analytical Methods in Geomechanics*, 36 (8), 1056–1076, 2012.
- Le Pense, S., Arson, C., Gatmiri, B., and Pouya, A. Simulation of the Unsaturated Excavation Damage Zone around a Tunnel Using a Fully Coupled Damage-Plasticity Model. In *Poromechanics V: Proceedings of the Fifth Biot Conference on Poromechanics*, pages 2556–2565, Vienna, Austria, 2013.
- Lemaitre, J. and Chaboche, J.-l. Aspect phénoménologique de la rupture par endommagement. *Journal de Mécanique Appliquée*, 2 (3), 317–365, 1978.
- Leong, E. C. and Rahardjo, H. Review of Soil-Water Characteristic Curve Equations. *Journal of Geotechnical and Geoenvironmental Engineering*, 123 (12), 1106–1117, 1997.
- Lewis, R. W. and Schrefler, B. A. *The finite element method in the deformation and consolidation of porous media*. John Wiley and Sons Inc., New York, NY, 1987.
- Lloret, A. and Alonso, E. E. Consolidation of unsaturated soils including swelling and collapse behaviour. *Géotechnique*, 30 (4), 449–477, 1980.
- Maleki, K. and Pouya, A. Numerical simulation of damage–Permeability relationship in brittle geomaterials. *Computers and Geotechnics*, 37 (5), 619–628, 2010.
- Masín, D. Predicting the dependency of a degree of saturation on void ratio and suction using effective stress principle for unsaturated soils. *International Journal for Numerical and Analytical Methods in Geomechanics*, 34 (1), 73–90, 2010.

- Mazars, J. *Application de la mécanique de l'endommagement au comportement non linéaire et à la rupture du béton de structure*. PhD thesis, Université Pierre et Marie Curie, 1984.
- Miller, E. E. and Miller, R. D. Physical Theory for Capillary Flow Phenomena. *Journal of Applied Physics*, 27 (4), 324–332, 1956.
- Mira, P., Pastor, M., Li, T., and Liu, X. A new stabilized enhanced strain element with equal order of interpolation for soil consolidation problems. *Computer Methods in Applied Mechanics and Engineering*, 192 (37-38), 4257–4277, 2003.
- Mualem, Y. A new model for predicting the hydraulic conductivity of unsaturated porous media. *Water Resources Research*, 12 (3), 513–522, 1976.
- Nuth, M. and Laloui, L. Effective stress concept in unsaturated soils: Clarification and validation of a unified framework. *International Journal for Numerical and Analytical Methods in Geomechanics*, 32 (7), 771–801, 2008.
- Olivella, S., Carrera, J., Gens, A., and Alonso, E. E. Nonisothermal multiphase flow of brine and gas through saline media. *Transport in Porous Media*, 15 (3), 271–293, 1994.
- Ortiz, M. A constitutive theory for the inelastic behavior of concrete. *Mechanics of Materials*, 4 (1), 67–93, 1985.
- Pereira, J.-M. and Arson, C. Retention and permeability properties of damaged porous rocks. *Computers and Geotechnics*, 48, 272–282, 2013.
- Péron, H. *Desiccation cracking of soils*. PhD thesis, École Polytechnique Fédérale de Lausanne, 2008.
- Philip, J. R. and De Vries, D. A. Moisture movement in porous materials under temperature gradients. *Transactions American Geophysical Union*, 38 (2), 222–232, 1957.
- Potts, D. M. and Gens, A. A critical assessment of methods of correcting for drift from the yield surface in elasto-plastic finite element analysis. *International Journal for Numerical and Analytical Methods in Geomechanics*, 9 (2), 149–159, 1985.
- Preisig, M. and Prévost, J. H. Stabilization procedures in coupled poromechanics problems: A critical assessment. *International Journal for Numerical and Analytical Methods in Geomechanics*, 35 (11), 1207–1225, 2011.
- Puzrin, A. M. and Houlsby, G. T. Fundamentals of kinematic hardening hyperplasticity. *International Journal of Solids and Structures*, 38 (21), 3771–3794, 2001.
- Rampello, S., Viggiani, G. M. B., and Amorosi, A. Small-strain stiffness of reconstituted clay compressed along constant triaxial effective stress ratio paths. *Géotechnique*, 47 (3), 475–489, 1997.
- Romero, E. *Characterisation and thermo-hydro-mechanical behaviour of unsaturated Boom clay: an experimental study*. PhD thesis, Universitat Politècnica de Catalunya, 1999.
- Roscoe, K. H. and Burland, J. B. On the generalized stress-strain behaviour of ‘wet’ clay. *Engineering plasticity*, 3, 539–609, 1968.

- Roscoe, K. H., Schofield, A. N., and Wroth, C. P. On the yielding of soils. *Géotechnique*, 8 (1), 22–53, 1958.
- Roscoe, K. H., Schofield, A. N., and Thurairajah, A. Yielding of clays in states wetter than critical. *Géotechnique*, 13 (3), 211–240, 1963.
- Rouainia, M. and Muir wood, D. A kinematic hardening constitutive model for natural clays with loss of structure. *Géotechnique*, 50 (2), 153–164, 2000.
- Schofield, A. N. and Wroth, C. P. *Critical state soil mechanics*. McGraw-Hill London, 1968.
- Schrefler, B. A. FE in environmental engineering: coupled thermo-hydro-mechanical processes in porous media including pollutant transport. *Archives of Computational Methods in Engineering*, 2 (March), 1–54, 1995.
- Schrefler, B. A., Zhan, X., and Simoni, L. A coupled model for water flow, airflow and heat flow in deformable porous media. *International Journal of Numerical Methods for Heat & Fluid Flow*, 5 (6), 531–547, 1995.
- Shao, J., Zhou, H., and Chau, K. T. Coupling between anisotropic damage and permeability variation in brittle rocks. *International Journal for Numerical and Analytical Methods in Geomechanics*, 29 (12), 1231–1247, 2005.
- Shao, J., Jia, Y., Kondo, D., and Chiarelli, A.-S. A coupled elastoplastic damage model for semi-brittle materials and extension to unsaturated conditions. *Mechanics of Materials*, 38 (3), 218–232, 2006.
- Shaw, P. and Brown, S. F. Behaviour of dry granular materials under repeated load biaxial and triaxial stress conditions. *Géotechnique*, 38 (4), 627–634, 1988.
- Sheng, D. and Zhou, A.-N. Coupling hydraulic with mechanical models for unsaturated soils. *Canadian Geotechnical Journal*, 48 (5), 826–840, 2011.
- Sheng, D., Sloan, S. W., Gens, A., and Smith, D. W. Finite element formulation and algorithms for unsaturated soils. Part I: Theory. *International Journal for Numerical and Analytical Methods in Geomechanics*, 27 (9), 745–765, 2003.
- Sheng, D., Sloan, S. W., and Gens, A. A constitutive model for unsaturated soils : thermomechanical and computational aspects. *Computational Mechanics*, 33 (6), 453–465, 2004.
- Sheng, D., Zhang, S., and Yu, Z. Unanswered questions in unsaturated soil mechanics. *Science China Technological Sciences*, 56 (5), 1257–1272, 2013.
- Shin, H. and Santamarina, J. C. Desiccation cracks in saturated fine-grained soils: particle-level phenomena and effective-stress analysis. *Géotechnique*, 61 (11), 961–972, 2011.
- Simo, J. C. and Ju, J. W. Strain- and stress-based continuum damage models—I. Formulation. *International Journal of Solids and Structures*, 23 (7), 821–840, 1987.

- Sloan, S. W., Abbo, A. J., and Sheng, D. Refined explicit integration of elastoplastic models with automatic error control. *Engineering Computations*, 18 (1-2), 121–154, 2001.
- Sophocleous, M. Analysis of water and heat flow in unsaturated-saturated porous media. *Water Resources Research*, 15 (5), 1195–1206, 1979.
- Sołowski, W. T. and Gallipoli, D. Explicit stress integration with error control for the Barcelona Basic Model. Part I: Algorithms formulations. *Computers and Geotechnics*, 37 (1-2), 59–67, 2010.
- Sulem, J., Vardoulakis, I., Papamichos, E., Oulahna, A., and Tronvoll, J. Elasto-plastic modelling of Red Wildmoor sandstone. *Mechanics of Cohesive-frictional Materials*, 4 (3), 215–245, 1999.
- Sultan, N., Cui, Y.-J., and Delage, P. Yielding and plastic behaviour of Boom clay. *Géotechnique*, 60 (9), 657–666, 2010.
- Sun, D., Sheng, D., and Sloan, S. W. Elastoplastic modelling of hydraulic and stress-strain behaviour of unsaturated soils. *Mechanics of Materials*, 39 (3), 212–221, 2007.
- Sun, D., Sheng, D., Xiang, L., and Sloan, S. W. Elastoplastic prediction of hydro-mechanical behaviour of unsaturated soils under undrained conditions. *Computers and Geotechnics*, 35 (6), 845–852, 2008.
- Swoboda, G. and Yang, Q. An energy-based damage model of geomaterials—I. Formulation and numerical results. *International Journal of Solids and Structures*, 36 (12), 1719–1734, 1999.
- Tarantino, a. A water retention model for deformable soils. *Géotechnique*, 59 (9), 751–762, 2009.
- Thomas, H. R. and He, Y. Analysis of coupled heat, moisture and air transfer in a deformable unsaturated soil. *Géotechnique*, 45 (4), 677–689, 1995.
- Tsang, C.-F., Bernier, F., and Davies, C. Geohydromechanical processes in the Excavation Damaged Zone in crystalline rock, rock salt, and indurated and plastic clays—in the context of radioactive waste disposal. *International Journal of Rock Mechanics and Mining Sciences*, 42 (1), 109–125, 2005.
- Vachaud, G., Gaudet, J., and Kuraz, V. Air and water flow during ponded infiltration in a vertical bounded column of soil. *Journal of hydrology*, 22, 89–108, 1974.
- Valès, F. *Modes de déformation et d'endommagement de roches argileuses profondes sous sollicitations hydro-mécaniques*. PhD thesis, École Polytechnique, 2008.
- van Genuchten, M. T. A closed-form equation for predicting the hydraulic conductivity of unsaturated soils. *Soil Science Society of America Journal*, 44 (5), 892–898, 1980.
- Van Marcke, P. and Bastiaens, W. Excavation induced fractures in a plastic clay formation: Observations at the HADES URF. *Journal of Structural Geology*, 32 (11), 1677–1684, 2010.

- Vermeer, P. A. and Verruijt, A. An accuracy condition for consolidation by finite elements. *International Journal for Numerical and Analytical Methods in Geomechanics*, 5 (1), 1–14, 1981.
- Viggiani, G. M. B. and Atkinson, J. H. Stiffness of fine-grained soil at very small strains. *Géotechnique*, 45 (2), 249–265, 1995.
- Volckaert, G., Bernier, F., Alonso, E. E., Gens, A., Samper, J., Villar, M., Martin-Martin, P., Cuevas, J., Campos, R., Thomas, H. R., Imbert, C., and Zingarelli, V. Thermal-hydraulic-mechanical and geochemical behaviour of the clay barrier in radioactive waste repositories (model development and validation). Technical report, European Commission, 1996.
- Wang, L. *Micromechanical experimental investigation and modelling of strain and damage of argillaceous rocks under combined hydric and mechanical loads*. PhD thesis, École Polytechnique, 2012.
- Wheeler, S. J., Sharma, R. S., and Buisson, M. S. R. Coupling of hydraulic hysteresis and stress-strain behaviour in unsaturated soils. *Géotechnique*, 53 (1), 41–54, 2003.
- White, J. a. and Borja, R. I. Stabilized low-order finite elements for coupled solid-deformation/fluid-diffusion and their application to fault zone transients. *Computer Methods in Applied Mechanics and Engineering*, 197 (49-50), 4353–4366, 2008.
- Wroth, C. P. and Houlsby, G. T. A critical state model for predicting the behaviour of clays. In *Workshop on Limit Equilibrium, Plasticity and Generalized Stress-strain in Geotechnical Engineering*, pages 592–627, 1980.
- Yazdani, S. and Schreyer, H. L. Combined plasticity and damage mechanics model for plain concrete. *Journal of engineering mechanics*, 116 (7), 1435–1450, 1990.
- Zhu, Q. Z., Kondo, D., and Shao, J. Micromechanical analysis of coupling between anisotropic damage and friction in quasi brittle materials: Role of the homogenization scheme. *International Journal of Solids and Structures*, 45 (5), 1385–1405, 2008.
- Zhu, Q. Z., Shao, J., and Kondo, D. A micromechanics-based thermodynamic formulation of isotropic damage with unilateral and friction effects. *European Journal of Mechanics - A/Solids*, 30 (3), 316–325, 2011.
- Zienkiewicz, O. C., Taylor, R. L., and Zhu, J. *The Finite Element Method: Its Basis and Fundamentals*. Butterworth-Heinemann, 2005.
- Zimmerman, R. W. *Compressibility of sandstones*. Elsevier Science, 1990.
- Zytynski, M., Randolph, M. F., Nova, R., and Wroth, C. P. On modelling the unloading-reloading behaviour of soils. *International Journal for Numerical and Analytical Methods in Geomechanics*, 2 (1), 87–93, 1978.